ICTRS
2012

First International Conference on
Telecommunications and Remote Sensing

Proceedings
Sofia, Bulgaria 29 - 30 August, 2012

Organized by:

In Cooperation with:

Technical Co-Sponsorship:

ICREST

БЪЛГАРСКА
АКАДЕМИЯ
на НАУКИТЕ
— 1869 —

TECHNICAL UNIVERSITY OF SOFIA

MINISTRY OF DEFENCE
DEFENCE INSTITUTE

CONTENTS

Remote Sensing

Telecommunications and Signal Processing

ABSTRACTS

KEYNOTE SPEAKERS

BISTATIC SYNTHETIC APERTURE RADAR TECHNOLOGY - TOPOLOGIES AND APPLICATIONS

Andon Dimitrov Lazarov

CITS, Bourgas Free University,62 San Stefano Str. Bourgas, Bulgaria
lazarov@bfu.bg

Abstract: Bistatic Synthetic Aperture Radar (BSAR) and Bistatic Forward Inverse Synthetic Aperture Radar (BFISAR) concepts are considered. Different BSAR topologies with transmitter of opportunity, stationary receiver with moving target are analyzed. Forward scattering RCS is defined. Mathematical models of BSAR and BFISAR signals and image reconstruction algorithms are presented. Results of numerical experiment are discussed.

1 INTRODUCTION

Bistatic synthetic aperture radar (BSAR) technique is under intensive research activities over the last ten years. It makes an impact on the progress in synthetic aperture radar (SAR) and inverse synthetic aperture radar (ISAR) technologies and meets strong requirements for the further enhancement of microwave remote sensing systems. It is expected that the implementation of BSAR concept in ISAR will enlarge the area of application and improve substantially the functionality of imaging radars.
Bistatic concept in SAR for Earth observation is analyzed in (Moccia A., 2002). Prospective and problems in space-surface BSAR are addressed in (Cherniakov M., 2002) and BSAR with application to moving target detection is described in (Whitewood A., 2003). Several BSAR techniques for image reconstruction have been proposed that provide effective tools for radar imaging of cooperative targets (D'Aria D., 2004). Effects of bistatic configurations on ISAR imaging have been largely investigated in (Martorella M., 2007).

2 BISTATIC SYNTHETIC APERTURE RADAR CONFIGURATIONS

2.1 Bistatic Radar Geometry

Bistatic radar geometry comprises a transmitter, located in point *A*, a receiver located in point *B*, and target located in point *T* (Fig. 1). Denote θ as a bistatic angle, $L = AB$ as a baseline, and Δ_R as range resolution
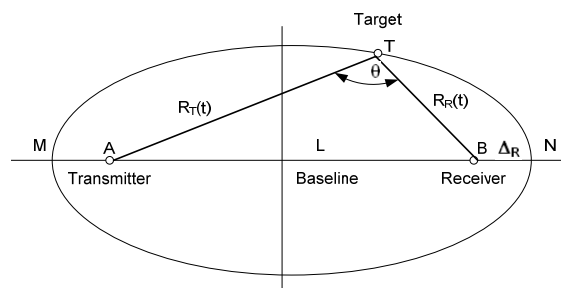
Figure 1: Bistatic radar geometry

Contours of constant bistatic range are ellipses with transmitter and receiver as two foci. The following equations can be written

$$R_\text{T}(t) + R_\text{R}(t) = L + n.\Delta_\text{R}, \qquad (1)$$

$$\cos\theta = \frac{R_T^2(t) + R_R^2(t) - L^2}{2R_T(t)R_T(t)}, \qquad (2)$$

where $n = 0,1,2, \ldots$ is the number of an isorange ellipse. The number $n = 0$ corresponds to zero range resolution on baseline *L*.

2.2 Bistatic Radar Equation

Bistatic radar equation represents signal-to-noise ratio as a function of parameters of electromagnetic propagation, radar and target, i.e.

$$\frac{P_R}{P_N} = \frac{P_T G_T G_R F_T^2 F_R^2 \lambda^2 \sigma_B L_p \cdot}{(4\pi)^3 R_T^2 R_R^2 k T_0 B F} \tag{3}$$

where P_R - receiver power; P_N - noise power; R_T - distance from the transmitter to the target; R_R - distance from the receiver to the target σ_B - bistatic radar cross − section of the target; G_T - transmitter gain; G_R-receiver gain; F_T^2-pattern propagation factor for the transmitter-to-target-path; F_R^2- pattern propagation factor for the target-to-receiver path; k - Boltzmann's constant; λ -wavelength; F – Figure of merit; T_0 -noise temperature.

The constant detection range is defined by $R_T R_R$ = const that describes ovals of Cassini around transmitter and receiver points (Fig. 2).
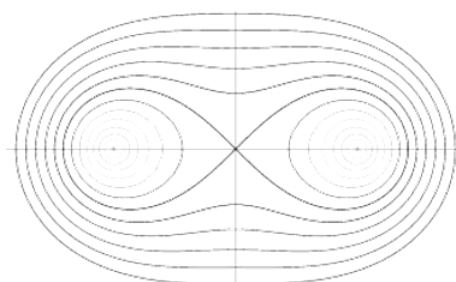
Figure 2: Ovals of Cassini

2.3 BSAR for Local Area Monitoring

A new topology of BSAR with non cooperative transmitter is presented in (Cherniakov M., 2009,). The topology includes Global Navigation Satellite Systems (GNSS) as transmitters of opportunity and a stationary receiver placed on the ground. It is a system for local area monitoring. BSAR with non cooperative transmitter is a sub-class class of bistatic SAR systems that comprises a spaceborne transmitter, and a receiver located on or near the Earth's surface (Fig. 3). As a sub-class of BSAR, it encompasses a variety of system topologies. Any communication or Global Positioning System (GPS) satellite can be used as a noncooperative transmitter while the receiver could be airborne, onboard a ground moving vehicle or stationary on the ground.

Different BSAR configurations have been considered (Whitewood A., 2007). It has been the investigated passive BSAR, with GNSS as transmitters of opportunity (such as GPS, GLONASS and Galileo) and an airborne receiver (Antoniou M., 2009).
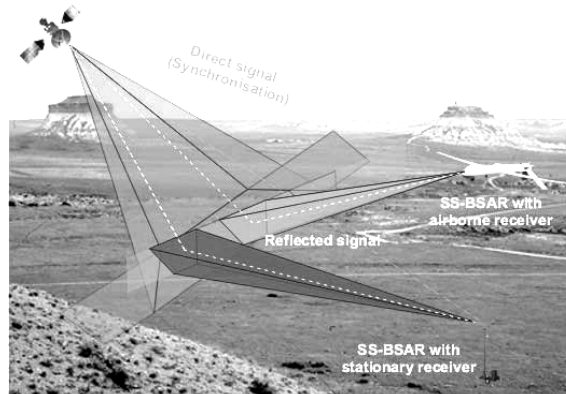
Figure 3: BSAR topologies

An image with a Galileo satellite as a transmitter and a ground moving vehicle as a receiver has been obtained (Fig. 4)

Figure 4: BSAR image of a building with Galileo as the transmitter and a moving ground vehicle as the receiver superimposed on a satellite optical photograph (a), optical photograph (b).

The BSAR topology with a satellite transmitter has military applications based on the potential of the system to operate covertly due to its passive nature, its ability to provide constant monitoring of any

remote region on the Earth due to the global coverage of the GNSS satellites. It is important to investigate whether this system can be implemented, to consider satellite availability, to identify whether fast update rates for change detection can be achieved, to examine basic radar functionality, which involves calculations on integration time, resolution and power budget.

2.3.1 Satellite availability and observation time

Satellite availability can help define the available observation time for imaging and the update rates for change detection. It means the number of satellites simultaneously visible at any point in the world and the position of each satellite with respect to the receiver to be defined. An optimal satellite can be used for imaging to minimize degradation in the system's range resolution due to the large bistatic angle (Willis N.J., 2007). It was found that approximately 6-8 satellites are simultaneously visible at a particular point on the Earth, at any time (Zuo R., 2007). Another issue is the achievable observation time. This is defined as the amount of time that a target on the Earth is within the beam of a satellite (assuming it is always within the beam of the receiver). Even though the beam of the GNSS satellites covers a large part of the Earth's surface, the observation time may vary significantly from one satellite to another because of their position with respect to the target. Fig. 5 shows results of Keplerian modelling to define observation time versus satellite number (Cherniakov M., 2009).
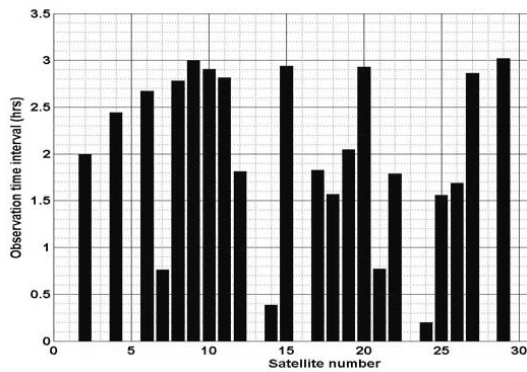
Figure 5: Observation time versus satellite number according to Keplerian modeling

The figure shows that within an interval of one day, 22 satellites are visible in a nearly quasi-monostatic mode, with observation times varying from 12 minutes to 3 hours. These values allow for very long integration times due to satellites' wide beam. It

provides fine azimuth resolutions, and enhances power budget of the system.

2.3.2 Azimuth resolution

GNSS satellites on MEO with ranges of 23000 km from the Earth, orbital speeds 4 km/s, and long observation time provide a significant improvement in azimuth resolution. The maximum azimuth resolution that can be achieved for data in Fig. 5 is shown in Fig. 6. The resolution is calculated through Doppler bandwidth of the associated GPS azimuth signals, and dividing with the average speed of the satellite towards the observed target. The figure shows that extremely high azimuth resolutions can be potentially achieved if the full observation time is processed. Even for an observation time of 12 minutes the resolution is reasonable.
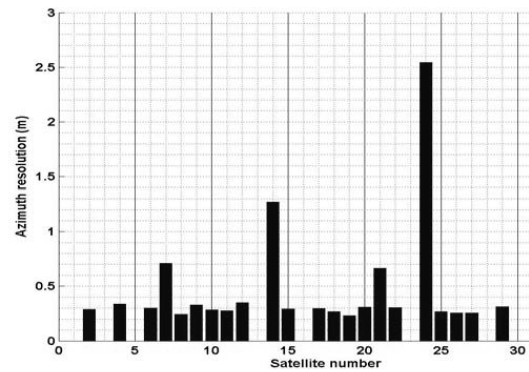
Figure 6: Potential azimuth resolution for SS-BSAR with stationary receiver.

2.3.3 Power Budget

Since GNSS satellites exhibit a low signal power density on the Earth's surface, long observation times will essentially enhance the signal-to-noise ratio (SNR) at the output of the image formation algorithm used. Assuming full target signal compression in both range and azimuth, the SNR can be derived as

$$SNR = \frac{P_D G_R \lambda^2 \sigma}{(4\pi)^2 R_R^2 k T_s} T_{\text{int}} \frac{T_{obs}}{\Delta u} \qquad (4)$$

where P_D is the signal power density of the GNSS satellites on the Earth, G_R is the gain of the receiving antenna, λ is the radar wavelength, σ is the target radar cross section, R_R is the receiver-to-target range, k is Boltzmann's constant, T_S is the receiver noise temperature, T_{int} is the integration time in the range direction (equal to the length of the transmitted

GNSS code sequence), T_{obs} is the observation time and Δu is the azimuth sample spacing.

The challenge in this task is the long integration time, over which the trajectory of the satellite can no longer be considered a straight line. It can be seen in Fig. 7, where the trajectory of one of the satellites in our previous example (Fig. 5, satellite number 14) has been plotted in 3-D space.
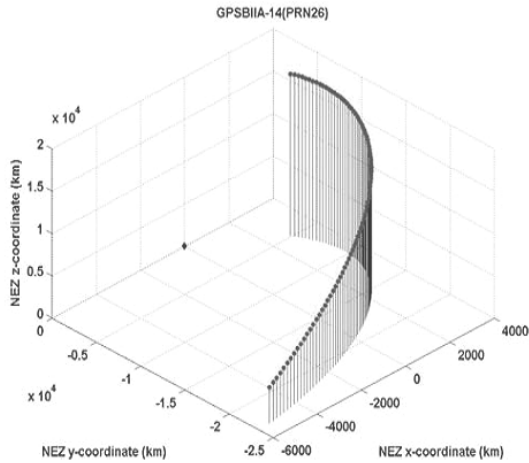
Figure 7: Example of a satellite trajectory over a long observation time (satellite number 14)

2.3.4 Signal synchronization in BSAR based on GLONASS satellite emission

BSAR coherent signal processing requires synchronization between the transmitter and the receiver (Fig. 8) (R.Saini, 2009).
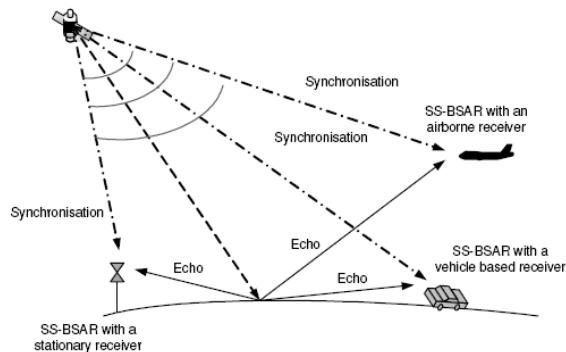
Figure 8: BSAR topolody with synchronization.

Fig. 9 illustrates block diagram of the structure of GLONASS signals transmitted in the L_1 frequency band. The C/A and P-code signals are in phase quadrature. The C/A code rate is 511 KHz and the code period is 1 msec. The C/A code sequence is added (mod 2) to a 100 Hz navigation message. The P-code has a chip rate of 5.11 MHz and is a truncated M-sequence repeated every 1 sec. The

navigation message on the P-code has a clock rate of 50 Hz. The P-code is used for the purpose of imaging, as it provides a reasonable range resolution of about 30m (quasi-bistatic case) and is no longer encrypted. It is worth mentioning that utilization of a GALILEO satellite E_5 signal (20-50 MHz bandwidth) would improve the range resolution to about 3-8 m.
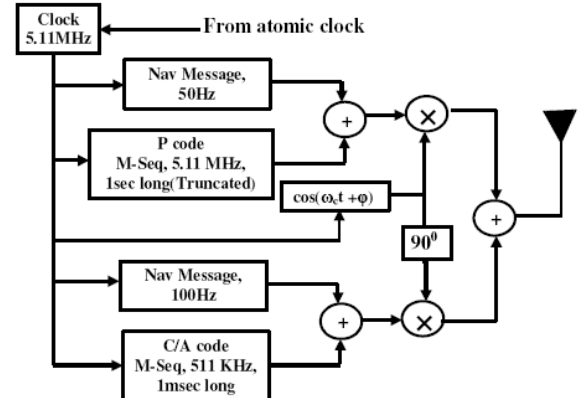
Figure 9: Signal structure of GLONASS

Usually in a radar signal processor, the range compression consists of a correlation of the radar channel signal with the heterodyne channel signal delayed for each range resolution cell in the multi-channel correlator (Fig. 10).
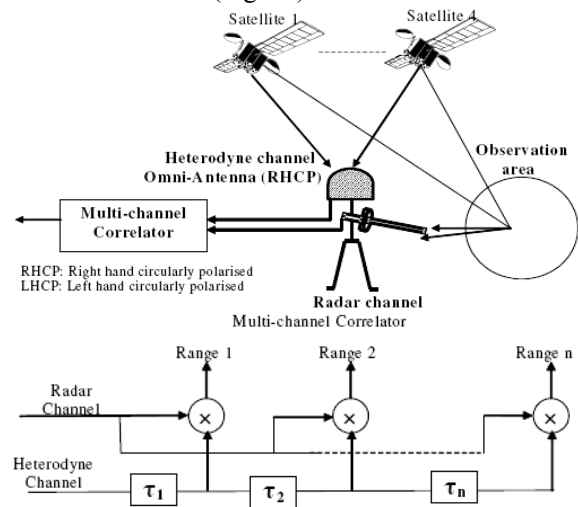
Figure 10: Heterodyne channel with omny antenna (*a*) and multi-channel correlator (*b*).

It was demonstrated that for GLONASS signal it is not possible to directly correlate the heterodyne channel with the radar channel. The signal received from the GLONASS satellite is a superposition of the C/A code and P-code signals, the spectra of which overlap; the P-code (5.11 MHz bandwidth) is used for the purpose of imaging. If the heterodyne

channel is directly correlated with the radar channel, the P-code will be masked by the C/A code at the output of the correlator. The bandwidth of the C/A code is only one-tenth that of the P-code but even if the C/A code of the desired satellite signal is filtered out in the heterodyne channel, the signal correlation properties are degraded by the C/A codes of interfering satellites. It was demonstrated that, if the radar channel signal is correlated with a locally generated signal containing only the P-code, the effect of the C/A code could be suppressed. However this technique needs navigation message decoding which, in turn, requires P-code synchronization. Fig. 11 illustrates a range compression algorithm. Fig. 12 shows a simplified synchronization block diagram.
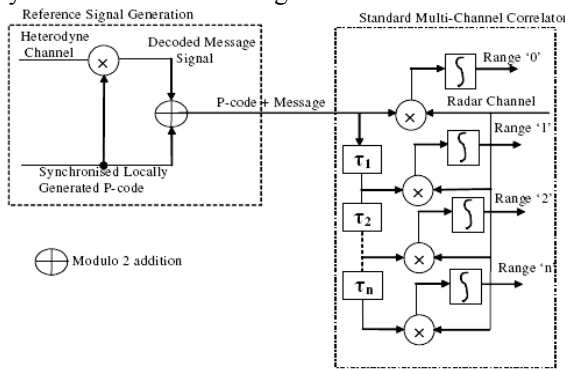
Figure 11: Range compression algorithm.
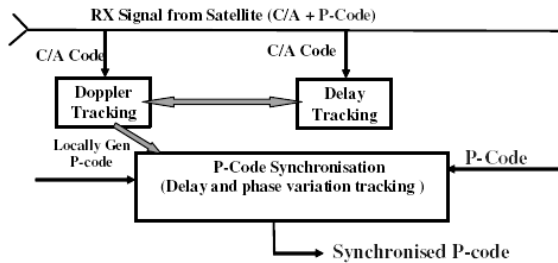
Figure 12: Synchronization block diagram

A synchronization block diagram is presented in Fig. 12. The P-code has a better delay tracking accuracy due to its wider signal bandwidth compared to the C/A code. The synchronization algorithm is based on a conventional delay locked loop, and consists of:
- Doppler extraction using the C/A code and applying conventional phase locked loops.
- Removing the frequency shift from the received P-code by extracting frequency variation.
- Synchronize the locally generated P-code to the Doppler-stripped P-code.
- Decode the navigation message signal by synchronized P-code, fraction of a chip. Once the

incoming P-code has been acquired, tracking, or fine synchronization, takes place.

2.4 Bistatic generalized inverse synthetic aperture radar

Consider geometry of BSAR scenario with a moving target illuminated by GPS waveform and a stationary GPS receiver. It refers to geometry of Generalized Inverse Synthetic Aperture Radar (GISAR) and Bistatic Synthetic Aperture Radar (BSAR) and regards as Bistatic Generalized Inverse Synthetic Aperture Radar (BGISAR). The problem posed is to describe the discrete geometry of BGISAR scenario and based on it to derive a mathematical model of a BGISAR signal (Lazarov A., 2011).

2.4.1 BGISAR Scenario

BGISAR scenario is illustrated in Fig. 13 where GPS transmitter, receiver (located on the land surface) and a target are all situated in $Oxyz$, where $\mathbf{R}^s(p)$ is the current position vector of the transmitter in discrete time instant p, $\mathbf{R}_{00'}(p)$ is the current position vector of the mass center of the target, $\mathbf{R}^r$ is the stationary position vector of the receiver. The target presented as an assembly of point scatterers is depicted in Cartesian coordinate system $OXYZ$, where $\mathbf{R}_{ijk}$ is the position vector of the ijkth point scatterer.
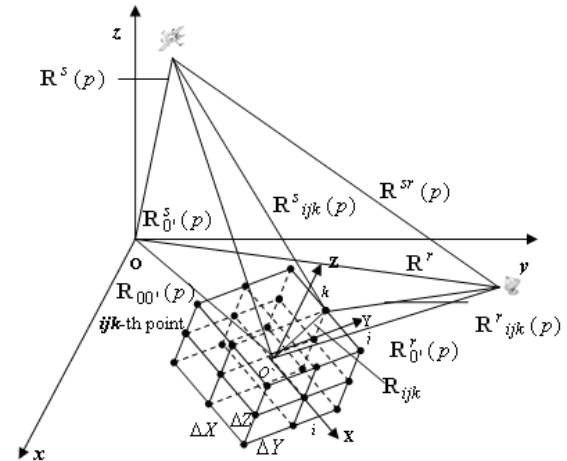
Figure 13: BGISAR geometry

In Fig. 13: $\mathbf{R}_{0'}^s(p)$ - the position vector of the target's mass center with respect to the transmitter, $\mathbf{R}_{0'}^r(p)$ - The position vector of the target's mass

center with respect to the receiver, $\mathbf{R}^s_{ijk}(p)$ - the position vector of the ijkth point scatterer with respect to the transmitter, $\mathbf{R}^s_{ijk}(p)$ - the position vector of the ijkth point scatterer with respect to the receive, ΔX, ΔY, ΔZ – dimensions of the resolution cell.

The round trip distance from GPS transmitter to the target and GPS receiver is defined by

$$R_{ijk}(p) = \left| \mathbf{R}^s_{ijk}(p) \right| + \left| \mathbf{R}^r_{ijk}(p) \right|. \qquad (5)$$

The deterministic component of the BGISAR signal, reflected by all point scatterers of the object for every p th GPS C/A pulse train has the form

$$S(p,t) = \sum_{ijk} a_{ijk} \mathbf{rect}[T_{ijk}(p)]\mathbf{exp}\left\{ \begin{matrix} -j[\omega(t - t_{ijk}(p)) \\ +\pi b(t)] \end{matrix} \right\} \quad (6)$$

where $T_{ijk}(p) = \dfrac{t - t_{ijk}(p)}{T}$ is the time parameter

$\omega = 2\pi c / \lambda$ is the angular frequency, $c = 3.10^8$ m/s is the velocity of the light, $b(t)$ is the binary parameter of the C/A phase code modulated pulse train, defined by coefficients of two Gold polynomials, a_{ijk} is the reflective coefficient of the ijkth point scatterer, three-dimensional (3-D) image function; T is the time duration of the C/A phase code, $t_{ijk}(p) = \dfrac{R_{ijk}(p)}{c}$ is the round trip delay to ijk th point scatterer; $t = t_{ijk\,min}(p) + (k-1)\Delta T$, ΔT is the time duration of the phase segment, k is the current number of segment, $K = T / \Delta T = 1023$ is the full number of segments of the C/A phase code, is the relative dimension of the target.

The image extraction procedure comprises

1. Phase correction, $\widetilde{S}(p,k) = \hat{S}(p,k).\mathbf{exp}(j\Phi(p))$,

2. Range compression by cross-correlation,

$$\widetilde{S}(\hat{p},\hat{k}) = \sum_{k=\hat{k}}^{\hat{k}+K-1} \widetilde{S}(p,k)\mathbf{exp}[j\pi b((k - \hat{k} + 1)\Delta T)],$$

3. Azimuth compression by Fourier transform,

$$a_{ijk}(\hat{p},\hat{k}) = \sum_{p=1,N} \widetilde{S}(p,\hat{k})\mathbf{exp}\left\{ j\left[\frac{2\pi}{N}\hat{p}p \right] \right\}.$$

2.4.2 BGISAR numerical experiment

A numerical experiment was carried out to verify the geometry and 3-D model of BGISAR signal with GPS C/A code phase modulation and to prove the correctness of developed digital signal image reconstruction procedure. It is assumed that the target, a flying helicopter is moving rectilinearly in a 3-D Cartesian coordinate system of observation $Oxyz$. GPS transmitter emits a C/A code train. GPS satellite velocity: $v = 3819,206$ m/s. Coordinates of the stationary GPS receiver: $x^r = 55$ m, $y^r = 45$ m and $z^r = 30$ m. The trajectory parameters of the target: velocity $V = 80$ m/s; guiding angles. Parameters of the GPS C/A pulse trains: wavelength $\lambda = 19,1.10^{-2}$ m (carrier frequency $f = 1.57.10^9$ Hz), registration time interval $T_p = 2,2.10^{-3}$ s, GPS C/A code PRF 1.023 MHz and respective time duration of the segment of the C/A pulse $\Delta T = 0.9775.10^{-6}$ s, time duration of GPS C/A code $T = 10^{-3}$ s; full number of GPS C/A pulses $K = 1023$, number of transmitted GPS C/A code trains during aperture synthesis $N = 1024$. In Fig. 2 results are presented.

(a)   (b)
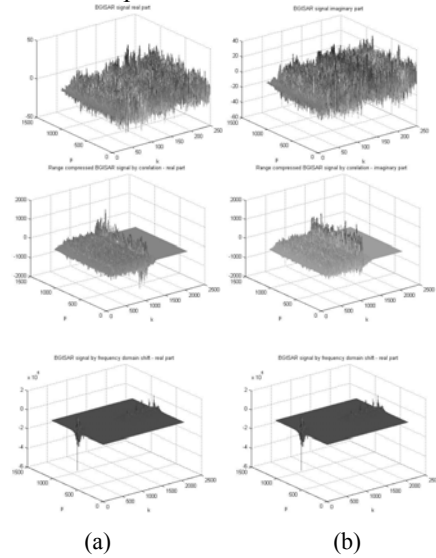
Figure 14. BGISAR signal processing stages: real (a) and imaginary (b) parts, range compressed by correlation and azimuth compressed by Fourier transform.

(a)   (b)
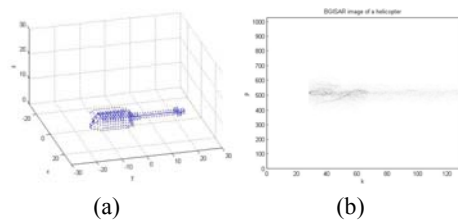
Figure 15. Original image of helicopter (a) BGISAR image of helicopter (b)

3 BISTATIC FORWARD SCATTERING RADAR CONFIGURATIONS

3.1 Bistatic forward scattering radar processing

Bistatic forward scattering radar (BFSR) is a sub-class of bistatic radars, with a moving target and bistatic angle between transmitter-target-receiver close to 180^0. The received signals are formed by diffraction of the emitted electromagnetic waves. The target can be considered as a secondary antenna which has the target's silhouette and with gain, defined by the target radar cross-section (RCS) which is independent from the target material. Such systems can be used for stealth targets detection.

3.1.1 BFSR Scenario

Consider a BFSR scheme using CW signals for situation awareness that includes a transmitter T and receiver R situated on the ground or see surface and a target with distances transmitter-target $R_T(t)$ and target-receiver $R_R(t)$, and bistatic angle $\theta(t)$ (Fig. 16). Targets (humans or vehicles) are moving across the transmitter-receiver baseline. A signature of a moving target is received at the background of clutter, noise and possibly interference.
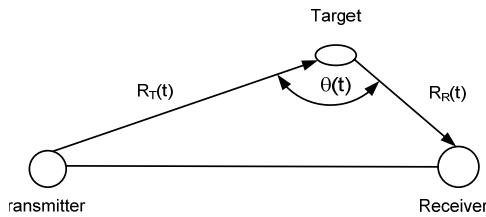
Figure 16: BFSR scenario.

The deterministic signal at the input of the receiving antenna is given by the sum of the direct transmitter-receiver (leakage) signal and the signal reflected from the target. The leakage signal is much stronger than the signal from the target which can be separated based on the Doppler signature induced by displacement of the target.

3.1.2 BFSR signal processing and parameter estimation

Signature processing includes signal compression and target resolution by maximization of signal-to-noise ratio (SNR) as the target signature could be buried under noise at longer baselines (Cheng Hu, 2008).

Let target's speed be a parameter estimated on the baseline. Assume that the signal is corrupted only by additive white Gaussian noise. SNR maximization is realized by correlating the received signal $S_T(t)$ with a reference function $S_0(t)$, complex conjugated of the target signature itself. The correlation process is described by the equation

$$S(\tau) = \int_{-\frac{T}{2}}^{\frac{T}{2}} S_T(t) S_0(t-\tau) dt \qquad (7)$$

where T is the coherent processing interval, τ is the correlation displacement.

This process is known as matched filtering, and referred to as optimal signal processing algorithm. If the reference function has a rectangular envelop, the signal processing is quasi optimal.
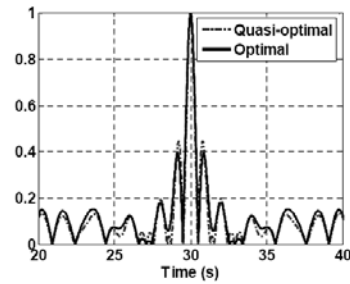
Figure 17: Signature compression by optimal and quasi optimal processing algorithms.

Compressed signatures for a single target obtain by optimal and quasi optimal processing algorithms are presented in Fig. 17.

3.2 BFSR radar cross section estimation

BFSR concept can be applied in monitoring and protecting coast lines and off shore territories. Using a chain of buoys, located on the sea surface and equipped with FSR transceivers, schematically shown in Fig. 18 (Liam Daniel, 2008).
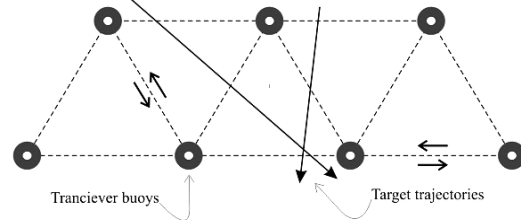
Figure 18: A chain of buoys, located on the sea surface and equipped with FSR transceivers

Objects crossing the baselines connecting adjacent transceiver buoys could be detected through analysis of their Doppler signature. Small targets with low radar reflectivity such as jet-skis, inflatable boats and swimmers could be detected.

BFSR RCS can be defined through optical approximation: BFSR RCS of a complex object is reduced to the radiation pattern of the silhouette shape of that object (black body approximation), and finding of the radiation pattern of this silhouette's uniformly (planar) illuminated complimentary plane aperture (Babinet's principle) (Fig. 19) (Daniel L., 2008).
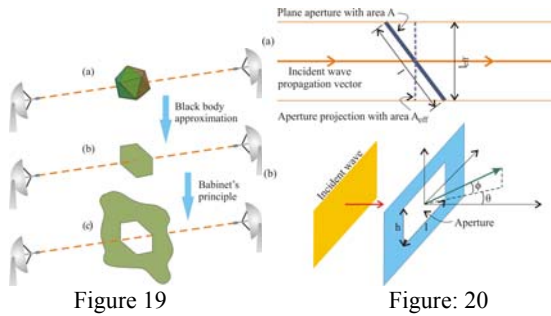
Figure 19   Figure: 20

Figure 19: Scatter from a complex object (a), reduced to scatter from a plane shape (b), further reduced to diffraction from an aperture (c).

Figure 20: Aperture projections in plane perpendicular to wave propagation vector and (b) angular definitions for analytic RCS (8).

In the direct forward scatter direction of incident wave propagation, the FS RCS $\sigma_{fs}(0°)$ is given by the following equation

$$\sigma_{FS}(0^0) = 4\pi \frac{(A_{eff})^2}{\lambda^2} \qquad (8)$$

λ is the wavelength of the illuminating signal and A_{eff} is the effective area of the aperture projected in the plane perpendicular to the incident wave propagation vector, shown in a top down view in Fig. 20(a). The calculation of RCS can be simplified even further by considering only purely rectangular shaped apertures. Thus the FS RCS in the analytical model approximation goes as,

$$\sigma(\theta,\phi) = \sigma_{FS}(0^0)\left[\frac{\sin\left(\frac{\pi l_{eff}}{\lambda}\sin\theta\right)}{\frac{\pi l_{eff}}{\lambda}\sin\theta}\right]\left[\frac{\sin\left(\frac{\pi h_{eff}}{\lambda}\sin\phi\right)}{\frac{\pi h_{eff}}{\lambda}\sin\phi}\right]$$

where l_{eff} and h_{eff} are the effective length and height of the aperture as defined like the effective area in (1) and also shown in Fig. 20(a). Angular definitions (θ,ϕ) are shown in Fig. 20(b).

3.2 BFSR automatic target classification network

The concept of a Forward Scattering Radar (FSR) wireless network has recently been presented for situational awareness in ground operations (Rashid N.E.A., 2008). Its primary objectives are the detection, parameter estimation (such as speed) and automatic target classification (ATC) of various ground targets (personnel, vehicles) entering or crossing its coverage area (Fig. 21).
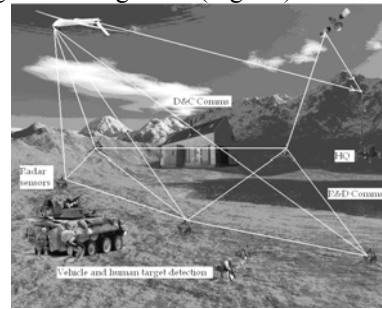
Figure 21: The concept of the FSR micro – sensors radar network (Sensors enlarged for visibility)

The system provides monitoring in remote or even inaccessible areas, and does not require manual installation of sensors. They could be spread into random positions directly on the ground from a remotely operated moving platform such as a UAV. The sensors in the wireless FSR network carry out:

- Communication to the central post (headquarter – HQ) using a wireless link through a UAV or a satellite for situational data transfer and receiving control commands (data and control – D&C).
- Neighboring nodes in the network create FSR channels and communicate to each other to transfer data and commands, if a direct link to a UAV or a satellite is impossible (radar and data lines – R&D.
- Sensors detect targets, roughly estimate target parameters and reject noise, clutter, interferences and reflections from unwanted targets (such as birds, animals).

3.3 Bistatic forward scattering inverse synthetic aperture radar

The geometry of BFISAR topology is presented in Fig. 22 (Lazarov A.). Consider stationary transmitter and receiver both located on sea surface and as a mariner target a ship all situated in a Cartesian coordinate system $Oxyz$. The target presented as an assembly of point scatterers is depicted in its own coordinate system $OXYZ$.
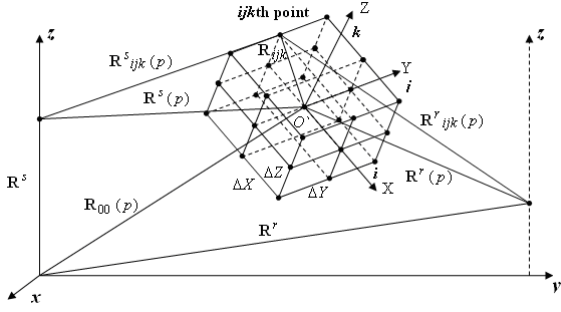
Figure 22: BFISAR Geometry

Assume linear frequency modulated (LFM) emitted signal. Then the deterministic component of BFISAR signal is superposition of signals reflected by all target's point scatterers, i.e.

$$\dot{S}(p,t) = \sum_{ijk} a_{ijk} \mathbf{rect}[T_{ijk}(t)]\mathbf{exp}\left\{-j\left[\begin{array}{c}\omega(t-t_{ijk}(p)) \\ + b(t-t_{ijk}(p))^2\end{array}\right]\right\}$$

where ω is angular frequency, b is the LFM rate, p is the number of emitted pulse.

Image reconstruction algorithm consists of

Phase correction: $\widetilde{S}(p,k) = \hat{S}(p,k).\exp[j\Phi(p,k)]$.

Range compression by inverse Fourier transform over discrete range coordinate k

$$\widetilde{S}(p,\hat{k}) = \frac{1}{K}\sum_{k=1}^{K}\widetilde{S}(p,k).\exp\left(j2\pi\frac{k\hat{k}}{K}\right), \ \hat{k} = \overline{1,K}$$

Azimuth compression by inverse Fourier transform over discrete azimuth coordinate p

$$a_{ijk}(\hat{p},\hat{k}) = \frac{1}{N}\sum_{p=1}^{N}\widetilde{S}(p,\hat{k}).\exp\left(j2\pi\frac{p\hat{p}}{N}\right), \ \hat{p} = \overline{1,N}.$$

3.3.1 BFISAR numerical experiment

Assume a target (ship on sea) is moving rectilinearly in $Oxyz$. Transmitter coordinates: $x^s = -250$ m;

$y^s = 0$ m; $z^s = 15$ m. Receiver coordinates: $x^r = 300$ m; $y^r = 0$ m; $z^r = 12$ m. Target parameters: velocity $V = 14$ m/s; LFM pulse's parameters: wavelength $\lambda = 3.10^{-2}$ m, pulse repetition period $T_p = 3,2.10^{-3}$ s, pulse width $T = 9.10^{-6}$ s, number of LFM samples $K = 256$, carrier frequency $f = 10^{10}$ Hz, sampling period $\Delta T = T/K = 1.56.10^{-8}$ s, signal bandwidth $\Delta F = 2.10^8$ Hz, LFM rate $b = 1,39.10^{14}$, number of transmitted pulses $N = 256$. Target geometry is depicted in a 3-D regular grid with cell's dimensions $\Delta X = \Delta Y = \Delta Z = 0.5$ m.

BFISAR signal, BFISAR range compressed signal and BFISAR azimuth compressed signal for $x_{00}(0) = 25$ m; $y_{00}(0) = 150$ m; $z_{00}(0) = 0$ m are presented in Figs. 23, 24 and 25.
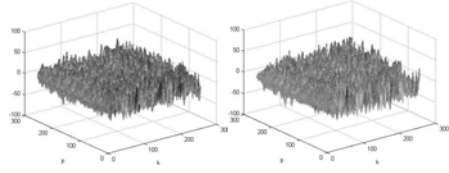
Figure 23: BFISAR signal: real (a) and (b) imaginary part.
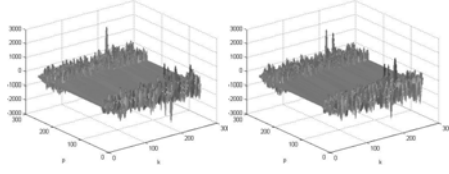
Figure 24: BFISAR range compresed signal: real (a) and (b) imaginary part.
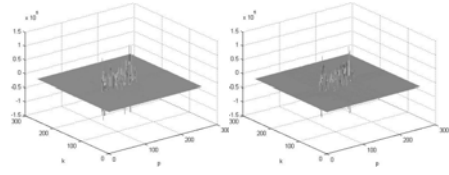
Figure 25: BFISAR azimuth compressed and shifted signal: real (a) and (b) imaginary part.

BFISAR images of the ship target at a position (*a*): $x_{00}(0) = 25$ m, $y_{00}(0) = 150$ m, $z_{00}(0) = 0$ m, and position (*b*): $x_{00}(0) = 25$ m, $y_{00}(0) = 50$ m, $z_{00}(0) = 0$ m, are presented in Fig. 26.
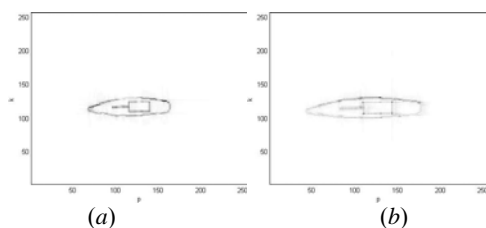
Figure 26: BFISAR images: y_{00}=150 m (a), y_{00} =50 m (b).

4   CONCLUSION

In this work bistatic radar concept and its realization are thoroughly discussed. Different BSAR configurations are analyzed. BSAR geometry and radar equation are defined. Detailed description of BSAR implementation with uncooperative satellite transmitter is presented. Special attention is given to BFSAR and BFISAR. Optimal and quasi optimal signal processing in target parameter estimation is defined. Optical approximation approach including black body approximation and Babinet's principle is applied in definition of forward scattering radar cross section. Analytical signal model of BGISAR and BFISAR and corresponding image reconstruction algorithms are presented. Results of numerical experiments are discussed. It is proven that bistatic synthetic aperture radar and even its forward scattering concept is applicable in target imaging with acceptable resolution.

ACKNOWLEDGEMENTS

REFERENCES

Moccia A., Rufmo, G., D'Errico M., Alberti, G., et. Al. 2002. BISSAT: A bistatic SAR for Earth observation In *IEEE International Geoscience and Remote Sensing Symposium (IGARSS'02)*, Vol. 5, June 24-28, pp. 2628-2630.

Cherniakov M. 2002. Space-surface bistatic synthetic aperture radar Prospective and problems, In *International Conference of Radar*, Edinburgh, UK, pp. 22-26.

Ender J. H. G., I. and A. R. Brenner 2004. New aspects of bistatic SAR: Processing and experiments. In *2004 Proceedings of International Geoscience and Remote Sensing Symposium (IGARSS)*, vol. 3, Anchorage, AK, Sept. 20—24, 2004, pp. 1758—1762.

Whitewood A., Muller B., Griffiths H., and Baker, C. 2003. Bistatic SAR with application to moving target detection. In *International Conference RADAR-2003*, Adelaide, Australia.

D'Aria D., A. M. Guarnieri, and F. Rocca, Focusing bistatic synthetic aperture radar using dip move out, *IEEE Transactions on Geoscience and Remote Sensing*, 42, no. 7, 2004, pp. 1362—1376.

Martorella M., Palmer J., Homer J., Littleton Br., and Longstaff D. 2007. On bistatic inverse synthetic aperture Radar, *IEEE, Transaction on Aerospace Electronic System*, vol. 43, no. 3, pp. 1125-1134.

Cherniakov M., Plakidis E., Antoniou M., Zuo R. 2009. Passive Space-Surface Bistatic SAR for Local Area Monitoring: Primary Feasibility Study. *In 6th European Radar Conference,* 30 Sept. - 2 Oct. 2009, Rome, Italy, pp 89-92.

Whitewood A.P., Baker C.J., Griffiths H.D. 2007. Bistatic radar using a spaceborne illuminator. In *IEE international radar conference*, Edinburgh, October 2007.

Antoniou M., Saini R., Cherniakov M. 2007. Results of a Space-Surface bistatic SAR image formation algorithm, *IEEE Trans. GRS*, vol. 45, no. 11, pp. 3359-3371.

He X., Cherniakov M., Zeng T. 2005. Signal detectability in SS-BSAR with GNSS non-cooperative transmitter. In *IEE Radar, Sonar and Navigation*, vol. 152, no. 3, pp. 124-132, June, 2005.

Antoniou M., Zuo R., Plakidis E., Cherniakov M. 2009. Motion compensation algorithm for passive Space-Surface Bistatic SAR, In *Int. Radar Conf.*, Bordeaux, France, October 2009.

Willis N.J., Griffiths H.D. 2007. *Advances in bistatic radar*, SciTech Publishing Inc.

Zuo R., Saini R., Cherniakov M. 2007. Non-cooperative transmitter selections for Space-Surface Bistatic SAR. *Anual Defence Technology Centre (DTC) Conference*, Edinburgh.

Saini R., Zuo R., Cherniakov M. 2009. Signal synchronization in SS-BSAR based on GLONASS satellite emission, DECE, University of Birmingham.

Cherniakov M., Plakidis E., Antoniou M., Zuo R. 2009. Passive Space-Surface Bistatic SAR for Local Area, Monitoring: Primary Feasibility Study, In *2009 EuMA,* 30 September - 2 October 2009, Rome, Italy

Daniel L., Gashinova M., Cherniakov M.. 2008. Maritime Target Cross Section Estimation for an Ultra-Wideband Forward Scatter Radar Network, In *2008 EuMA, Amsterdam*, pp. 316-319.

Lazarov A., Kabakchiev Ch., Rohling H., Kostadinov T. 2011. Bistatic Generalized ISAR Concept with GPS Waveform. In *IRS, Leipzig*, pp. 849-854.

Lazarov A., Kabakchiev Ch., Cherniakov M., Gashinova M., Kostadinov T. 2011. Ultra Wideband Bistatic Forward Scattering Inverse Synthetic Aperture Radar Imaging. In *2011 IRS, Leipzig*, pp. 91-96.

BRIEF BIOGRAPHY

Andon Dimitrov Lazarov received MS degree in Electronics Engineering from Sent Petersburg Electro-technical State University, Russia in 1972, and Ph. D. degree in Electrical Engineering from Air-Defense Military Academy, Minsk, Belarus in 1978, and Doctor of Sciences degree from Artillery and Air-Defense University, Bulgaria. From 2000 to 2002 he is a Professor at the Air Defence Department with Artillery and Air-Defense University. From 2002 he is a Professor with Bourgas Free University. He teaches Discrete Mathematics, Coding theory, Antennas and Propagation, Digital Signal Processing, Mobil Communications. His field of interest includes SAR, ISAR and InSAR modeling and signal processing techniques. He has authored above 150 research journal and conference papers. He is a secretary of Commission F of URSI Committee – Bulgaria, and a member of the IEEE, AES-USA, and in reviewer and editorial boards of IET - Canada, PIER & JEMWA – USA, Journal of radar technology, Beijing, China. EURASIP Journal on advances in signal processing - USA.

ELECTRIC VEHICLE ON ELECTRIFIED ROADWAY POWERED WHILE RUNNING "EVER-PWR"

Takashi Ohira

Toyohashi University of Technology, Japan
ohira@tut.jp

Abstract: Electric vehicles (EVs) are strongly expected to replace gasoline-engine motors as a green transportation. However, currently used EVs have inherent disadvantages such as too short cruising range by one charge, too long time of battery charging, too heavy weight, and too high maintaining cost. These are all due to bulky batteries onboard. To overcome those problems, there are many attempts to apply the power-while-running scheme like the electric railway to electric vehicles. One approach to this scheme is the magnetic coupling between two coils, which was first demonstrated in MIT and worldwide known as wireless electricity. This approach may be useful for charging the vehicles when they are staying at the parking lot or some facility. It would be difficult to keep a high power transfer efficiency when the vehicle is running. This is because the coils must be accurately placed to have a common axis to obtain a high efficiency. This lecture presents a novel scheme to achieve a high transfer power efficiency even while the vehicle is running. The idea stems from the railway, but how can it be done without an overhead wire? We focus on the tire with a built-in steel belt, which always touches a road on the surface. Supposing a pair of electrodes just beneath the road surface, the steel belt can pick up the power through displacement current in the tire. This scheme is called Electric Vehicle on Electrified Roadway Powered While Running or "EVER-PWR". The audience may say is it really feasible. So the lecture shows a spectacular demonstration at least in a video on the screen. As a measurement result using a scale model of EVER-PWR, an incredible power transfer efficiency exceeding 77% is exhibited. This is a major step toward the development of quite promising green vehicle technology for our sustainable future.

BRIEF BIOGRAPHY

Takashi Ohira received the B.E. and D.E. degrees in communication engineering from Osaka University, Osaka, Japan, in 1978 and 1983. In 1983, he joined NTT Electrical Communication Laboratories, Yokosuka, Japan, where he was engaged in research on monolithic integration of microwave semiconductor devices and circuits. He developed GaAs MMIC transponder modules and microwave beamforming networks aboard Japanese domestic multibeam communication satellites, Engineering Test Satellite VI (ETS-VI) and ETS-VIII, at NTT Wireless Systems Laboratories, Yokosuka, Japan. Since 1999, he has been engaged in research on wireless ad-hoc networks and microwave analog adaptive antennas aboard consumer electronic devices at ATR Adaptive Communications Research Laboratories, Kyoto, Japan. Concurrently he was a Consulting Engineer for National Space Development Agency (NASDA) ETS-VIII Project in 1999, and an Invited Lecturer for Osaka University from 2000 to 2001. From 2005, he was Director of ATR Wave Engineering Laboratories, Kyoto, Japan. Currently, he is Professor of Toyohashi University of Technology. He coauthored Monolithic Microwave Integrated Circuits (Tokyo: IEICE, 1997). Prof. Ohira was awarded the 1986 IEICE Shinohara Prize, the 1998 APMC Prize, and the 2004 IEICE Electronics Society Prize. He serves as European Microwave Association Award Councilor and IEICE Microwave Technical Group President. He is an IEEE Fellow, Founder of IEEE MTT-S Kansai Chapter, and Founder of IEEE MTT-S Nagoya Chapter.

COGNITIVE RADIO FOR GREEN RADIO COMMUNICATIONS: GREEN COGNITIVE RADIO

Jacques Palicot

SUPELEC / Institut d' Electronique et de Télécommunications de Rennes, France
jacques.palicot@supelec.fr

Abstract: Green Cognitive Radio (GCR) is a Cognitive Radio (CR) with intelligence-enhanced functionalities, which is aware of sustainable development (SD) for energy efficiency and takes it as an additional crucial constraint in the decision making process of the holistic cognitive cycle. The Brundtland Commission of the United Nations (UN) defined SD as the development that "meets the needs of the present without compromising the ability of future generations to meet their own needs". From then, several United Nations' Conferences (from Rio de Janeiro '92 to Durban '11) have confirmed this important issue. One of the most obvious aspects and challenges of SD is the earth climate change and the ever-growing CO_2 emission. Currently, 3% of the world-wide energy is consumed by the ICT (Information and Communications Technology) infrastructure, which causes about 2 % of the world-wide CO_2 emissions and surprisingly is comparable to the world-wide CO_2 emissions by all commercial airplanes. These values of carbon footprint are extreme impressive. They have been confirmed by a lot of scientific studies and reported in many relevant international conferences and workshops. Generally, Green Radio is closely related to reducing energy consumption, but Green Radio could also be envisaged in a more widespread sense, such as to optimize spectrum usage (Green spectrum), to decrease spectrum pollution (which may have great consequences for astronomic observations), to reduce electromagnetic radiation/interference levels in order to enable harmonized coexistence of multiple wireless communications systems (i.e., less interference) as well as a reduced human exposure to harmful radiations, to recycle and reuse ICT equipment, and in many other related contexts. The radio spectrum is also considered as a natural and public resource, which should be carefully used, shared world-widely and economized efficiently. Therefore, in our point of view, what is classically meant for Green Communications should be fundamentally extended and even reformed. Recently, we have claimed in that Cognitive Radio is a paradigm–shift enabling technology for realizing Green Radio. Basically, we proposed an intelligent solution based on CR approach, keeping in mind the following key objective: "Decreasing the electromagnetic level by sending the right signal in the right direction with the right power, only when it is necessary, for achieving the same QoS by taking advantage of advanced intelligence". This is the essential concept of Useful Radio Waves.

BRIEF BIOGRAPHY

Jacques Palicot received, in 1983, his PhD degree in Signal Processing from the University of Rennes. Since 1988, he has been involved in studies about equalization techniques applied to digital transmissions and new analog TV systems. Since 1991 he has been involved mainly in studies concerning the digital communications area and automatic measurements techniques. Prof. Palicot has taken an active part in various international bodies EBU, CCIR, URSI, and within RACE, ACTS and IST European projects. He has published various scientific articles notably on equalization techniques, echo cancellation, hierarchical modulations and Software Radio techniques. He is currently involved in adaptive Signal Processing and in new techniques as Software Radio and Cognitive radio. From November 2001 to September 2003 he had a temporary position with INRIA/IRISA in Rennes. He serves as Associate Editor for EURASIP JASP since 2008. He also served as lead guest editor several Special Issues on Software Radio, Cognitive Radio and Green Radio. He was Technical Program Chairman of CROWNCOM 2099 and Co General Chairman of ISCIT 2011. Since October 2003 he is with Supélec in Rennes where he leads the Signal Communications and Embedded Electronics (SCEE) research team.

RECENT SPS PROJECTS IN JAPAN

Naoki Shinohara

Research Institute for Sustainable Humanosphere, Kyoto University, Gokasho, Uji, Kyoto, Japany
shino@rish.kyoto-u.ac.jp

Abstract: Solar Power Satellite/Station (SPS) is one of important energy system in future, which is supported by radio wave technologies. The electric power which is generated in the SPS is transmitted to the Earth by microwave or laser. We need a high efficiency and light weight for microwave power transmission (MPT) system in order to reduce total cost of the SPS. There were some MPT phased array, for example, a phased array in the MILAX experiment in 1992 in Japan, a magnetron phased array in MPT airship experiment in 2009 in Japan, and a phased array in the Hawaii experiment in 2008 in US and Japan. However, there were not enough for the future SPS. Recently in Japan, there are two trials to develop a MPT phased array. One is a new phased array for collaborative inter-universities researches, which has been developed in Kyoto University in FY2010. The other is the SPS research and development project, in which we are developing thin and high efficiency phased array for MPT from FY2009. The Japanese SPS projects are based on 'Basic plan for space policy' which was established by Strategic Headquarters for Space Policy in June 2009. Beam forming and target detecting algorisms and technologies are also as important as the development of the high efficiency and light weight phased array. There are various beam forming and target detecting techniques for the SPS, for example, retrodirective target detecting with a pilot signal, Rotating Electromagnetic Vector (REV) method, Position and Angle Correction (PAC) method, etc. The Japanese SPS projects involve the verification of the various beam forming and target detecting techniques. In this paper, I show mainly developments of phased array and beam forming and target detecting techniques in the recent Japanese SPS projects.

1 INTRODUCTION

In June, 2009, Japanese Government established 'Basic plan for space policy' in order to expand Japanese space activities and technologies. In the plan, the SPS was selected on measure nine systems and programs for the utilities and R&D of space as follows;

"As a program that corresponds to the following major social needs and goals for the next 10 years, a Space Solar Power Program will be targeted for the promotion of the 5-year development and utilization plan." and "Government will conduct ample studies, then start technology demonstration project in orbit utilizing "Kibo" or small sized satellites within the next 3 years to confirm the influence in the atmosphere and system check."(Basic plan for space policy1, 2009) (Basic plan for space policy2, 2009).

Three years passed from the establishment of the Basic plan for space policy. During three years, Japanese government has changed from the Liberal Democratic Party, which had political power for a long time, to the Democratic Party of Japan. Unfortunately, there was less progress of the space policy by the Democratic Party of Japan in Japan in this three years. However, in June 20th, 2012, Japanese government established new law concerning space development which is called "Law of partly improvement of law of establishment of Cabinet Office". In the new law, they declare that Cabinet Office will have jurisdiction over Japanese space development instead of several Ministries, including Ministry of Education, Culture, Sports, Science and Technology which has jurisdiction over JAXA, which had jurisdiction over the Japanese space development simultaneously. They also declare that new space policy decision commission

will be established instead of old Space Activities Commission which leaded the Japanese space activities. Seven members of new space policy decision commission are selected in July 26th, 2012. Prof. Hiroshi Matsumoto of Kyoto University, Prof. Hiroshi Yamakawa of Kyoto University, and Prof. Shin-ichi Nakasuka of University of Tokyo are the members of new space policy decision commission.

Under the tempestuous circumstance of Japanese space policy, the Japanese SPS project and related development of a microwave power transmission (MPT) are making our way.

2 DEVELOPMENT OF PHASED ARRAY IN JAPAN

From FY2009, J-spacesystems (former USEF) starts the SPS and the MPT R&D project(Fuse, 2011). The author is committee chair of the assessment committee of the project. The purposes of the project are (1) development of high efficiency phased array and rectenna array, and (2) field MPT experiment with the developed phased array and rectenna. A historical review of the phased array is shown in Fig.1. There are two kinds of the phased array. One is a phased array with semi-conductors. The other is a phased array with magnetrons which are mainly developed in Kyoto University, Japan. There are a lot of the phased array for radar and SAR in the world. However, the phased array for the MPT and the SPS requires higher accuracy of beam forming with higher efficiency of DC-RF conversion than those for the radars. The newest phased array, which will be developed in J-spacesystems' SPS project in FY2013, will have thinnest thickness (<4cm), highest efficiency (>70% at HPA) at 5.8GHz with GaN semi-conductor and MMIC technologies.

Semi-Conductors
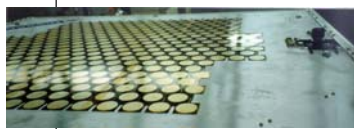
1992 (for Airplane Experiment)
2.45GHz, Total Power >1.2kW
96 array module, 3in1 sub-array
HPA PAE >40% (GaAs)
By Kyoto Univ. and Kobe Univ.
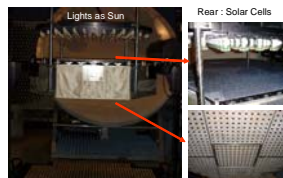
2000 SPTITZ (for SPS)
5.8GHz, Total Power >25W
100 array module with Solar Cell,
System Eff. >15% (GaAs)
by JAXA and Kyoto Univ.

2010 5.8GHz,
Total Power >1.9kW
256 array module
HPA PAE >70% (GaN)
thickness <30cm
in Kyoto Univ.
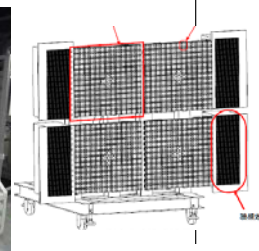
2013 5.8GHz,
Total Power >1.6kW
304 array module
4in1 sub-array
HPA PAE >70% (GaN)
thickness <4cm
By METI&USEF

Magnetrons

2000 SPORTS2.45
2.45GHz, Total Power >4kW
12 magnetron array
Eff. >70% in Kyoto Univ.

2001 SPORTS5.8
5.8GHz, Total Power >2.7kW
9 magnetron array
Eff. >65% in Kyoto Univ.

2009 for Airship Exp.
2.45GHz, Total Power >440W
2 magnetron array in Kyoto Univ.

METLAB
in Kyoto Univ.

SPSLAB
in Kyoto Univ.

A-METLAB
in Kyoto Univ.

1990   2000   2010

Fig.1 History of Developed Phased Array for MPT

At the end of FY2010, a new phased array was installed in Kyoto University as multipurpose research equipment(Honma, 2011)(Yamanaka, 2010). The characteristics of the phased array in Kyoto University are as follows:

1) 5.8 GHz CW, no modulation.
2) Separated module antenna/active circuits system.
3) Rigid antenna plane.
4) 256 elements.

5) Active phased array with one active circuit for one antenna.

6) 1.5 kW output microwave power.

7) F-class power amplifiers with GaN FETs.

8) >7 W output in high-power amplifier as final stage.

9) >70% power added efficiency in microwave high-power amplifier as the final stage (Fig. 21).

10) >40% as total DC-microwave conversion efficiency.

11) 5-bit MMIC phase shifters.

12) <30 cm thickness as universal experimental equipment.

The phased array system consists of phased array equipment, beam control units, and a cooling unit. The beam control units consist of an antenna control unit, a PC, and the retrodirective equipment. The rectenna array system consists of the rectenna array, a DC/DC converter, a load, and the retrodirective equipment. Figure 2 shows a simulated beam pattern, and Fig. 3 shows measured beam patterns when the main beam is steered to EL = (−15, −10, −5, 0, 5,10, 15) degrees. In each beam steering angle, the obtained steering accuracy was within 0.1 degrees.

Figure 4 shows measured azimuth-elevation beam pattern which is measured by near field scanner in Kyoto University. The near field scanner is installed in new anechoic chamber called Advanced METLAB with the phased array at the same time (Fig.5). It is plane-polar type near field scanner. It can measure the multi-beam pattern with control of beam direction of the phased array simultaneously. It can also measure the 10mφ and 10kWCW phased array of satellite for the SPS. The phased array and the near field scanner are open for use by inter-universities and international collaborative studies. We would like use the research facilities in Kyoto University in order to advance the Japanese SPS project.

Fig.3 Measured Elevation Beam Pattern of Phased Array (Beam Steering Angle: EL=-15, -5, 0, 5, 15 Degrees(AZ=0 Degrees)).

Fig.4 Measured Azimuth and Elevation Beam Pattern of the Phased in Kyoto University

Fig.2 Simulated Beam Pattern of the Phased Array in Kyoto University

Fig.5 Anechoic Chamber A-METLAB and Plane-Polar Type Near Field Scanner in Kyoto University

3 NEW ALGORISM OF BEAM FORMING AND TARGET DETECTING FOR SPS

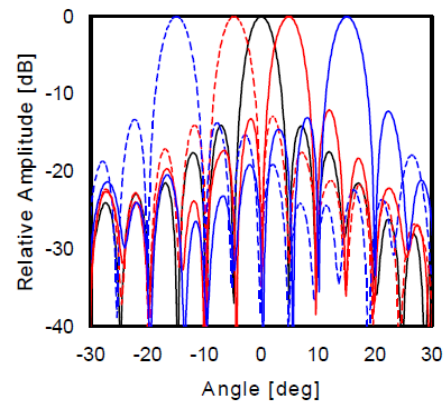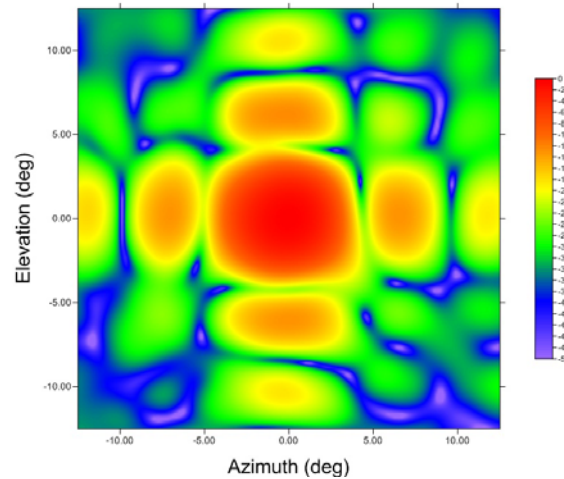The panel-structure SPS is designed by Japanese SPS committee. It consists of a large number of power generation/transmission panel modules. This type of SPS is suitable for mass production and easy to maintenance. However, joints of the panel modules are flexible and the panel-structure SPS is difficult to maintain flatness of the transmission antenna surface. In order to achieve the high beam direction control accuracy, we have to correct the output phase errors caused by the antenna surface distortion.

Mitsubishi Heavy Industry's SPS research group proposed new beam correction methods which is called a PAC (Position and Angle Collection) method. The PAC method is one of the beam correction methods for the panel-structure SPS. In the PAC method, we measure phases of a pilot signal, which was sent from a power receiving site on the Earth, on every panel module. We estimate the panel module positions by using the measurement phases. Then, considering the panel module positions, we correct the output phases of pilot signal.
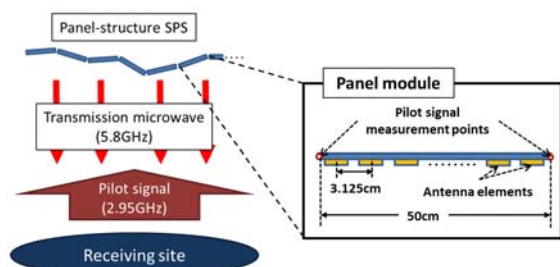
Fig. 6 Schematic Diagram of a SPS 1D Array Model.

In Kyoto University, we simulated the PAC method by a 1D array model shown in Figure 6. Taking account of the SPS system, we set these parameters. At first, we simulated the accuracy of the PAC method. From the simulations, the pilot signal measurement points have to be put on the both ends of each panel module in order to achieve the high beam direction control accuracy. However, the spacing of two measurement points is much longer than the half wavelength of the pilot signal and ambiguities occur in the panel position estimation method. Because of the ambiguities, we can correct the output phase errors only when the

panel module gradients are in the range of -5 degrees to 5 degrees. Thus, we propose an improved panel position estimation method. By using this estimation method, we can use the PAC method even if the panel module gradients are in the range from -50 degrees to 50 degrees(Ishikawa, 2012).

4 CONCLUSIONS

There is no experimental satellite project for the SPS in the world. Based on the developments of the new phased array for the MPT, we hope the first experimental satellite will be launched in Japan.

REFERENCES

Basic plan for space policy1, 2009, http://www.kantei.go.jp/jp/singi/utyuu/basic_plan.pdf

Basic plan for space policy2, 2009, http://www.kantei.go.jp/jp/singi/utyuu/keikaku/pamph_en.pdf

Fuse, Y., T. Saito, S. Mihara, K. Ijichi, K. Namura, Y. Honma, T. Sasaki, Y. Ozawa, E. Fujiwara, and T. Fujiwara, "Outline and Progress of the Japanese Microwave Energy Transmission Program for SSPS", *Proc. of 2011 IEEE MTT-S International Microwave Workshop Series on Innovative Wireless Power Transmission: Technologies, Systems, and Applications (IMWS-IWPT2011),* pp.47-50, 2011

Homma, Y., T. Sasaki, K. Namura, F. Sameshima, T. Ishikawa, H. Sumino and N. Shinohara, "New Phased Array and Rectenna Array Systems for Microwave Power Transmission Research", *Proc. of 2011 IEEE MTT-S International Microwave Workshop Series on Innovative Wireless Power Transmission: Technologies, Systems, and Applications (IMWS-IWPT2011),* pp.59-62, 2011

Yamanaka, K., Y. Tuyama, H. Ohtsuka, S. Chaki, M. Nakayama, and Y. Hirano, "Internally-matched GaN HEMT High Efficiency Power Amplifier for Space Solar Power Stations", *Proc. of Asia-Pacific Microwave Conference 2010*, pp.119-122, 2010

Ishikawa, I., and N. Shinohara, "Study on Microwave Power Beam Correction Method with Deployment System for Panel Structure SPS", *Proc. of 2012 IEEE MTT-S International Microwave Workshop Series on Innovative Wireless Power Transmission: Technologies, Systems, and Applications (IMWS-IWPT2012)*, pp.25-28, 2012

BRIEF BIOGRAPHY

Naoki Shinohara received the B.E. degree in electronic engineering, the M.E. and Ph.D (Eng.) degrees in electrical engineering from Kyoto University, Japan, in 1991, 1993 and 1996, respectively. He was a research associate in the Radio Atmospheric Science Center, Kyoto University from 1998. He was a research associate of the Radio Science Center for Space and Atmosphere, Kyoto University by recognizing the Radio Atmospheric Science Center from 2000, and there he was an associate professor since 2001. he was an associate professor in Research Institute for Sustainable Humanosphere, Kyoto University by recognizing the Radio Science Center for Space and Atmosphere since 2004. From 2010, he has been a professor in Research Institute for Sustainable Humanosphere, Kyoto University. He has been engaged in research on Solar Power Station/Satellite and Microwave Power Transmission system. He is a member of the IEEE, URSI, the Institute of Electronics, Information and Communication Engineers (IEICE) and the Institute of Electrical Engineers of Japan (IEEJ).

PAPERS

Solar Power Satellite Systems

FEASIBILITY STUDY ON
MICROWAVE POWER TRANSMISSION TO A ZIGBEE DEVICE
FOR WIRELESS SENSOR NETWORK

Tomohiko Mitani, Takuya Ichihara, Nozomu Suzuki, and Naoki Shinohara

Research Institute for Sustainable Humanosphere, Kyoto University, Gokasho, Uji, Kyoto, Japany
mitani@rish.kyoto-u.ac.jp

Abstract: The objective of the present study is to drive or charge a ZigBee device wirelessly by microwave power transmission. Wireless sensor network is expected to monitor several systems in order to control various infrastructures, such as electric power consumption, actively. However, power supply for sensor terminals is a critical problem to realize a fruitful wireless sensor network system. Primary batteries needs to be changed soon or later, wired power supply confines their installation location, and natural energy utilization like solar cells limits their regular operation. We therefore suggest wireless power supply for the sensor terminals by microwave power transmission. We adopt a ZigBee device as a wireless sensor terminal because of its low power consumption. We experimentally investigated electromagnetic compatibility between ZigBee and microwave power transmission, and found that there were some frequencies and power levels of microwave power transmission not to interrupt ZigBee. We also developed a microwave power receiving system which consists of a receiving antenna, a rectification circuit, a dc-dc converter, and a power storage circuit or a secondary battery. Finally we succeeded establishment of ZigBee network while driving a ZigBee device without batteries by microwave power transmission. Through the experiments, we found out intermittent microwave power transmission was preferable to CW microwave power transmission with respect to electromagnetic compatibility and rf-dc efficiency.

1 INTRODUCTION

Wireless sensor network is becoming an attractive application for monitoring systems such as energy conservation systems of buildings and houses, traffic management systems, environment monitoring systems etc. A vast number of wireless sensor terminals are scattered over a wide area, and send and receive monitoring information through ad hoc network. The collected information will be utilized to control various infrastructures, such as electric power consumption, actively.

One of the critical issues of the wireless sensor network is the way to supply electric power for sensor terminals. Primary batteris need to be changed soon or later even though power consumption of the sensor terminals is quite small. That will make the running cost of the wireless sensor network expensive. Wired power supply can provide stable operation of the sensor terminals; whereas it confines their installation location and burdens the wireless sensor network with wired cost. Natural energy utilization like solar cells with a charging system will drive the sensor terminal permanently; however their installation location and regular operation are limited because the natural energy is quite unstable.

We therefore suggest wireless power supply to the sensor terminals by microwave power transmission (MPT), in order to realize a fruitful wireless sensor network. MPT is able to provide a stable power for the sensor terminals, transmits power even for a long distance, supplies the power for multiple terminals simultaneously, and even drives the terminals without batteries. By utilizing MPT for the wireless sensor network, we can provide new applications of the wireless sensor network as well as the envisioned ones. A great potential application is a wireless sensor network system for disaster relief, as shown in Figure 1. Wireless sensor terminals located in any places normally sleep but work in emergency situations by receiving the power from vehicles or helicopters via

long-range MPT. The activated terminals can collect and send disaster information via short-range wireless communication. Another application is "energy harvesting" from radio communication (Kawahara, 2009). The energy harvesting system by receiving VHF or UHF energy from TV towers were reported in 2009 (Sample, 2009). Mobile communication systems and wireless local area network systems, as shown in Figure 2, will be potential candidates as energy harvesting source in microwave band.

The objective of the present study is to drive or charge a wireless sensor terminal by MPT. We adopt a ZigBee device as wireless sensor terminal because of its low power consumption. In this paper we describe our current status of MPT to a ZigBee device, including our previous studies on development of a microwave power receiving circuit (Suzuki, 2010), and feasibility of intermittent MPT (Ichihara, 2012).
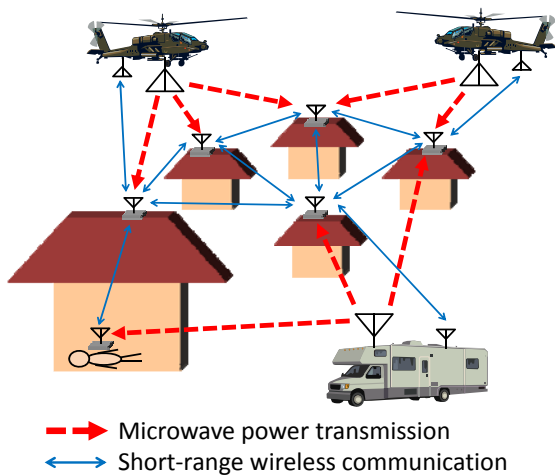
Figure 1: A conceptual image of a wireless sensor network system for disaster relief.
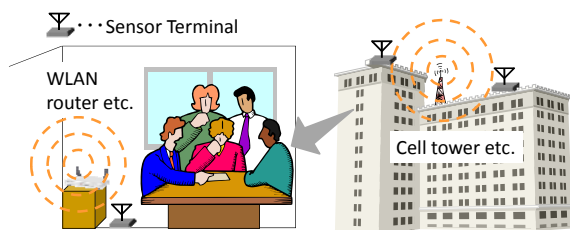
Figure 2: A conceptual image of energy harvesting from radio communications in microwave band.

2 OUTLINE OF MPT SYSTEM TO ZIGBEE DEVICE

2.1 Zigbee Device

ZigBee is one of the radio communication standards and appropriate for the sensor network for the following reasons: its power consumption is lower than wireless LAN and Bluetooth, its production cost is low, and its network capacity is large. Its low power consumption is beneficial for a MPT system from the viewpoint of electromagnetic compatibility between MPT and ZigBee.

In the present study, we are using IEEE802.15.4/ZigBee Evaluation and Development Kit TWE-EK-001 produced by Tokyo Cosmos Electric Company (TOCOS) as ZigBee devices. ZigBee network consists of the coordinator, a router and an end device. The coordinator is only one in a ZigBee network system and it coordinates the network. The router has the function of relaying data from other routers and end devices as well as monitoring. The end device only has the function of monitoring and data sending. Therefore the power consumption of the end device is lower than the coordinator and the router. Table 1 shows measured average power consumptions of a router and an end device of this kit. The power consumption of the router is stable whether or not it joins in the network; whereas the power consumption of the end device is quite small when it joins in the network. We have studied on MPT to an end device in the present paper.

In our configuration, the router and the end device sent data for nearly 2 milliseconds every 1.14 seconds. The coordinator decided to drop them from its network if it had not received data from them for 15 seconds. When it had dropped out of the network, the device was requested to join in the network again.

Table 1: Measured average power consumption of ZigBee devices.

Device type	Joining	Not joining
Router	57.4 mW	57.1 mW
End device	9.46 mW	61.8 mW

2.2 Microwave Power Receiving Circuit

Figure 3 shows a schematic of a microwave power receiving circuit. The microwave power receiving

circuit consists of a receiving antenna, a rf-dc rectifier, a power storage circuit, and a dc-dc converter. The combination of the receiving antenna and the rf-dc rectifier is called "rectenna". The power storage circuit can be omitted when the transmitted microwave power is large enough to drive a ZigBee device directly. The dc-dc converter converts the rectenna output voltage to a regulated voltage for a stable ZigBee device operation.

We adopt 2.4 GHz ISM-band, which is the same frequency band as ZigBee, as MPT frequency, from the viewpoint of efficient frequency usage. In this study, continuous or intermittent microwave without modulation transmits power to the receiving circuit.
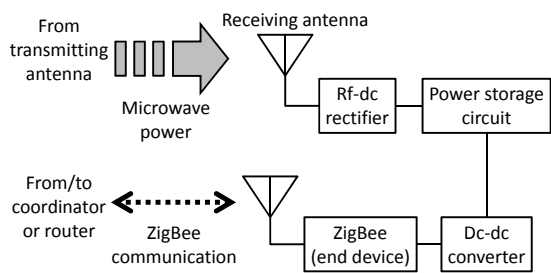
Figure 3: A schematic of microwave power receiving circuit.

3 EXPERIMENTAL STUDY ON COMPATIBITITY BETWEEN MPT AND ZIGBEE

We firstly conducted experimental measurements of electromagnetic compatibility between MPT and ZigBee, in order to investigate how MPT affected ZigBee. Also the measurements contributed to fix the frequency and maximum transmitting power of MPT in our study.

We defined and evaluated two indices on MPT power density: communicable power density (CPD) and joinable power density (JPD). CPD is the threshold of MPT power density which does not affect ZigBee. A ZigBee device can communicate with the other one under the CPD when it has already joined in the network. JPD is the threshold of MPT power density under which a ZigBee device can join in the network. The CPD is generally larger than the JPD.

3.1 Measurement Setup

Figure 4 shows the experimental configuration. The ZigBee frequency was set to 2.46 GHz (22 ch), and

the network had just two devices of the coordinator and an end device. First, the coordinator, which was put behind the transmitting horn antenna, established communication with the end device. Then, the end device was irradiated with non-modulated microwave as alternative to MPT. We measured CPD with increasing the non-modulated microwave power until the communication was disabled. After that, we measured JPD with reducing the non-modulated microwave power until the coordinator established communication with the end device again.

We investigated two types of non-modulated microwave irradiation: CW microwave irradiation and intermittent microwave irradiation. During the intermittent microwave irradiation, the non-modulated microwave turned on and off under the conditions of a pulse frequency and a duty ratio.
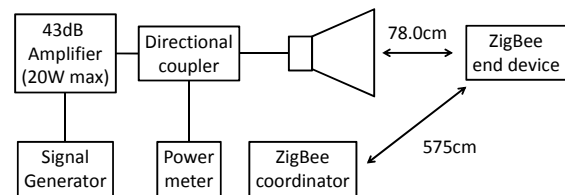
Figure 4: Experimental configuration of electromagnetic compatibility between MPT and ZigBee.

3.2 Measurement Results

3.2.1 CW microwave irradiation

We conducted CW microwave irradiation to a ZigBee end device, with changing the frequency from 2.4 GHz to 2.5 GHz (20 MHz step). We measured the maxima of the CPD and JPD at all the frequency points.

Experimental results of the CPD and JPD are shown in Figure 5. At all the frequency points, the CPDs were lower than 1 mW/cm^2 – the maximum power density determined by International Commission on Non-Ionizing Radiation Protection (ICNIRP, 1998). Around the ZigBee frequency, the power density of 5 pW/cm^2 even interrupted ZigBee. From these results, CW MPT is quite difficult to be compatible with ZigBee, in order to supply enough power wirelessly for a ZigBee device. Although we have not checked yet, CW MPT at another frequency band except 2.4 GHz band might be compatible with ZigBee.
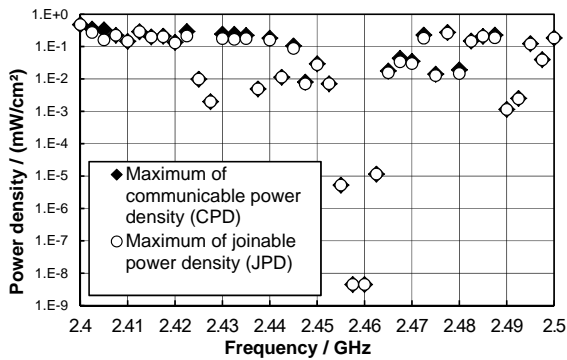
Figure 5: Measurement results of the CPD and JPD when the ZigBee end device was irradiated with CW microwave.

Figure 6: Measurement results of error rates when a ZigBee end device was irradiated with intermittent microwave under the peak power density of 1.91 mW/cm^2.

3.2.1 Intermittent microwave irradiation

Under the same condition as shown in Figure 4, we conducted intermittent microwave irradiation to a ZigBee end device. We fixed the intermittent microwave frequency of 2.46 GHz, at which we obtained the lowest maximum of the CPD and JPD in the CW microwave irradiation case. The end device was irradiated with intermittent microwave, within the pulse frequency range from 1 Hz to 200 Hz and the duty ratios of 0.1, 0.5 and 0.9.

From experimental results, 1.91 mW/cm^2 of the peak power density with any duty ratios allowed the end device to participate in the network and communicate with the coordinator. This means the CPD and JPD of the intermittent microwave is more than 10^8 times larger than those of CW microwave, when the MPT frequency is the same as the ZigBee frequency.

We also measured error rates of ZigBee during the intermittent microwave irradiation. Experimental results under the peak power density of 1.91 mW/cm^2 are shown in Figure 6. Since we fixed the peak power density in the measurements, the average power density was dependent on the duty ratio: 0.191 mW/cm^2, 0.955 mW/cm^2 and 1.72 mW/cm^2 at the duty ratios of 0.1, 0.5 and 0.9, respectively. The experimental results show that the ZigBee end device could communicate with the coordinator almost perfectly at the duty ratio of 0.1; whereas it seemed difficult for the ZigBee end device to send data stably at the duty ratio of 0.9.

In the measurements, interference would occur stochastically because we made the period of intermittent microwave irradiation irrelevant to that of ZigBee. Therefore, it is important to build a scheduling rule between intermittent MPT and ZigBee for a robust wireless sensor network with MPT.
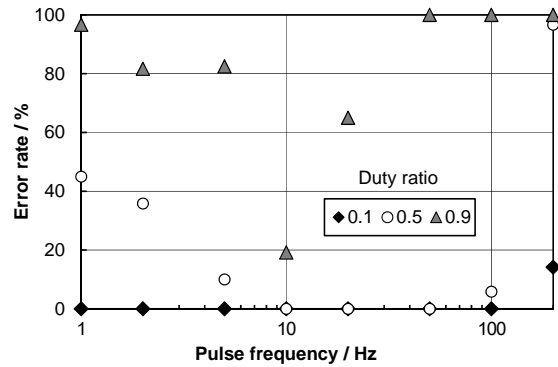
4 DEVELOPMENT OF A RECEIVING CIRCUIT

4.1 Rectenna

Rectenna consists of a receiving antenna and a rf-dc rectifier. As with the experiments in Section 2, we focused on the MPT frequency of 2.46 GHz.

Circular patch antenna was adopted as receiving antenna. Figure 7 shows a photograph of the circular patch antenna. The measured antenna gain was 6.5 dBi.
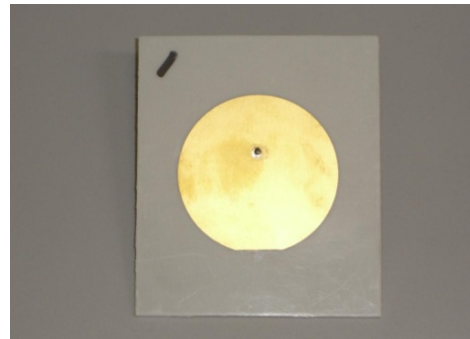
Figure 7: Photograph of the circular patch antenna.

We developed a single-shunt type rf-dc rectifier, whose photograph is shown in Figure 8. We adopted Schottky barrier diode (Avago HSMS-2860) as rectifier diode. Measurement results of rf-dc conversion efficiency are shown in Figure 9. The rectifier provided the maximum rf-dc conversion efficiency of 65 % at 2.46 GHz when the output load was 138.1 ohms, in the CW microwave case (Suzuki, 2010). The rf-dc conversion efficiency started to be dropped at an input power of 180 mW. This drop in conversion efficiency is related to the breakdown voltage of the diode.

We also investigated rf-dc conversion efficiency when the intermittent microwave was input to the rectifier. The duty ratio of the intermittent microwave was changed from 1 (CW) to 0.1, the pulse frequency was 1 kHz, and the average input power was 16 mW, 65 mW and 101 mW. Since we fixed the average input power, the peak input power was dependent on the duty ratio. The peak input power was equal to the average input power at the duty ratio of 1; whereas it became 10 times larger than the average input power at the duty ratio of 0.1. Figure 10 shows measurement results of rf-dc conversion efficiency in the intermittent microwave case. Of great interest is that the rf-dc conversion efficiency depended on the peak input power. Even if the average power is small, one can obtain the maximum rf-dc conversion efficiency by adjusting the duty ratio of intermittent microwave. The rf-dc conversion efficiency dropped down at low duty ratios when the average input power was 65 mW and 101 mW, because the peak input power became over the input power of 180 mW, where the rf-dc conversion efficiency started to be dropped.
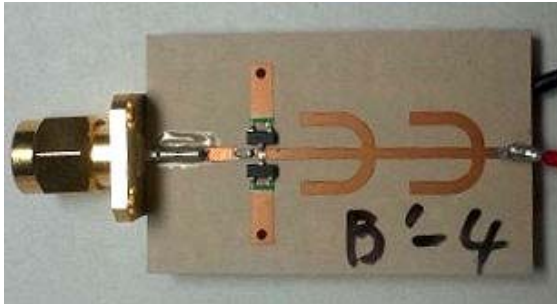
Figure 8: Photograph of the rf-dc rectifier (Suzuki, 2010).
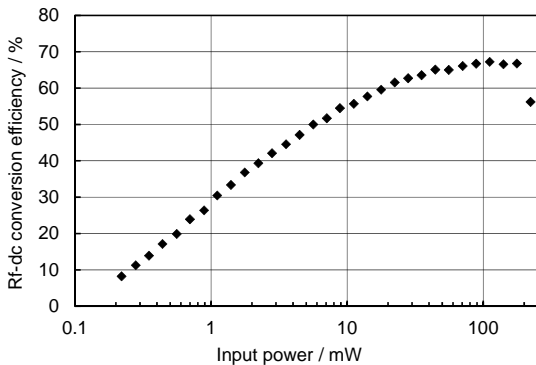
Figure 9: Rf-dc conversion efficiency of the rectifier in the CW microwave case.
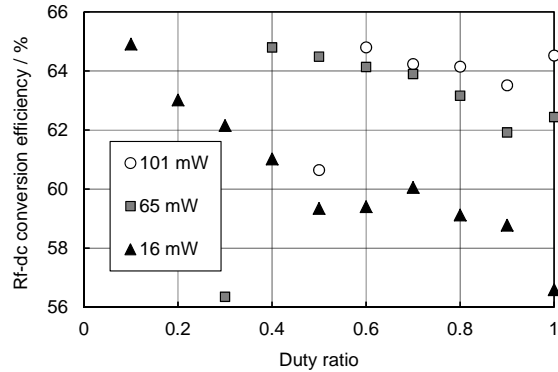
Figure 10: Rf-dc conversion efficiency of the rectifier in the intermittent microwave case.

4.2 Dc-dc converter

The rectenna output voltage became over 4 V at the input microwave power of 180 mW from the measurement results; whereas the ZigBee input voltage should be in the range from 2.7 V to 3.6 V. We therefore adopted a step-down dc-dc converter (Texas Instruments TPS62120) as dc-dc converter. This dc-dc converter provided an efficiency of over 90 % in an output voltage range around 3 V.

5 INTERMITTENT MPT DEMONSTRATION TO ZIGBEE DEVICE

We conducted demonstration experiments of power supply to a ZigBee end device by intermittent MPT. A demonstration configuration and a photograph of the demonstration are shown in Figure 11 and Figure 12, respectively. The MPT frequency was 2.46 GHz, and the pulse frequency was changed from 1 Hz to 50 Hz. Three rectennas were connected in series. The ZigBee end device had no batteries, that is, it was driven only by intermittent MPT. In this demonstration, we fixed a peak power density of 2.4 mW/cm^2 at the rectenna position.
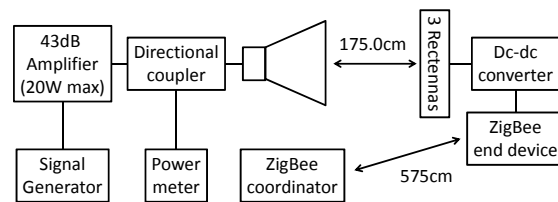
Figure 11: Configuration of intermittent MPT demonstration to a ZigBee end device.
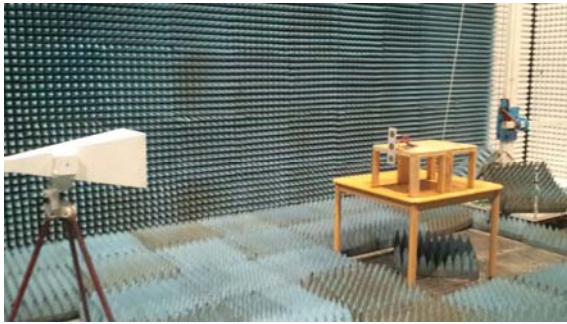
Figure 12: Photograph of intermittent MPT demonstration to a ZigBee end device.

From the demonstration experiments, the end device was driven by intermittent MPT at any pulse frequency when the duty ratio of the intermittent MPT was above 0.4. We therefore succeeded battery-less operation of the ZigBee device by MPT. Moreover, when the pulse frequency was 10 Hz, the end device could communicate with the coordinator with no error, while its power was being supplied by MPT.

6 CONCLUSIONS

We succeeded MPT to a ZigBee device which was driven without batteries. Intermittent MPT was preferable to CW MPT because of the following reasons: ZigBee was better compatible with MPT, and higher peak power of MPT was allowed. The latter factor contributed to higher rf-dc conversion efficiency of the rectifier even at the low average power. Moreover we confirmed that the ZigBee end device worked and communicated correctly with the coordinator while its power was being supplied by intermittent MPT.

As future works, we will study on scheduling management between MPT and ZigBee. Although we succeeded intermittent MPT demonstration to a ZigBee device as a feasibility study, scheduling management will be essential for realizing a fruitful wireless sensor network. Also we will have to study how to transmit microwave power to multiple ZigBee devices in a wide area.

ACKNOWLEDGEMENTS

REFERENCES

Ichihara, T., Mitani, T., Shinohara, N., 2012. Study on Intermittent Microwave Power Transmission to a ZigBee Device. In *Proc. of 2012 IEEE MTT-S International Workshop Series on Innovative Wireless Power Transmission: Technologies, Systems, and Applications (IMWS-IWPT 2012)*, pp.209-212.

International Commission on Non-Ionizing Radiation Protection (ICNIRP), 1998. Guidelines for Limiting Exposure to Time-varying Electric, Magnetic, and Electromagnetic Fields (up to 300 GHz). *Health Physics*, 74 (4), pp.494-522.

Kawahara, Y., Lakafosis, V., Sawakami, Y., Nishimoto, H., Asami, T., 2009. Desing Issues for Energy Harvesting Enabled Wireless Sensing Systems. In *Proc. of Asia-Pacific Microwave Conference 2009 (APMC 2009)*, pp.2248-2251.

Sample, A., Smith, J. R., 2009. Experimental Results with two Wireless Power Transfer Systems. In *Proc. of IEEE Radio and Wireless Symposium 2009 (RWS2009)*, pp.16-18.

Suzuki, N., Mitani, T., Shinohara, N., 2009. Study and Development of a Microwave Power Receiving Circuit for ZigBee Device. In *Proc. of Asia-Pacific Microwave Conference 2010 (APMC 2010)*, pp.45-48.

MICROWAVE WPT TECHNOLOGY DEVELOPMENTS FOR SSPS APPLICATION

Takashi Saito , Yoshiharu Fuse, Shoichiro Mihara, Shuji Nakamura, Koichi Ijichi
Japan Space Systems(J-spacesystems) 3-5-8 Shibakoen, Minato-ku, Tokyo 105-0011 JAPAN
{Saito-Takashi, Fuse-Yoshiharu, Mihara-Shoichiro, Nakamura-Shuji, Ijichi-Koichi}@jspacesystems.or.jp

Yukihiro Homma, Takuro Sasaki
Mitsubishi Electric Corporation (MELCO) 8-1-1 Tsukaguchi-Honmachi,Amagasakicity,Hyogo,661-8661 JAPAN
Homma.Yukihiro@df.MitsubishiElectric.co.jp, Takuro.Sasaki@dn.MitsubishiElectric.co.jp

Eiichiro Fujiwara, Yuichiro Ozawa, Teruo Fujiwara
IHI Aerospace Co., Ltd. (IA) 900 Fujiki, Tomiokacity,Gunma,370-2398 JAPAN
{yuichiro-ozawa, e-fujiwara}@iac.co.jp, qfuji@js5.so-net.ne.jp

Abstract: Japan Space Systems(J-spacesystems), formerly known as Institute for Unmanned Space Experiment Free Flyer (USEF), has been studying Space Solar Power System as future electricity alternative energy source. Since 2009, J-spacesystems started new research and development project of the Microwave Ground Wireless Power Transmission under a support of Ministry of Economy, Trade and Industry. This project includes the study for highly-efficient and thin structured phased array antenna, and the study for highly-efficient rectenna element. Also this project plans to demonstrate ground wireless power transmission as a previous stage to the next space proof of SSPS. In this paper, outline and progress of this project are introduced.

1   INTRODUCTION

Japan Space Systems(J-spacesystems, formerly USEF) has been studying Space Solar Power System (SSPS) under a support of Ministry of Economy, Trade and Industry(METI) and the other related agency since 1990s. These studies were ranging from laboratory tests to concept study of SSPS. (Mihara et al., 2009).

In 2008, the Japanese new space policy(the Basic Space Law) was enacted and the Basic Plan for Space Policy was established in 2009. They have selected "5 systems for utilization" and "4 programs od R&D" . SSPS is one of the R&D programs. This Plan is a five-year-program, from FY2009 to FY2013, foreseeing the next ten years, describing

the basic policy and the measures which the Government should take during this period. (Strategic Headquarters for Space Policy, 2009)

In 2009, METI requested for propals for the Microwave Power Transmission(MPT) ground test(demonstration) according to the Basic Plan, and the proposal of the team of J-spacesystems and companies(Mitsubishi Electric Co. and IHI Aerospace Co.) was adopted. (Fuse et al., 2011)

This is also a joint program between J-spacesystems and the Japan Aerospace Exploration Agency (JAXA). We are planning to conduct a joint MPT ground experiment in fiscal 2014. We will demonstrate the technologies needed to transmit a kW class microwave precisely to the receiving site

located 50 m from the power transmitting section. In this joint effort, J-spacesystems is in charge of the power transmitting section and the power receiving section, and JAXA is in charge of the Beam Steering Control (BSC) section. (Miyakawa et al., 2011)

2   SSPS REFERENCE MODELS

2.1 Single-bus type Model (FY2002)

Figure 1 illustrates the concept of the tethered-SSPS which is capable of 1.2GW power supply maximum and 0.75GW average on the ground. It is composed of a power generation/transmission panel of 2.0km×1.9km suspended by multi-wires(tethers) deployed from a bus system(single) which is located at 10 km upward. The panel consists of 400 subpanels of 100m×95m with 0.1m thickness. Each subpanel has 9500 power generation/transmission modules of 1m × 1m size. In each power module, the electric power generated by the solar cells is converted to the microwave power and no power line interface exists between the modules. The power module has thin film solar cells both on the upper and lower planes. The microwave transmitting antennas are on the lower plane. The module contains a power processor, microwave circuits, and their controller. Each module transmits a microwave power of 420W maximum. (Sasaki et al., 2006)
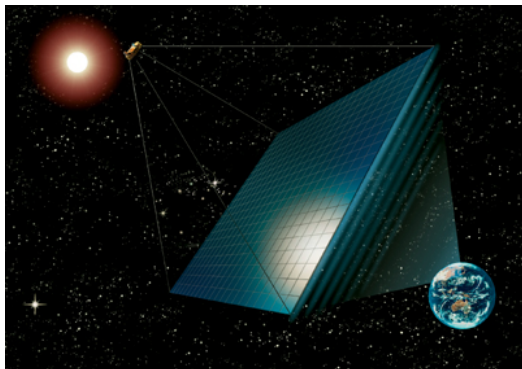
Figure 1: Single -bus type SSPS

2.2 Multi-bus type Model (FY2006)

In 2006, the multi-bus type of SSPS was newly proposed. Figure 2 shows the satellite structure of the multi-bus tethered SSPS. The new SSPS system has a multi-module structure. (see Figure 3)
In "Unit"SSPS, tethers link the bus system with the power generation/transmission modules.

So, a "Unit" SSPS is a small "single-bus type". Each "Unit" itself can transmit power(2.1MW) to Earth. Several "Units" are assembled to "Unit Assemly", and "Unit Assemly" s to "Multi-bus type"SSPS in a similar way.
The concept of this type is, so to speak, "Start Small, Let it Grow". (Yoshioka et al., 2011)
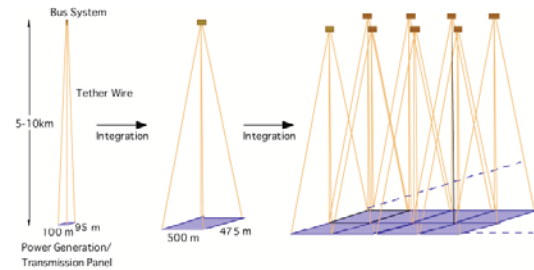
Figure 2: Multi-bus type SSPS
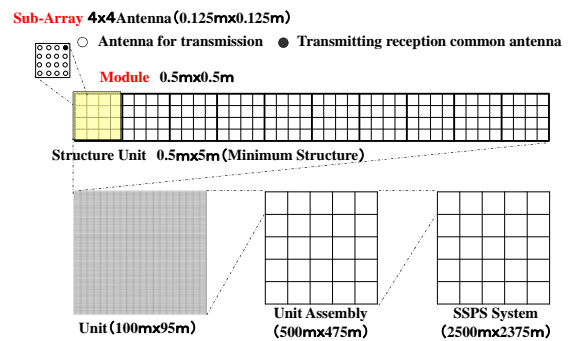
Figure 3: hierarchical structure of power transmitting panels

3 MPT GROUND EXPERIMENT   MODEL

3.1 Total System

Figure 4 shows the outline of the MPT Ground Experiment Model, and Figure 5 shows its tree diagram. The model consists of three sections;
- Power Transmitting Section
- Power Receiving Section
- Beam Steering Control Section (JAXA)

As for Beam Steering Control Section, Japan Aerospace Exploration Agency (JAXA) is in charge of the section.
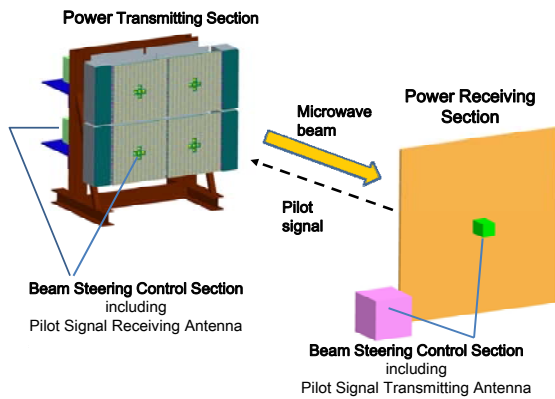
Figure 4: MPT Ground Experiment Model
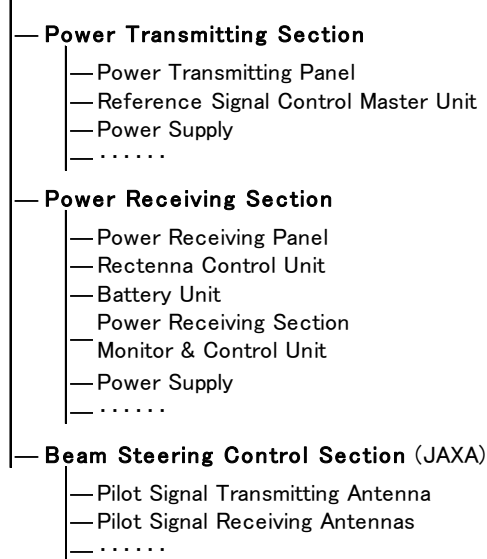
Figure 5: Tree Diagram of Ground Experiment Model

To realize SSPS, each section needs to have following features;
for Power Transmitting Section,
- light weight and thin power transmitting modules (transportation and construction cost)
- high efficiency (heat discharge and power generation cost)

for Power Receiving Section,
- electrical robustness (stable operation and maintenance cost)
- high efficiency (power generation cost)

for Beam Steering Control Section
- beam steering control accuracy (safety)

To solve these problems, our solutions are;
for Power Transmitting Section,
- to develop a thin sub-array
- to apply highly efficient HPA to GaN HEMT, F-class amplifier

for Power Receiving Section,
- to find out the cause of rectenna damage
- to develop a highly efficient diode

for Beam Steering Control Section
- retro directive method (using pilot signal)
- rotating electromagnetic vector method (REV method)

Beam Steering Control Section has;
- Pilot Signal Transmitting Antenna (Power Receiving Section)
- Pilot Signal Receiving Antenna (Power Transmitting Section)

The microwave beam frequency is 5.8GHz, and the pilot signal frequency is 2.4GHz band. (Miyakawa et al., 2010)

3.2 Power Transmitting Section

3.2.1 Basic Design

The basic design concept of the power transmitting section is as follows;
- High power (kW-class)
- High efficiency of DC-RF conversion
- Thin phased array (Sub-array)
- Principled reference signal control

Tree diagram of Power Transmitting Section is shown in Figure 6. And the system block diagram of the power transmitting section is shown in Figure 7.

```
Power Transmitting Section
 ├─Power Transmitting Panel
 │  ├─Power Transmitting Module（x4）
 │  │  ├─Sub-array（x76）
 │  │  │  ├─Antenna（x4）
 │  │  │  ├─HPA Module
 │  │  │  └─Beam Forming Network（BFN）
 │  │  ├─Divider
 │  │  ├─First Stage HPA Module
 │  │  ├─BFN for Control Signal（BFNC）
 │  │  ├─Power Supply Card
 │  │  └─Reference Signal Control Slave Unit
 ├─Reference Signal Control Master Unit
 └─Power Supply
```
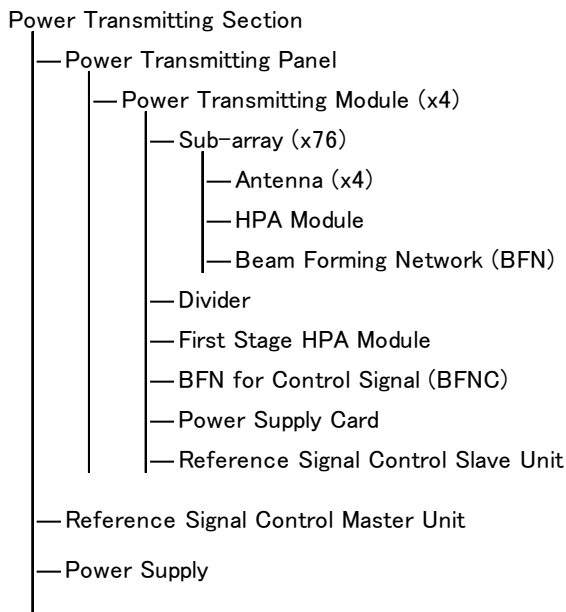
Figure 6: Tree Diagram of Power Transmitting Section

Figure 7: Block diagram of the power transmitting section
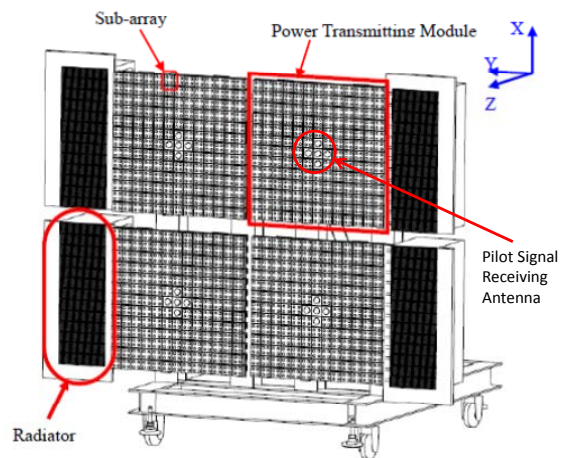
Figure 8: Outline view of power transmitting section.

Four power transmitting modules, which are phased array antennas, constitute of the power transmitting section.

A sub-array is the minimum unit. It consists of a BFN, an HPA module(MDL) and four sub-array antennas. A BFN receives microwave, DC power and control signal, and feeds them to the HPA MDL. Each HPA MDL has a phase-shifter, a driver amplifier, a high power amplifier and so on. Then, it provides microwave to four sub-array antennas.

A power transmitting module has 76 Sub-arrays. The module size is 60cm square. One module can output more than 400W. So the power transmitting panel(4 modules) size is about 1.2m square and the output power is about 1.6kW.

Figure 8 shows the outline view of Power Transmitting Section. Pilot Signal receiving antenna is set in the center of each power transmitting module (PT module). It is used for beam steering control.
Each PT module transmits microwave beam to the right direction according to the phase control signal from the beam steering control section. A PT module generates microwave in accordance with the reference signal from RSC master unit. This microwave is amplified by HPA modules (first stage and sub-array) using DC power from the main power supply, and divided by the divider, distributed to the sub-array antennas, and then transmitted.

As for SSPS, relative positions among the power transmitting modules may change. Power Transmitting Section has a function to simulate this situation by moving PT modules manually, for the purpose of verifying the effectiveness of the beam control method under that condition .

Table 1 shows the specifications of power transmitting section.

Table 1: Specifications of Power Transmitting Section

Item	Specification
Microwave Frequency	5.8GHz±75MHz
Power Transmitting Modules	Number: 4 Size: ≈0.6m x 0.6m Thickness: ≤40mm (Sub-array) Efficiency: ≥30% (PT module) Mass: ≤19kg (Sub-arrays)
High Power Amplifier (HPA)	GaN HEMT with F-class 76 HPAs (per PT module) Efficiency (PAE): ≥60% Ave.
Antenna Spacing	0.65λ (33.6±1 mm)
Phase Shifter	5 bit (MMIC)
Transmitting Power	≥400W (per PT module) ≥1600W (total)

As for the following items, our policy is;
- to get low loss Sub-array antenna for high efficiency, rather than for thickness.
- to get thin, light Sub-array structure
- to make a good balance between high efficiency and thickness of HPA module

GaN HEMT with F-class power amplifier is applied to the power transmission section. GaN HEMT has attracted much attention as the state-of-the-art microwave power transistor due to its high voltage and high power density capability. F-class operation was applied for high efficient power amplifier operation. In this work, an internally matched GaN HEMT high efficient amplifier is developed, in which 2nd harmonic at input side and 2nd and 3rd harmonic at outside are tuned with internal matching circuit. Very high Power Added Efficiency(PAE) 70%, with 7W output power was successfully obtained. Figure 9 is the photograph of hermetic sealed metal packaged GaN HEMT high efficienct amplifier. (Yamanaka et al., 2010)
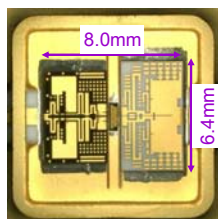
Figure 9: Metal packaged GaN HEMT amplifier

For space application, antenna thickness is very important parameter. Because the huge sized SSPS requires light weight for lower cost transportation and also requires the expansion structure in space.

Figure 10 is the ideal image of thin sub-array structure. Vertical circuit for the connection of the micro wave circuit board to the antenna array substrate was applied for the thickness reduction. The achievement of the thickness was 44.4mm in our early design. We are trying to reduce the thickness with keeping low loss performance. (Namura et al., 2010)
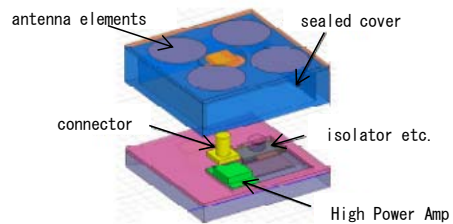
Figure 10: Sub-array radiation part structure image
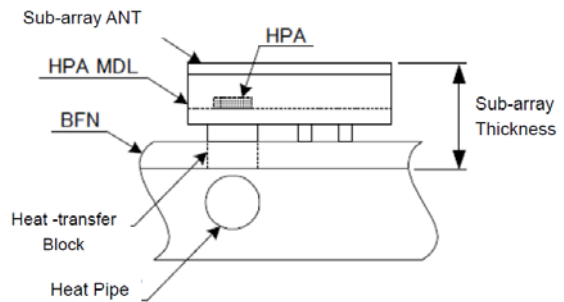
Figure 11: Sub-array thickness

According to above studies, a new design target is set as Table 2.

Table 2: Design Target (typical)

Item	Specification	Target
Output Power	≥400W per PT module	411W per PT module
Efficiency	≥30% as PT Section	35% as PT Section
Sub-array Thickness	≤40mm	34mm
Sub-array Mass	≤19kg	19kg

3.2.2 Element Test

In FY2011, a performance verification test of the HPA module(trial product, see Figure 12) was done. It consists of HPA module, Sub-array ANT, BFN etc. It became certain that all test results meet the design target (see Table 3).
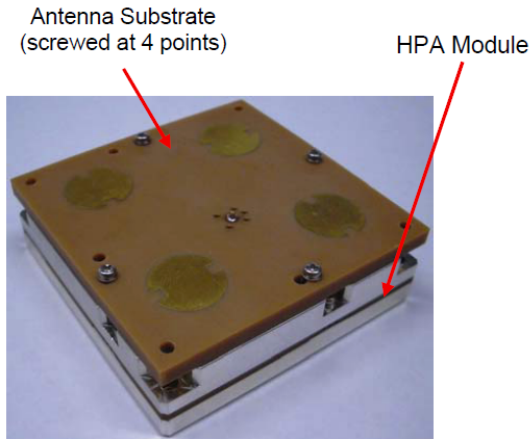
Figure 12: HPA module(trial product)

Table 3: HPA module(trial product) Test Result

Item	Design (average)	Test (average)
Output Power	≥6.1W	6.17W
Efficiency(PAE)	≥40.2%	41.50%
Accuracy of Phase-Shift	≤3deg rms	2.1deg rms
Spurious	≤ - 60dBc	- 65.7dBc
Size	62x62x14.6mm	62x62x14.6mm
Mass	92g	91.3g

We are going to examine the ongoing design of PT module(e.g., performance, size, mass, heat radiation) and make a prototype of sub-array.

3.3 Power Receiving Section

3.3.1 Basic Design

A tree diagram of Power Receiving Section is shown in Figure 13. And the system block diagram of the power receiving section is shown in Figure 14. Power receiving panel consists of 37 power receiving modules. The pilot signal transmitting antenna is set in the center module. (see Figure 15 and Figure 16)
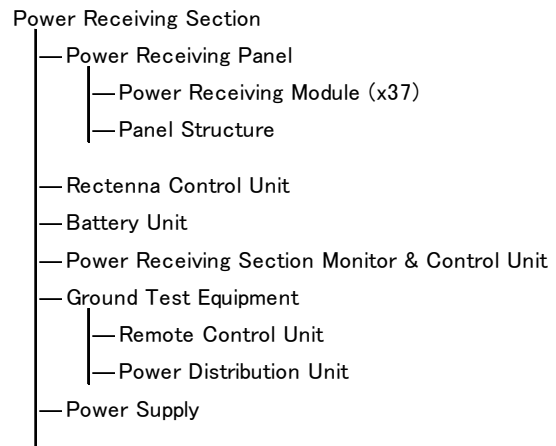
Figure 13: Tree Diagram of Power Receiving Section
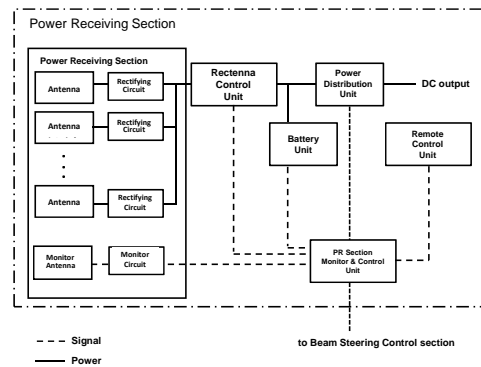
Figure 14: Block diagram of the Power Receiving Section

Table 4 shows the specifications of power receiving section. The diodes used in the power receiving module are "regular type"(commercialized product) .

The RF-DC efficiency(antenna to rectenna control unit) is estimated by efficiencies of :
- antenna polarization
- rectifying circuit
- rectenna control unit.

As a result, the RF-DC efficiency is estimated to be 56.8%.
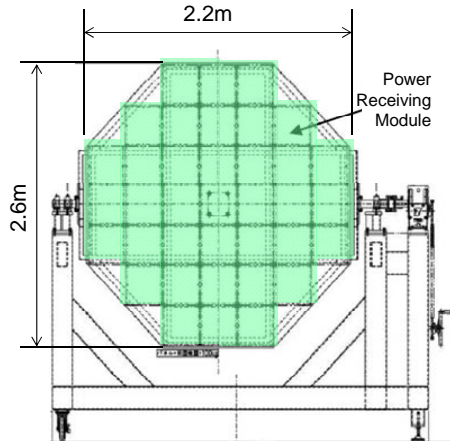
Figure 15: Power Receiving Section
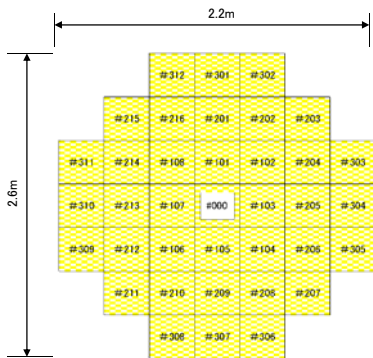
Figure 16: Power Receiving Panel (Rectenna Array)
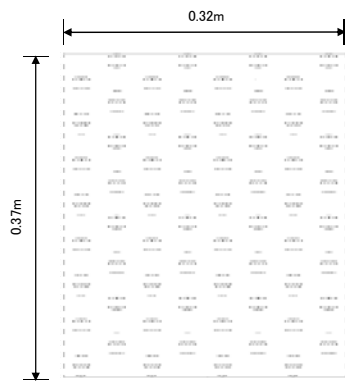
Figure 17: Power Receiving Module

Table 4: Specifications of Power Receiving Section

Item	Specification
Power Receiving Panel	Size : 2.6m × 2.2m
Power Receiving Module	Number: 37 Size: 0.37m x 0.32m
Diode type	Schottky barrier diode
RF-DC Efficiency	≥ 50% (Regular type, Power Receiving Panel) ≥ 80% (Advanced type, Rectenna Element)
Receiving Power	≥300W (estimated)

3.3.2 Element Test

Figure 18 is the typical block diagram of a rectenna. Self-bias rectifying circuit is used in a rectenna. This circuit has input filter, rectifying diode and output filter. Most of the power loss will be caused by the loss in rectifying diode. There have been several reports on the causes of the loss in diode. (McSpadden et al., 1998)

In parallel to designing power receiving module, we are trying to develop a high efficient Schottky barrier diode for rectifier using GaN material (Advansed type). In this development, an experimental evaluation of the manufacturing process and the manufacturing condition have been done. (Ozawa et al., 2010)

We are considering improvement of efficiency with studying parameters as follows:

- Cj_0: junction capacitance(zero bias)
- Rs: series resistance
- Vbi: built-in voltage
- Vbr: breakdown voltage
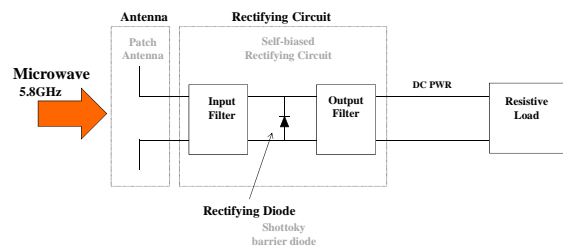
Figure 18: block diagram of a rectenna

A trial modelshows more efficiency than that of existing "Regular type". We continue making an effort to improve "Advansed type" diode.

4 MPT GROUND TESTS

We are planning the indoor and outdoor MPT tests. They wil be completed by fiscal 2014.

4.1 Indoor Test

Outline of the indoor(laboratory) test is shown in Table 5.

Table 5: Outline of the indoor test

Facility	anechoic chamber
Test Equipment	Power Transmitting Module × 4
Power Transmitting Distance	≥10 meters
Beam Pointing Accuracy	≤0.5 degrees (rms)
Microwave Frequency	5.8GHz±75MHz
Pilot Signal Frequency	2.4GHz band (Miyakawa et al.,2011)

4.2 Outdoor Test

Outline of the outdoor(field) test is shown in Table 6.

Table 6: Outline of the outdoor test

Facility	outdoor field
Test Equipment	MPT Ground Experiment Model (Power Transmitting Module × 4)
Power Transmitting Distance	≈ 50 meters
Transmitting Power	≈ 1.6kW (411W×4)
Power Flux Density @center, 50m	315W/m2±20% (estimated)
Output Power	≈ 0.3kW (estimated)

The objectives of the field test, or the demonstration, are;

- to transmit kW-class power
- to prove precise beam pointing accuracy(retro-directive, REV method)
- to demonstrate WPT (e.g., to feed electricity from rectenna to home electrical appliances

The energy electricity flux density at the receiving position center is calculated in Figure 19.
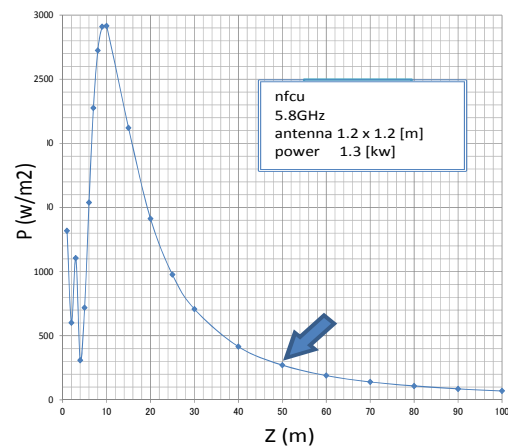
Figure 19: Electricity flux density

An energy distribution at 50m point is analyzed as shown in Figure 20. The black flame in the figure is shape of the receiving panel.
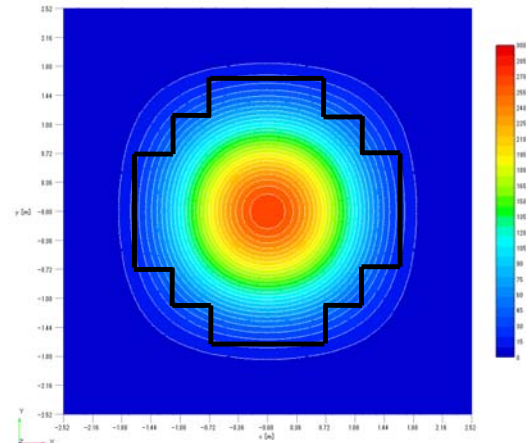
Figure 20: Energy distribution at 50m point

Figure 21 shows a WPT demonstration image. Layout of power transmitting/receiving sections is to be determined, avoiding any radio wave interference.
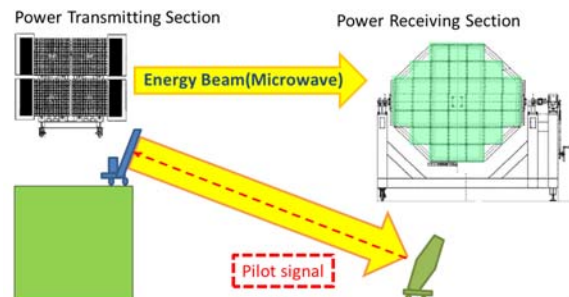
Figure 21: WPT Demonstration Image

CONCLUSION

Microwave Ground WPT project is currently going on. Basic design and element tests are in progress. We are planning to conduct the MPT ground experiment in FY 2014 in collaboration with JAXA. We have started to develop a concrete plan for the demonstration. And we should always be conscious that this ground demonstration is a preliminary step toward the next step of demonstration in space.

ACKNOWLEDGMENTS

REFERENCES

Fuse, Y., Mihara, S., Saito, T., Ijichi K., Namura, K., Homma, Y., Sasaki, T., Ozawa, Y., Fujiwara, E., Fujiwara, T., 2011. *Microwave Energy Transmission Program for SSPS*, CHGBDJK.2 URSI GAS2011, Aug. 2011

McSpadden, Lu Fan, J., Kai Chang, K., 1998. *Design and Experimental of a High-Conversion-Efficiency 5.8-GHz Rectenna*, IEEE Trans. MTT, Vol.46, No.12, 1998, pp2053-2060

Mihara, S., Saito, T., Kobayashi, Y., Kanai, H., 2007. *Activities for the Realization of Space Solar Power Syatem at USEF*, S1-I-1408 URSI ISRSSP2007, Sep. 2007

Miyakawa, T., Sasaki, S., Yajima, M., Maki, K., Mihara, S., Fuse, Y., Saito, T., Ijichi, K., Homma, Y., Sasaki, T., Ozawa, Y., Fujiwara, E., Fujiwara, T., 2011. *Development Status of Microwave Power Transmission Demonstration on Ground for Space Solar Power Systems*, IAC-11-C3.2.2, 62nd International Astronautical Congress, Oct. 2011

Namura, K., Honma, Y., Sasaki, T., Samejima, F., Ishikawa, T., Fuse, Y., Saito, T., Mihara, S., 2010. *Studies on Transmission Subsystem for Ground WPT Experiment System*, 1S12 54th Space Science technology symposium, 2010

Ozawa, Y., Fujiwara, E., Fujiwara, T., 2010. *Study on technical demonstration model of microwave receiving System*, 1S14 54th Space Science Technology Symposium, 2010

Sasaki, S., Tanaka, K., Higuchi, K., Okuizumi, N., Kawasaki, S., Shinohara, N., Senda, K., Ishimura, K., 2006. A New Consept of solar power satellite: Tethered-SPS, Acta Astronica 60, 2006, p153-165

Strategic Headquarters for Space Policy, 2009. *Basic Plan for Space Policy*, June 2009

Yamanaka, K., Tsuyama, Y., Ohtsuka, H. Chaki, S., Nakayama, M., Hirano, Y., 2010. *Internally-Matched GaN HEMT High Efficiency Power Amplifier for Space Solar Power Stations*, WE3A-1, APMC2010

Yoshioka, K., Matsuoka, H., Hayami, H., Collins, P., Sasaki, S., Takano, T., Asakura, K., Nakano, S., 2009. *Essays on the Solar Power Satellite*, Keio University Press, 2009

COMPACT GAN HIGH POWER AMPLIFIERS FOR SPACE COMMUNICATION, SENSING AND GREEN POWER TRANSMISSION

Shigeo Kawasaki and Yuta Kobayashi

ISAS/JAXA, Sagamihara, Japan
kawasaki.shigeo@jaxa.jp, kobayashi.yuta@jaxa.jp
+81-50-3362-5732, +81-50-3362-6450

Abstract: On the base of a green-eco technology, S-bandhigh power GaN amplifiers have been developed with a microwave power transmission function in the space electronics equipment. High DC-to-RF conversion efficiency of 63 % was achieved in the 20W GaN amplifier operating at 2.25 GHz and its design technique was extended to realize 1 kW SSPA for the space communication. Furthermore, wireless sensor operation and battery charging was also demonstrated by means of microwave power transmission.

1 INTRODUCTION

The RF technology has been used for communication and sensing, so far. As the third usage of the microwaves, wireless power transmission and energy harvesting have been paid much attention as one of solutions of environmental problems. With the enormous interest brewing, researchers around the world started to develop the wireless energy transfer/power transmission and energy harvesting/scavenging. This is the green-eco wireless power technology for the green life (environmental issues), ecology (nature-human interaction) and economy (cost effectiveness). Specifically, it will have a great impact on many applications such as compact and battery-less wireless communications and wireless sensor systems. Wireless power delivery generated from clean energy may be called wireless green power transmission.

The wireless power transmission (WPT) is usually categorized into three, the EM Coupling, the Magnetic Resonance (MR), and the Microwave WPT (MPT). It has been known that the carrier wave without modulation can be delivered the energy wirelessly. This is the basic feature of MPT. Comparing with wired systems and other WPT technologies, the MPT has become one of the most important technologies on demand to future space

missions as well as green eco technologies (N. Shinohara, 2009). For instance, the MPT module with some sensors can reinforce health monitoring functions in a space craft without wire-harness and solve a payload problem by removing some of onboard electrical power subsystems (EPS) in the space craft.

Reading the space electronics, a compact communication system is needed both in the onboard communication system and in the ground station. On behalf of operation of a space ground station, such as the Usuda Deep Space Center (UDSC) shown in Fig. 1, a high power and high efficiency solid state power amplifier is strongly requested. For this purpose, a wide band-gap semiconductor such as GaN and SiC is promising. Further, reduction of payload is important issue in the onboard system. In order to solve this problem, realization of a high power and high efficiency RF amplifier using the wide band gap semiconductor is requested. This is also the effective solution for the single event, total dose radio-isotope problem, and high temperature operation (N. Adachi, 2005).

Regarding power receiving in the MPT, power detection by a rectenna directory connected with an antenna and a detector is typical (M. Furukawa, 2006) (M. Hori, 2011) (T. ITO, 1979). As described before, wireless power is intentionally delivered to the rectenna. In the case of MPT, the high

Fig. 1.The kW-class SSPA for the space communication

breakdown-voltage RF detector is required to obtain high converted DC power, for instance, battery charging due to MPT. On the other hand, electromagnetic energy harvesting can be done in the RF environment. This harvester also consists of the rectenna but the harvested RF energy includes leaked RF energy from a transmitter in other place. The harvesting energy which tune into RF energy may include that from a energy converter/transfer. When the collected energy is weak, this may be called as "scavenging".

In this paper, the wireless power transmission is explained as the green-eco technology. From this view point, demonstration of space communication and wireless sensor by means of microwave power transmission is described by using high power GaN amplifiers. The 1kW SSPA combined with the high power GaN amplifiers is shown.In addition, thermal sensor operation and battery charging by microwave power transmission are introduced.

2 MICROWAVE GAN CIRCUITS FOR SPACE COMMUNICATION AND MPT

2.1 Semiconductor devices

In space communication, high efficient power device is necessitated. In this view point, a wide band-gap semiconductor is very promising. Among them, the gallium nitride (GaN) has recently been focused on as a high power and high efficiency device in the microwave region. Therefore, the GaN is one of the most significant elements to achieve effective use of energy in space not only for communications but

also for power transmissions. The GaN has several superior material properties, such as wide band gap, high saturation velocity, and good thermal conductivity. Due to these properties, the GaN is considered to have advantages in high efficiency, and high temperature conditions in addition to the high power characteristics. Thus, GaN is expected to be used in space applications such as, high power amplifiers (DC-to-RF conversion modules) and rectifiers (RF-to-DC conversion modules).

2.2 High power amplifiers

The S-band GaN based high power amplifiers (HPAs) have been designed, developed, and evaluated for space applications of the communication, a wireless sensor and microwave energy transfer intended for the green-eco technology. As examples for the onboard application, the 20W and 100W GaN amplifiers with the high power added efficiency were developed.

2.2.1 The 20W-class GaN HPA

The 20-W-class single-stage high power amplifier was designed in the S-band by using the commercial available CAD(Agilent: Advanced Design System) with small signal S-parameters. The package type of 20-W-class GaN HEMT on a Si substrate and the circuit substrate (Rogers RO4350 : the copper thickness of 70 um, the substrate thickness of 0.762 mm, the permittivity of 3.46) were used. The size of the 20-W-class amplifier was 50*55*17 mm. The circuit overview is shown in Fig. 2.

The measured small signal S-parameters from the 20W-class GaN HPA are shown in Fig. 3. Between 2.1 and 2.4 GHz, it was observed from Fig 3 that peaks of measured return loss of S11 and S22were achieved below -10 dB and the peak of measured forward gain of S21 was larger than 15 dB. In addition, characteristics of input-output, gain, drain efficiency and power added efficiency (PAE) from the fabricated 20W HPA at 2.25 GHz are shown in Fig. 4. It is confirmed that P1dB and P3dB were 42.2 dBm and 43.7 dBm and the PAE at these points were 55.1 % and 63.3 %, respectively. (Y. Kobayashi, 2012)

2.2.2 The 100W-class GaN HPA Unit

The 100-W-class single-stage high power amplifier was also designed and fabricated in the S-band with the package type 100W-class GaN HEMT on the Si substrate and the circuit substrate (RogersRO4350). The size of the 100-W-class is 100*76*30 mm shown in Fig. 5.
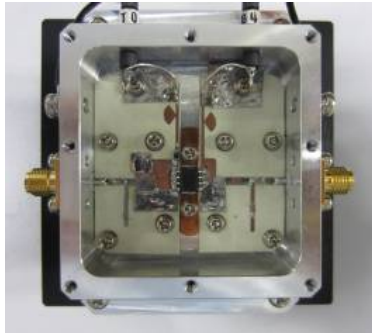
Fig. 2. 20 W-classGaN HPA

Fig. 5. 100 W-classGaN HPA

Fig. 3. Measured S-Parameters
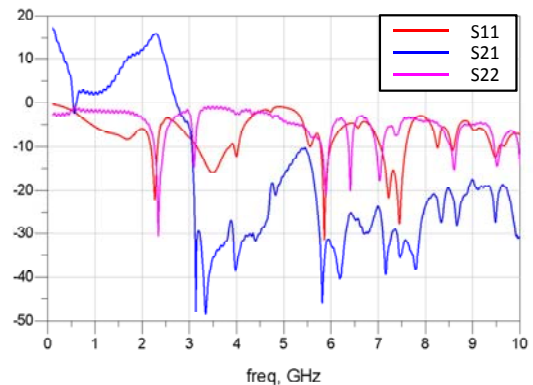
Fig. 6. Measured S-Parameters
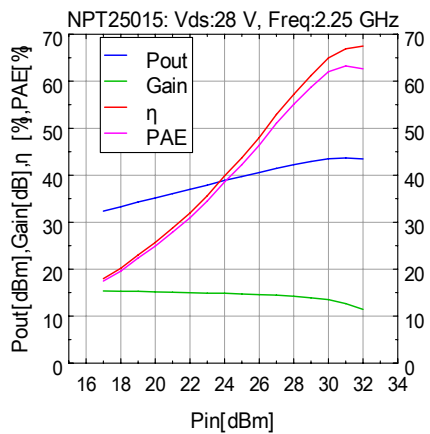
Fig. 4. Input-output characteristics
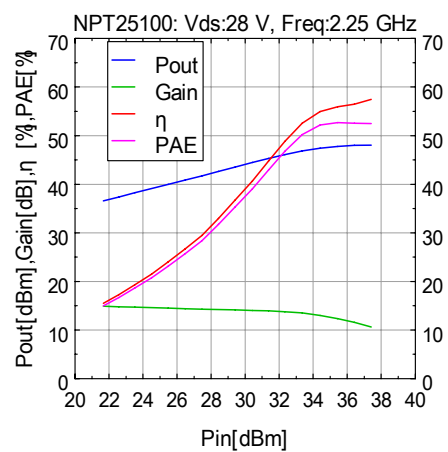
Fig. 7. Input-output characteristics

The measured small signal S-parameters of the 100W-class GaN HPA are shown in Fig. 6. In this figure, it was found that the S11 was measured with smaller than -11 dB, the S22 was smaller than -6.5 dB, and S21 was larger than 15 dB at the frequency rangebetween 2.1-2.4 GHz. In addition, the input-output characteristics of the 100W-class HPA at 2.25 GHz are shown in Fig. 7. It is confirmed that P1dB and P3dB were 45.3 dBm and 48.0 dBm and the power added efficiency (PAE) at these points were 43.0 % and 52.6 %, respectively.

3 APPLICATION AND TEST

For the space green power transmission as well as the ground-to-satellite application, the 1 kW GaN solid state power amplifier (SSPA) using a power combiner technique was fabricated. The total DC-to-RF conversion efficiency of more than 50 % was achieved. Using these components, some preliminary experiments of space power transmission have also been conducted.

Wireless power transmission (WPT) is one of the most important technologies for future space missions. WPT can be applied to not only inside of space crafts but also outside of ones. Comparing wired systems, there are various advantages using WPT. For instance, WPT with some sensors can easily reinforce health monitoring functions of space crafts and WPT between space crafts will be able to reduce onboard electrical power subsystems (EPS) of each space craft. However, the resources such as size, weight, power consumptions are generally limited in a space craft. In addition, mission requirements and environments are completely different in each mission, especially in space science or space exploration missions. Besides, from a radio frequency (RF) technical standpoint, the higher the frequency of WPT is, the smaller the size of WPT components become. However, in high-frequency WPT, circuit designs are more complicated and free-space span losses are larger than those of low-frequency WPT. Therefore, the specifications of WPT such as frequency, power, etc. must not be determined without considering both mission requirements and RF features.

3.1 High power GaN amplifier combiner for space communication ground station

A 1kW-class GaN high power amplifier equipment was designed and fabricated in the S-band. It consists of three parts, a GaAs driver amplifier, 200W-classs high power amplifier units and a circular waveguide combiner. The Block diagram and overview of 1kW-class GaNSSPA Unit are shown in Fig. 8 and Fig. 9, respectively.

Input-output characteristics of the 1kW-class SSPA Unit including nonlinear amplification at 2.1 GHz, allocated for earth-to-space link are shown in Fig. 10. More than 60 dBm output power was achieved in this evaluation. In addition, measured combining efficiency can be seen in table 1. High combining efficiency of 87.1 % was obtained.
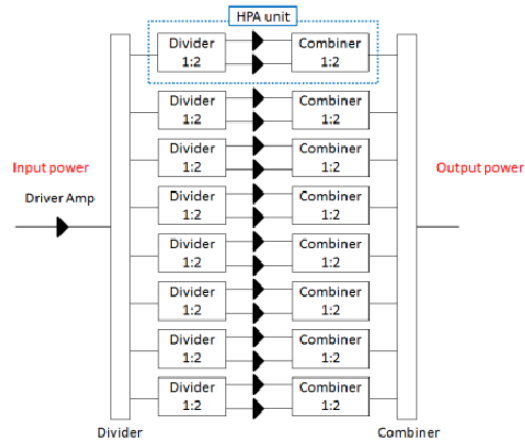
Fig. 8. Block diagram of 1-kW-class GaN HPA equipment
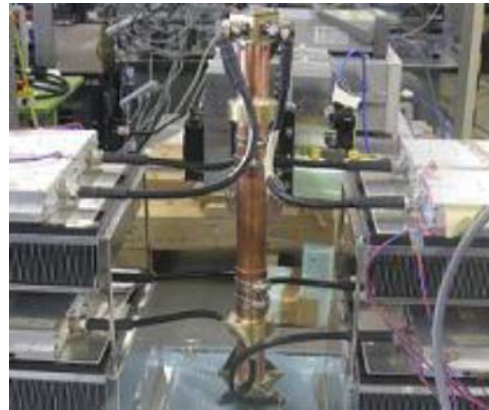
Fig. 9. 1-kW-class GaN HPA equipment
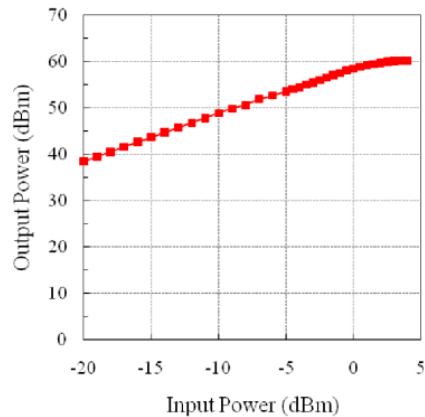
Fig. 10. 1-kW-class HPA equipment characteristics

Further, the output power stability during more than half an hour operation is shown in Fig. 11. About 5 % degradation of the output power was observed. (H. Noji, 2011)

Table 1 Combining efficiency of 1-kW-class HPA equipment

HPA1 output power	158.5 W
HPA2 output power	141.3 W
HPA3 output power	154.9 W
HPA4 output power	147.9 W
HPA5 output power	154.9 W
HPA6 output power	138.0 W
HPA7 output power	147.9 W
HPA8 output power	144.5 W
Total input power to combiner	1188 W
Output power from combiner	1035 W
Combining efficiency	87.1 %
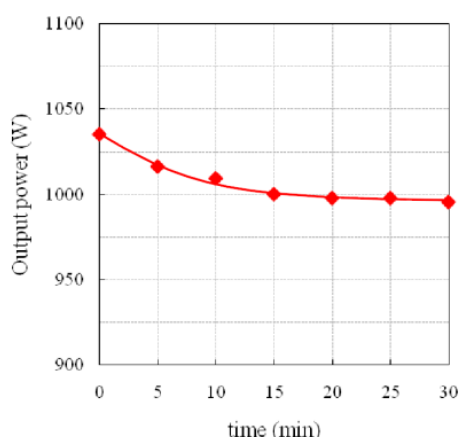
Fig. 11. Ouput power stability of 1-kW-class HPA equipment

3.2 The wireless sensor and batter charging by MPT

The applications of GaN modules for space use are numerous such as onboard communication system, ground station communication system, wireless power transmission system, and wireless sensor network system. Here, the combination of microwave power/energy transmission with the sensor network, namely the wireless sensor and energy transfer (WiSEnT), was conducted. The WiSEnT with a thermal sensor was evaluated inside an anechoic chamber as the first step toward future spacecraft health monitoring system. The thermal sensor was connected with the rectifier directly and it can operate without any batteries. The thermal sensor was operated as the normal sensor system with a battery and the fundamental data were obtained through the preliminary experiment. These are indicated in Fig. 12.

Further, the application of the GaN based HPA to MPT for the purpose of battery charging with a rectifier was checked inside an anechoic chamber. The block diagram of MPT experiment is shown in Fig. 13. The inside and outside appearances of the

anechoic chamber are shown in Fig. 14 and 15 respectively. In Figs. 13 and 14, the distance between transmission and receiving antenna was 1.2 m.

In Fig. 13, 2.25 GHz sine wave generated by the SG was amplified by the GaN HPA. Then, the amplified signal was supplied to the divider. After that, the divided signals were radiated by the 16-element transmission array antenna. The radiated signal was received by the 16-element receiving array antenna and combined by the power combiner. Then, the combined signal was converted into DC signal by the rectifier. After that, the DC signal was supplied to the DC/DC converter and the converted signal was supplied to the battery. The transmission and receiving RF powers divided by directional couplers were measured by power meters. The measured power of transmission antenna (EIRP) and that of rectifier realized 58.8 dBm and 33.3 dBm, respectively.

The battery voltage during the MPT experiment is shown in Fig. 16. The Figure 16 indicates that the charging achieved totally up to 1615.5 Ws (=0.449 Wh) in about 6 hours 43 minutes. The DC/DC converter was inserted between the rectifier and the battery so as to keep the conversion efficiency of the rectifier high. In general, the efficiency strongly depends on the load resistance of a rectifier and it is important to keep the resistance at the optimum value. However, a load resistance of a battery is usually changing while it is charging. Therefore, when the output signal of a rectifier is directly supplied to a battery, the conversion efficiency changes widely. In Fig. 13, however, it is indicated that the battery charging rate was not constant. Therefore, the load resistance of the rectifier must have been changing although the DC/DC converter was used.
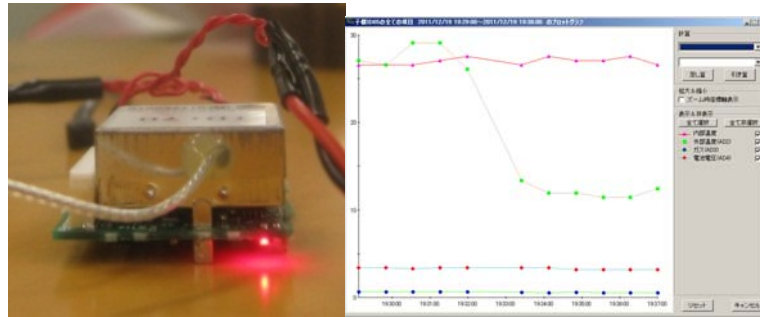
Fig. 12. The preliminary experiment for the thermal sensor operating with microwave power transmission
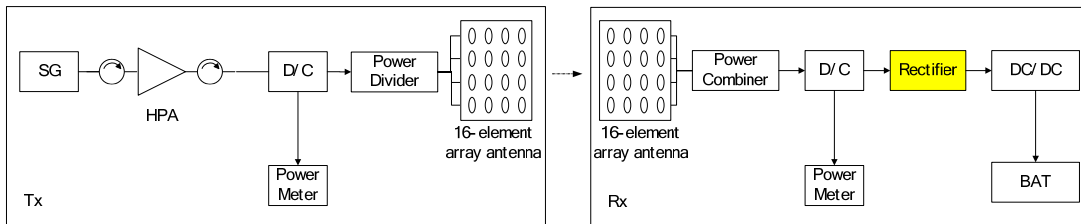
Fig. 13. Block diagram of WPT experiment
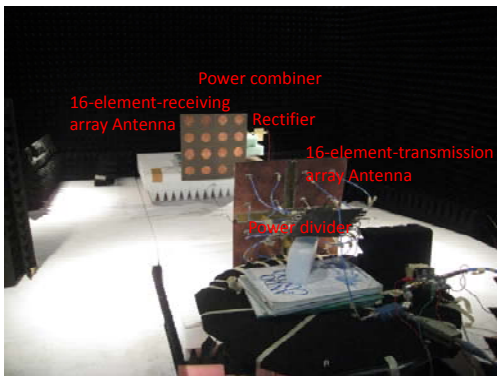
Fig. 14.Componentsused inside of anechoic chamber
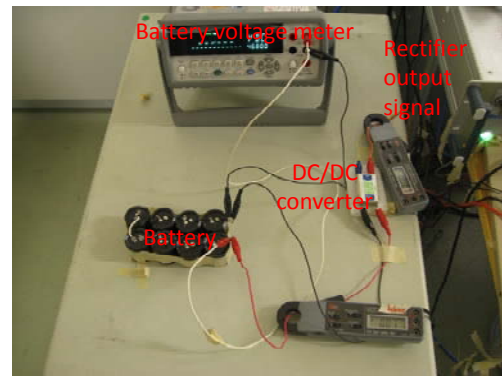
Fig. 15. Components used forbattery charging
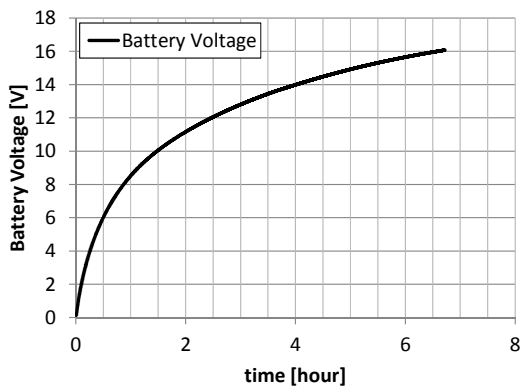
Fig. 16. Battery voltage

3.3 Space environmental testing

For an actual space use, the space environmental testing such as temperature, thermal vacuum, and radiation are significant. GaN is expected to tolerate these harsh environmental testing due to its characteristics. The space environmental testing listed in table 2 was conducted with the 20-W-class GaN HPA. The test facilities are shown in Fig. 17.

Table 2 Conditions of space environmental testing

Test name	Conditions
Temperature	-5 degC ,25 degC, 55degC
Thermal vacuum	Thermal cycle(-20 to 60 degC) 1E-4 ~ 1E-3 Pa
Radiation	^{60}Co, Total Ionizing Dose (TID) : 320 krad (Rate: 20krad/h) (After radiation test, aging test was done.) (100 degC, 168hours continuous operation)

(a) Temperature

(b) Thermal vacuum

© JAEA

(c) Radiation (@JAEA)
Fig. 17. Test facilities

Results of thermal vacuum testing and radiation testing are shown in Figs. 18 and 19 respectively. Figure 18 indicates that the GaN amplifier continued to function normallyduring the thermal cycle
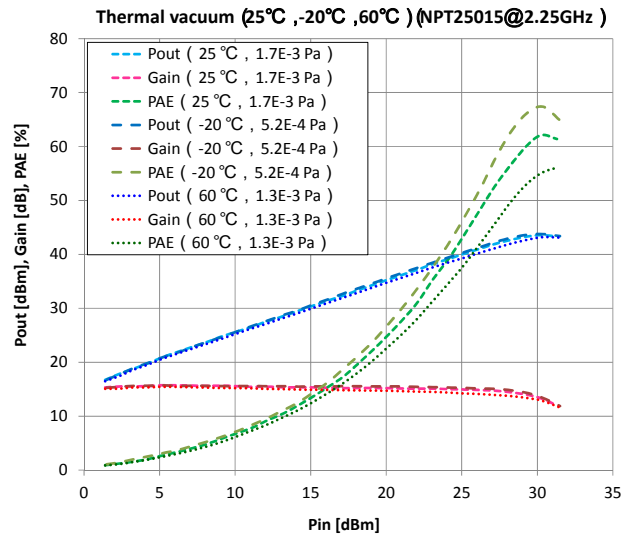
Fig. 18. Result of thermal vacuum testing
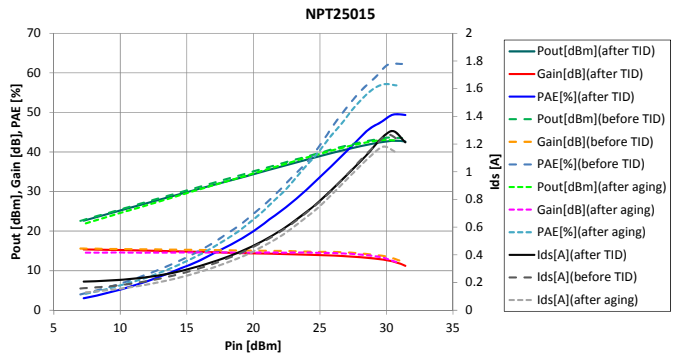
Fig. 19. Result of radiation testing

although the PAE of each temperature were a little different. Further, Fig. 19indicates theGaN amplifier, once degraded by the radiation, came back to its previous operation by the aging test. This is named as annealing effect. From these results, it was greatly enhanced that the GaN will be able to be used in the space.

4   SUMMARY

In this paper, the design, fabrication, and evaluation of high power and high efficiency GaNHPAs were described. Further, the battery charging experiment for the space MPT to a rover was demonstrated. In addition, the environmental testing results for space use are shown.

The 20W-class GaNHPA realized 43.7 dBm output signal power with 63.3 % PAE at 2.25 GHz, the 100W-clas HPA realized 48.0 dBm with 52.6 %,

and 1kW-class SSPA unit realized 60.1 dBm output signal power with 87.1 % combining efficiency at 2.1 GHz.The experiments of thermal sensor operation and battery charging by MPT using the GaN HPAs werecarried out. The thermal sensor operated as the normal one with a battery supported by MPT. In addition, the battery was charged up by the converted DC power under the condition where the EIRP was 58.8 dBm, the rectifier input power was 33.3 dBm, and the distance between the power transmitter and the receiver was 1.2 m. Further, the GaN amplifier could continue to function normally during the space environmental testing of temperature, thermal vacuum, and radiation.

Through these experiments, it is believed that flexibilities for the future missions in terms of size, weight, and power consumption using GaN will be improved.

ACKNOWLEDGEMENTS

REFERENCES

N. Shinohara and S. Kawasaki., 2009. Recent Wireless Power Transmission Technologies in Japan for Space Solar Power Station/Satellite.*RWS2009 Digest*, MO2A-4, San Diego, Jan. 2009, pp. 13-15.

M. Furukawa, et al, 2006. 5.8-GHz Planar Hybrid Rectenna for Wireless Powered Applications, *APMC2006 Digest*, FR2E-1, Yokohama, Dec. 2006.

M. Hori, et al., 2011. The 5.8GHz Receiving and Rectenna Arrayfor Wireless Communication and Power Transmission, *IEICE technical report in Japanese*, MW2010-135(2011-1), Jan. 2011.

T. Ito, et al., 1979. Fundamental Experiment of a Rectenna Array for Microwave Power Reception, *IEICE Trans.communication*, vol.E76-B, no.12, pp.958-968, Dec.1979.

N. Adachi, et al., 2005. High temperature operation of AlGaN/GaN HEMT, *Microwave Symposium Digest*, 2005 IEEE MTT-S International, June 2005.

H. Noji, et al., 2011.A 1kW-Class S-band Compact Waveguide Combiner Unit with GaN HPAs for WPT and Space Communication, *41st European Microwave Conference*, Manchester, UK, Oct. 2011.

Y. Kobayashi, et al., 2012. The S-band GaN-Based High Power Amplifier and Rectenna for Space Energy Transfer Applications, *Proceedings of IMWS-IWPT2012*, Kyoto, Japan, May 2012.

Remote Sensing

RADAR CROSS SECTION ANALYSIS OF TWO CANONICAL, PARALLEL-PLATE WAVEGUIDE CAVITIES WITH MATERIAL LOADING

Kazuya Kobayashi

Department of Electrical, Electronic, and Communication Engineering, Chuo University
1-13-27 Kasuga, Bunkyo-ku, Tokyo 112-8551, Japan
kazuya@tamacc.chuo-u.ac.jp

Abstract: A rigorous radar cross section analysis is carried out for two canonical cavities formed by a semi-infinite parallel-plate waveguide and by a finite parallel-plate waveguide using the Wiener–Hopf technique. Exact and approximate solutions are obtained, and the scattered field inside and outside the cavities is evaluated analytically. Numerical examples on the radar cross section (RCS) are presented for various physical parameters and far-field scattering characteristics of the cavities are discussed in detail.

1 INTRODUCTION

Analysis of the electromagnetic scattering from open-ended metallic waveguide cavities has received much attention recently in connection with the prediction and reduction of the radar cross section (RCS) of a target. This problem serves as a simple model of duct structures such as jet engine intakes of aircrafts and cracks occurring on surfaces of general complicated bodies. There have been a number of investigations on the scattering by two-dimensional (2-D) and three-dimensional (3-D) cavities of various shapes based on high-frequency techniques and numerical methods. It appears, however, that the solutions obtained by these methods are not uniformly valid for arbitrary cavity dimensions.

The Wiener–Hopf technique is known as a powerful, rigorous approach for solving diffraction problems related to canonical geometries. In the previous papers, we have considered two different parallel-plate waveguide cavities with material loading, and carried out a rigorous RCS analysis using the Wiener–Hopf technique (Koshikawa et al., 1994; Koshikawa and Kobayashi, 1997, 2000). As a result, it has been shown that our final solutions provide accurate, reliable results over a broad frequency range. We have also verified that, for large cavities, the absorbing layer loading inside the cavities results in significant RCS reduction.

This paper is in continuation with our past research on the cavity RCS. We shall consider two canonical, 2-D parallel-plate waveguide cavities with material loading, and carry out a comparative RCS study of these cavities. The first geometry (referred to as Cavity I) is a cavity formed by a semi-infinite parallel-plate waveguide with an interior planar termination, where three different material layers are coated on the surface of the terminated plate. The second geometry (referred to as Cavity II) is a cavity formed by a finite parallel-plate waveguide with a planar termination at the aperture of the waveguide, where the same material layers as in Cavity I are coated on the surface of the terminated plate. It is noted that geometries of interior regions of the two cavities are exactly the same as each other. The exterior features are, however, totally different since Cavity I has two parallel semi-infinite plates, being joined to its outer right-angled corners. In the previous papers, we have rigorously analyzed the plane wave diffraction by Cavity I (Koshikawa and Kobayashi, 1997, 2000) and by Cavity II (Koshikawa et al., 1994) using the Wiener–Hopf technique. The purpose of this paper is to compare the solutions for Cavity I and Cavity II and investigate the effect of geometrical differences of the two cavities on the far-field backscattering characteristics. Both E and H polarizations are considered. The results of this paper have been

presented in our recent paper (Kobayashi and Koshikawa, 2006) from somewhat different aspects.

The time factor is assumed to be $e^{-i\omega t}$ and suppressed throughout this paper.

2 RIGOROUS WIENER–HOPF ANALYSIS

2.1 Cavity I: Cavity Formed by a Semi-Infinite Parallel-Plate Waveguide

We first consider the plane wave diffraction by Cavity I. As mentioned above, Cavity I is formed by a semi-infinite parallel-plate waveguide with an interior planar termination. The problem geometry is shown in Figure 1(a), where $-\Gamma < -d_1 < -d_2 < -d_3 < -d_4 < 0$, and the upper and lower plates at $x = \pm b$ and the endplate at $z = -d_1$ are infinitely thin, perfectly conducting, and uniform in the y-direction. The material layers I $(-d_1 < z < -d_2)$, II $(-d_2 < z < -d_3)$, and III $(-d_3 < z < -d_4)$ inside the waveguide are characterized by the relative permittivity/permeability (e_{rm}, m_{rm}) for $m = 1, 2,$ and 3, respectively.

Let the total field f^t be defined by $f^t(x,z) = f^i(x,z) + f(x,z)$, where $f^i(x,z) = e^{-ik(x \sin q_0 + z \cos q_0)}$ is the incident plane wave of E or H polarization for $0 < q_0 < p/2$ with $k \, [\in \, w(m_0 e_0)^{1/2}]$ being the free-space wavenumber. The term $f(x,z)$ is the unknown scattered field and satisfies the 2-D Helmholtz equation. For convenience of analysis, we assume that the vacuum is slightly lossy as in $k = k_1 + ik_2$ with $0 < k_2 = k_1$.

Introducing the Fourier transform for the scattered field and applying boundary conditions in the transform domain, the problem is formulated in terms of the modified Wiener–Hopf equations of the second kind, which are solved exactly in a formal sense using the factorization and decomposition procedure. It should be noted that the formal solution involves infinite series with unknown coefficients. Applying a rigorous asymptotics with the aid of the edge condition, approximate expressions of the infinite series are derived leading to an efficient approximate solution of the Wiener–Hopf equations. This approximate solution involves numerical inversion of matrix equations. The results are uniformly valid for arbitrary cavity dimensions. The scattered field in the real space is derived explicitly by taking the inverse Fourier transform and evaluating the resultant integrals.

2.2 Cavity II: Cavity Formed by a Finite Parallel-Plate Waveguide

We now consider the diffraction problem for Cavity II, which is formed by a finite parallel-plate waveguide with a planar termination at the aperture. The geometry of the cavity is shown in Figure 1(b), where f^i is the incident field of E or H polarization, where $-L < D_1 < D_2 < D_3 < L$, and the cavity plates are perfectly conducting and of zero thickness. The material layers I $(-L < z < D_1)$, II $(D_1 < z < D_2)$, and III $(D_2 < z < D_3)$ inside the cavity are characterized by the relative permittivity/permeability (e_{rm}, m_{rm}) for $m = 1, 2,$ and 3, respectively. Comparing Cavity I and Cavity II, it is seen that the interior cavity geometries are exactly the same as each other.

(a) Cavity I.
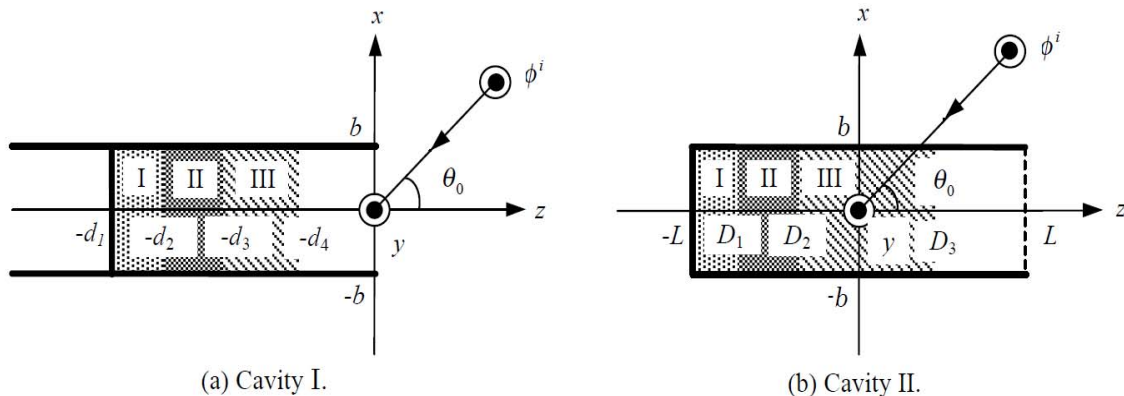
(b) Cavity II.

Figure 1: Geometry of the cavities.
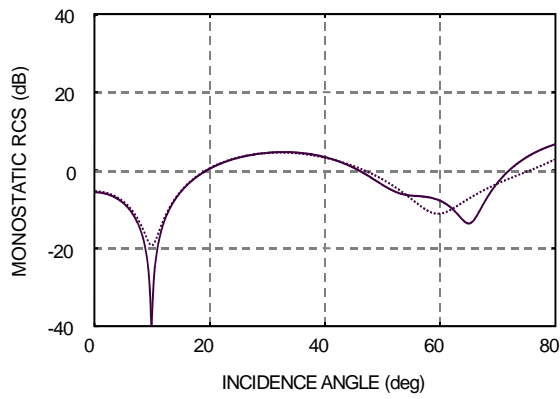
(a) *E* polarization, $kb = 3.14$.
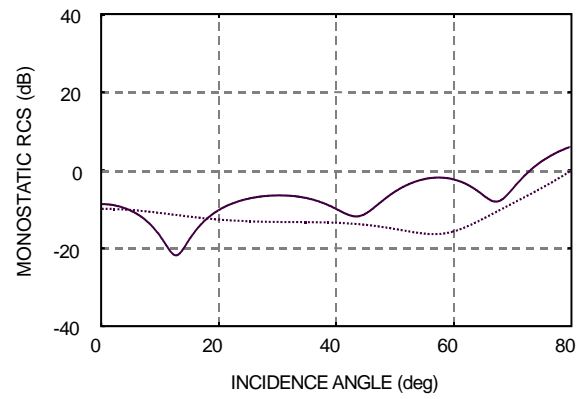
(d) *H* polarization, $kb = 3.14$.
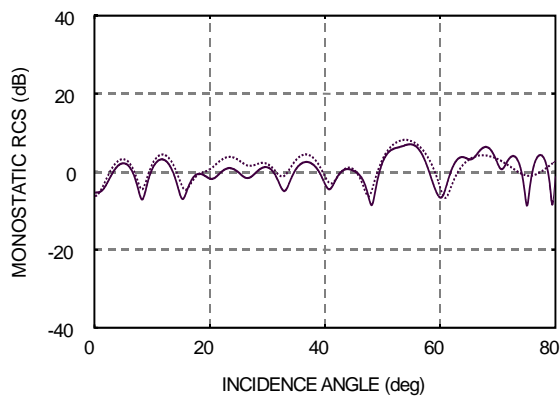
(b) *E* polarization, $kb = 15.7$.
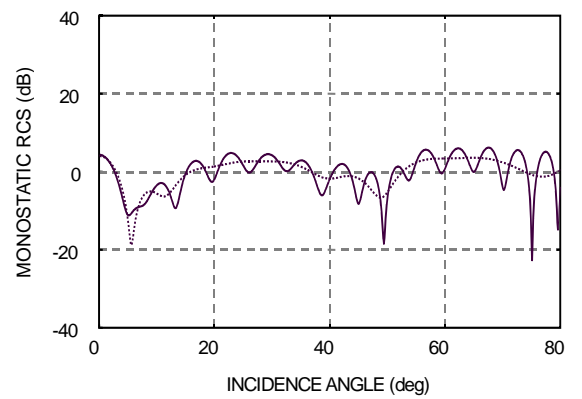
(e) *H* polarization, $kb = 15.7$.
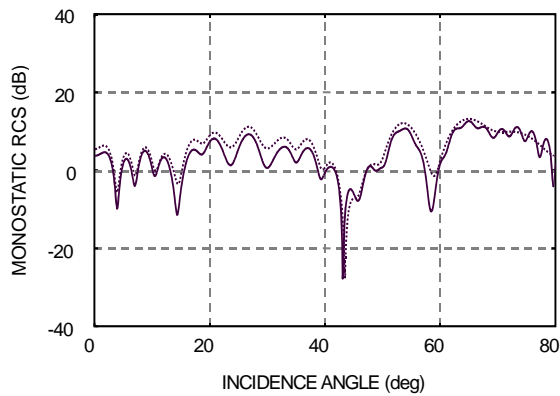
(c) *E* polarization, $kb = 31.4$.
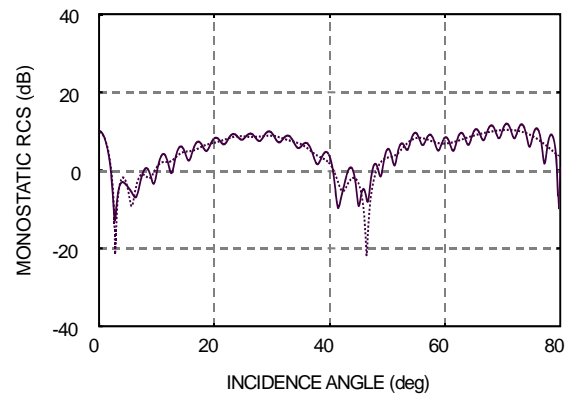
(f) *H* polarization, $kb = 31.4$.

Figure 2: Monostatic RCS versus incidence angle for $d_1 / 2b = L / b = 1.0$. —— : Cavity I, —— : Cavity II. The three-layer material inside the two cavities is Emerson & Cuming AN-73 with $kt = 2.08$.

Taking the Fourier transform of the Helmholtz equation and solving the resultant transformed wave equations, a scattered field expression in the Fourier transform domain is derived. Applying boundary conditions in the transform domain, the problem is formulated in terms of the modified Wiener–Hopf equations of the third kind. The Wiener–Hopf equations are solved exactly in a formal sense via the factorization and decomposition procedure as in the case of Cavity I leading to an exact solution. The solution involves branch-cut integrals with unknown integrands as well as infinite series with unknown coefficients. Assuming the cavity depth $2L$ to be large compared with the wavelength, high-frequency asymptotic expansions of the branch-cut integrals are explicitly derived. As for the infinite series in the formal solution, we apply the edge condition to obtain their approximate expressions. This procedure leads to an approximate solution of the Wiener–Hopf equations, which is valid for the cavity depth large compared with wavelength. The scattered field in the real space is derived by taking the Fourier inverse and evaluating the resultant integrals.

3 NUMERICAL RESULTS AND DISCUSSION

We shall now show representative numerical examples of the RCS for both E and H polarizations to discuss the far field scattering characteristics of the cavities in detail. In particular, the effect of geometrical differences of the two cavities on the scattered far field is investigated. The RCS per unit length is defined by

$$s = \lim_{r \to \Gamma} (2pr \, |f / f^i |^2),$$

where (r, q) is the cylindrical coordinate defined by

$$x = r \sin q, z = r \cos q \text{ with } -p < q < p.$$

Figures 2(a-c) and 2(d-f) show numerical results of the normalized monostatic RCS s / l [dB] as a function of incidence angle q_0 for E and H polarizations, respectively, where l is the free-space wavelength. In numerical computation, cavity dimensions have been taken as

$$kb = 3.14, 15.7, 31.4$$
$$\text{with } d_1 / 2b = L / b = 1.0.$$

We have chosen Emerson & Cuming AN-73 as

an existing three-layer material, where the material constants are

$$e_{r1} = 3.4 + i10.0, e_{r2} = 1.6 + i0.9, e_{r3} = 1.4 + i0.35,$$
$$m_{r1} = m_{r2} = m_{r3} = 1.0,$$

and the thickness of each layer is such that

$$d_1 - d_2 = d_2 - d_3 = d_3 - d_4 = D_1$$
$$+L = D_2 - D_1 = D_3 - D_2 (= t / 3).$$

The thickness of the three-layer material is taken as $kt = 2.08$.

It is seen from the figure that, the RCS curves for Cavity I and Cavity II with $kb = 3.14$ and E polarization (Figure 2(a)) show close features for

$$0° < q_0 < 55°,$$

whereas in all the other examples, there are differences on the backscattering characteristics between the two cavities. These differences are clearly observed in the H-polarized case, since the RCS curves for Cavity II oscillate rapidly in comparison to those for Cavity I. This oscillation for Cavity II is due to the fact that the multiple diffraction occurs between the leading edges at the aperture and the outer edges of the right-angled back corners.

4 CONCLUSIONS

In this paper, we have carried out a rigorous Wiener–Hopf analysis of the plane wave diffraction by two different cavities with three-layer material loading, formed by a semi-infinite parallel-plate waveguide (Cavity I) and by a finite parallel-plate waveguide (Cavity II). Both E and H polarizations have been considered. We have shown representative numerical examples of the monostatic RCS to discuss far-field backscattering characteristics of the cavities in detail. The results of this paper can be used as reference solutions for validating more general approximate methods. In recent papers, we have analyzed the diffraction problems involving more complicated waveguide cavities (Shang and Kobayashi, 2009a, 2009b; Zheng et al., 2010).

REFERENCES

Koshikawa, S., Momose, T., Kobayashi, K., 1994. RCS of a parallel-plate waveguide cavity with three-layer material loading. *IEICE Trans. Electron.*, vol. E77-C, no. 9, pp. 1514–1521.

Koshikawa, S., Kobayashi, K., 1997. Diffraction by a terminated, semi-infinite parallel-plate waveguide with three-layer material loading. *IEEE Trans. Antennas Propagat.*, vol. AP-45, no. 6, pp. 949–959.

Koshikawa, S., Kobayashi, K., 2000. Diffraction by a terminated, semi-infinite parallel-plate waveguide with three-layer material loading: the case of *H* polarization. *Electromagnetic Waves & Electronic Systems*, vol. 5, no. 1, pp. 13–23.

Kobayashi, K., Koshikawa, S., 2006. Wiener–Hopf analysis of the radar cross section of two canonical, parallel-plate waveguide cavities with material loading. *Proc. 2006 International Workshop on Electromagnetic Wave Scattering (EWS 2006)*, pp. 2.25–2.30 (invited paper).

Shang, E. H., Kobayashi, K., 2009a. Diffraction by a terminated, semi-infinite parallel-plate waveguide with four-layer material loading. *Progress In Electromagnetics Research B*, vol. 12, pp. 1–33.

Shang, E. H., Kobayashi, K., 2009b. Diffraction by a terminated, semi-infinite parallel-plate waveguide with four-layer material loading: the case of *H* polarization. *Progress In Electromagnetics Research B*, vol. 12, pp. 139–162.

Zheng, J. P., Shang, E. H., Kobayashi, K., 2010. Wiener–Hopf analysis of the plane wave diffraction by a finite parallel-plate waveguide with four-layer material loading. *Proc. 2010 URSI International Symposium on Electromagnetic Theory (EMTS 2010)*, pp. 1120–1123 (invited paper).

TARGET DETECTION USING FORWARD SCATTERING RADAR WITH GPS RECEIVERS

Christo Kabakchiev

Faculty of Mathematics & Informatics, Sofia University, 125 Tzarigradsko shose Blvd., Sofia, Bulgaria
ckabakchiev@fmi.uni-sofia.bg, ckabakchiev@yahoo.com

Vera Behar

Institute of Information & Communication Technologies, BAS, 25-A Acad. G.Bonchev Str., Sofia, Bulgaria
behar@bas.bg

Herman Rohling

Department of Telecommunications,TU hamburg-Harburg, Hamburg,Germany
rohlingr@tu-harburg.de

Keywords: Forward scattering radar, target detection, GPS signal processing

Abstract: A possible algorithm for target detection in a GPS-based Forward Scattering Radar is considered. The FSR system consists of a transmitter mounted on a satellite of GPS and a receiver located on the Earth's surface. Theoretical calculations are presented using the secondary application of the GPS L5 signal. The numerical results illustrate the idea of target detection in GPS-based FSR.

1 INTRODUCTION

Forward Scattering Radar (FSR) is a specific type of bistatic radars that operate in the narrow area of the forward scattering effect where the bistatic angle is close to 180^0, and the target moves near the transmitter-receiver baseline. In FSR the Babinet's principle is exploited to form the forward scatter signature of a target (Chernyak, 1999). According to this principle, the drastic enhancement in scattering is created due to the forward scattering effect. This type of radar provides a countermeasure to 'stealth' technology because due to the forward scattering effect, the Radar Cross Section (RCS) of targets extremely increases (by 2-3 orders) and mainly depends on the target's physical cross section and is independent of the target's surface shape and the absorbing coating on the surface. However, FSR has some fundamental limitations, which are the absence of range resolution and operation within very narrow angles ($\pm10^0$) (Cherniakov et al., 2006).

In this paper a passive FSR system where the satellites of the GPS system are exploited as 'illuminators of opportunity' is considered. (Fig. 1). The civil L1 signal is transmitted by satellites at 1572.42 MHz and contains the coarse acquisition (C/A) code, which is unique for each satellite. The C/A code modulated signal is a BPSK signal with a chip rate of 1.023 MHz and the repetition interval of 1ms. The L1 signal frequency bandwidth is 2.046 MHz. The idea to apply a GPS L1 receiver to FSR for air target detection is firstly discussed in (Koch and Westphal, 1995). Some experimental results of a GPS L1 receiver concerning detection of air targets are shown and discussed in (Suberviola et al., 2012). However, modernization of GPS provides a good opportunity to use the improved properties of a new designed civil GPS signal L5 in FSR, which exploits GPS as a non-cooperative transmitter. The major innovations of the signal L5 signal, with respect to GPS L1 signal, are the additional NH code modulation and the use of a pilot channel free of data (Mongredien et al., 2006).
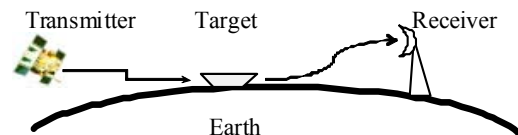
Figure 1. FSR topology

The L5 signal is transmitted at 1176.45 MHz with a received power of -154 dBw, which makes the L5 signal four times stronger than the L1 signal. Two quadrature components of the L5 signal, referred as I5 and Q5, are bi-phase modulated with a different PRN of length 10230 chips. The PRN codes are generated at a 10.23 MChips/s rate, resulting in 1 ms period. Therefore, the bandwidth of the L5 signal is increased to 20.46 MHz, which is ten times wider than the bandwidth of the L1 signal. The I5 and Q5 components are then modulated by a 10-bit NH-sequence and a 20-bit NH-sequence, respectively. Each bit of the NH-sequences is 1ms, resulting in 10ms period of the I5 component and 20ms period of the Q5 component, respectively.

A possible algorithm for air target detection in a GPS L5-based FSR system is described in (Behar and Kabakchiev, 2011), and the detection probability characteristics are calculated in (Behar et al., 2011) for the case when low-flying and poorly maneuverable (for example, helicopters) air targets are detected on the background of a white Gaussian noise, or in the presence of: Urban Interference Environment or a Stand-off-Jammer (SOJ).

Our main aim in this paper is to show perspectives of GPS-L5-based FSR systems to reliably detect ground or marine targets when GPS satellites are located at small elevation angles. Our task here is to present a possible algorithm for marine target detection and target parameter estimation in a GPS receiver used in FSR and also to roughly estimate the potential maximum target detection range in conditions of sea clutter. A set of experimental records of signals from a small boat provided by the team of Birmingham University is used in order to estimate Signal-to-clutter-plus-noise ratio (SNR) and calculate the probabilities characteristics.

2 SIGNAL PROCESSING

The general block-scheme of a possible algorithm for target detection and parameter estimation is shown in Fig.2.
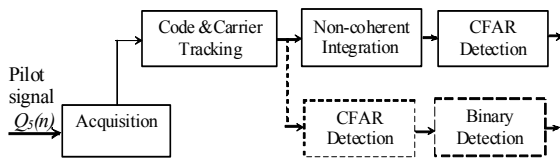
Figure 2. FSR signal processing

The Q5 component from the front end including filtering and down conversion is then sampled by the A/D converter. The signal from satellite k after the A/D conversion can be described as

$$Q_5(n) = A(n)c_Q(n)NH_{20}(n)\cos(\omega_{IF}n) + N(n) \quad (1)$$

where n is discrete in time, ω_{IF} that is the intermediate frequency to which the front end has down converted the carrier frequency, $N(n)$ is the total noise, and $c_Q(n)$ is the PRN code. The main goal of acquisition is the roughly estimation of the Doppler frequency and the ($c_Q \cdot NH_{20}$) code delay of the visible satellite. The tracking loops ensure that the prompt correlator is synchronized with the incoming pseudorandom ($c_Q \cdot NH_{20}$) code. They also synchronize the receiver local oscillator in frequency and phase with each satellite signal carrier within the period of the Q5 component of the GPS L5 signal. In this manner, the correlation magnitude remains in the real part only (in-phase component). Two variants of algorithms can be used for target detection. The first of them firstly integrates signal within a moving window and then uses a CFAR detector to indicate the target signal detection (CFAR detection with non-coherent integration). According to the second algorithm, a CFAR detector firstly indicates whether the target signal is present in each sample of the correlator output. After that the binary detector indicates the target signal detection (CFAR detection with binary integration).

For a GPS L5 receiver, the frequency bandwidth is 20.46 MHz, and the noise level N_r in decibels is nearly -131 dB. The signal-to-noise ratio at the RF front-end output of the GPS receiver can be written as (Glennon et al., 2006):

$$SNR = P_{rec} / N_r = P_t G_r \sigma /(4\pi R_{tg}^2 N_r) \quad (2)$$

According to [2,6,7], the forward scatter RCS σ of a target depends only on the physical cross section of the target (A_{tg}) and can be calculated approximately as:

$$\sigma = 4\pi A_{tg}^2 / \lambda^2 = 4\pi(hl)^2 / \lambda^2 \quad (3)$$

In (3), A_{tg} is the target physical cross section, and the parameters h and l are geometrical dimensions of a target. In order to obtain the SNR expression at the input of a CFAR detector in FSR, we replace the parameter σ in (2) by its expression (3).

$$SNR = P_t G_r (hl)^2 /(\lambda^2 R_{tg}^2 N_r) \quad (4)$$

At the output of the Code& Tracking loops the signal-to-noise ratio is given by:

$$SNR = P_t G_r (hl)^2 G_{SP} /(\lambda^2 R_{tg}^2 N_r) \quad (5)$$

where G_{SP} is the processing gain of the cross-correlator.

3 DETECTION PROBABILITY

The signal to-noise ratio (4) could be improved by non-coherent or binary integration over M samples. In the extreme case, when, for example, the target moving in the forward scattering zone at velocity V and crosses the baseline at an angle of nearly 90^0, the maximum integration time corresponding to target visibility within the main lobe of the target scattering pattern is given by:

$$T_{tg} = 2d_R{}^2 \lambda /(Vl) \qquad (6)$$

where d_R is the distance from the receiver to the point of crossing and it can be assumed that $d_R=R_{tg}$. The number of integrated samples M can be determined from (5) as:

$$M = E[T_{tg} / T_{Q5}] \qquad (7)$$

where T_{Q5} =20$msec$ and E[.] is the integer part of the fraction in brackets.

3.1 CFAR Detection with Non-coherent Integration

In a CFAR detector, after non-coherent integration of M samples of the signal intensity at the envelope detector output, the following test statistics is formed for each sample n in the time domain:

$$q_M(n) = \sum_{k=n-M/2}^{n+M/2-1} |s(k)|^2 \qquad (8)$$

The intensity in n^{th} time discrete indicates signal detection if the test statistics (7) exceeds an adaptive threshold H_n. According to [7], the decision rule for detection is:

$$\Phi_M(n) = \begin{cases} 1, & if\ q_M(n) \geq H_n(K) \\ 0, & otherwise \end{cases} \qquad (9)$$

The parameter K in (9) is the length of the reference window used to estimate the total noise level. When the noise intensity is unknown, the detection threshold $H_n(K)$ in (9) is formed adaptively for each integrated sample $q_n(M)$ of the signal intensity at the envelope detector output. In a cell-average CFAR detector the threshold $H_n(K)$ is formed as:

$$H_n(K) = T_\alpha \cdot w_n(K) \qquad (10)$$

where Tα is the scale factor, $\omega_n(K)$ is the average power of the total noise calculated over samples if the reference window.

$$w_n(K) = \sum_{k=1}^{K} |s(k)|_n^2 \qquad (11)$$

The probability of false alarm p_{FA} maintained at the output of a CFAR detector can be calculated using the following expression (Behar et al., 2011):

$$P_{FA} = \sum_{n=0}^{K-1} \binom{K+n-1}{K-1} \frac{T_\alpha^n}{(1+T_\alpha)^{K+n}} \qquad (12)$$

In the worst case when the signal intensity from the target independently fluctuates according to the χ^2-law, the probability of detection at the output of a CFAR detector is evaluated as follows [7]:

For $1 \leq M \leq 2$:

$$P_D = \sum_{j=L-1}^{1} \binom{2-M}{1-j} \frac{\alpha^{1-j}}{\beta^{M-j-1}} \sum_{n=0}^{j} \binom{K+n-1}{1} \frac{(\alpha T_\alpha)^n}{(1+\alpha T_\alpha)^{K+n}} \qquad (13)$$

For $M>2$

$$P_D = \sum_{i=0}^{M-3} \binom{M-2-i}{1} \frac{(-\alpha)^2}{\beta^{M-1-i}} \sum_{j=0}^{i} \binom{K+j-1}{j} \frac{T_\alpha^j}{(1+T_\alpha)^{K+j}} + \\ + \sum_{m=0}^{1} \binom{M-2-m}{M-3} \frac{(-\alpha)^{1-m}}{\beta^{M-m-1}} \sum_{n=0}^{m} \binom{K+n-1}{n} \frac{(T_\alpha\alpha)^n}{(1+T_\alpha\alpha)^{K+n}} \qquad (14)$$

The parameters α and β in (13) and (14) are evaluated as follows:

$$\alpha = 1/(1+M \cdot SNR/4) \quad and \quad \beta = 1-\alpha \qquad (15)$$

The parameter SNR in (15) is the average signal-to-noise ratio evaluated by (5). The scale factor Tα used in (13) and (14) is determined as a root of the equation (12) for a fixed value of the false alarm probability P_{FA}.

3.2 CFAR Detection with Binary Integration

All decisions $\Phi(n)$ at the CFAR detector output obtained within M consequential time samples are summarized and compared with a fixed integer threshold L. The binary decision rule for target detection is:

$$\Phi_M(L) = \begin{cases} 1, & if\ \sum_{n=1}^{M} \Phi(n) \geq L \\ 0, & otherwise \end{cases} \qquad (16)$$

The probability of false alarm at the binary detector output is:

$$P_{FA} = \sum_{n=L}^{M} \binom{M}{n} (p_{FA})^n (1-p_{FA})^{M-n} \qquad (17)$$

The parameter p_{FA} in (17) is the probability of false alarm maintained at the CFAR detector output, which is calculated by (13). The probability of target

detection at the binary detector output is calculated analogically:

$$P_D = \sum_{n=L}^{M} \binom{M}{n} (p_D)^n (1-p_D)^{M-n} \quad (18)$$

The parameter p_D in (18) is the detection probability at the CFAR detector output calculated for M=1.

3.3 Probability of Target Detection

According to the block-scheme of signal processing (Fig.2), the probability of target detection can be expressed by the following expression:

$$P_{t\,arg} = P_{acq} \cdot P_D \quad (19)$$

The parameter P_{acq} in (19) is the probability of GPS signal acquisition. For the sake of simplicity we assume that outside the geometrical shadow of the target (dead zone) this parameter is close to 1.

4 NUMERICAL RESULTS

Before we calculate the probability of target detection using the expressions (12-19) need to determine the SNR at the cross-correlator output in one period of the Q5 component of the GPS L5 signal (T_{Q5}=20msec) because the SNR values are used for calculating the parameters α and β in (15).
The SNR at the cross-correlator output is calculated for a small target (h=1m and l=1m) as a function of the distance to the target R_{tg}. The SNR values obtained are plotted in Figure 3. The following parameters of the GPS L5 signal are used in calculations: carrier frequency – f_o=1176MHz (λ=0.2551m); frequency bandwidth – ΔF=20.46MHz, the GPS L5 signal power near the Earth's surface – P_t=-154dBW.
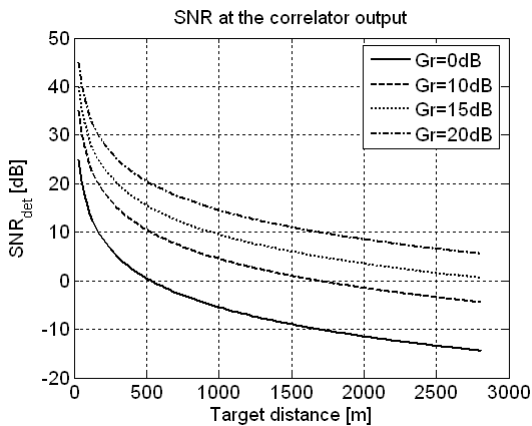
Figure 3. SNR at the correlator output within 20msec

As shown in Figure 3, the SNR is calculated for four values of the antenna gain: G_r= [0; 10; 15; 35] dB.
    The number of integrated samples at the correlator output and the corresponding them integration time for the case when the target crosses the forward scattering zone and moving within it perpendicular to the baseline with velocity 7.5 m/s are plotted in Figure 4 depending on the distance to the target.
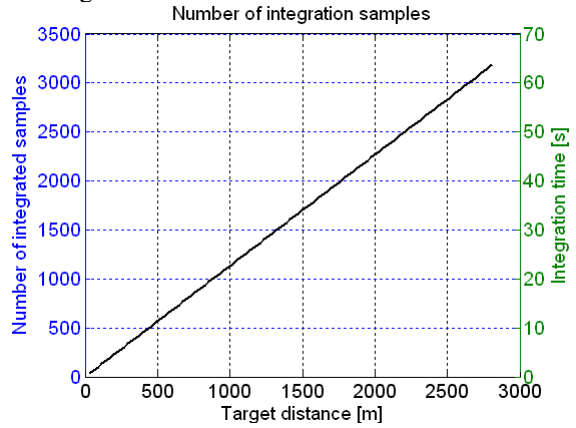
Figure 4. Number of integration samples (left) and the corresponding integration time (right)

It can be seen that the integration time can be very large and can reach to 60-70 sec for a target moving with velocity 7.5 m/s (27km/hour).
    The probability of small target detection with non-coherent integration of the correlator outputs is calculated as a function of the target distance and shown in Figure 5. The probability of detection is calculated by equations (12, 13, 14) for the false alarm probability of 10^{-7}. The SNR values at the correlator output, which are used for calculation of the probability characteristics by (12, 13, and 14), are shown in Figure 3.
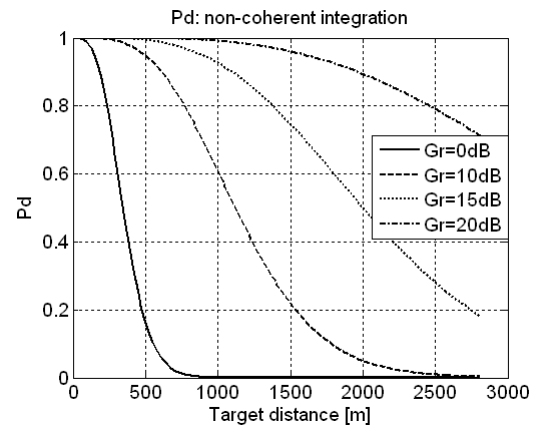
Figure 5. Probability of detection with non-coherent integration for P_{FA}=10^{-7}

The number of integrated samples (*M*) used for calculation of the probability characteristics is shown in Figure 4 (left). The size of a reference window (*K*) used in (13) and (14) is *K*= 60.

The probability of small target detection with binary integration of the correlator outputs is calculated as a function of the target distance and shown in Figure 6. The probability of detection is calculated by equations (17, 18) for the false alarm probability of 10^{-7}. After CFAR detection at the correlator output the decision rule "*L* out of *M*" is used for target detection. The values of the detection probability plotted in Figure 6 are calculated for the binary threshold *L*=2*M*/3, where *M* is the number of integrated samples.

Comparing the two probabilities of detection, with non-coherent and binary integration, it can be seen that the detectability of targets strongly depends on the antenna gain that the receiver creates in the direction of the visible GPS satellite. Obviously, the greater the gain of the antenna in the direction of visible GPS satellites, so at large distances can be detected a moving target in the forward scattering area. For example, a small target that crosses the forward scattering zone can be detected with probability of 0.9 at the distance 2000m (with non-coherent integration) or 1700m (with binary integration) if the receiver antenna creates in the direction of the visible GPS satellite the gain of at least 20dB. The numerical results presented in Figure 5 and 6 also illustrate that in case of the omnidirectional antenna of the receiver (Gr=0dB), small targets can be detected only at very close distances (200m-300m) regardless of the type of integration (non-coherent or binary).

Obviously, in conditions of interference, the SNR in Figure 3 must be corrected taking into account the ''interference-to-noise'' ratio (INR).
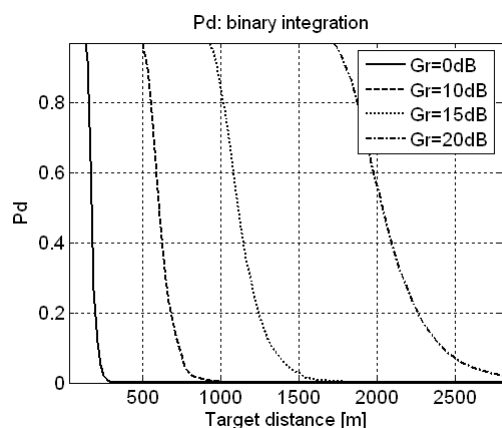
Fig.6 Probability of detection with binary integration
L=2M/3 and P_{FA}=10^{-7}

4   CONCLUSIONS

It is shown that forward scattering radar with a non-cooperative GPS-based transmitter can be used for detection of small targets on the background of a white Gaussian noise if the receiver antenna creates in the direction of the visible GPS satellite the appropriate gain.

ACKNOWLEDGEMENTS

REFERENCES

Chernyak, V., 1999, *Fundamentals of Multisite Radar Systems*, Gordon and Breach Science Publishers.

Cherniakov, M., Abdullah, R., Jancˇovicˇ, P., , Salous, M., Chapursky, V., 2006, Automatic ground target classification using forward scattering radar. In *IEE Proc. on Radar Sonar Navig.,* vol. 153, no. 5, pp. 427 – 437, October 2006.

Koch,V., Westphal, R., 1995, New approach to a multistatic passive radar sensor for air/space defense. In *IEEE AES Systems Magazine*, pp. 24-32, November, 1995.

Suberviola, I., Mayordome, I., Mendizabal, J., Experimental results of air target detection with GPS forward scattering radar, 2012, In *IEEE Geoscience and Remote Sensing Letters*, vol. 9, no. 1, pp.47-51, January 2012.

Mongredien, C., Lachapele, G., Gannon, M., Testing GPS L5 acquisition and tracking algorithms using a hardware simulator, 2006. In *Proc. of ION GNSS*, Fart Wart TX, , pp. 2901-2913, September 2006.

Behar V., Kabakchiev, Ch., Detectability of Air Target Detection using Bistatic Radar Based on GPS L5 Signals, 2011. In *Proc. IRS'2011,12-th Intern. Radar Symp.*, Leipzig, pp. 212-217, September 2011.

Behar, V., Kabakchiev, Ch., Rohling, H., Air Target Detection Using Navigation Receivers Based on GPS L5 Signals, 2011. In *Proc. of ION GNSS' 2011, 24th International Technical Meeting of The Satellite Division of the Institute of Navigation*, Portland OR, pp. 333-337, September 2011.

Glennon, E., Dempster, A., Rizos, C., Feasibility of air target detection using GPS as bistatic radar, 2006. In *Journal of Global Positioning Systems*, vol. 5, no. 1-2, pp. 119-126, 2006.

BSAR SIGNAL MODELING AND SLC IMAGE RECONSTRUCTION

T.P. Kostadinov, A.D. Lazarov

Institute of Information and Communication Technologies, Bulgarian Academy of Sciences, G. Bonchev 2, Sofia, Bulgaria,
Dept. of Informatics and Technical Sciences Burgas Free University, San Stefano 63 Burgas, Bulgaria
kostadinov.todor@yahoo.com, lazarov@bfu.bg

Abstract: In this paper, a Bistatic Synthetic Aperture Radar (BSAR) signal model and Single Look Complex (SLC) image obtained by multiple satellite BSAR system are considered. Geometry and kinematics of BSAR scenario, including a BSAR satellite transmitter and multiple receivers as well as a complicated surface of observation are described. BSAR signal model based on linear frequency modulated emitted waveform and BSAR scenario is derived. Standard Fourier transformation is applied to extract an SLC BSAR image of high quality on range and cross range directions. To verify the BSAR signal model and image extraction procedure a numerical experiment is carried out.

1 INTRODUCTION

In recent years raise in the interest of Bistatic Synthetic Aperture Radar (BSAR) technology is a fact. BSAR concept in SAR for Earth observation and BSAR spaceborne performance are analyzed in (Moccia A., 2002). Application of a BSAR method increases the quality of imaging and improves the functionality of the imaging radars (Moccia, A., 2005). Bistatic configurations of synthetic aperture radar imaging systems have been investigated in (Loffeld, O., 2003). New bistatic SAR techniques for imaging are proposed in (Ender, J. H. G, 2004). The problems of the focusing of SAR image are considered in (D'Aria, D., 2004). Passive space-surface bistatic SAR for local area monitoring is described in (Cherniakov M., 2009). Maritime target cross section estimation for an ultra-wideband forward scatter radar network is considered in (Daniel L., 2008). Results of a space-surface bistatic SAR image formation algorithm are presented in (Antoniou M., 2007).

BSAR in essence is a bistatic configuration, with a moving satellite transmitter, and two or more stationary receivers, spatially separated by a base line. The scene of observation includes stationary and/or moving objects. In latter case the system is referred to Generalized Bistatic Inverse Synthetic Aperture Radar (BISAR).

In the present work a scenario with satellite transmitter two receivers and stationary object is discussed. All components of bistatic SAR configuration are described in one and the same coordinate system. First, an accent is made on definition and implementation of BSAR geometry and kinematical vector equations. Second, a special attention is dedicated to processes of BSAR signal formation and image reconstruction procedure that comprises range and azimuth compressions implemented by Fourier transforms.

The rest of the paper is organized as follows. In Section 2 BSAR scenario that comprises geometry and kinematical equations of satellite transmitter carrier is described. In Section 4 a linear frequency waveform and BSAR signal model in topology with one satellite transmitter and two receivers are discussed in details. In Section 4 an image reconstruction algorithm is derived. In Section 5 results of a numerical experiment are graphically illustrated and thoroughly discussed. In Section 6 conclusions are made.

2 BSAR GEOMETRY

Three dimensional (3-D) BSAR scenario presented in Fig. 1 comprises satellite transmitter described by current position vector $\mathbf{R}^s(p)$ in discrete time instant p, stationary receivers described by current position vectors $\mathbf{R}^r_1$ and $\mathbf{R}^r_2$, and a target of interest, all situated in Cartesian coordinate system $Oxyz$. The target is presented as an assembly of point scatterers in the same Cartesian coordinate system as the transmitter and the receivers.
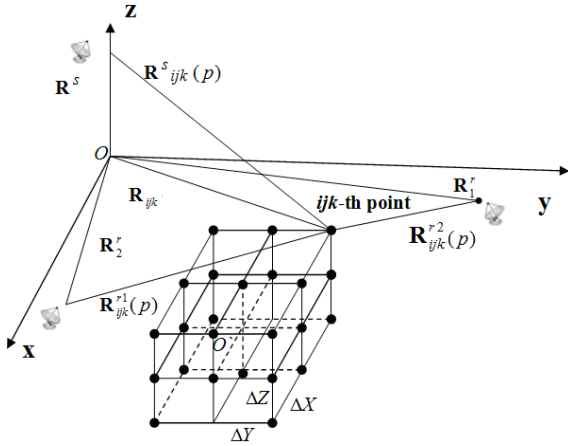
Figure 1: 3-D geometry of BSAR scenario

Denote $\mathbf{R}^s_{ijk}(p) = \left[x_{ijk}(p), y_{ijk}(p), z_{ijk}(p) \right]^T$ as a range distance vector measured from the satellite transmitter with the current vector position $\mathbf{R}^s(p)$ to the ijkth point scatterer of the object space at the moment p, is described by the vector equation

$$\mathbf{R}^s_{ijk}(p) = \mathbf{R}^s(p) + \mathbf{V}\left(\frac{N}{2} - p \right)T_p + \mathbf{R}_{ijk} \qquad (1)$$

where $\mathbf{V}$ is the satellite's vector-velocity, T_p is the pulse repetition period, N is the number of emitted pulses

$$\mathbf{R}_{ijk} = [x_{ijk}, y_{ijk}, z_{ijk}]^T \qquad (2)$$

is the position vector of the target.

Range distance vector between the ijkth point scatterer and the first receiver is defined by:

$$\mathbf{R}^{r1}_{ijk} = \mathbf{R}^r_1 - \mathbf{R}_{ijk} \qquad (3)$$

Range distance vector between the ijkth point scatterer and the second receiver is defined by:

$$\mathbf{R}^{r2}_{ijk} = \mathbf{R}^r_2 - \mathbf{R}_{ijk} \qquad (4)$$

Round trip distance transmitter-ijkth point scatterer-first receiver expressed as

$$R^1_{ijk}(p) = \left| \mathbf{R}^s_{ijk}(p) \right| + \left| \mathbf{R}^{r1}_{ijk} \right|. \qquad (5)$$

Round trip distance transmitter-ijkth point scatterer-second receiver expressed as

$$R^2_{ijk}(p) = \left| \mathbf{R}^s_{ijk}(p) \right| + \left| \mathbf{R}^{r1}_{ijk} \right|. \qquad (6)$$

3 LFM PULSES AND BSAR SIGNAL MODEL

The satellite transmitter transmits a series of electromagnetic waves to the moving target, which are described analytically by sequence of N linear frequency modulated pulses each of which is described by

$$\dot{S}(t) = \mathbf{rect}\frac{t}{T}\mathbf{exp}\left\{ -j\left[\omega t + bt^2 \right] \right\}, \qquad (7)$$

where $\omega = 2\pi\dfrac{c}{\lambda}$ is the angular frequency; $c = 3.10^8$ m/s is the speed of the light; λ is the wavelength of the signal; T is the time duration of a LFM pulse; $b = \dfrac{2\pi\Delta F}{T}$ is the LFM rate. The bandwidth of the transmitted pulse provides the dimension of the range resolution cell.

The deterministic component of the BSAR signal, reflected by ijkth point scatterer of the target and registered by first and second receiver can be described by the expression (Lazarov A., 2011)

$$\dot{S}^{1,2}_{ijk}(p,t) = a_{ijk}\mathbf{rect}\frac{t - t^{1,2}_{ijk}(p)}{T} \times$$
$$\times \mathbf{exp}\left\{ -j\left[\omega\left(t - t^{1,2}_{ijk}(p)\right) + b\left(t - t^{1,2}_{ijk}(p)\right)^2 \right] \right\} \qquad (8)$$

where

$$\mathbf{rect}\frac{t-t_{ijk}^{1,2}(p)}{T} = \begin{cases} 1, 0 \le \dfrac{t-t_{ijk}^{1,2}(p)}{T} < 1, \\ 0, \dfrac{t-t_{ijk}^{1,2}(p)}{T} < 0 \\ 0, \dfrac{t-t_{ijk}^{1,2}(p)}{T} \ge 1 \end{cases} \quad (9)$$

where a_{ijk} is the reflection coefficient of the ijkth point scatterer, a 3-D image function; $t_{ijk}^{1,2}(p) = \dfrac{R_{ijk}^{1,2}(p)}{c}$ is the time delay of the signal from the ijkth point scatterer; t is the time dwell or the fast time of the BSAR signal which in discrete form can be written as

$$t = [k_{ijk\,\min}^{1,2}(p) + k - 1]\Delta T \quad (10)$$

where $k = \overline{1, [k_{ijk\,i\max}^{1,2}(p) - k_{ijk\,\min}^{1,2}(p)] + K}$ is the sample number of a LFM pulse; $K = \dfrac{T}{\Delta T}$ is the full number of samples of the LFM pulse, ΔT is the time duration of a LFM sample, $k_{ijk\,\min}^{1,2}(p) = \left\lceil \dfrac{t_{ijk\,\min}^{1,2}(p)}{\Delta T} \right\rceil$ is the number of the radar range bin where the signal, reflected by the nearest point scatterer of the target is detected, $t_{ijk\,\min}^{1,2}(p) = \dfrac{R_{ijk\,\min}^{1,2}(p)}{c}$ is the minimal time delay of the BSAR signal reflected from the nearest point scatterer of the target $K(p) = k_{ijk\,\max}^{1,2}(p) - k_{ijk\,\min}^{1,2}(p)$ is the relative time dimension of the target; $k_{ijk\,\max}^{1,2}(p) = \left\lceil \dfrac{t_{ijk\,\max}^{1,2}(p)}{\Delta T} \right\rceil$ is the number of the radar range bin where the signal, reflected by farthest point scatterer of the target is detected; $t_{ijk\,\max}^{1,2}(p) = \dfrac{R_{ijk\,\max}^{1,2}(p)}{c}$ is the maximum round trip time delay of the BSAR signal reflected from

the farthest point scatterer of the target and received in both receivers.

The range vector coordinates from the satellite transmitter to the ijk-th point scatterer can be calculated by the following equations

$$\begin{aligned} x^s_{ijk}(p) &= x_s - V_x T_p[(N/2) - p] - x_{ijk}, \\ y^s_{ijk}(p) &= y_s - V_y T_p[(N/2) - p] - y_{ijk}, \\ z^s_{ijk}(p) &= z_{0s} - V_z T_p[(N/2) - p] - z_{ijk} \end{aligned} \quad (11)$$

The distance from satellite transmitter to the ijkth point scatterer is defined by

$$R_{ijk}^s(p) = \left[\left(x_{ijk}^s(p)\right)^2 + \left(y_{ijk}^s(p)\right)^2 + \left(z_{ijk}^s(p)\right)^2 \right]^{\frac{1}{2}} \quad (12)$$

The range vector - coordinates from the ijk-th point scatterer to the receivers can be calculated by the following equations

$$\begin{aligned} x_{ijk}^{1,2} &= x_r^{1,2} - x_{ijk}, \\ y_{ijk}^{1,2} &= y_r^{1,2} - y_{ijk}, \\ z_{ijk}^{1,2} &= z_r^{1,2} - z_{ijk} \end{aligned} \quad (13)$$

The distance from ijkth point scatterer to the receivers is defined by

$$R_{ijk}^{1,2} = \left[\left(x_{ijk}^{1,2}\right)^2 + \left(y_{ijk}^{1,2}\right)^2 + \left(z_{ijk}^{1,2}\right)^2 \right]^{\frac{1}{2}} \quad (14)$$

The deterministic components of the BSAR signal return from the target and registered in first and second receivers are defined as a superposition of signals reflected by point scatterers placed on the target, i.e.

$$\dot{S}^{1,2}(p,t) = \sum_{ijk} \dot{S}_{ijk}^{1,2}(p,t)$$

$$= \sum_{ijk} \left(\begin{array}{l} a_{ijk}\mathbf{rect}\dfrac{t-t_{ijk}^{1,2}(p)}{T} \times \\ \times \mathbf{exp}\left\{ -j\left[\begin{array}{l} \omega\left(t - t_{ijk}^{1,2}(p)\right) + \\ + b\left(t - t_{ijk}^{1,2}(p)\right)^2 \end{array} \right] \right\} \end{array} \right) \quad (15)$$

which in discrete form can be written as

$$\dot{S}^{1,2}(p,t) = \sum_{ijk} \dot{S}^{1,2}_{ijk}(p,t)$$

$$= \sum_{ijk} a_{ijk} \mathbf{rect} \frac{(k^{1,2}_{ijk\,min}(p)+k)\Delta T - t^{1,2}_{ijk}(p)}{T}$$

$$\times \mathbf{exp}\left\{-j\left[\begin{array}{c}\omega\left((k^{1,2}_{ijk\,min}(p)+k)\Delta T - t^{1,2}_{ijk}(p)\right)+ \\ +b\left((k^{1,2}_{ijk\,min}(p)+k)\Delta T - t^{1,2}_{ijk}(p)\right)^2\end{array}\right]\right\} \quad (16)$$

where

$$\mathbf{rect}\frac{(k^{1,2}_{ijk\,min}(p)+k)\Delta T - t^{1,2}_{ijk}(p)}{T}$$

$$= \begin{cases} 1 \text{ if } 0 \le \dfrac{(k^{1,2}_{ijk\,min}(p)+k)\Delta T - t^{1,2}_{ijk}(p)}{T} < 1 \\[2mm] 0 \text{ if } \dfrac{(k^{1,2}_{ijk\,min}(p)+k)\Delta T - t^{1,2}_{ijk}(p)}{T} < 0 \\[2mm] 0 \text{ if } \dfrac{(k^{1,2}_{ijk\,min}(p)+k)\Delta T - t^{1,2}_{ijk}(p)}{T} \ge 1 \end{cases} \quad (17)$$

where $k = \overline{0,[k^{1,2}_{ijk\,max}(p) - k^{1,2}_{ijk\,min}(p)] + K - 1}$.

For programming implementation all terms, including image function a_{ijk}, rectangular function

$$\mathbf{rect}\frac{(k^{1,2}_{ijk\,min}(p)+k)\Delta T - t^{1,2}_{ijk}(p)}{T} \quad (18)$$

and exponential function

$$\mathbf{exp}\left\{-j\left[\begin{array}{c}\omega\left((k^{1,2}_{ijk\,min}(p)+k)\Delta T - t^{1,2}_{ijk}(p)\right)+ \\ +b\left((k^{1,2}_{ijk\,min}(p)+k)\Delta T - t^{1,2}_{ijk}(p)\right)^2\end{array}\right]\right\} \quad (19)$$

are presented as multidimensional matrices to which entry-wise product is applied.

Demodulation (dechirping) of the BSAR signal return is performed by multiplication with a complex conjugated emitted waveform, i.e.

$$\hat{S}^{1,2}(t,p) = S(t,p) \times \mathbf{rect}\frac{t}{T}\exp\left[-j(\omega t + bt^2)\right]$$

$$= \sum_{ijk} a_{ijk}\mathbf{rect}\frac{t - t^{1,2}_{ijk}(p)}{T} \times$$

$$\exp\left\{j\left[\begin{array}{c}\omega\left(t - t^{1,2}_{ijk}(p)\right)+ \\ +b\left(t - t^{1,2}_{ijk}(p)\right)^2\end{array}\right]\right\}.\exp\left[-j(\omega t + bt^2)\right] \quad (20)$$

which yields

$$\hat{S}^{1,2}(t,p) = \sum_{ijk} a_{ijk}\mathbf{rect}\frac{t - t^{1,2}_{ijk}(p)}{T}$$

$$\times \exp\left\{-j\left[(\omega + 2bt)t^{1,2}_{ijk}(p) - b\left(t^{1,2}_{ijk}\right)^2(p)\right]\right\} \quad (21)$$

Denote the current angular frequency of emitted LFM pulse as $\omega(t) = \omega + 2bt$, where ω is the carrier angular frequency, and b is the chirp rate, $t = k\Delta T$ is the discrete time parameter, where k is the sample number, ΔT is the sample time duration. Then the current discrete frequency can be written as $\omega_k = \omega + 2b(k\Delta T)$ or

$$\omega_k = k\left(\frac{\omega}{k} + 2b(\Delta T)\right) = k\Delta\omega_k.$$

Then expression (24) can be rewritten as (Lazarov A., 2011)

$$\hat{S}^{1,2}(t,p) = \sum_{ijk} a_{ijk}\mathbf{rect}\frac{t - t^{1,2}_{ijk}(p)}{T}$$

$$\times \exp\left[-j\left(2\omega(t)\frac{R^{1,2}_{ijk}(p)}{c} - b\left(\frac{2R^{1,2}_{ijk}(p)}{c}\right)^2\right)\right] \quad (22)$$

which in discrete form can be written as

$$\hat{S}^{1,2}(k,p) = \sum_{ijk} a_{ijk}\mathbf{rect}\frac{(k^{1,2}_{ijk\,min}(p)+k)\Delta T - t^{1,2}_{ijk}(p)}{T}$$

$$\times \exp\left[-j\left(2\omega_k\frac{R^{1,2}_{ijk}(p)}{c} - b\left(\frac{2R^{1,2}_{ijk}(p)}{c}\right)^2\right)\right] \quad (23)$$

The expression (23) can be interpreted as a projection of the three-dimensional image function a_{ijk} onto two-dimensional BSAR signal plane

$\hat{S}^{1,2}(k,p)$ by the projective operator, the exponential term

$$\exp\left[-j\left(2\omega_k\frac{R_{ijk}^{1,2}(p)}{c}-b\left(\frac{2R_{ijk}^{1,2}(p)}{c}\right)^2\right)\right] \quad (24)$$

Then the 2-D mage function, $a_{ijk}^{1,2}$ can be extracted from 2-D BSAR signal in two receivers by the inverse operation

$$a_{ijk}^{1,2}=\sum_{p=1}^{N}\sum_{k=1}^{K}\hat{S}^{1,2}(k,p).\exp\left[j\left(2\omega_k\frac{R_{ijk}^{1,2}(p)}{c}-b\left(\frac{2R_{ijk}^{1,2}(p)}{c}\right)^2\right)\right] \quad (25)$$

where k is the discrete coordinate measured onto the line of sight of the object's geometric centre, p is the azimuth discrete coordinate.

4   IMAGE RECONSTRUCTION ALGORITHM

First order Taylor expansion of the exponential term

$$\exp\left[j\left(2\omega_k\frac{R_{ijk}^{1,2}(p)}{c}-b\left(\frac{2R_{ijk}^{1,2}(p)}{c}\right)^2\right)\right] \quad (26)$$

and its substitution in (23) yields the following image extraction procedure

$$a_{ijk}^{1,2}(\hat{p},\hat{k})=\sum_{p=1}^{N}\left[\sum_{k=1}^{K}\left(\begin{array}{c}\hat{S}^{1,2}(p,k).\\ .\exp\left(j2\pi\frac{k\hat{k}}{K}\right)\end{array}\right)\right].\exp\left(j2\pi\frac{p\hat{p}}{N}\right) \quad (27)$$

Range compression

$$\tilde{S}^{1,2}(p,\hat{k})=\frac{1}{K}\sum_{k=1}^{K}\hat{S}^{1,2}(p,k).\exp\left(j2\pi\frac{k\hat{k}}{K}\right) \quad (28)$$

Azimuth compression

$$a_{ijk}^{1,2}(\hat{p},\hat{k})=\frac{1}{N}\sum_{p=1}^{N}\tilde{S}^{1,2}(p,\hat{k}).\exp\left(j2\pi\frac{p\hat{p}}{N}\right) \quad (29)$$

where $\hat{p}=\overline{1,N}$ and $\hat{k}=\overline{1,K}$ are ijkth point scatterer's azimuth and range discrete coordinates, respectively.

Range and azimuth (cross range) compressions are implemented by standard fast Fourier transforms.

5   NUMERICAL EXPERIMENT

To prove the properties of the 3-D SAR signal model with linear frequency modulation and to verify the correctness of the BSAR image reconstruction procedures including 2-D FFT range compression and azimuth compression a numerical experiment is carried out. It is assumed that the geometry of the target and the movement of the radar system are depicted in a 3-D Cartesian coordinate system of observation $Oxyz$. Vector coordinates of the initial point scatterer are as follow $x_{ijk}^0=0$ m, $y_{ijk}^0=0$ m, $z_{ijk}^0=0$ m; The target object of interest is a six storage building and has the following dimensions – height 15m, width 120m, dept 55 m; The satellite initial coordinates are: $x_s=-8,5$ km, $y_s=1,2$ km, $z_{0s}=200$ km; the satellite velocities are $V_x=V_y=1404$ m/s $V_z=0$ m/s, vector-coordinates of the firs receiver are: $x_1^r=2,5$ km, $y_1^r=1,2$ km, $z_1^r=300$ m; vector-coordinates of the second receiver are: $x_2^r=2,5$ km, $y_2^r=2,2$ km, $z_2^r=300$ m. The distance between the first receiver and the second one is a 1000 m on y direction. This distance is called base line. The BSAR pulse parameters: the wavelength is $\lambda=3.10^{-2}$ m; the time duration of the LFM pulse $T=10^{-6}$ s; the pulse repetition period $T_p=5.10^{-3}$ s; the carrier frequency $f=10$ GHz; the frequency bandwidth of the LFM pulse $\Delta F=3.10^8$ Hz; the number of emitted pulses $N=512$, the number of samples of LFM pulse $K=256$. The mathematical expectation of the normalized intensities of the point scatterers placed on the ship target is $a_{ijk}=0.01$.

Experimental results are presented in the following figures. In Figs. 2 and 7 a demodulated BSAR signal with real and imaginary parts, measured in first and second receiver, respectively, are depicted. In Figs. 3 and 8 range compressed BSAR signal with real and imaginary parts, measured in first and second receiver, respectively, are depicted. In Figs. 4 and 9 azimuth compressed BSAR signal with real and imaginary parts, measured in first and second receiver, respectively, are depicted. In Figs. 5 and 10 frequency azimuth compressed BSAR signal with real and imaginary parts, measured in first and second receiver, respectively, are depicted. In Figs. 6 and 11 single look complex images are presented with a module (*a*) and phase (b) of the images obtained in first and second receiver, respectively.

(*a*)   (*b*)

Figure 6: Single looks complex image in the first receiver: module (a), phase (b).

(*a*)   (*b*)

Figure 2: Demodulated BSAR signal: real part (*a*), imaginary part (*b*) in first receiver.

(*a*)   (*b*)
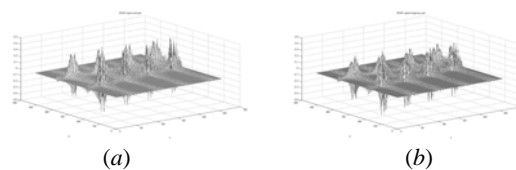
Figure 7: Demodulated BSAR signal: real part (*a*), imaginary part (*b*) in second receiver.

(*a*)   (*b*)

Figure 3: Range compressed BSAR signal: real part (*a*), imaginary part (*b*) in first receiver.

(*a*)   (*b*)
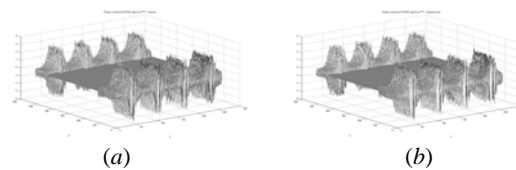
Figure 8: Range compressed BSAR signal: real part (*a*), imaginary part (*b*) in second receiver.

(a)   (b)

Figure 4: Azimut compressed BSAR signal: real part(*a*), imaginary part (*b*).

(a)   (b)
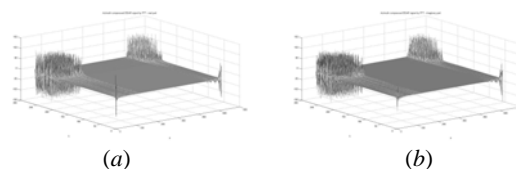
Figure 9: Azimuth compressed BSAR signal: real part (*a*), imaginary part (*b*) in second receiver.

(a)   (b)

Figure 5: Frequency shifted azimut compressed BSAR signal: real part (*a*), imaginary part (*b*).

(*a*)   (*b*)
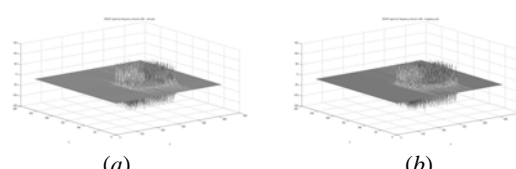
Figure 10: Frequency shifted azimuth compressed focused BSAR signal: real part (*a*), imaginary part (*b*).

(*a*) (*b*)
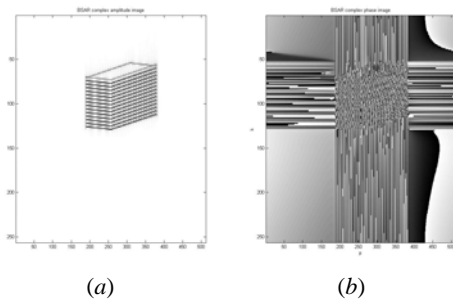
Figure 11: Single looks complex image in the second receiver: module (*a*), phase (*b*).

The comparison analysis of two single look complex images illustrates the functionality of the geometry, kinematics and signal models in BSAR scenario with multiple receivers. Between the two SLC images there are differences in the module and phase due to the baseline between the receivers. The phase difference in SLC images can be used to generate a complex interferogram that can be applied for three dimensional measurements of the observed object.

6   CONCLUSION

In the present work BSAR approach of signal formation and image reconstruction has been used. Mathematical expressions to determine the range distance to a particular point scatterer from the object space have been derived. The model of the BSAR signal return based on a linear frequency modulated transmitted signal, 3-D geometry and reflectivity properties of point scatterers from the object space has been described. The mathematical expression of BSAR target image – six storage building has been derived. Based on the concept of BSAR signal formation a classical image reconstruction procedure including range compression and azimuth compression implemented by Fourier transformation has been analytically derived. To verify the three dimensional BSAR geometry and kinematics, signal model, algorithms and image reconstruction, a numerical experiment has been carried out and results have been graphically illustrated. The multiple receiver BSAR geometry and kinematics, equations of LFM BSAR signal model can be used for modelling of signal formation process and to test image reconstruction procedures.

REFERENCES

Moccia A., Rufmo, G., D'Errico, M., Alberti G., et. al. 2002. BISSAT: A bistatic SAR for Earth observation, In *International Geoscience and Remote Sensing Symposium (IGARSS'02)*, Vol. 5, June 24-28, 2002, pp. 2628-2630.

Moccia, A., Salzillo, G., D'Errico, M., Rufino, G., Alberti, G. 2005. Performace of bistatic synthetic aperture radar. In *IEEE Trans. on AES*, vol. 41, No. 4 2005, pp. 1383 – 1395

Loffeld, O., Nies, H., Peters, V., and Knedlik, S. 2003.Models and useful relations for bistatic SAR processing", In *International Geoscience and Remote Sensing Symposium* (IGARSS), vol. 3, Toulouse, France, July 21—25, pp. 1442—1445.

Ender, J. H. G., Walterscheid, I., and Brenner, A. R. 2004. New aspects of bistatic SAR: Processing and experiments." In *International Geoscience and Remote Sensing Symposium* (IGARSS), vol. 3, Anchorage, AK, Sept. 20—24, pp. 1758—1762.

D'Aria, D., Guarnieri, A. M., and Rocca, F. 2004. Focusing bistatic synthetic aperture radar using dip move out. *IEEE Transactions on Geoscience and Remote Sensing*, 42, no. 7, pp. 1362—1376.

Lazarov A., Kabakchiev Ch., Rohling H., Kostadinov T. 2011. Bistatic Generalized ISAR Concept with GPS Waveform. In *2011 IRS - Leipzig*, pp. 849-854.

Lazarov A., Kabakchiev Ch., Cherniakov M., Gashinova M., Kostadinov T. 2011. Ultra Wideband Bistatic Forward Scattering Inverse Synthetic Aperture Radar Imaging. In *2011 IRS - Leipzig*, pp. 91-96.

Cherniakov M., Plakidis E., Antoniou M., Zuo R. 2009. Passive Space-Surface Bistatic SAR for Local Area, Monitoring: Primary Feasibility Study, In *2009 EuMA*, 30 September - 2 October 2009, Rome, Italy

Daniel L., Gashinova M., Cherniakov M.. 2008. Maritime Target Cross Section Estimation for an Ultra-Wideband Forward Scatter Radar Network. In *2008 EuMA*, Amsterdam, pp. 316-319.

Antoniou M., Saini R., Cherniakov M. 2007. Results of a Space-Surface bistatic SAR image formation algorithm, In *IEEE Trans. GRS*, vol. 45, no. 11, pp. 3359-3371.

POSSIBILITY TO THE REMOTE SENSING APPLICATION OF THE SIX-PORT TECHNOLOGY

Toshiyuki Yakabe

University of Electro-Communications
1-5-1 Chofugaoka Chofu-Shi, Tokyo, 182-8585, Japan
E-mail: yakabe@uec.ac.jp

Abstract: The six-port technology and its many useful applications are now being recognized once again in modern society. Since the six-port based wave-correlator (SPC) technology is well known for its unique ability to accurately measure the complex wave ratio (amplitude and phase difference between two waves), many applications of the SPC have been extensively investigated including a SPC based vector network analyzer (SPC-VNA).

In this paper, we start with the basic concepts and fundamentals on both the six-port based reflectometer and the six-port based wave-correlator. Next, we introduce one of the best microwave applications of the six-port technology, i.e. a prototype SPC-VNA using a developed MMIC of the SPC. Finally, we will discuss about possibility to the remote sensing technology as an alternative application of the developed MMIC SPC.

1   INTRODUCTION

The six-port technology and its many useful applications are now being recognized once again in modern society, and are published in book form. The six-port based wave correlator (SPC) technology is well known for its unique ability to accurately measure the complex wave ratio (amplitude and phase difference between two waves), besides many applications including a SPC based vector network analyzer (SPC-VNA). The SPC-VNA is very interesting for us, however, it is important to understand a basic theory firmly first of all.

In this paper, we start with the basic concepts and fundamentals on both the six-port based reflectometer and the six-port based wave-correlator. Next, we introduce one of the best microwave applications of the six-port technology, i.e. a prototype SPC-VNA using a developed MMIC of the SPC. Finally, we will discuss about possibility to the remote sensing technology as an alternative application of the developed MMIC SPC.

2   SIX-PORT FUNDAMENTALS

2.1   Six-Port Refrectometer

As an alternative measurement technique for the complex reflection coefficient Γ of a device under test (DUT), the six-port reflectometer was proposed by Engen and Hoer in the 1970s. The six-port reflectometer comprises a signal source port, a measurement port, and four sidearm ports to which power detectors are connected as shown in Fig. 1.
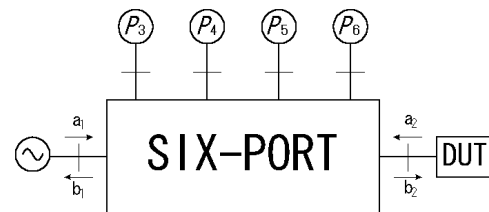
Figure 1. Six-port reflectometer

The incident and emergent scattering variables at the measurement port are denoted by a_2 and b_2 respectively. When the DUT of reflection coefficient $\Gamma = a_2 / b_2$ is connected to the port, the four sidearm port power readings P_h, (h=3, 4, 5, 6) may be written as

$$P_h = \alpha_h |A_{hi} a_2 + B_h b_2|^2 = \tag{1}$$
$$= \alpha_h |b_2|^2 |A_h \Gamma + B_h|^2 ,$$

where A_h and B_h are complex constants depending on the six-port reflectometer and α are the power conversion parameters of the power meter connected to the sidearm ports. If we denote an arbitrary sidearm port by subscript h, and one of the other four ports by i,

$$i=3, 4, 5, 6, \ i \neq h,$$

then the power ratio $_h P_i \equiv P_i / P_h$ with port h as reference port can be expressed as

$$_h P_i \equiv \frac{P_i}{P_h} = \left| \frac{A_i \Gamma + B_i}{A_h \Gamma + B_h} \right|^2 = {}_h K_i \left| \frac{1 + k_i \Gamma}{1 + k_h \Gamma} \right|^2 , \tag{2}$$
$$= b + c$$

where $_h K_i$, k_i, and k_h are calibration parameters of the six-port reflectometer which should be determined in advance.

.

2.2 Six-port Wave Correlator

A six-port wave-correlator is shown in Fig. 2. In this case, the six-port wave correlator is operated as a two-channel wave receiver. Two ports incident waves are denoted by a_2 and a_1, and defined their complex wave ratio W= a2/a2, then the four sidearm port power readings P_h, (h=3, 4, 5, 6) may be written as same formulas as (1) and (2),
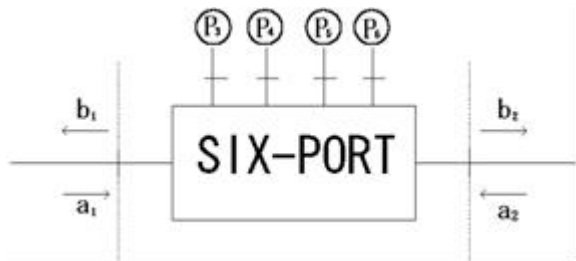
.Figure. 2. Six-port wave correlator

$$P_h = \beta_h |C_h a_2 + D_h a_1|^2 = \tag{3}$$
$$= \beta_h |a_1|^2 |C_h W + D_h|^2 ,$$

$$_h P_i \equiv \frac{P_i}{P_h} = \left| \frac{C_i \Gamma + D_i}{C_h \Gamma + D_h} \right|^2 = {}_h T_i \left| \frac{1 + t_i W}{1 + t_h W} \right|^2 , \tag{4}$$

where β are the power conversion parameters. C_h and D_h are complex constants, and $_h T_i$, t_i, and t_h are calibration parameters f the six-port wave-correlator which should be determined in advance. Although the choice of h is wholly arbitrary, we set h=4 (i=3,5,6) in harmony with Engen's notation.

Then, (4) can be rewrite,

$$_4 P_i = {}_4 T_i \left| \frac{1 + t_i W}{1 + t_4 W} \right|^2 , \tag{5}$$

where real $_4T_3$, $_4T_5$, $_4T_6$ and complex t_3, t_4, t_5, t_6 are the system parameters of the wave correlator, and W is the correlation ratio of the two incident waves a_2 and a_1. By expanding (5) into quadratic form, we have three circles in the complex W plane with the centers zi and radii Li described as

$$z_i = - \frac{t_4 \, {}_4 P_i - t_i \, {}_4 T_i}{{}_4 P_i - {}_4 T_i}^2 ,$$
$$L_i = \left| \frac{t_4 - t_i}{{}_4 P_i - {}_4 T_i} \right| \sqrt{{}_4 T_i \, {}_4 P_i} . \tag{6}$$

Since the locus of each circle represents the possible values for W, the complex W is the intersection of three circles as shown in Fig. 3.
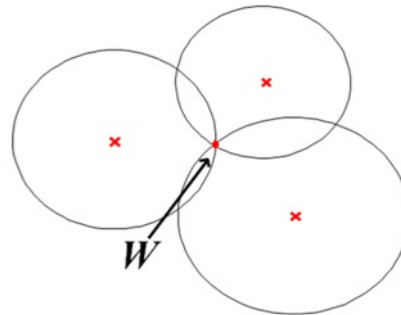
Figure. 3. Complex W plane

3   ALTERNATIVE VNA BASED ON MMIC SPC

A Prototype MMIC six-port correlator based VNA to measure the scattering parameters of a two-port DUT is shown in Fig. 4. This configuration is composed of directional couplers, switches, isolators, circulators, and matching loads.
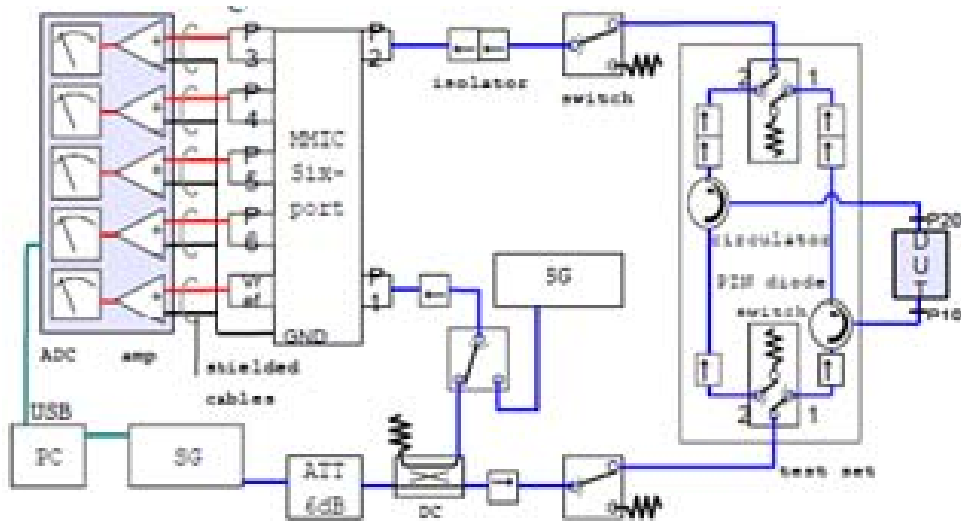
Figure. 4. Scheme of the MMIC six-port correlator based vector network analyzer

For determining the system parameters of the six-port correlator, three lines of different length are used as standards for measuring the transmission S-parameters, and three shorts with different length are used as standards for measuring the reflection S-parameters. The system performance was evaluated by measuring various two-port passive components. Figure 5 illustrates the measured S-parameters of a UWB filter. The measurement is conducted from 9 to 12 GHz with 151 points. For comparison, the measured results using a commercial VNA (Agilent N5230C) are also shown in the same figure. One can see the agreement between the two measured data is very good up to the dynamic range of 60 dB for S21. The measurement results of S11 are also in very good agreement.
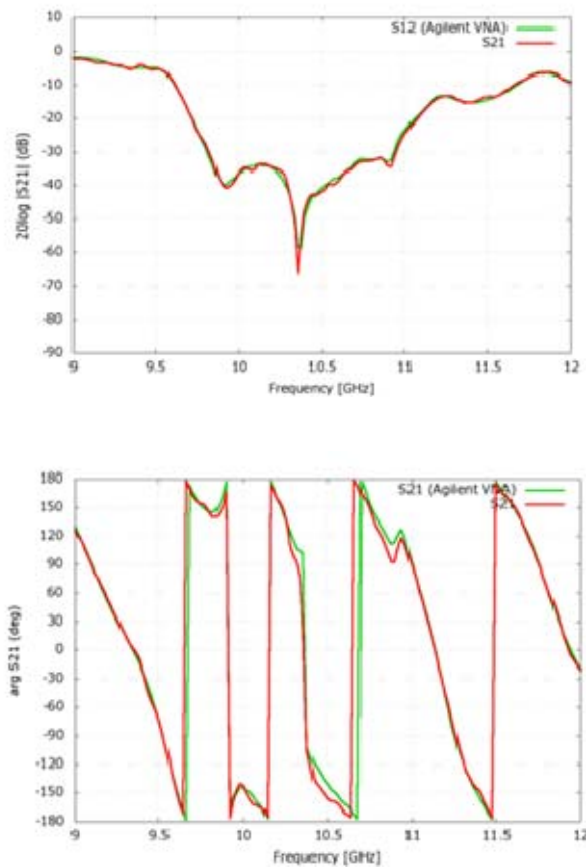
Figure. 5. S-parameters of a UWB filter measured by the developed six-port VNA and a commercial VNA

4 CONCLUSIONS AND A POSSIBILITY TO THE REMOTE SENSING OF MMIC 6PC

In this time, we introduce the six-port based wave-correlator (SPC) technology. With our improved its calibration theory, our developed MMIC SPC has a good ability to accurately measure the complex wave ratio (amplitude and phase difference between two waves). That is why we are studying and developing an alternative VNA using the SPC. Now, we are developing a compact and MMIC PSC-VNA for high frequency student experimental equipment with reasonable price as education support. In near future, we will pursue possibility of the application to the remote sensing.

REFERENCES

A Loelpin. G., Vinci, B. Laemmel, D. Kissinger and R. Weigl, Dec. 2010,. "The Six-Port in Modern Society," IEEE Microwave Magazine, vol. 11, no. 7, pp. S35-S43

Ghannouchi F. M. and A. Mohammadi, Sep. 2009, The Six-Port Technique with Microwave and Wireless Applications, ARTECH HOUSE, ISBN-13: 978-1-60807-033-6.

Engen G. F. and C. A. Hoer, Nov. 1972,. "Application of an arbitrary 6-port junction to power-measurement problems," IEEE Trans. Instrum. Meas., vol. IM-21, no. 4, pp. 470-474

Engen G. F., Dec. 1977., "The six-port reflectometer: An alternative network analyzer," IEEE Trans. Microwave Theory Tech., vol. MTT-25, pp. 1075-1080

Yakabe T., M. Kinoshita and H. Yabe, Nov. 1994 "Complete calibration of a six-port reflectometer with one sliding load and one short," IEEE Trans. Microwave Theory Tech., vol. 42, pp. 2035-2039.

Yakabe T., F. Xiao, K. Iwamoto, F. M. Ghannouchi, K. Fujii and H. Yabe, April 2001., "Six-port based wave correlator with application to beam direction findig," IEEE Trans. Instrum. Meas., vol. 50, no. 2, pp. 377-380

Yakabe T., K. Hirose, H. Matsuura, K. Fujii and F. Xiao, June 2010., "An X-band MMIC six-port correlator based vector network analyzer," 2010 Conference on Precision Electromagnetic Measurements, pp. 714-715

Yakabe T., K. Hirose, H. Matsuura, K. Fujii and F. Xiao, Sep. 2010., "Evaluation of prototype MMIC six-port wave correlator based VNA," 2010 Asia-Pacific Radio Science Conference, p. AB-3

A NEW METHOD FOR MOVING TARGET DETECTION IN SAR IMAGERY

Murat Hakan Yusufoglu, Mesut Kartal

Informatics Institute, Istanbul Technical University, Istanbul, Turkey
hakan.yusufoglu@gmail.com, kartalme@itu.edu.tr

Abstract: This paper presents a new algorithm for detection and parameter estimation of moving targets in synthetic aperture radar (SAR) images. The proposed algorithm is capable of detecting targets moving in both range and azimuth directions, and also motion parameter estimation of the detected targets. This new algorithm uses "sub-aperture processing" and "shear averaging algorithm" for detection of range and azimuth direction movements respectively. Detection algorithm is processed in range and azimuth directions independently; therefore, algorithm is suitable for parallel processing. In addition to this property, detection performance and motion parameter estimation accuracy is high because of the non-sequential processing of range and azimuth motion detection. Computer simulations gives promising results of detecting moving targets in all directions and also extracting motion parameters of the detected target.

1 INTRODUCTION

Synthetic aperture radar technology brings new developments in modern world. Today, numerous SAR applications are seen in very different areas. These applications include environmental research, scientific, civilian and military purposes. The main application area of SAR is aimed for detailed imaging of specific earth terrains. By using SAR imagery technology, any terrain image can be collected easily. These detailed images are useful for researching terrain properties.

Detection and motion parameter estimation of moving targets within the observed region is also possible by using the SAR images. Information of detected moving objects can be used in very different applications, such as monitoring traffic flow (Palubinskas and Runge, 2008), observation of military field, tracking of a specific moving target and motion parameter estimation of the targets.

Different algorithms are proposed for detection of moving targets. They are detecting moving targets by using displaced phase centre antenna (Jung, 2009, and Qin, Zhang and Dong, 2006), along track interferometry (Kohlleppel and Gierull, 2008), single-channel radar processing (Li, Xu, Peng and Xia, 2006, Liu, Yuan, Gao and Mao, 2007, Kirscht, 1998, and Kirscht, 2002), and focusing algorithms (Fienup, 2001).

As discussed by Kirscht (1998), moving targets are appeared defocused or at wrong positions depending on the direction of the target motion within the SAR image. If a target moves in azimuth direction, motion causes blurring effect in azimuth direction, and if it moves in range direction, motion also causes a displacement in azimuth direction or for a higher range velocity of the target, it even disappears (Kirscht, 1998 and Fienup, 2001). Many algorithms are evaluated based on these blurring and displacement effects on the images to detect moving targets.

Our proposed algorithm is capable of detecting targets moving not only in azimuth direction, but also in range direction. "Sub-aperture processing" and "shear averaging algorithm" is used to detect moving targets in range and azimuth directions respectively. Detection algorithm for range direction and for azimuth direction can be processed separately. This property gives the advantage of using parallel processing techniques. Therefore range and azimuth movement processes can be completed simultaneously. Also, independent motion detection processing of range and azimuth movements gives more accurate detection results.

2 THE PROPOSED ALGORITHM

In the proposed algorithm, single-channel SAR system is considered and spotlight mode raw data is used. A good clutter cancellation is applied before starting the algorithm steps.

Motion effects on the SAR images as discussed by Kirscht (1998) and Fienup (2001) are used in the algorithm. Target motion in azimuth direction, causes smear effect due to the motion induced phase errors. On the other hand, target motion in range direction causes displacement of the targets in azimuth direction.

After all moving targets has been detected number of detected targets, their velocities and movement directions are reported. Range and azimuth movement detection processes are detailed in the following subsections.

2.1 Range Direction Movement Detection

In the proposed algorithm, range direction movement is detected by using sub-aperture processing (Franceshetti and Lanari, 1999). Raw data is divided in two equal blocks across the azimuth direction, and two SAR images are formed. This process provides looking to the same observed region in two different time intervals. The first image contains data from beginning to the divided position of the antenna. Therefore, an image is generated for "t" time position of the antenna. The second image contains data from the divided position to the end position of the antenna. So, second image is generated for "t + 1" time position of the antenna.

After generation of the images, these two images are overlapped with the help of the SAR system parameters. By taking the difference between the two overlapped images, stationary targets will be disappeared and only moving targets within the observed region are detected.

After moving target has been detected, position difference of the target between the first and the second images gives the range direction movement information of the target. This information is used to extract range direction motion parameters.

2.2 Azimuth Direction Movement Detection

Shear averaging algorithm is used for detecting moving targets in azimuth direction. There are numerous algorithms for detecting azimuth movement. But shear averaging algorithm is chosen for its sensitivity to the azimuth component of velocity, providing very fast calculation, higher order phase errors detection ability, and not requiring a prominent point scatterer on the target (Fienup, 2001).

In the algorithm, whole image is divided into small patches. By processing each patch, moving targets can be detected by using "shear averaging algorithm" detailed by Fienup (1989). If good clutter cancellation is applied at the beginning of the algorithm, only targets will be stayed in the image. So, moving targets can accurately be detected with very low false alarm rate.

In the proposed algorithm, following steps are used to detect azimuth motion.

  a. Divide the image into patches.
  b. Take a patch data, g(u,v).
  c. Calculate G(u,v) by taking azimuth FFT of g(u,v).
  d. Calculate shear averaged quantity.
  e. Calculate phase error estimate in azimuth coordinate.
  f. Make phase correction.
  g. Take inverse Fourier of corrected data.
  h. Calculate standard deviation of the phase error.
  i. Compare standard deviation value with the threshold value to detect moving target.
  j. If a moving target is detected, find the azimuth velocity of the target by using the system model.

Threshold value could be calculated by processing either whole image or only patch data. The whole image processing gives a fixed threshold value. But, for good detection results in simulations, dynamic threshold value is calculated for each patch.

In "jth" step of the algorithm, azimuth velocity is calculated by finding the displacement of position of maximum amplitude within the unfocused and focused images. From simulation results, a relationship between real target velocity and detected target velocity is extracted and shown in Figure 1. This relation is used as a reference system model for the velocity estimation of the detected targets.

By combining the range and azimuth direction detection results, the real movement direction and velocity of the target is calculated.
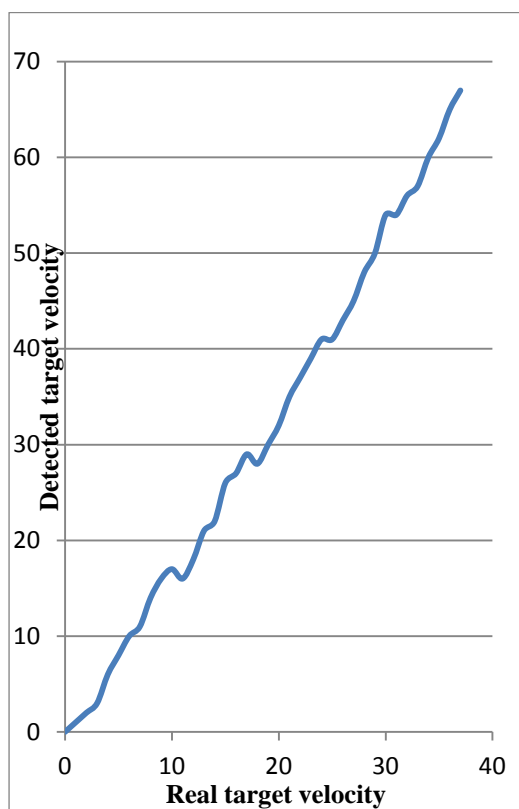
Figure 1: System model, extracted from simulation results, is used to find the azimuth velocity estimation of moving targets in azimuth direction.

3 SIMULATION RESULTS

The performance of the proposed algorithm is tested with Matlab simulation. In the simulation scenario, moving and stationary targets are put within the simulation data. The simulated scene used in the simulations is shown in Figure 2. Simulated SAR system parameters are given in the Table 1.

Simulated scene contains 3 targets. Only the rightmost target is non-stationary, and the other two are stationary. The moving target is marked in the images shown in Figure 3 and Figure 4. In these figures, moving targets have a constant velocity of 3.9m/s (14km/h) only in range and azimuth direction, respectively.

In the simulation scenarios, moving targets with different velocities between 0.39m/s to 15.6m/s are considered. All moving targets in the azimuth direction are detected successfully, and target velocities are estimated by using the system model given in Figure 1. On the range velocity detection

process, moving targets with velocities smaller than 1.56m/s couldn't be detected by using two sub-apertures. But all other targets and also their movement direction are detected successfully.

Table 1: Simulation system parameters.

Center Frequency	10 GHz
Pulse duration	1 µs
Radar PRF	200 Hz
Sampling Frequency	180 MHz
Chirp rate	1.5×10^{14}
Platform velocity	200 m/s
Slant range scene center	10 km
Resolution range	0.3 m
Resolution azimuth	0.3 m
Squint angle	0°
Scene size	200 m x 200 m
SAR image size	512x512 pixels
Number of sub-apertures	2
Aperture size (Az x Range)	256x512 pixels
Patch size (Az x Range)	128x16 pixels
Moving target velocity	3.9 m/s

Excluding targets with very low range velocities, the moving targets are detected and separated from stationary targets by sub-aperture processing. Also, their motion parameters are extracted. In addition to range direction detection results, azimuth movement, its direction and velocity of the target are detected successfully.
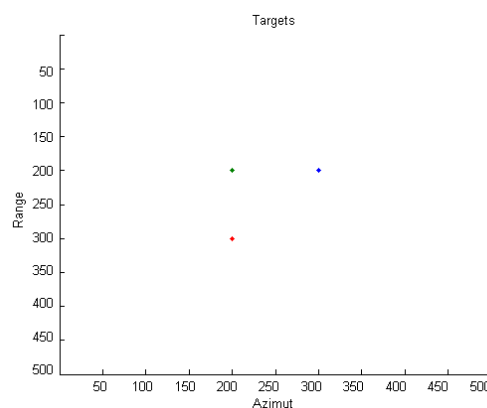
Figure 2: Simulated scene.
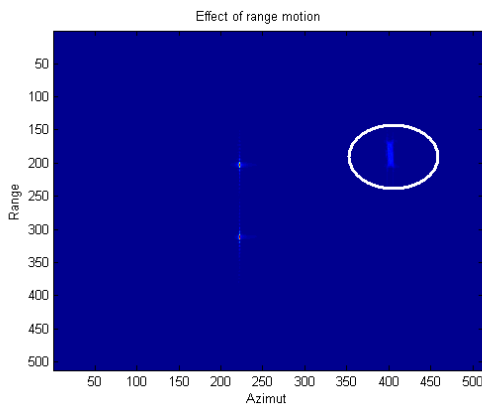
Figure 3: Range-only motion.
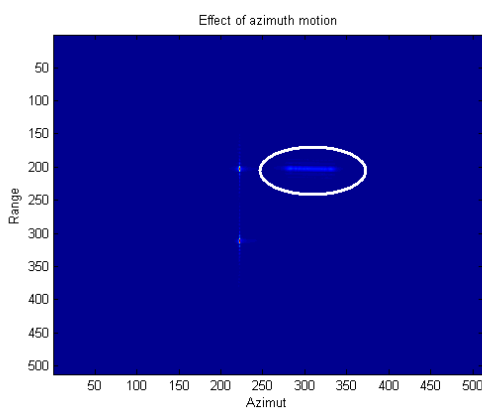
Figure 4: Azimuth-only motion.

4 CONCLUSION

A new algorithm for detecting both range and azimuth motion of moving targets in SAR images is proposed. The combination of sub-aperture processing and shear averaging algorithms provides the detection of the movement in all directions. Detection algorithm is processed in range and azimuth directions independently; therefore parallel processing techniques could be used. By parallel processing, moving targets can be detected very fast. Algorithm is capable of not only moving target detection, but also motion parameter estimation of the moving targets. Moreover, detection performance and motion parameter estimation accuracy is high because of the non-sequential processing of range and azimuth direction movement.

REFERENCES

Fienup, J.R., 1989. Phase Error Correction by Shear Averaging. In *Optical Society of America, Signal Recovery and Synthesis III, digest of papers.*

Fienup, J.R., 2001. Detecting Moving Targets in SAR imagery by focusing. In *IEEE Transactions on Aerospace and Electronic Systems.*

Franceshetti, G. and Lanari, R., 1999. *Synthetic Aperture Radar Processing*, CRC Press. London.

Jung, J.H., 2009. Ground Moving Target Displacement Compensation in the DPCA based SAR-GMTI System. In *2009 IEEE Radar Conference.*

Kirscht, M., 1998. Detection, Velocity Estimation and Imaging of Moving Targets with Single–Channel SAR. In *Proc. of European Conference on Synthetic Aperture Radar, EUSAR '98.*

Kirscht, M., 2002. Detection and imaging of arbitrarily moving targets with single-channel SAR. In *RADAR 2002.*

Kohlleppel, R. and Gierull, G., 2008. Enhancement of along-track interferometry for ground moving target indication. In *International Geoscience and Remote Sensing Symposium.*

Li, G., Xu, J., Peng,Y. and Xia, X., 2006. Detection, Velocity Estimation and Imaging of Fast Moving Targets Using Single Antenna SAR. In *International Conference on Radar, 2006.*

Liu, S., Yuan, Y., Gao, F. and Mao, S., 2007. Method of moving target detection based on sub-image cancellation for single-antenna airborne synthetic aperture radar. In *Journal of Systems Engineering and Electronics.*

Palubinskas, G. and Runge, H., 2008. Detection of Traffic Congestion in SAR Imagery. In *Proc. of 7th European Conference on SAR. Fridrichshafen, Germany.*

Qin, F., Zhang, X., and Dong, M., 2006. A method of hybrid ATI and DPCA technique to detect moving target. In *CIE '06, International Conference on Radar.*

BISATIC SAR SLC IMAGE MODELLING AND INTERFEROMERIC GENERATION

Dimitar Minchev, Andon Lazarov

Burgas Free University, Faculty of Computer Science and Engineering, Burgas, Bulgaria
mitko@bfu.bg, lazarov@bfu.bg

Abstract: This work addresses the model of Bistatic Interferometric Synthetic Aperture Radar BInSAR imaging process. BInSAR geometry with multiple satellite receivers is thoroughly mathematical described. A linear frequency modulated (LFM) SAR signal model and single look complex (SLC) image are derived. To verify proposed models an implementation of the processing chain, implemented in MATLAB environment is performed.

1 INTRODUCTION

Imaging capability of Synthetic Aperture Radar (SAR) Distributed Satellite-borne Systems (DSS) with Bistatic Interferometric Synthetic Aperture Radar (BInSAR) on board is already proven Earth Remote Sensing technique. BInSAR DSS system error analysis and design method are investigated in (Li Wei, 2002). The potential benefits, drawbacks and problems associated with a close formation flight for an along-track interferometry SAR mission is discussed in (Eberhard, 2004). A generalized approach of formation configuration of BInSAR DDS from the point of system performance optimization is presented in (Huang, 2007). Concept for decomposition of solid baseline, a new method to avoid the max detection error and simulation experiment accompanied by very good result is shown in (Xilong, 2007). Effective method to eliminate the effect of baseline instability on SAR image and interferometric measure is proposed in (Zhang, 2007). A multi-baseline polarimetric synthetic aperture radar interferometry (Pol-InSAR) technique that allows more appropriate reconstruction of the quasi-three-dimensional spatial distribution of scattering processes within natural media is presented in (Stebler, 2002).

The main purpose of this work is to propose a universal geometrical model of the Earth surface topography, as well as mathematical model of the reflected LFM SAR signals from that relief and algorithms for complex image extraction and interferogram generation.

2 GEOMETRY AND KINEMATICS OF SAR SCENARIO

Consider Bistatic Interferometric Synthetic Aperture Radar (BInSAR) geometry (*Fig.1*), defined in coordinate system *Oxyz*. SAR system is located on a satellite with a trajectory given by the following vector equation.

$$\mathbf{R}(p) = \mathbf{R}_0 + \mathbf{V}T_p\left(\frac{N}{2} - p\right) \qquad (1)$$

where: $\mathbf{R}_0 = \mathbf{R}(0)$ is the distance vector from the origin of the coordinate system to the satellite in the moment $t = 0$; $\mathbf{V}$ is the satellite velocity vector; T_p is the signal repetition period; p is the index of emitted pulses; N is the full number of emitted pulses. The vector equation (1) is projected in coordinate system *Oxyz*, which yields

$$x(p) = x_0 - V_x T_p\left(\frac{N}{2} - p\right)$$

$$y(p) = y_0 - V_y T_p\left(\frac{N}{2} - p\right) \qquad (2)$$

$$z(p) = z_0 - V_z T_p\left(\frac{N}{2} - p\right)$$

where $x(p)$, $y(p)$ and $z(p)$ are the satellite coordinates in the moment p; $x_0 = x(0)$, $y_0 = y(0)$ and $z_0 = z(0)$ are the satellite coordinates in the moment $p = N/2$; $V_x = V\cos\alpha$, $V_y = V\cos\beta$, $V_z = V\cos\delta$ are coordinates of the velocity vector; $\cos\alpha$, $\cos\beta$, $\cos\beta$ are the guiding cosines of the velocity vector.

The surface depicted in coordinate system $Oxyz$ analytically can be presented as a two dimensional function, i.e. z as a function of coordinates x and y, which in discrete form is given by the following equation (3)

$$z_{mn} = z_{mn}(x_{mn}, y_{mn}) =$$
$$3(1 - x_{mn})^2 \exp\left[-(x_{mn})^2 - (y_{mn}+1)^2\right]$$
$$-10\left(\frac{x_{mn}}{5} - x_{mn}{}^3 - y_{mn}{}^5\right)\exp\left[x_{mn}{}^2 - y_{mn}{}^2\right] \qquad (3)$$
$$-\frac{1}{3}\exp\left[-(x_{mn}+1)^2 - y_{mn}{}^2\right]$$

where $x_{mn} = m\Delta M$ and $y_{mn} = n\Delta N$ are discrete coordinates in the plane Oxy; ΔM and ΔN are dimensions of the grid's cell; m and n - relative discrete coordinates (*indexes*) on axes Ox and Oy. Coordinates; x_{mn}, y_{mn} and z_{mn} define the distance vector $\mathbf{R}_{mn}$ of each point scatterer.
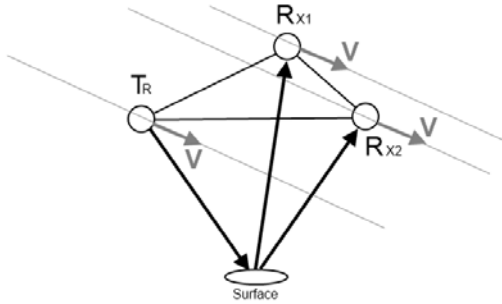
Figure 1: Bistatic InSAR Geometry.

Assume that in each grid's cell with dimensions (ΔM and ΔN) and coordinates (x_{mn}, y_{mn}) one prominent point scatterer is located. During the process of observation the distance vector $\mathbf{R}_{mn}(p)$ from SAR located on the satellite to the dominant point scatterer, defined by the geometrical vector $\mathbf{R}_{mn}$, can be expressed by the following vector equation

$$\mathbf{R}_{mn}(p) = \mathbf{R}(p) - \mathbf{R}_{mn} \qquad (4)$$

The geometry information of the observed surface is contained in the phase of the complex amplitude of the reflected signal from each point scatterer which is proportional to the module of the distance vector $R_{mn}(p)$ defined by the expression

$$R_{mn}(p) = \sqrt{[x(p) - x_{mn}]^2 + [y(p) - y_{mn}]^2 + [z(p) - z_{mn}]^2} \qquad (5)$$

While modelling the process of observation the value of the parameter $R_{mn}(p)$ is calculated for each p, m and n.

3 LFM SAR SIGNAL MODELING AND SLC IMAGE RECONSTRUCTION

3.1 SAR signal modelling algorithm

1. Compute the distance from SAR to each point scatterer from the observed surface for each particular moment p by equation (5).

2. Compute time delay parameter for each point scatterer from the surface $t_{mn}(p)$ by the expression

$$t_{mn}(p) = \frac{R_{mn}^{TR}(p) + R_{mn}^{RX1}(p)}{c} \qquad (6)$$

where $c = 3.10^8$ m/s is the speed of light, R_{mn}^{TR} is the distance from transmitter to the surface; R_{mn}^{RX1} is the distance from the surface to the receiver satellite.

3. Compose an one-dimensional array with entities of all time delays $t_{mn}(p)$ arranged in ascending order and define minimum $t_{mn\min}(p)$.

4. Compute generalized time parameter of the reflected signal:

$$E_{mn}(k, p) = t_{mn\min}(p) + (k-1)\Delta T - t_{mn}(p) \qquad (7)$$

5. Compute LFM signal, reflected by mn–th point scatterer for each sample k = {1, 2, …, 256} and emitted pulse p = {1, 2,…, 256}.

$$S_{mn}(k, p) = a_{mn}.\exp\left\{j\left[\omega E_{mn}(k, p) + b(E_{mn}(k, p))^2\right]\right\} \qquad (8)$$

6. The results of the computation of are placed in a two dimensional array $[k, p]$.

The SAR signal, reflected from a particular point scatterer is limited within pulse duration, which can be described by element wise multiplication of the signal $S_{mn}(k, p)$ (8) with a rectangular function i.e.

$$S_{mn,\text{rect}}(k, p) = \mathbf{rect}\left(\frac{E}{T_k}\right).S_{mn}(k, p) \qquad (9)$$

where

$$\mathbf{rect}\left(\frac{E}{T_k}\right) = \begin{cases} 1, 0 \le \dfrac{E}{T_k} < 1 \\ 0, \dfrac{E}{T_k} < 0, \ \dfrac{E}{T_k} \ge 1 \end{cases} \qquad (10)$$

is the rectangular function described by two dimensional matrix [k, p], containing zeros and ones in positions according to conditions (10).

The element wise multiplication of the matrix $S_{mn}(k, p)$ with rectangular matrix function $\mathbf{rect}\left(\dfrac{E}{T_k}\right)$ yields a matrix $S_{mn,\text{rect}}(k, p)$, which contains all necessary values of the SAR, reflected by particular pint scatterer. Superposition of reflected SAR signals over dimensions m and n yields the values of the interferon complex SAR signal $S(k, p)$, written as entities of a two dimensional matrix [p, k], i.e.

$$S(k, p) = \sum_{m=1}^{M} \sum_{n=1}^{N} S_{mn,\text{rect}}(k, p) \qquad (11)$$

3.2 SAR SLC image reconstruction

1. Demodulation of the SAR signal by multiplication of two dimensional matrix $S(k, p)$ with complex conjugated emitted signal, i.e.

$$\widetilde{S}(k, p) = S(k, p) . \exp\left\{ j\left[\omega(k-1)\Delta T + b((k-1)\Delta T)^2 \right] \right\} \qquad (12)$$

2. SLC image reconstruction by standard two dimensional fast Fourier transform

$$I(\bar{k}, \bar{p}) = \text{FFT}_p[\text{FFT}_k(\widetilde{S}(k, p)]) \qquad (13)$$

The matrix $I(\bar{k}, \bar{p})$ represents the complex image of the observed surface, containing amplitude and phase information for each pixel from the surface.

In Fig. 2 real (a) and imaginary (b) parts of the complex SAR signal are presented.

3.3 Interferogram generation

An interferogram is generated by complex conjugate multiplication of obtained two Single Look Complex (SLC) images.

4 NUMERICAL EXPERIMENT

Distributed Satellite-borne Systems (DSS) with Bistatic Interferometric Synthetic Aperture Radar (BInSAR), formed by three SAR satellite systems observe Earth surface witch is modelled by Matlab "peaks" function. T_R is the transmit satellite, while

R_{X1} and R_{X2} are receivers satellites. Satellites' trajectory parameters and SAR data are presented in Table 1.

Table 1: Trajectory and SAR parameters.

	T_R	R_{X1}	R_{X2}
x_0	2.10^4	10^4	$1,2.10^4$
y_0	2.10^4	10^4	10^4
z_0	8.10^5	8.10^5	8.10^5
Np	512	512	512
N_k	512	512	512
m_n	256	256	256
Δ	2	2	2
V(m/s)	1000	1000	1000
T_p (s)	0.025	0.025	0.025
T_k (s)	0.0025	0.0025	0.0025
F (Hz)	10^{10}	10^{10}	10^{10}
ΔF(Hz)	$2.5.10^7$	$2,5.10^7$	$2,5.10^7$

Baseline between T_R and R_{X1} is $10^4 . \sqrt{2}$ = 14142,136 meters. Baseline between T_R and R_{X2} is 12806,248 meters. Baseline between R_{X1} and R_{X2} is 2000 meters. Computational results are shown in Figs. 2-6.
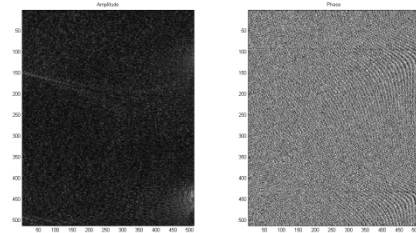
Figure 2: SAR1 SLC image
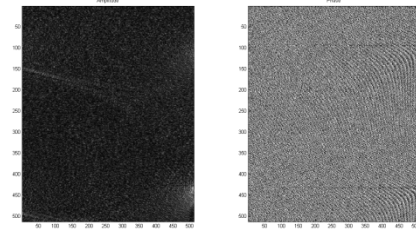
Figure 3: SAR2 SLC image
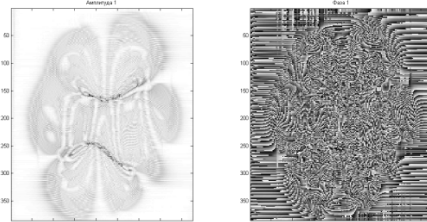
Figure 4: Reconstructed RX1 SAR image (amplitude and phase)
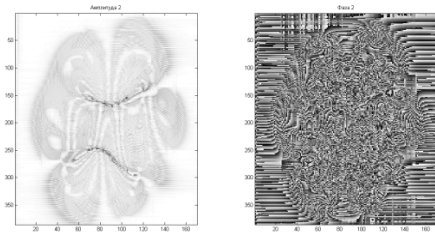
Figure 5: Reconstructed RX2 SAR image (amplitude and phase)
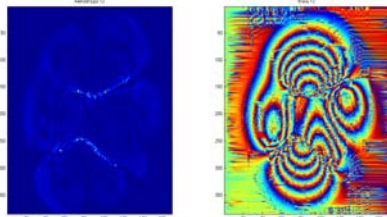
Figure 6: Interferometric phase based on RX1 SLC image and RX2 SLC image

In Fig. 6 clearly can be seen interferometric fringes proportional to heights and depths of the observed surface.

5 CONCLUSION

In this work a model of Bistatic Interferometric Synthetic Aperture Radar (BInSAR) imaging process is discussed. Bistatic InSAR geometry with thoroughly mathematical description of the observed surface and kinematic equations is suggested. LFM SAR signal's model is derived. SLC image reconstruction algorithm with two dimensional FFT procedures is implemented. To verify proposed geometrical and signal models a simulation of the processing chain, implemented in MATLAB environment is illustrated. SAR complex interferogram containing amplitude and phase information is produced.

ACKNOWLEDGEMENTS

REFERENCES

Li Wei, Li Chunsheng, 2002. A novel system parameters design and performance analysis method for Distributed Satellite-borne SAR system, Advances in Space Research, Volume 50, Issue 2, 15 July 2012, Pages 272-281, ISSN 0273-1177, 10.1016 /j.asr. 2012.03.026, http://www.sciencedirect.com/science /article/pii/S0273117712002244

Xilong, S., Anxi, Y., Zhen, D., Diannong, L., 2007. Research on differential interferometry for spaceborne bistatic SAR, (2007) International Geoscience and Remote Sensing Symposium (IGARSS), art. no. 4423252, pp. 2118-2121., http://www.scopus.com /inward/record.url?eid=2-s2.0-82355161233&partner ID=40&md5=5834d01988df2fddf978780e3d16301a

O Stebler, E Meier, D Nüesch, 2002. Multi-baseline polarimetric SAR interferometry—first experimental spaceborne and airborne results, ISPRS Journal of Photogrammetry and Remote Sensing, Volume 56, Issue 3, April 2002, Pages 149-166, ISSN 0924-2716, 10.1016/S0924-2716(01)00049-1, http://www.scien cedirect.com/science/article/pii/S0924271601000491

Zhang, Q.-L., Lu, Y.-B. 2007. The study on imaging algorithm of formation flying satellites InSAR system, 2007 1st Asian and Pacific Conference on Synthetic Aperture Radar Proceedings, APSAR 2007, art. no. 4418547, pp. 27-31., http://www.scopus.com/inward/ record.url?eid=2-s2.0-47349123731&partner ID=40&md5=ade1b6b133e46f02bc5116b25b012cac

Huang, H., Liang, D., 2007. Optimization design approach of distributed spaceborne InSAR formation, Hangkong Xuebao/Acta Aeronautica et Astronautica Sinica, 28 (5), pp. 1168-1174., http://www.scopus.com/inward/ record.url?eid=2-s2.0-35348988096&partner ID=40&md5=6e9eb60a36628c5d67a06ebf58346dec

Eberhard Gill, Hartmut Runge, 2004. Tight formation flying for an along-track SAR interferometer, Acta Astronautica, Volume 55, Issues 3–9, August–November 2004, Pages 473-485, ISSN 0094-5765, 10.1016/j.actaastro.2004.05.044., http://www.scien cedirect.com/science/article/pii/S0094576504001870

Telecommunications and Signal Processing

FREQUENCY MODULATED CONTINUOUS TECHNOLOGYFOR RADIO CHANNEL MEASUREMENTS IN THE 60 GHZ BAND

Stuart M Feeney and Sana Salous

School of Engineering, University of Durham, South Road, Durham, U.K
sana.salous@durham.ac.uk

Keywords: 60 GHz, channel sounder, ISM band, MIMO, UWB and FMCW.

Abstract: The architecture of an UWB multi-band channel sounder is presented. The sounder architecture provides an FMCW source to enable measurements in the frequency range up to 1 GHz (which covers the TV white space / digital dividend), the 2.2 – 2.9 GHz band (ISM and LTE) and the 4.4 – 5.9 GHz band (ISM / WiLAN). Additional frequency converters support operation in the 16 GHz and 60 GHz bands. Here we have configured a 2 by 2 MIMO system in the 60 GHz band specifically targeting channel measurements to support the development of on-body networks and short range backhaul communication networks. Performance results in the 2.4 GHz ISM band demonstrate the resolution of the sounder.

1   INTRODUCTION

The availability of broad blocks of spectrum in the 60 GHz band provides the opportunity to support very high data rate systems. This includes in-flight entertainment content delivery to the seat-back in high capacity passenger aircraft (Garcia, et al., 2009). In addition the 60 GHz band is attractive for on-body networks since antennas can be physically small and the excess absorption assists covert operation of equipment for military applications. Initial on-body measurements (Hall, Hao and Cotton, 2010) at 60 GHz were performed with a 60 GHz SISO channel sounder with ~ 1 GHz of channel width (Feeney and Salous, 2008). These initial measurements stimulated the development of a new system which has 2 by 2 MIMO capability and 6 GHz channel width. The new sounder is also able to support higher sweep repetition rates (more than 2.5 kHz) which provides an unambiguous Doppler measurement to +/- 1.25 kHz. The architecture of the sounder also facilitates the generation of sweep signals which can be used in a broad range of bands which are appropriate for short range wireless applications in cluttered environments.

Additionally the new architecture also addresses the physical size and power limitation of the original sounder which limited operation to either a laboratory environment or within a vehicle (Landrover) that had been specifically adapted to support the operation of the sounder receiver. The new sounder can be operated directly from a 12 V vehicle (or battery pack) supply and is contained within a single 3U rack. Each of the transmitter and receiver consume ~90 W.

2   FMCW CHANNEL SOUNDING

The equipment has been designed to perform channel sounding using the FMCW technique. The FMCW sounder transmitter stimulates the channel with CW signal which is swept across the channel with a constant rate of change of frequency with respect to time. At the receiver a similar sweep provides the local oscillator input to a frequency mixer which is operated as a correlator. The output from the mixer is a beat frequency between the local oscillator and the received signals.   Different multipath components produce different beat frequencies.   Thus the multipath structure is delineated via spectral analysis using either a

spectrum analyser for online monitoring or FFT processing following digitisation. A second stage of spectral analysis over a number of frequency sweeps for each time delayed multipath component gives the delay-Doppler function which can be used to estimate the power delay profile and the Doppler spectrum of the channel. Other channel functions such as the time variant frequency function can be also evaluated via a second FFT on each sweep or envelope detection of the received output of the detector.

3   SYSTEM DESCRIPTION

The system block diagram of the 2 by 2 MIMO 60 GHz sounder is shown in Figure 1.
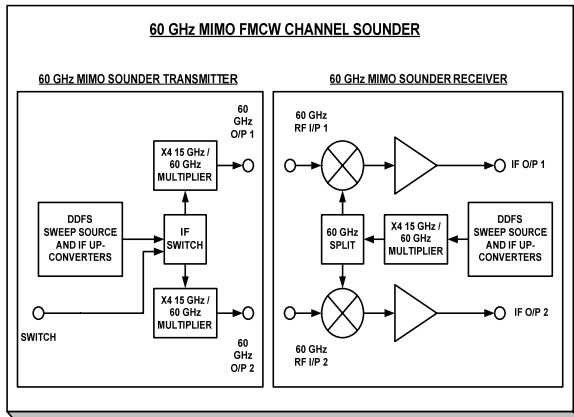
Figure 1: Block diagram of 60 GHz sounder.

At the transmitter and receiver identical sweep generation systems are used as shown in Figure 2.
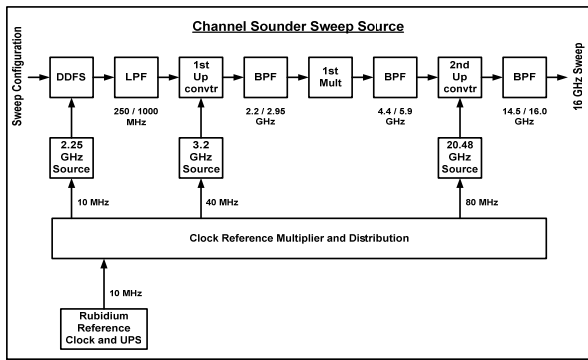
Figure 2: Sweep Generator Block Diagram.

The sweep generator contains three sub-modules: reference unit, sweep source and auxiliary converter. These modules are housed in 3U 19" rack cases and can be operated from mains or 12 V battery power.

The reference unit contains a Rubidium disciplined OCXO with an uninterruptable supply with internal battery back-up (~1 hour). This enables continuous operation of the Rubidium standard should the system be temporarily moved from the mains supply as for example to be set up in a vehicle or moved to location. The reference module also includes a distribution module which provides multiplication and buffering of the 10 MHz internal standard. Outputs are provided at 10 MHz, 20 MHz, 40 MHz and 80 MHz. These signals are used as references for the various phase locked loops in the sweep generator, for system synchronisation and for clock for the analogue to digital converter in the data acquisition unit. Figure 3 shows the UPS and the reference multiplier and distribution boards located on the underside of the reference module.
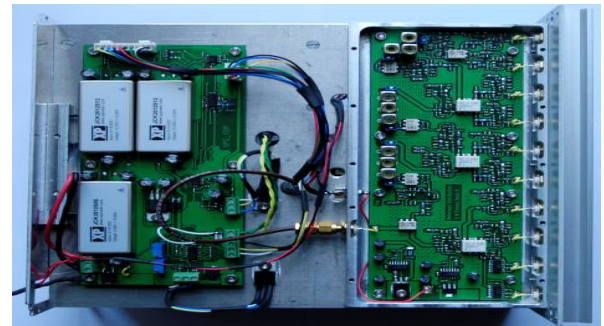
Figure 3: Reference module internal view.

The sweep source module consists of several stages of up-conversion to cover the various frequency bands. At baseband, a Direct Digital Frequency Synthesiser, DDFS which is configured via a USB interface uses a 2.25 GHz PLL clock source (f_{ck}) derived from the 10 MHz reference. This enables the generation of frequency sweeps up to 1 GHz. The DDFS has a frequency update rate equal to $f_{ck}/32$ which enables the generation of short duration sweeps or equivalently high waveform repetition rates for high Doppler coverage. The DDFS has the capability of either to free run or to be synchronised to an external trigger signal. An additional marker signal is available to confirm the start of the sweep which can be used to synchronise the data acquisition unit or to trigger other DDFS units. The DDFS output is band-limited to eliminate alias signals using a 15 pole low-pass filter which has been fabricated as a distributed design on a Rogers 4003 substrate. The filter and its measured response are displayed in Figure 4. Taking the output of the DDFS directly, measurements in the Digital dividend band around 800 MHz and the VHF

band can be performed using suitable RF front ends at the transmitter and at the receiver.
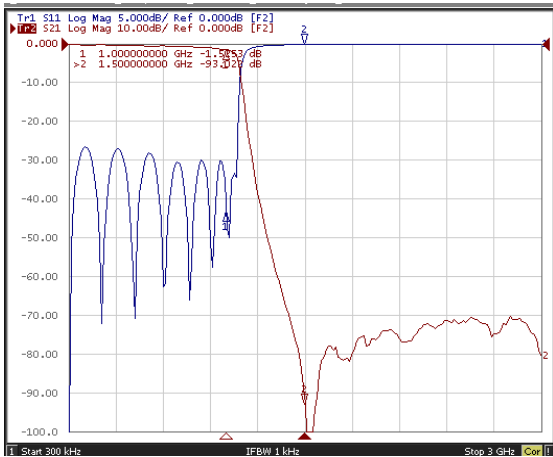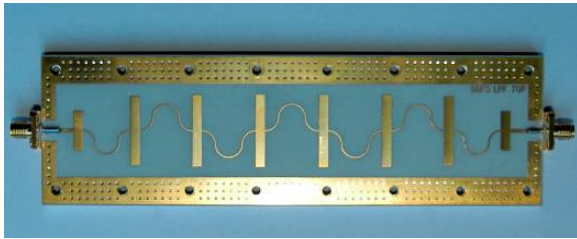
Figure 4: DDFS low pass filter and its frequency response.

To cover the LTE band and ISM bands the frequency range 2.2-2.95 GHz was chosen as the first intermediate frequency (IF) following the DDFS output. This gives an overall 750 MHz instantaneous bandwidth when the DDFS is programmed to sweep from 250 MHz up to 1 GHz. This IF is realised by up-converting the DDFS output using a heterodyne converter which uses a high-side local oscillator at 3.2 GHz derived from a 40 MHz reference. The lower sideband output of the heterodyne converter is selected using a nine pole band-pass filter. This filter provides more than 50 dB of attenuation to the upper sideband and local oscillator residual response.

The 3.2 GHz PLL in the up-converter and the 2.25 GHz PPL used as a clock to the DDFS have a similar PCB design as shown in Figure 5 where the frequency band is selected via appropriate choice of the VCO and the loop filter parameters. This provides an efficient design and fabrication advantage for reproducibility of the sounder. The first heterodyne up-converter is shown in Figure 6.
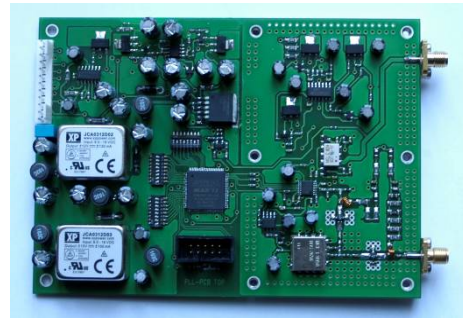
Figure 5: 2.25 and 3.2 GHz sources.
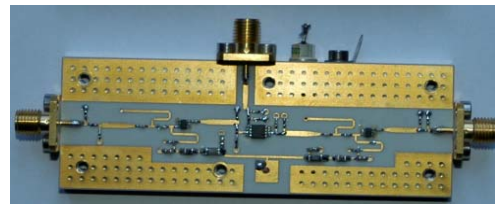
Figure 6: First heterodyne up-converter.

The second IF frequency is generated by doubling the frequency output of the first heterodyne up-converter. When swept across the 2.2-2.95 GHz band, this generates a 1.5 GHz frequency sweep from 4.4-5.9 GHz which provides high resolution of multipath. This frequency range also covers the second ISM band and the C band at 5.2 GHz. The realised frequency doubler consists of an amplifier and then a MMIC balanced doubler as shown in Figure 7. A band-pass filter provides attenuation of the fundamental and other harmonic outputs from the doubler. The 5 GHz band-pass filter is shown in Figure 8.
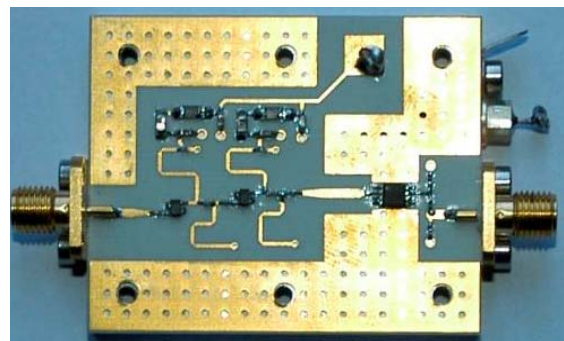
Figure 7: Frequency doubler to 4.4-5.9 GHz.
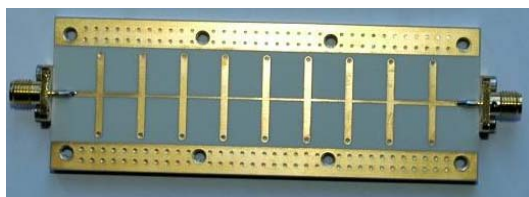
Figure 8: 4.4-5.9 GHz Band Pass Filter.

The second heterodyne stage up-converts the 4.4-5.9 GHz to 14.5-16 GHz using a high side local oscillator (LO) injection at 20.48 GHz. The LO signal is derived from a 5.12 GHz PLL with 80 MHz reference followed by two doubler stages. The output signal is available at the front panel at a nominal level of +17 dBm and is connected via external cables to the final stage of up-conversion to the 60 GHz band. This approach avoids the use of cables at 60 GHz with associated high loss and reduced dynamic range. This is particularly crucial for on-body networks where it is necessary to have the 60 GHz units on the user when performing measurements.

The 60 GHz transmitter module shown in figure 9 takes the 14.5-16.0 GHz signal and routes it to two separate times four (X4) multiplier modules via a two way PIN switch. This approach avoids the use of a 60 GHz switch which would provide limited isolation and incur losses at 60 GHz. This approach has demonstrated very high (more than 100 dB) of channel isolation at the transmitter. Each transmitter channel provides an active output power of nominally +7 dBm (5 mW).

Figure 9: Two channel 60 GHz transmitter module.

The receiver uses a single X4 multiplier to produce the reference signal for the correlator signal in the 60 GHz band. The output of the multiplier is routed to two separate mixers via a 3 dB multi-hole directional coupler. Each down-converter

mixer/correlator has a signal-conditioning pre-amplifier on the mixer output. The directivity of the directional coupler in addition to the LO / RF isolation provided within the fundamental mode balance mixers provides a measured channel isolation of more than 50 dB. The pre-amplifier has a noise figure of ~5 dB, the mixer conversion loss is ~7 dB and including image noise the total receiver noise figure is ~15 dB.

4 SWEEP OUTPUT

The measured sweep output from the DDFS (after low-pass filtering) is shown in Figure 10 where the slope due to the $\sin x/x$ response of the DDFS can be observed. Although the DDFS does not have a compensation circuit for the $\sin x/x$ function, the slope does not impact on the compression of the received signal. However, if frequency variations across the swept bandwidth are of interest, then the output can be compensated for in processing. The plot in Figure 10 demonstrates excellent attenuation of the DDFS clock (2.25 GHz) and the primary alias response (1.25-2 GHz).
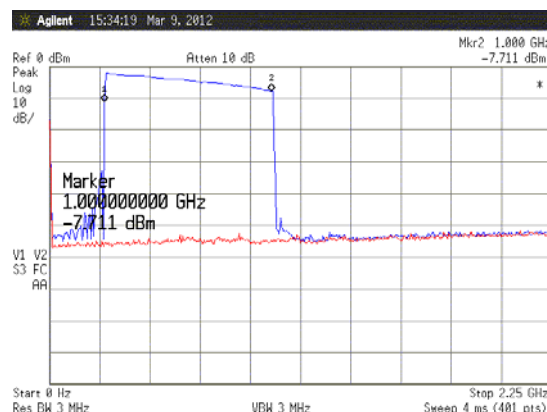
Figure 10: Output of DDFS after LPF.

The output from the sweep generator in the 14.5 GHz to 16 GHz band is shown in Figure 11 which demonstrates a substantially flat signal. This has been achieved through driving the amplifier close to compression. This approach can be used at any stage of the sweep generator if desired. However, in general the main sources of distortion for the compression of the chirp signal are phase non-linearity, and amplitude ripple in the pass band. Phase non-linearity reduces the resolution by broadening the width of the compressed pulse and amplitude ripple produces sidebands in the

compressed signal which reduce the dynamic range of the measured impulse response of the channel.
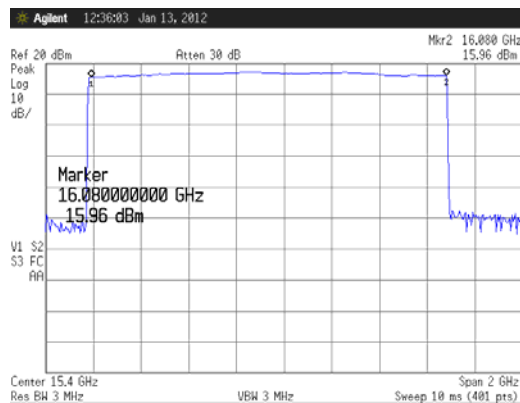
Figure 11: Frequency sweep after upconversion to the 14.5-16 GHz band.

5 MIMO ISOLATION

The measured isolation between the transmit channels and the receive channels is shown in Figure 12. The primary response between the active transmitter and the active receiver is shown in the blue trace. The green trace indicates the residual response from the non-active receiver channel. This demonstrates more than 50 dB of receiver channel isolation.

The red trace indicates the output from the receiver channel when the transmitter output channels are switched. This demonstrates ~100 dB of transmitter isolation.
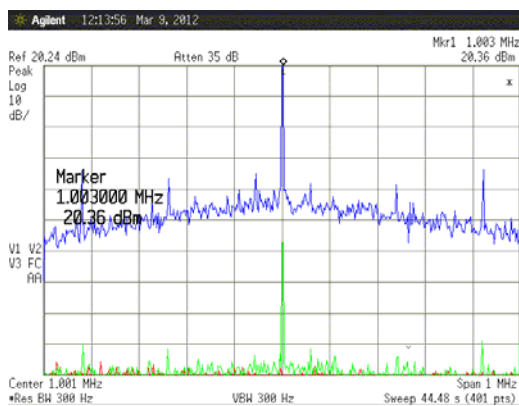
Figure 12: Measured MIMO isolation.

6 PHASE NOISE

The instantaneous dynamic range for an FMCW sounder is determined by the close to carrier phase noise of the sweep signals. Close in phase noise broadens the skirts of the compressed pulse and thus limits the resolution of multipath components. In addition close synchronisation between the transmitter and receiver sweeps is required to support Doppler discrimination. A time drift between the transmitter and receiver sources reduces the time interval over which Doppler analysis can be carried out which is particularly crucial for high resolution sounders.

This system uses 10 MHz Rubidium standards. The synthesisers within the equipment use digital phase / frequency comparators. This type of device has a phase noise floor which is proportional to frequency. The phase noise degradation due to division within the PLL is proportional to the frequency squared. Subject to the actual noise floor of the 10 MHz reference and the noise performance of the PLL digital devices the net phase noise degradation can be minimised by exploiting multiplication of the reference. Multiplication of the reference reduces the available range of PLL frequencies which can be realised. Here we have been able to exploit this technique at 3.2 GHz (40 MHz reference) and 5.12 GHz (80 MHz). The net improvement in the phase noise at 3.2 GHz is ~6 dB and ~8 dB at 5.12 GHz.

The PLLs use relatively wide closed loop bandwidths (~100 kHz) with high phase margin (~75°). This approach minimises "noise bumps" in the phase noise response and is highly tolerant of loop parameter changes.

The DDFS sources were replaced with synthesised signal generators at 650 MHz and 650.125 MHz to produce a constant beat note at the output of the receiver at 1 MHz. This response is shown in Figure 13. Data have been recorded using 300 Hz resolution bandwidth to provide comparison with the prior 60 GHz system. The total system signal to noise ratio due to phase noise is ~52 dB at 300 Hz bandwidth. This represents an improvement of ~7 dB to the prior system (Feeney and Salous, 2008).

With 2.5 k sweeps / second this should provide more than 40 dB instantaneous dynamic range with

an effective system bandwidth of 3 kHz (2.5 kHz FFT bin-width).
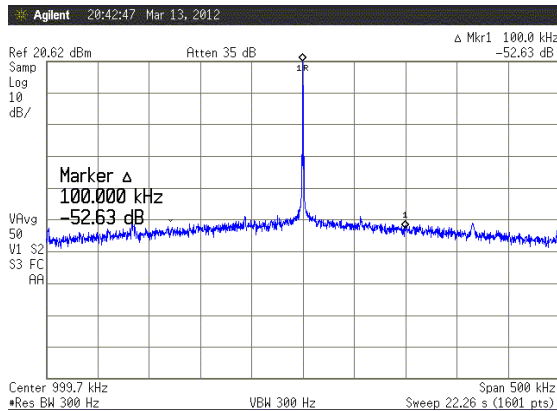
Figure 13: Complete system phase noise.

7 PERFORMANCE RESULTS IN THE ISM BAND

The sounder was tested from back to back measurements and in an indoor environment to verify its performance. Figure 14 shows the impulse response of the sounder in the 2.2-2.95 GHz band with both the overall 750 MHz swept bandwidth and for 375 MHz obtained by dividing the sweep into two 375 MHz sections. The figure shows that a dynamic range of about 60 dB is achieved with minimum distortion to the impulse response.
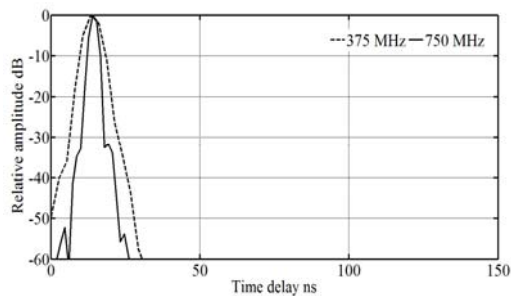
Figure 14: Back to back performance of channel sounder in the ISM band.

The sounder performance was also tested on the air in an indoor environment and Figure 15 shows the corresponding power delay profile obtained across 750 MHz bandwidth and across 375 MHz bandwidth. Although the reduced time delay resolution is evident in the lower bandwidth, the overall shape of the power delay profile shows a similar trend.
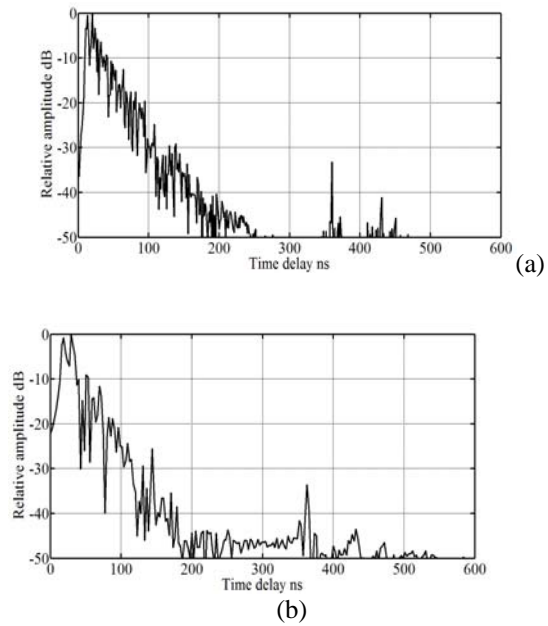
Figure 15: Indoor measurement in the ISM band with (a) 750 MHz swept bandwidth, (b) 375 MHz swept bandwidth.

8 CONCLUSIONS AND FURTHER WORK

A new compact FMCW sweep generator platform to support measurements in multiple frequency bands has been developed. The sounder has programmable bandwidth which at baseband can extend up to 1 GHz. With various stages of up-converters it can generate signals with bandwidths up to 750 MHz in the 2.2-2.95 GHz, and 1.5 GHz bandwidth in the 4.4-5.9 GHz band. Additional equipment to provide 2 by 2 MIMO capability within the 58-64 GHz band has been produced. Enhanced phase noise and excellent MIMO channel isolation has been demonstrated. Integration to the data acquisition system to complete the system is under way along with multiple transmitters and multiple receivers to enable simultaneous measurements in the two ISM bands in addition to the 60 GHz band. The sounder will be used in various indoor environments representative of test-beds in the CREW consortium to generate a typical channel model and to study the benefits of cooperative sensing. Other applications of the sounder include studies such as on-body network and car to car communication.

ACKNOWLEDGEMENTS

REFERENCES

Garcia, A. P., Kotterman, W., Thomä, R. S., Trautwein, U., Brückner, D., Wirnitzer, W. and Kunisch, J.; (2009); 60 GHz in-Cabin Real-Time Channel Sounding. *Communications and Networking in China, 2009*. ChinaCOM 2009.

Hall, P. S., Hao, Y. and Cotton, S. L.; (2010); Progress in Antennas and Propagation for Body Area Networks.

Proceedings of International Symposium on Signals, Systems and Electronics (ISSSE2010).

Feeney, S. and Salous, S.; (2008); Implementation of a channel sounder for the 60 GHz band. *URSI General Assembly;* Chicago, 2008.

EVALUATION OF ESD EFFECTS ON SOLAR ARRAY
in Different Space Missions

Omid Shekoofa, Maryam Baghban Kondori

Space Research Institute (SRI) of Iranian Space Agency (ISA), 14th St. Sa'adat Abad, Tehran, Iran
omid.shekoofa@sri.ac.ir, m.baghban@sri.ac.ir

Abstract: This paper studies the electrostatic discharge effects on solar arrays in different orbits. This paper starts with a statistical overview of solar array failures and their relations with ESD events. Then the space environmental conditions and their impacts on ESD occurrence are discussed for the most commonly used orbits for satellite missions. Spacecraft charging phenomena and different modes of charging are studied further in the paper. Finally the effects of ESD events on the elements and subassemblies of solar arrays are investigated.

1   INTRODUCTION

Increase in energy demand in new high power telecommunication and observation satellites leads to need for higher power generation by their electrical power subsystems (EPS), which requires larger area of solar arrays (SA). Larger SA provide more power, and deliver it to the loads through higher voltage buses, which made them more susceptible to Electrostatic Discharge (ESD).

At the same time increase in power consumption may require a higher level of current drawn from a typical primary regulated bus, that in turn augments the risk of ESD event on SA cables and the whole harness subsystem of the satellite. Therefore more knowledge about ESD and its impacts on the EPS, especially on SA design and operation, is an essential requirement in designing high power satellites.

2   SOLAR ARRAY FAILURES

Immunity against ESD is an essential requirement in subsystem level for designing the EPS of a satellite. Among all the EPS elements and parts, SAs are the most susceptible one to ESD effects. ESD events can take palce on SA and most of its subassemblies like solar cells, coverglasses, metallic frames, cables and connectors, in different conditions which are exist in various space missions.

During ten years of space missions (1996-2006), more than 47% of the numbers of insurance claims for the satellite failures were because of the EPS faults and anomalies. Almost the half of the costs of these failures are related to SA anomalies, and more than 90% of the array anomalies are due to the failures in their elements and subassemblies operation. The majority of these in-orbit failures and anomalies are originated from ESD events on SA. The bar-chart in figure 1 shows the number of SA anomalies in different orbits during 1996-2006 and the pic-chart at top right side of figure 1, displays the percentages of these anomalies (Rodiek, 2008).
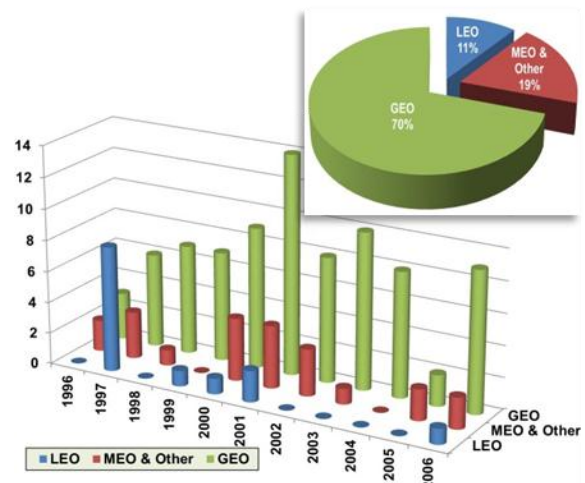
Figure 1. The numbers of solar array anomalies in different orbits during 1996-2006 (bar-chart), and the percentages of these anomalies (pic-chart at top right)

In order to avoid such dominant risk in SA operation, it is required to consider the ESD phenomenon, the enviromental conditions for ESD occurrence and its causes in designing SA. It is also needed to apply adequate ESD control and mitigation techniques in the EPS manufacturing and assembly process.

3   ESD & SPACE ENVIRONMENT

The main reasons for ESD occurance on SA is the accumulation of electrical charges on the SA surface. Whenever charge buildup takes place, there will be the risk for ESD event. The existent space environment which surrounds the whole satellite, generates the required conditions for causing the ESD events. Satellites in different orbits encounter different environmental conditions like plasma and Sub-storms. Therefore they experience different levels of internal and external charging which might lead to different levels of risks for ESD occurrence.

In table 1, three different levels are defined for the possibility of spacecraft (SC) charging in different orbits (Mazur, 2003). These levels are in compliance with the illustrated information in figure 1. Table 1 also shows different possibilities for charging on SC surface and internal parts which will be discussed in continue of this paper.

Table 1: Spacecraft charging levels in different orbits

Orbit	Surface	Internal
LEO, Inclination <60	Low	Low
LEO, Inclination >60	Medium	Low
PLEO	High	Medium
MEO	High	High
GPS	High	High
GTO	High	High
GEO	High	High
HEO	High	High
Interplanetary	Low	Low

According the information of table 1 and regarding the importance of GEO and LEO orbits for satellite missions, the environmental conditions in these orbits are considered in more detail in sections 3.1 to 3.3, and summarized in table 3 (ISO 11221:2011).

3.1 GEO Conditions

GEO is characterized by the presence of electrons with energies (E_e) greater than 1keV. In GEO orbit two different conditions may be considered:

- Quiet condition: refers to a condition where in the absence of solar sub-storms the current of the incident electrons (J_e) is less than the photoelectron current (J_{ph})
- Stormy conditions: where J_e is higher than J_{ph}

3.2 LEO Conditions

LEO is characterized by the presence of low energy but dense ionospheric plasma. For an object in this condition, current from electrons of energies 0.1 to 0.2 eV dominates over any other current source to spacecraft.

3.3 Polar LEO Conditions

Polar LEO (PLEO) is characterized by auroral electrons, with energies greater than 1keV, which coexist with the low energy ionospheric plasma.

Table 2: The specifications of different orbits' conditions

	Conditions	Specifications
GEO Quiet	High energy electrons (No magneto-spheric substorms)	$E_e> 1keV$ $J_e < J_{ph}=10\mu A.m^{-2}$
GEO Stormy	High energy electrons + Emitted secondary electrons (Magneto-spheric substorms)	$E_e> 1keV$ $J_e > J_{ph}$
LEO	Low energy but dense plasma,	Particles density ≈ 10^8 to 10^{12} m^{-3}
LEO	Attracted ions to the negatively charged SC body	J_e is generated by electrons with $E_e ≈$ 0.1 to 0.2 eV
LEO	SA bus voltage level	$V_{SA-BUS}>100$ V
PLEO	Auroral electrons + Low energy ionospheric plasma LEO-like dense plasma+ GEO-like high energy plasma	$E_e >1keV$ $J_e= 1mA.m^{-2} > J_{ph}$

Since the actual space environments are not known precisely, it is common to use a simulated environment for numerical simulations and calculations purposes instead. For example, NASA recommended "worst case" charging environment is presented in table 3. Sensitivity studies have shown that the actual condition for SC charging is much less severe than these conditions (Katz, I., and others, 2000).

Table 3: NASA Simulated Environment Parameters

Parameter		Value	Dimension
Electron number density	n_e	1.12×10^6	m^{-3}
Electron temperature	T_e	12	keV
Ion number density	n_i	2.36×10^5	m^{-3}

Parameter		Value	Dimension
Ion temperature	T_i	29.5	keV

4 SPACECRAFT CHARGING

The essential reason for ESD occurrence is the SC charging. In different missions with various orbit parameters, different charging conditions may exist. For example, a typical ESD event can occur under the following conditions (NASA Report, 2007):

- Vacuum pressure $<10^{-5}$ torr, and either
- Dielectric surface voltage is greater than 500V
- The electric field between a dielectric surface and a conductor is greater than 10^5 volts/cm.

Each of these two electrical characteristics can be generated by a certain environmental condition. This is why the probability of ESD occurrence directly depends on the space condition in the studied orbit. For instance the electrical characteristics, such as electrostatic potentials (V_{ES}) of the various parts of the SC, in a GEO satellite can be totally different than the similar parameters for a LEO satellite due to the different charging levels. Some of these differences are presented in Table 4.

Table 4: Charged parts and the relevant electrical effects in different orbits

	Charged Parts	Electrical Effects
GEO	SC body (between adjacent surfaces)	$V_{ES} = V_{SC} \approx$ several hundred to several thousand volts (particularly during sunlit)
LEO	SC body	Charging rate ≈ -5 V/s.
	Coverglass and underlying cell	$V_{ES} \approx$ several hundred volts $dv/dt \approx 3$ V/s
	The front surface of the SA faces the Sun	J_e (consisted of charges which are constantly bled off via photoemission from cell coverglasses)
	Gaps between the solar cells, (shaded by the edges of the solar cells)	Negatively charged
PLEO	SC body	$V_{SC} < V_{SA\text{-}BUS}$

5 CHARGING MODES

According to table 1 there are two types of charging for spacecrafts: surface charging and internal charging. Surface charging consists in the charging on visible and touchable areas of the external part of the satellite. Internal charging is resulted from the penetration of energetic electrons into the satellite enclosures (like Ebox) and deposit charge very close a victim site. Since ESD on SA mainly occurs because of surface charging, this type of charging will be more discussed.

5.1 Surface Charging

Surface charging may cause ESDs and arcing on solar arrays and their power cables. It is generally caused by electrons of 5-50 keV in GEO, 2-20 keV in PEO, or high voltage arrays in LEO (Cho, M, 2007). Table 5 provides more information on the causes and effects of charging in different orbits (Ley, W., and others, 2009) (Leung, P, 2010). It should be mentioned that there are two types of potential gradients noted in table 4 as follow:

- Normal Potential Gradient (NPG) which is resulted of differential charging where the insulating surface or dielectric reaches a negative potential with respect to the neighboring conducting surface or metal. It is sometimes referred as Negative Dielectric Positive Metal (NDPM) condition.

- Inverted Potential Gradient (IPG), which is also called Positive Dielectric Negative Metal (PDNM) mode, is the result of differential charging where the insulating surface or dielectric reaches a positive potential with respect to the neighboring conducting surface or metal.

Table 5: Charging causes and issues in different orbits

	Charging Causes	Charging Issues
GEO Quiet	$E_e \approx 5\text{-}50$ keV	No serious surface charging issue
GEO Stormy	SC potential: − Dielectric charged: + In sunlit: 10^2 to 10^3 orders of Volts between adjacent surfaces	IPG
LEO	High voltage arrays V_{SC} floats with respect to the ionospheric plasma potential, within $V_{SA\text{-}BUS}$ range	IPG Min (V_{SC})= $V_{SA\text{-}BUS}$ $V_{Discharge} \approx -200$ V

	Charging Causes	Charging Issues
PLEO	$E_e \approx 2\text{-}20$ keV Driving V_{SC} to a potential more negative than $V_{SA\text{-}BUS}$	Min $(V_{SC})= V_{SA\text{-}BUS}$

5.2 Charging Status during In-orbit Operation

When the satellite continuously passes through cyclic sunlit and eclipse phases, the environmental conditions of the satellite change in the same cyclic manner. In table 6 typical values are mentioned for the main parameters which lead to ESD event during sunlit and eclipse phases in GEO orbit (Payan, D. and others, 2012). For example while the $V_{SC}<0$, an IPG can be formed due to the ion incident at the ram side of the spacecraft. On the other hand, a NPG can exist even if the V_{SC} is near the LEO plasma potential, i.e., nearly zero (ISO 11221: 2011).

Table 6: Typical electrical characteristics in GEO

	At the ram side of SC and/or in Light Phase	At the wake side of SC and/or in Eclipse
GEO Quiet	Ee $\approx$ 20 KeV Je $\approx$ 30-80 pA.cm^{-2}	SC: Negative Potential
GEO Quiet		IPG: due to the ion incident
GEO Quiet		Ee $\approx$ 20 KeV Je $\approx$ 30-80 pA.cm^{-2}
GEO Stormy	IPG: because of the secondary emissions due to the auroral electron incident	Conditions are met to prepare an ESD event when the SC will be powered again at eclipse exit
GEO Stormy	NPG: due to SA surface potential	
GEO Stormy	$V_{Dielectric} < V_{SC}$ $J_{ph} \approx 2$ nA.cm^{-2}	
GEO Stormy	Max $V_{SC} \approx$ the potential barrier stops the Je leading to a new equilibrium voltage	

These charging statuses could be considered from another point of view, as provided in table 7. This table presents the several impacts of ESD on conductive and insulator parts in different ram and dark sides of the solar arrays (ISO 11221: 2011).

Table 7: Impacts on conductive and insulator parts

	Conductive Parts	Insulator Parts
GEO	Solar cell electrode, interconnector, or bus-bar are negatively charged, equal to V_{SC}	Coverglass, adhesive, or facesheet, have negative potentials, but the values can be different from V_{SC} by 1 kV or greater

	Conductive Parts	Insulator Parts
LEO	Conductive parts have potentials ranging from $-V_{SA\text{-}BUS}$ to $+V_{SA\text{-}BUS}$ ESD issues arise only when $V_{SA\text{-}BUS}$ exceeds the primary arc or snap over threshold voltage	Differential charging on the solar array surface appears as the insulator parts have potentials close to the ambient plasma potential
PLEO	Solar array front surface is facing the ram side in PEO, the aurora may drive the spacecraft body potential negative	insulator surface may be charged by ionospheric ions to a potential close to the ambient plasma potential

6 EFFECTS ON SOLAR ARRAYS

Common problems due to ESD on SA can be divided into two categories according to the duration of their influences:

- Transient effects like primary arcs, EMI and its consequent effects
- Permanent damage like secondary arcs, ESDs, and which cause power cabling or solar array failure

These effects, which threaten the reliability and durability of SA operation seriously, could also be divided into the following categories:

6.1 ESD Direct Effects

Discharge arcs are the first and the most important impacts of ESD events. They have insufficient energy or currents to lead to permanent damage of SA. There are two types of arcing with different levels of risks: Primary and Secondary Arcs. Primary arcs are not so hazardous; however analysis showed that these short duration primary charging arcs could trigger long duration secondary discharges, especially between solar cells supported by the solar array current itself, which can be considred as the source of more severe risks (Katz, I. and others, 2000).

6.1.1 Primary Arcs

If the voltage difference reaches a sufficient level, some electric arc discharges will occur which called primary arcs. These discharges carry very little energy and are harmless. However, they can set free plasma which settles in the gaps between the cells. Several hundred discharge events can lead to a plasma concentration establishing a low ohmic

connection to the adjacent solar cell. Primary arcs can only be avoided by a conductive coating of SA surface. Unfortunately this solution facilitates the conditions for a more severe disadvantage, i.e. allowing secondary electric arcs. A better solution can be applied by considering appropriate distances between the adjacent solar cells during the solar cell string design. In this technique the voltage difference between adjacent cells as a function of the gap size between the cell edges never reaches the discharge level and that the driving current remains low enough. The latter is achieved by adding a decoupling diode in series to each string and by parallel connection of the strings to an array behind the diode (Ley, W., and others, 2009).

6.1.2 Secondary Arcs

Secondary arcs will occur if the difference between the nominal operating point voltages of the adjacent cells is high enough and if an appropriate photocurrent is generated within the cells. These sustained arcs could carry sufficient energy to cause permanent damage by evaporation of solar cell material and of the underlying insulation (string failures). The trend to higher voltage and higher power solar arrays makes this type of destructive arcing more probable (Ley, W., and others, 2009).

6.2 ESD Indirect Effects

6.2.1 EMI Generation

One of the most important indirect effects of ESD event is the Electromagnetic Interference (EMI). EMI can be generated both in conducted emissions (CS) and radiated emissions (RS) types. CS occurs as a result of the replacement current that originates when charge is blown off the dielectric surface inducing a replacement current to flow from the satellite structure. RS is generated by the ESD current pulse. The rapid surface potential change induces noise in circuits through capacitive coupling. The discharge current can also induce an inductively coupled signal into the victim circuit. Furthermore, RS can cause diverse forms of field-to-circuit coupling (NASA Report, 2007).

6.2.2 Current Leakage

Since satellite structure parts are made of conducting material, the body serves as a grounding point in the spacecraft circuit. Currents to/from conductive parts exposed to space, and the capacitance between the SC body and ambient space determine the body potential with respect to the ambient space plasma. These current leakages can also reduce the efficiency of SA operation as presented in table 8 for a positively charged solar array (Scolese, C.J, 2007).

Table 8: Leakage current influence on solar arrays power

Altitude [km]	Electron density N_e [cm^{-3}]	Leakage Current [nA.cm^{-2}]	Power loss [%]
500	6×10^5	824.5	7.72
700	2×10^5	274.8	2.57
1000	7×10^4	96.19	0.90
2000	2×10^4	28.38	0.265
300000	1×10^2	0.29	0

7 CONCLUSIONS

The effects of ESD event on solar arrays were discussed in this paper. The relations between the environmental conditions and ESD events were investigated and compared for different orbits firstly. Then the charging modes were considered especially for surface charging which is more applicable to solar array in-orbit operations. Finally some impacts of ESD events were discussed for the operation of solar arrays in GEO, LEO and polar LEO orbits.

REFERENCES

Rodiek, J.A., 2008. Solar array reliability in satellite operations, *Photovoltaic Specialists Conference, PVSC '08, 33rd IEEE*

Mazur, J. E., 2003, Crosslink Magazine, Vol4, No.2, An Overview of the Space Radiation Environment

ISO 11221:2011, Space systems -- Space solar panels -- Spacecraft charging induced electrostatic discharge test methods

Katz, I., Davis, V. A., and others, 2000, ESD triggered solar array failure mechanism, *6th Spacecraft Charging Technology Conference,*

NASA Report, 2007, Analysis of Radiated EMI from ESD Events Caused by Space Charging

Cho, M., 2007, Present status of ISO Standardization Efforts of Solar Panel ESD Test Methods, *10th Spacecraft Charging Technology Conference, June, 2007, Biarritz, France*

Ley, W., Wittmann, K., Hallmann W., 2009, *Handbook of Space Technology*, 1st edition, John Wiley & Sons

Leung, P., Scott, J., Seki, S. and Schwartz, J.A., 2010, Arcing on Space Solar Arrays

Payan, D., Paulmier, T., Balcon, N., Dirassen, B., 2010, ESD risk on solar panels at eclipse exit on geostationary orbit

Scolese, C.J, 2007, Low Earth Orbit Spacecraft Charging Design Handbook, *NASA Technical Handbook,*

GRAY-LEVEL IMAGE CONTOURS EXTRACTION
& COMPRESSION USING WAVELET TRANSFORM

Ali Abdrhman Ukasha

Faculty of Engineering, Sebha University, Brack, Libya
elokshy@yahoo.com

Keywords: Wavelet transform, Image compression, Contour extraction & compression, Ramer & Trapezoid methods.

Abstract: This paper presents a method of contour extraction and compression from grey level image. Single step parallel contour extraction (SSPCE) method is used for the binary image after inverse wavelet transform is applied to the details images. Then the contours are compressed using either Ramer or Trapezoid methods in spatial domain. The proposed algorithms are applied in spectral domain using single-level wavelet transform (WT). Effectiveness of the contour extraction and compression for different classes of images is evaluated. In the paper the main idea of the proposed procedure for both contour extraction and image compression are performed. To compare the results, the mean square error, signal-to-noise ratio criterions, and compression ratio (bit per pixel) were used. The simplicity to obtain compressed image and extracted contours with accepted level of the reconstruction is the main advantage of the proposed algorithms.

1   INTRODUCTION

Contour representation and compression are required in many applications e.g. computer vision, topographic or weather maps preparation, medical images and moreover in image compression. The transform coding method compresses image data by representing the original signal with a small number of transform coefficients. It exploits the fact that for typical images a large amount of signal energy is concentrated in a small number of coefficients. The goal of transform coding is to minimize the number of retained transform coefficients while keeping distortion at an acceptable level. Transform coding is an integral part of one of the most widely known standards for lossy image compression, the JPEG (Joint Photographic Experts Group) standard. Contour extraction and image compression can be obtained using transforms such as Fourier (Brigham, 1974), Walsh (Walsh, 1923), DCT (Clarke, 1985), Wavelet (Vetterli, Martin, Kovacevic, 1995) and Periodic Haar Piecewise-Linear (PHL) which is based on the integration of Haar functions (Dziech, Belgassem, Nern, 2000) and (Dziech, Belgassem, Aboukhres, 1996). In this paper the discrete wavelet transform will be used. The forward wavelet transform is applied to the grey-level image as shown in Figure 1.

To obtain the compressed image and binary image, inverse wavelet transform is applied to the approximation coefficients image and details coefficients images respectively. The contours are extracted from binary image using single step parallel contour extraction (SSPCE) method (Dziech, Besbas, 1997) and (Besbas, 1998). Finally the compressed contours are obtained using either Ramer or Trapezoid methods.
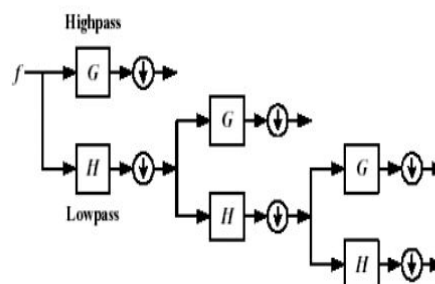
Figure 1: Image analysis using discrete wavelet transform.

Flowchart of the algorithm for image compression and contour extraction is depicted in Figure 2.
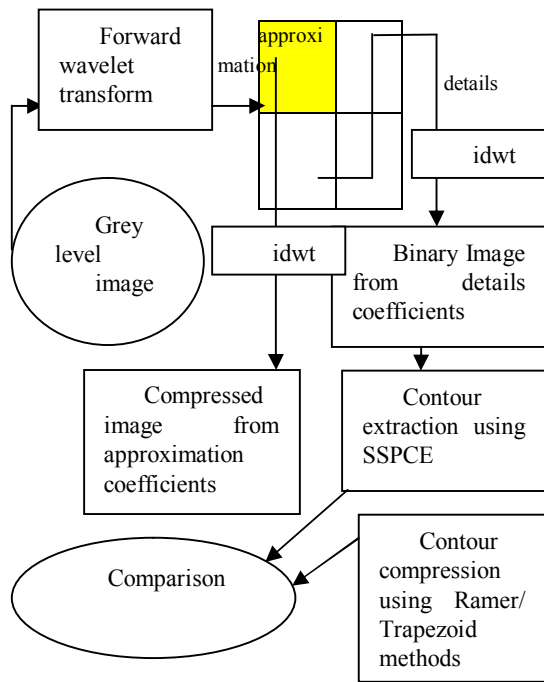
Figure 2: Block diagram of image compression and contour extraction of grey level image using single level of wavelet transform.

2   DISCRETE WAVELET TRANSFORM (DWT)

The Wavelet analysis is an exciting new method for solving difficult problems in mathematics, physics, and engineering, with modern applications as diverse as wave propagation, data compression, signal processing, image processing, pattern recognition, computer graphics, the detection of aircraft and submarines and other medical image technology (Vetterli, Martin, Kovacevic, 1995) and (Gonzalez, 1987). Wavelets allow complex information such as music, speech, images and patterns to be decomposed into elementary forms at different positions and scales and subsequently reconstructed with high precision.

Wavelets are obtained from a single prototype wavelet called mother wavelet by dilations and shifting using the equation

$$\Psi_{a,b}(t) = \frac{1}{\sqrt{a}}\Psi(\frac{t-b}{a}) \qquad (1)$$

3   RAMER ALGORITHM

Contour is represented as a polygon when it fits the edge points with a sequence of line segments. There are several algorithms available for determining the number and location of the vertices and also to compute the polygonal approximation of a contour. The well known is Ramer method which is based on the polygonal approximation scheme (Ramer, 1972).

The simplest approach for the polygonal approximation is a recursive process (Splitting methods). Splitting methods work by first drawing a line from one point on the boundary to another. Then, we compute the perpendicular distance from each point along the segment to the line. If this exceeds some threshold, we break the line at the point of greatest error.

The idea of this first curve approximation is illustrated in Figure 3.
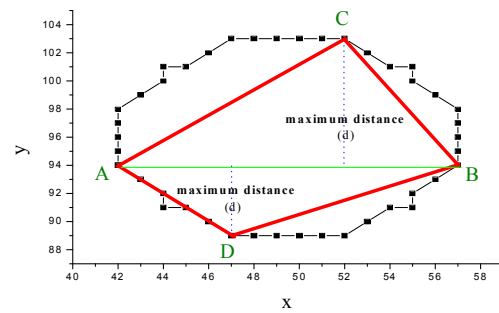
Figure 3: Curve approximation by Ramer algorithm.

4   TRAPEZOID ALGORITHM

The idea of this algorithm consists in segmentation of the contour points to get trapezoid shapes (points of SP, B, C, and EP) (Ukasha, Dziech, Elsherif, 2009) and (Ukasha, 2010).

The first and last points of each segment are called starting point (SP) and ending point (EP) respectively. The fit criterion is the ratio between distance between B and C points (dBC), and the distance between C and EP points (dCEP), as illustrated in Figure 4, and is defined by equation (2).

$$(dBC \ / \ dCEP) < th \qquad (2)$$
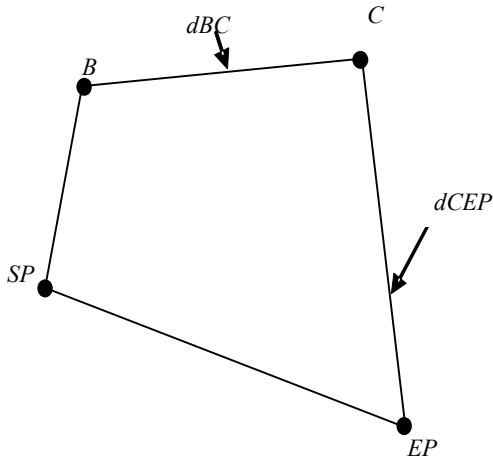
Figure 4: Illustration of the basic trapezoid idea for the Trapezoid method.

5 APPLIED MEASURES

The proposed image compression and contour extraction method is related to the data compression and extraction problems. To evaluate its compression ability, the following compression ratio was introduced if each pixel is implemented by eight bits.

$$bpp = \frac{ZS * 8}{(n * m)} \qquad (3)$$

where:

NOZ - number of zero coefficients

ZS - coefficients number in the desired zonal

  n * m - size of the image

The mean square error (MSE) and peak signal-to-noise ratio (PSNR) criterions were used to evaluate the distortion introduced during the image compression and contour extraction procedures. The MSE criterion is defined by the following equation:

$$MSE(I,\tilde{I}) = \frac{1}{(n * m)} \sum_{i=0}^{n} \sum_{j=0}^{m} (I(i,j) - (\tilde{I}(i,j))^2 \qquad (4)$$

where I is the original image, and $\tilde{I}$ is the reconstructed image.

6 EXPERIMENTS RESULTS

To visualise the experimental results a set of five test grey levels images were selected. Selected images are shown in Figure 5.

(a)   (b)

Figure 5: Test images: a) Tools (256x256), and b) Baby (128x128).

The decomposition of Tools image using first level of DWT is shown in Figure 6.
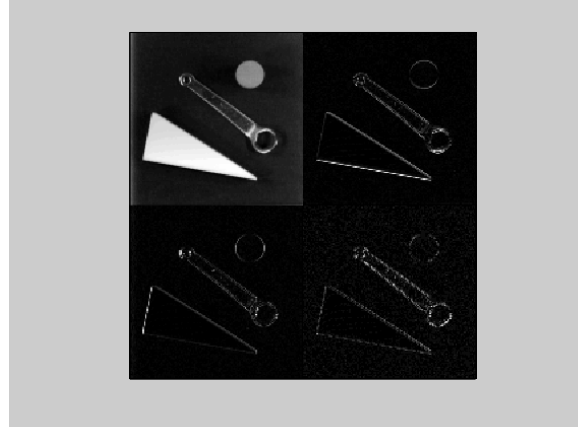
Figure 6: Tools image decomposition using first level of DWT.

The compressed Tools image can be obtained using approximation coefficients only as shown in Figure 7 (related results are shown in the Table 1).

(a)   (b)
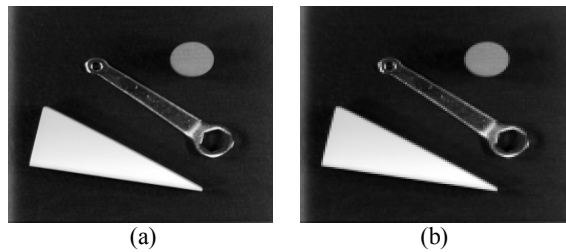
Figure 7: Tools image reconstruction using approximation coefficients: a) Original image, and b) Compressed image.

Table 1: Tools image results.

	MSE	PSNR [db]	Bit Per Pixel (bpp)
b)	24.61	34.22	2

The extracted contours using SSPCE method for contour extraction of Tools image are obtained using horizontal, vertical, and diagonal coefficients as shown in Figure 8.

(a)   (b)
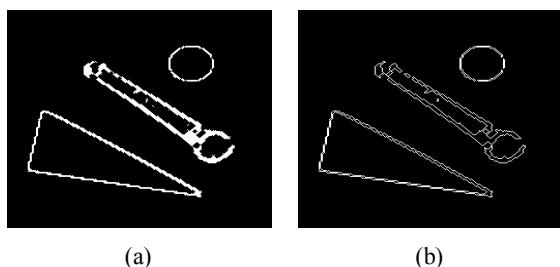
Figure 8: Tools image: (a) Binary image from details coefficients, and (b) Contours extraction using SSPCE method.

The compressed contours for Tools image are obtained using Ramer and Trapezoid methods are shown in Figure 9 (related results are shown in the Table 2).

Table 2: Tools image results.

Method (Compression) / Measures	MSE	PSNR [db]	CR	Elapsed Time
a) Ramer	0.0175	17.58	69.46	10.65
b) Trapezoid	0.0174	17.59	69.34	10.40
c) Ramer	0.0199	17.02	78.99	8.82
d) Trapezoid	0.0197	17.05	78.57	8.31
e) Ramer	0.0226	16.47	89.80	7.35
f) Trapezoid	0.0225	16.47	89.62	7.27

where CR is the compression ratio.

(a)   (b)

(c)   (d)

(e)   (f)
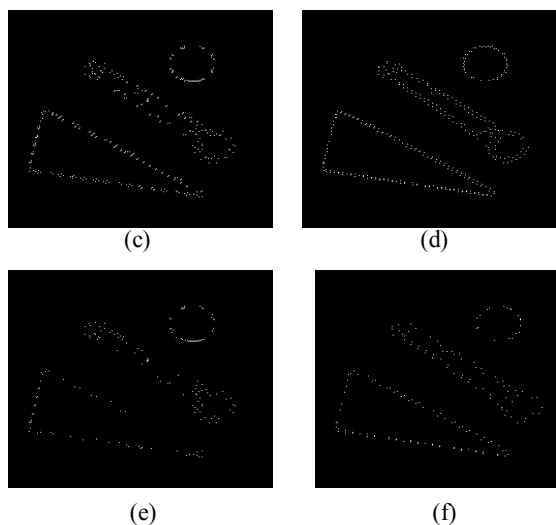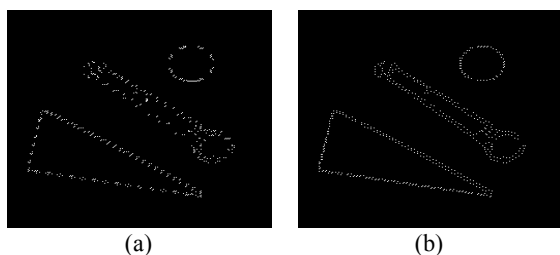
Figure 9: Tools image contour compression using Ramer and Trapezoid methods.

The decomposition of Baby image using first level of DWT is shown in Figure 10.
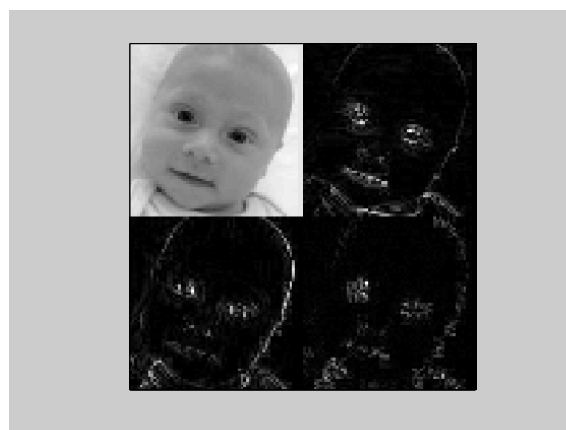
Figure 10: Baby image decomposition using first level of DWT.

The compressed Baby image can be obtained using approximation coefficients only as shown in Figure 11 (related results are shown in the Table 3).

(a)   (b)

Figure 11: Baby image reconstruction using approximation coefficients: a) Original image, and b) Compressed image.

Table 3: Baby image results.

	MSE	PSNR [db]	Bit Per Pixel (bpp)
b)	15.86	36.13	2

The extracted contours using SSPCE method for contour extraction of Baby image are obtained using horizontal, vertical, and diagonal coefficients as shown in Figure 12.

(a)   (b)

Figure 12: Baby image: (a) Binary image from details coefficients, and (b) Contours extraction using SSPCE method.

The compressed contours for Baby image are obtained using Ramer and Trapezoid methods are shown in Figure 13(related results are shown in the Table 4).

(a)   (b)

(c)   (d)

(e)   (f)
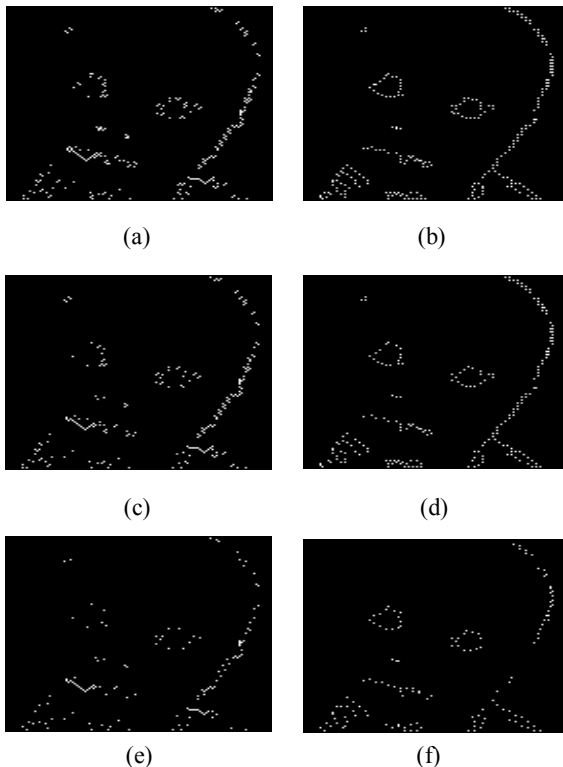
Figure 13: Baby image contour compression using Ramer and Trapezoid methods.

Table 4: Baby image results.

Measures / Method (Compression)	MSE	PSNR [db]	CR	Elapsed Time
a) Ramer	0.0195	17.11	56.16	3.44
b) Trapezoid	0.019	17.08	56.51	2.88
c) Ramer	0.0216	16.45	62.32	3.17
d) Trapezoid	0.0216	16.65	62.32	2.77
e) Ramer	0.0263	15.80	75.88	2.98
f) Trapezoid	0.0263	15.80	75.88	2.56

The proposed algorithm is compared with binary image which is obtained using suitable thresholding criteria as shown in Figure 14 (related results are shown in Figure 15 and in Table 5).

(a)   (b)
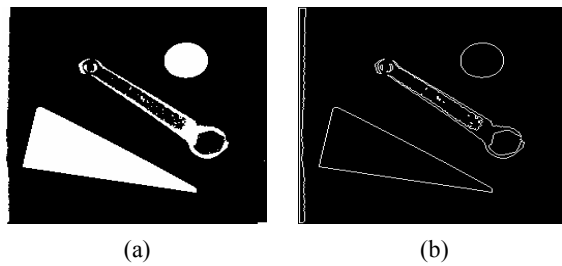
Figure 14: Tools image: (a) Binary image using threshold, and (b) Contours extraction using SSPCE method.

Table 5: Tools image results (Threshold).

Measures / Method (Compression)	MSE	PSNR [db]	CR	Elapsed Time
a) Ramer	0.0183	17.38	69.47	9.89
b) Trapezoid	0.0182	17.39	69.36	9.13
c) Ramer	0.0207	16.84	78.82	8.59
d) Trapezoid	0.0205	16.88	78.06	8.09
e) Ramer	0.0236	16.27	89.84	7.04
f) Trapezoid	0.0236	16.28	89.67	6.58
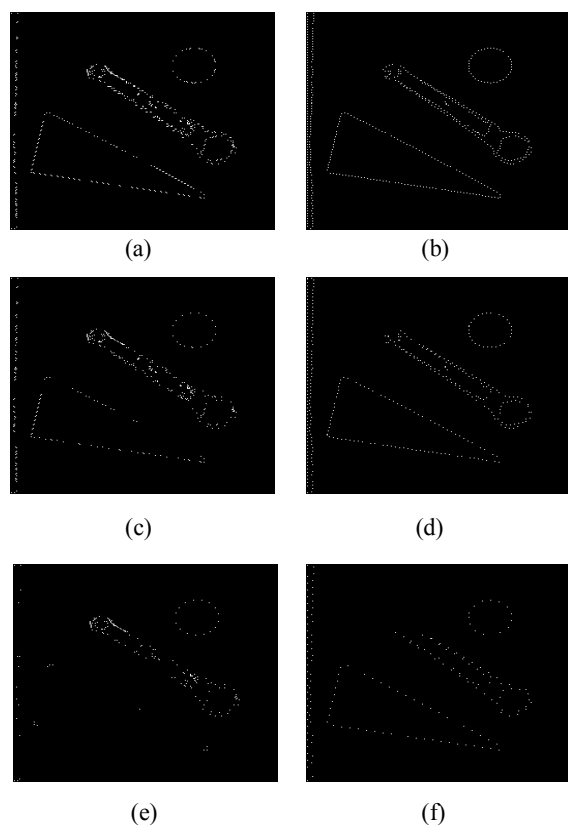
Figure 15: Tools image contour compression using Ramer and Trapezoid methods (by threshold).

The results presented show that the proposed algorithm has the best extraction property and contour compression with better quality compared with the binary image using threshold value. The results show that SNR is improved by this algorithm by about 0.2 decibels for some images.

6   CONCLUSIONS

The good quality of contour extraction and compression are the main advantage of the proposed algorithm compared with the binary image using suitable threshold value. By using single level of discrete wavelet transform the two sub-images are obtained (compressed image and extracted contour). Ramer and Trapezoid methods are used to compress the extracted contours without significant visible distortion.. The reconstruction quality improvement of compressed contour about o.2 decibels. Important advantage of the proposed method is the simplicity of implementation both in terms of memory requirement and fit criterion complication.

REFERENCES

Brigham, E.O., 1974. *The Fast Fourier Transform,* Prentice-Hall, Englewood Cliffs.

Walsh, J., 1999. A closed set of normal orthogonal functions. Amer. J. Math.

Clarke, R. J., 1985. Transform Coding of Images, Academic Press.

Dziech, A., Belgassem, F., Nern, H. J., 2000. Image data compression using zonal sampling and piecewise-linear transforms. *Journal of Intelligent And Robotic Systems. Theory & Applications.* Kluwer Academic Publishers.

Dziech, A., Belgassem, F., Aboukhres, S., 1996. Periodic Haar Piecewise Linear Transform. *Proceedings of the IMACS/IEEE-SMC Multiconference.* Lile-France.

Ramer, U., 1972. An iterative procedure for the Polygonal approximation of plane curves *Computer Graphics and Image Processing.* Academic Press.

Vetterli, Martin, Kovacevic, 1995. *Wavelets and Subband Coding*, Printice Hall Inc.

Dziech, A., Besbas, W., 1997. Fast Algorithm for Closed Contour Extraction. *Proc. of the Int. Workshop on Systems, Signals and Image Processing.*

Besbas, W., 1998. *Contour Extraction, Processing and Recognition*, Ph.D Thesis. Poznan University of Technology. Poznan.

Ukasha, A., Dziech, A., Elsherif, E., 2009. An efficient method of contour compression. *International Conference on Visualization, Imaging and Image Processing (IASTED/VIIP).*

Ukasha, A., 2010. Arabic Letters Compression using New Algorithm of Trapezoid method. *International Conference on Signal Processing, Robotics and Automation (ISPRA'10).*

Gonzalez, R. C., 1987. *Digital Image Processing*, Addison Wesley, 2nd edition.

IMPROVING INTERFERENCE IMMUNITY OF SPATIAL EVENT DETECTION SYSTEMUSING ARRAY ANTENNA

Hiroyuki TSUJI, Miho KOSHIKAWA and Mikio SUZUKI

National Institute of Information and Communications Technology (NICT), 4-2-1 Koganei, Tokyo, Japan
{tsuji, miho-koshikawa, suzuki.mikio}@nict.go.jp

Abstract: This paper proposes new techniques for improving the co-channel interference immunity of the event detection system which realizes indoor event detection scheme. Similar to the conventional methods the signal subspace-based approach sometimes suffers from interference in the same frequency band because the interference signals with different incident angles affect the signal subspace of the received signals at the receiving array antenna. Two types of new event detection methods are proposed to realize immunity against noise and interference in this paper. The first method proposed in this paper exploits the cyclostationarity of communication signals to distinguish the desired signal from the interference and suppresses noise and interfering signals without major hardware design changes. Another approach that improves immunity against co-channel interference is to utilize the transmission control scheme used for personal area network systems. In the proposed method of the study, carrier sense multiple access with collision avoidance (CSMA/CA) technique is utilized to distinguish the desired signal from the other transmitted signals. As a result of the detection of the presence of signals from other stations, the proposed system can avoid the transmitted interference signals from other systems. We are also developing an evaluation equipment to confirm the effectiveness of the proposed approach.

1 INTRODUCTION

We have been developing a new indoor event detection system which can detect events such as home or office intrusion by using signal subspace spanned by an eigenvector obtained by an array antenna, and delivers superior performance compared with conventional event detection methods based on received signal strengths (RSS) (Ikeda, Tsuji, and Ohtsuki, 2009)(Tsuji, Koshikawa, and Suzuki, 2011). Similar to the conventional methods, however, the signal subspace-based approach sometimes suffers from interference in the same frequency band because the interference signals with different incident angles affect the signal subspace of the received signals at the receiving array antenna. In this paper two types of new event detection methods are proposed to realize immunity against noise and interference of the event detection system, which realizes indoor event detection scheme by exploiting the cyclostationarity of the desired signal or the medium access control scheme defined in IEEE standard 802.15.4. The first method proposed in this paper exploits the

cyclostationarity of communication signals to distinguish the desired signal from the interference that impinges on an array antenna and suppresses noise and interfering signals without major hardware design changes (Gardner, 1994)(Gardner, 1988). Another approach that improves immunity against co-channel interference is to utilize the transmission control scheme based on an IEEE 802 standard for personal area networks. Generally in the personal area networks the medium access control (MAC) enables the transmission of MAC frames through the use of the physical channel which is shared with other wireless systems. In the proposed method of the study, carrier sense multiple access with collision avoidance (CSMA/CA) technique, which realizes a wireless network multiple access method, is utilized to distinguish the desired signal from the other transmitted signals. As a result of the detection of the presence of signals from other stations, the proposed system can avoid the transmitted signals (interference) from other systems. We are also developing an evaluation equipment to confirm the effectiveness of MAC - based approach. In this paper, we first introduce the basic idea of the event.

detection system using the signal subspace obtained by array antenna, and explain the ideas of the two approaches for improving the immunity interference. Finally, an evaluation equipment of the event detection system is introduced to realize the real-time event detection.

2 EVENT DETECTION METHOD USING SIGNAL SUBSPACE BY ARRAY ANTENNAS

2.1 Array Antenna Signal Model

First, we explain the principle of the original event detection system using the signal subspace obtained by array antennas.

The basic setup of the indoor event detection system consists of a pair of a transmitter and an array antenna receiver. Here, we consider an array of M sensors and a transmitter emitting a narrow band that impinges on the arrays from direction θ. The received signal at the array antenna can be modelled as

$$x(t) = a(\theta)s(t) + u(t) \qquad (1)$$

where $x(t)$ is an $M \times 1$ vector of the complex envelopes of the observed signals, $a(\theta)$ is the steering vector, $s(t)$ is the source signal, and $u(t)$ is an $M \times 1$ vector of antenna measurement noises.

Next, in an environment of multipath propagation such as indoor environments, the above concept is expanded to a model describing the arrival of multiple narrow band coherent signals. Therefore, the received signal vector $x(t)$ for multiple coherent signals is provided as below:

$$x(t) = \sum_{k=1}^{P} c_k a(\theta_k)s(t) + u(t) \qquad (2)$$

$$= a's(t) + u(t)$$

$$a' \equiv \sum_{k=1}^{P} c_k a(\theta_k)$$

where P is the total number of coherent signals and c_k represents the complex attenuation of the k-th signal with respect to the first signal, $s(t)$.

Assume that the observation noise is Gaussian white noise with a variance of σ^2 having no correlation with the signal source, and the $M \times M$ covariance matrix of $x(t)$ is provided as

$$R_{xx} = E\left\{ x(t)x(t)^H \right\} \qquad (3)$$

$$= Sa'a'^H + \sigma^2 I$$

where H indicates conjugate transposition and $S = E\{s(t)s(t)^H\}$. The event detection method studied in (Ikeda, Tsuji, and Ohtsuki, 2009) uses the signal subspace obtained by the covariance matrix of $x(t)$. The covariance matrix R_{xx} in (3) can be decomposed by the spectral factorization as

$$R_{xx} = ASA^H + \sigma^2 I \qquad (4)$$

$$= V \Lambda V^H$$

where V is the unitary matrix and Λ is the diagonal matrix of the real eigenvalues λ_i, $i=1,\dots,M$ having an order of $\lambda_1 \geq \lambda_2 \geq \dots \geq \lambda_M$. Each matrix is expressed as

$$\Lambda = \begin{bmatrix} \lambda_1 & 0 & 0 \\ 0 & \ddots & 0 \\ 0 & 0 & \lambda_M \end{bmatrix} \qquad (5)$$

$$V = [v_1, \cdots, v_M] \qquad (6)$$

Here, the eigenvalue λ_i and eigenvector v_i, satisfy the relationship $R_{xx}v_i = \lambda_i v_i$. The eigenvalue-eigenvector pair can be used to separate the signal space and noise space. Since $Sa'a'^H$ is a rank-one matrix in (3), span$\{v_1\}$ is considered as the signal subspace. Then the signal subspace detection method studied in (Ikeda, Tsuji, and Ohtsuki, 2009) detects the event using the following criterion:

$$P(t) = \left| v_{no}^H v_{ob}(t) \right| \qquad (7)$$

where v_{no} is the eigenvector v_1 obtained in advance when no event occurs and $v_{ob}(t)$ is the eigenvector associated with the largest eigenvalue obtained by the sensors during the period under observation. When no event occurs at time t, the value of the criterion in (7) is expected to be approximately one because the signal subspace spanned by v_{no} is expected to be almost the same as by $v_{ob}(t)$. On the other hand, the value of the criterion becomes less than one if the signal subspace spanned by $v_{ob}(t)$ varies due to the change of the radio propagation between the array antenna and the transmitter. The signal subspace detection method can therefore detect events by comparing the criterion with the specified threshold.

2.2 Experimental Results by Signal Subspace Detection

We confirmed the effectiveness of the event detection method discussed in (Ikeda, Tsuji, and Ohtsuki, 2009) through experimental results.

The experiment was conducted in a 7×9 m room, as shown in Figure 1. Since the room had metal walls, there was a very high possibility of generating numerous multipath signals between the transmitter and receiver. The array receiver was an 8-element uniform linear array with a half-wavelength element placed at a height of 2.52 m. The array receiver's location is indicated by Rx in Figure 1. Tx indicates the transmitter's location. The antenna height of the transmitter was 1 m and the center frequency of the transmitted signal was 2.335 GHz.

First, the vector v_{no} in (7) was obtained when no event occurred. As the blue line shows in Figure 2, we observed the constant values of the criteria given in (7) when no event occurred during the observation period. Next, the red line in Figure 2 shows the result of the changes of criteria when a person pulls the door B open and enters the room. Figure 3 shows the results when the door A or door B is opened. These indicate that the signal subspace event detection method discussed in (Ikeda, Tsuji, and Ohtsuki, 2009) can detect several events and also recognize the difference of the events via the experiment.
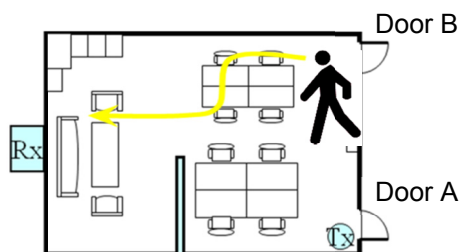
Figure 1: Layout of test area for event detection experiment.
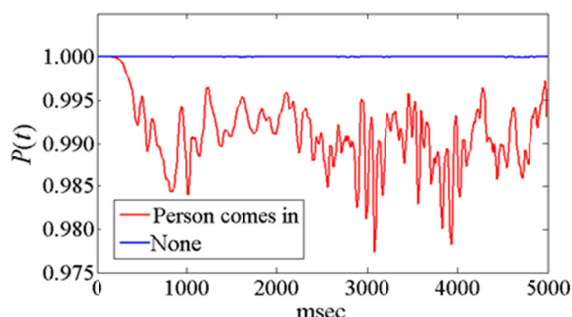
Figure 2: Changes of criteria when a person enters the room.
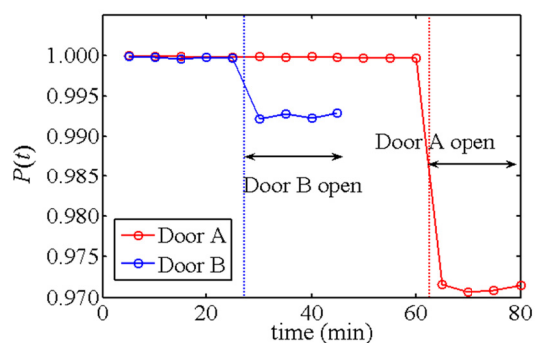
Figure 3: Changes of criteria when door is opened.

3 CYCLOSTATIONARY-BASED EVENT DETECTION METHOD

Similar to the conventional event detection methods, the approach of the signal subspace detection method in (Ikeda, Tsuji, and Ohtsuki, 2009) may make an incorrect decision if intentional or unintentional interference with the same frequency band impinges on array sensors. This is because the interference signals with different incident angles affect the signal subspace of the received signals at the array antenna. Therefore, mitigation techniques of unknown interference signals should be considered. One possible solution to deal with the problem is to apply a spread spectrum technique in order to separate the desired signals from the interference. This technique, however, may cause the circuit size to expand and drive up costs. Here, alternative approach that is computationally simple and offers good detection performance is proposed, using the signal's cyclostationarity (Tsuji, Koshikawa, and Suzuki, 2011).

3.1 Array Signal Cyclostationarity

Cyclostationarity indicates certain signal characteristics. Most modulation signals show cyclostationarity characterized by modulation scheme and speed. Such techniques as the SCORE algorithm and Cyclic MUSIC, which form beams by selecting signals and estimating the direction of signal arrival, have received attention in recent years (Gardner, 1994)(Gardner, 1988). These methods use statistics of up to the second rank. Thus, compared with conventional methods using higher rank statistics, the necessary calculation is rather limited. In addition, since signals can be selected according

to differences in modulation scheme and modulation speed, this technique can be applied to signals of a frequency band in which a variety of modulation schemes and speeds exist. Here, we propose utilizing the cyclostationarity of the signal for the event detection system in order to improve performance in immunity against interference.

3.2 Cyclostationarity:

It is recognized that signal has a spectrum correlation with a cyclic frequency of α, unless the cyclic auto-correlation function of (8) is constantly zero.

$$r_{xx}^{\alpha}(\tau) = \left\langle x(t+\tau/2) x^{*}(t-\tau/2) e^{-j2\pi\alpha t} \right\rangle_{\infty} \quad (8)$$

where $<\cdot>_{\infty}$ indicates infinite time averaging. The covariance matrix of the signal received by the array antenna can be defined as shown below, based on the cyclic correlation function:

$$R_{xx}^{\alpha}(\tau) = \left\langle x(t+\tau/2) x^{H}(t-\tau/2) e^{-j2\pi\alpha t} \right\rangle_{\infty} \quad (9)$$

As previously reported in multiple studies, most modulation signals (e.g., AM, PSK, PAM, FSK) feature $r_{xx}^{\alpha} \neq 0$ at a certain cyclic frequency α and lag τ, where the value of α changes with the modulation scheme and the modulation speed. Thus, even if other signals are included in the time and frequency areas of the received signal, the cyclic covariance function can be used to select the desired wave.
If we choose α to be a cyclic frequency of only the desired signal $s(t)$, then we have from (9)

$$R_{xx}^{\alpha}(\tau) = r_{ss}^{\alpha}(\tau) a'a'^{H} \quad (10)$$

$$r_{ss}^{\alpha}(\tau) = \left\langle s(t+\tau/2) s^{*}(t-\tau/2) e^{-j2\pi\alpha t} \right\rangle_{\infty}$$

The matrix (10) is obviously a rank-one matrix and the right (or left) eigenvector associated with its one eigenvector is a' (or a'^{H}).

3.3 Cyclostationarity-Based Event Detection Method

The characteristics of the interference signals with the same frequency band are unknown. Meanwhile we can purposefully generate a transmitting signal as the desired signal with a specified cyclic frequency. As mentioned in 3.2, the cyclic frequency is determined with the modulation scheme and speed. This means we know the cyclic frequency of the desired signal in advance and the cyclic frequency

can be used for discriminating between the desired signal and the interference. The proposed method's concept is simple. In the proposed method, the cyclic covariance function is used to distinguish the desired signal from the interference. The covariance matrix in (4) can be replaced by the cyclic covariance matrix in (10). Then the eigenvector of the cyclic covariance matrix is used to define the following new criterion for detecting events as

$$\tilde{P}(t) = \left| \tilde{v}_{no}^{H} \tilde{v}_{ob}(t) \right| \quad (11)$$

where $\tilde{v}_{no}$ is the eigenvector obtained in advance when no event occurs and $\tilde{v}_{ob}$ is the eigenvector obtained by the signals during the period under observation, as in the original event detection method.

Even if the interference with different cyclic frequency than the desired signal impinges on the array, the signal subspace obtained from the cyclic covariance matrix remains the same. Therefore, the event detection method with the cyclostationarity of the desired signal is performed by comparing the value of the criterion in (11) with a specified threshold $\tilde{P}_{th}(t)$. Note that the criterion defined in (11) becomes identical to that in (7) if the cyclic frequency is set at zero.
Thus, the event detection method proposed here can be summarized as follows:

1. Choose α to be a cyclic frequency of the desired signal.

2. Calculate the eigenvector $\tilde{v}_{no}$ of $R_{xx}^{\alpha}(t)$ when no event occurs.

3. Update the value of $\tilde{P}(t)$ with $\tilde{v}_{ob}$ obtained by the array.

4. If $\tilde{P}(t) < \tilde{P}_{th}(t)$, an event is to be expected.

5. Repeat steps 3 and 4.

3.4 Simulation Results

Numerical examples were performed to evaluate the proposed method's effectiveness. The linear array consists of eight isotropic sensors spaced uniformly, having half the carrier wavelength. Unless otherwise specified, signal power is given in dB SNR (signal-to-noise ratio) and the noise is additive white Gaussian noise (AWGN) uncorrelated from sensor to sensor. The source signal is a BPSK signal, which is filtered using a square root raised cosine filter with a roll-off factor of 0.5. The three total coherent signals with different angles (θ=10°, −60°, and 20°)

and SNRs (0dB, −10dB, and −10dB) impinge on the array, and an AM interference of compatible bandwidth arrives from −20° in the middle of the observation period (t=100). Each symbol rate of the BPSK signals is 0.2, which is normalized by the sampling frequency. Therefore, the cyclic frequency of the desired signal can be determined as 0.2. In this case, the interference has different cyclic frequency from the desired signals. The proposed method is conducted with α = 0.2 and τ = 0. The event detection method studied in (Ikeda, Tsuji, and Ohtsuki, 2009) is also performed for comparison with the proposed method.

In the first simulation example, the SNR of the interference is set at 5 dB. The resulting values of the criteria defined in (7) and (11) are shown in Figure 4. We observe that the value of the criteria given by (11) stays roughly constant during the observation period while the value obtained by (7) decreases slightly after the interference comes in at t =100.

In the second simulation, the SNR of the interference is set at 10 dB and the other simulation conditions are the same as in the first one. We observe that the interference provides significant change of the criterion in (7) but has little influence on the value in (11) in Figure 5.

These results show that the proposed detection method utilizing the cyclostationarity of the desired signal is effective for improving immunity against interference with different cyclic frequency.
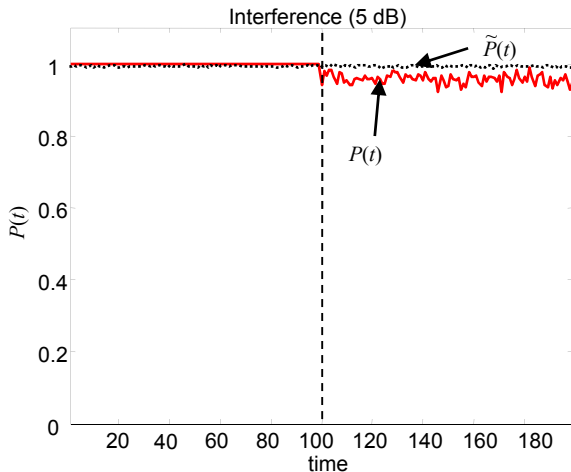
Figure 4: Changes of criteria (interference SNR=5dB).
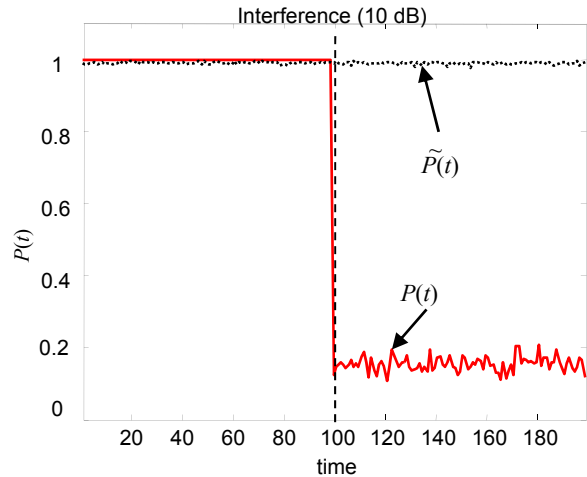
Figure 5: Changes of criteria (interference SNR=10dB).

4 UTILIZATION OF THE TRANSMISSION CONTROL SCHEME BASED ON SHORT RANGE WIRELESS SYSTEM

Here, another approach that is structurally-simple and offers good detection performance is proposed using the transmission control scheme based on an IEEE standard for short range wireless system.

We consider that CSMA/CA technique is of use in the differentiation between desired and interference signals. We take particular note of the IEEE 802.15.4 standard which uses CSMA/CA. The reason is that the systems based on the standard such as ZigBee has few analog stages and uses digital circuits wherever possible and that the software is designed to be easy to develop on small and inexpensive microprocessors. And that it is relatively easy to detect the timing of receiving of the desired signal from an IEEE 802.15.4 compliant RF transceiver chip.

Figure 6 shows a simplified block diagram of the equipment of the event detection system proposed here. The receiver with an array antenna is connected with a node terminal A, which receives the signal from the other node terminal B. The node terminal B knows the address of the node terminal A and sends packets periodically to the node terminal A. The array antenna of the receiver receives the signals from the node B and also may receive unknown interference occasionally. The node terminal A connected to the receiver gives the timing of the receiving period and the result of receiving the desired packets if the node terminal A

receives the desired signal successfully without interference. As the result of implementing the scheme, the array antenna receiver can avoid the transmitted signals from the other systems.

4.1 Experimental Results

We are developing an evaluation equipment to confirm the effectiveness of MAC-based approach. The equipment has four received antenna elements and is connected to the receiving node terminal based on IEEE 802.15.4 standard. The receiving node terminal is programmed to set a bit when it receives a start of frame delimiter and to set another bit after the cyclic redundancy checksum (CRC) of the received signal is verified. Due to the limit of the paper, we show only a result of the behavior of the receiving node terminal when it receives the desired and interference signals where the transmitting node terminal sends a packet at 100 msec interval and meanwhile another transmitting node terminal as interference with different node address sends a packet at 48 msec interval.
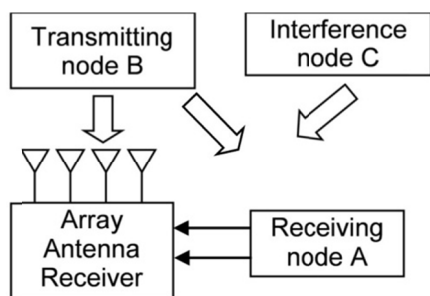
Figure 6: Block diagram of the equipment of the event detection system

As shown in Figure 7, we observed that the receiving node A outputted bits when the start of frame delimiters (F1, F2 and F3) were received and that it outputted a bit (C2) only if the start frame delimiter packet (F2) was received from the node B.
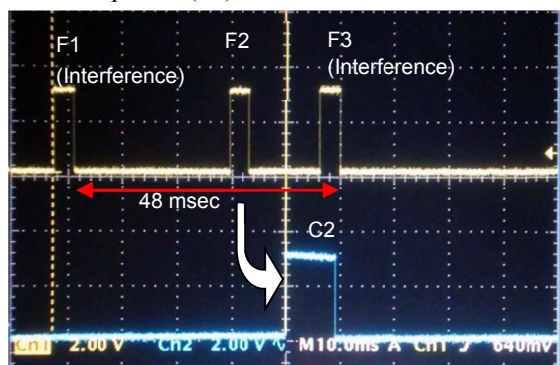
Figure 7: Start of frame delimiter bit and CRC bit

5 DEVELOPMENT OF EVENT DETECTION EQUIPMENT

An evaluation equipment of the event detection system was developed to realize the real-time event detection. The equipment was made smaller, and the real-time algorithm was implemented in the unit by introducing several kinds of efforts so that it would be possible to use with most engineers. The basic specifications of the equipment are summarized in Table 1, and the appearance of the equipment is shown in Figure 8. The equipment has four received antenna signal terminals and one output terminal which is used for the transmitting signal. The receiving circuit and the digital signal processor are also included in the unit. The unit also has a USB connection to control the digital signal processor and to take data from the unit by an external PC. One of the features of the equipment is that the unit can connect to the node receiving terminal which gives the start of frame delimiters information of the receiving transmitting signal and also the condition of the received signal to the equipment. This feature easily enables the implementation of several schemes of interference immunity.

6 CONCLUSIONS

This paper proposed new techniques for improving the co-channel interference immunity of the event detection system which realized indoor event detection scheme by exploiting the cyclostationarity of the desired signal or the medium access control scheme defined in wireless personal area network. The proposed methods could distinguish the desired signal from the interference that impinges on array antenna without major hardware design changes. In future work, some experiments will be conducted to confirm the effectiveness of the total performance of the equipment

Table 1: Specifications of the event detection equipment.

Frequency band	2400 MHz ISM band
Reception bandwidth	600 kHz
Reception level	-80 dBm to -20 dBm
Number of antenna input	4
Number of transmitting port	1
Interface	USB 2.0
Dimensions	200 (W) ×140(D) ×50(H) [mm]
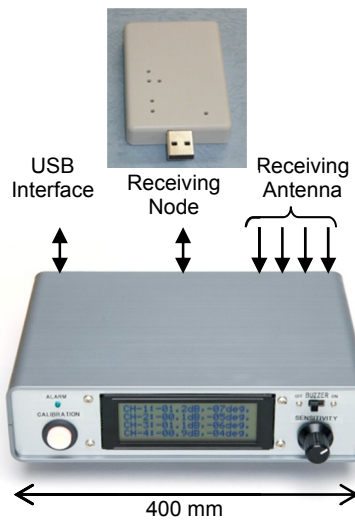
Figure 8: Appearance of the event detection equipment

REFERENCES

Ikeda S., Tsuji H., and Ohtsuki T., 2009, Indoor Event Detection with Eigenvector Spanning Signal Subspace for Home or Office Security, in *IEICE Trans. on Commun., vol. E92-B, no. 7, pp. 2406-2412, July* 2009.

Tsuji H., Koshikawa M., and Suzuki M., 2011, Cyclostationarity–Based Spatial Event Detection Using Signal Subspace of Array Antenna, In *Proc. of the 14th Wireless Personal Multimedia Communications Symposium (WPMC'11), Brest, France, 3-7, Oct. 2011.*

Gardner W. A., 1994, *Cyclostationarity in Communications and Signal Processing*, IEEE, New York.

Gardner W. A., 1988, *Simplification of MUSIC and ESPRIT by exploitation of cyclo-stationarity*, In Proc. IEEE, vol. 76, no.7, pp. 845-847.

A STUDY ON DRAIN EFFICIENCY OF EDSM/EPWM TRANSMITTER USING CLASS-E AMPLIFIER

Makoto Taromaru

Faculty of Engineering, Fukuoka University, Nanakuma 8, Johnan-ku, Fukuoka, Japan
taromaru@fukuoka-u.ac.jp

Abstract: Drain efficiency of EPWM (envelope pulse width modulation) transmitter composed of a class-E amplifier is evaluated by circuit simulation, and the pulse modulation method to the constant envelope RF signal by PWM pulses is studied. The class-E amplifier is designed as normal for continuous wave (CW) and constant envelope signals. Each transistor is modeled with an ideal switch and an on-resistor, where the drain-source capacitance is modeled as a linear one together with the shunt capacitor. Simulation results show that the conventional PWM switching method gating the input RF signal produces unnecessary transient responses making the drain voltage rise and the output signal distorted; the efficiency is degraded. Another method that gates the DC supply voltage by the PWM pulses works as expected and intended, and the result shows the drain efficiency is as high as that of a class-E amplifier driven with a CW signal.

1 INTRODUCTION

Linear modulation schemes, band-limited PSKs and multilevel QAM combined with OFDM (Orthogonal Frequency Division Multiplex) are widely used for recent mobile radio communications such as for wireless LANs, and terrestrial digital television broadcasting due to high spectrum efficiency and tolerance to multipath distortion, The modulated radio signal, however, has dynamically varying envelope and high peak power to average power ratio (PAPR). Although power amplifiers of class-B/C/D/E/F can operate with high efficiency especially in saturated region, these nonlinear amplifiers cannot be used for those linear modulation signal due to degradation of modulation accuracy and spectral regrowth at the adjacent channels.

Several techniques using nonlinear amplifiers for linear modulations have been proposed, Doherty (Doherty, 1936), Cartesian loop, feed-forward, and so on (Raab et al., 2002). Among these techniques, Kahn Envelope Elimination and Restoration (EER) (Kahn, 1952) is recently being studied well and its applicability is shown for microwave transmitters (Raab et al.,

2002) and the IEEE 802.11a/g wireless LAN systems using QAM with OFDM (Diet et al., 2004). Furthermore for better linearity and efficiency, direct RF modulation techniques by the PWM pulses digitized from the envelope signal have been studied for these ten years (Adachi et al., 2002; Wang, 2003; Taromaru et al., 2007; Yokozawa and Yamao, 2011). This transmitter architecture is called envelope delta-sigma modulation (EDSM)(Dupuy and Wang, 2004), or envelope pulse width modulation (EPWM)(Yokozawa and Yamao, 2011; Takahashi and Yamao, 2010). With the EDSM/EPWM architecture, the direct pulse modulation causes considerable switching spurious or quantization noise at the output of the power amplifier, which should be eliminated with a band-pass filter (BPF). Some experiments or circuit simulation studies have been made for EDSM/EPWM transmitter using class-E (Wang, 2003; Dupuy and Wang, 2004) and class-F (Takahashi and Yamao, 2010; Choi et al., 2007) amplifiers. However, the burst RF mode operation and the transient response due to the pulse modulation are not well studied although the transient response directly affects the drain efficiency.

In this paper, drain efficiency of EPWM transmit-
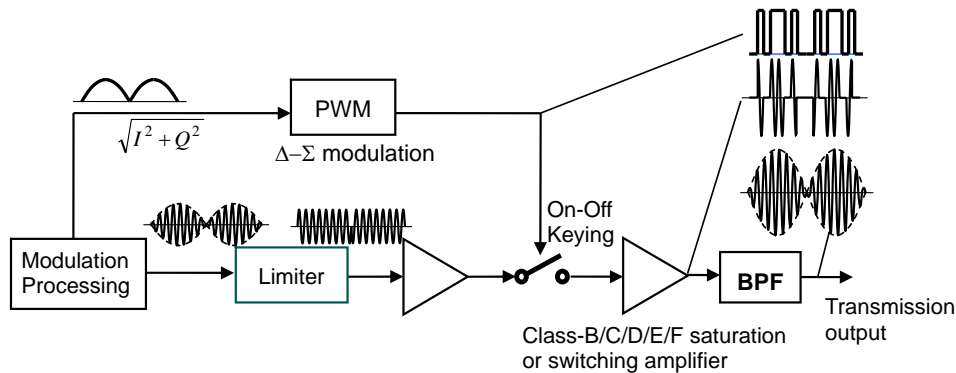
Figure 1: EDSM/EPWM transmitter

ter composed of a class-E amplifier is evaluated by circuit simulation, and the method of pulse modulation by PWM pulses is studied.

2 EDSM/EPWM Transmitter Using Class-E Power Amplifier

2.1 EDSM/EPWM Architecture

Figure 1 shows the block diagram of the EDSM/EPWM transmitter architecture. The left half portion, which is common to conventional EER transmitters, generates digitized PWM pulses of the envelope signal $A(t) = \sqrt{I^2(t) + Q^2(t)}$ and the phase-modulated constant envelope RF signal expressed as $\mathrm{Re}\big[[\{I(t) + jQ(t)\}/A(t)]\exp(j2\pi f_c t)\big]$, where $I(t)$ and $Q(t)$ are the in-phase and quadrature component of the desired modulation respectively, $\mathrm{Re}\,z$ is the real part of complex number z, and f_c is the carrier frequency. In this architecture, the PWM pulse directly drives the RF switch, which is implemented as Gilbert cell mixer or DC bias switching of the amplifier circuit to make the RF signal in burst shape. The burst RF signal becomes amplitude modulated signal whose envelope is proportional to the duty ratio of the PWM pulse through the BPF. With this architecture, all RF amplifiers can be nonlinear ones and free from AM-PM conversion because the amplifiers are driven by a constant envelope signal or zero. Additionally, since the amplitude is controlled by the pulse width, near 100% deep AM can be performed, so long as the isolation of the RF switch is enough.

2.2 Class-E Amplifier

Figure 2 shows the circuit topology of the class-E amplifier. The MOS transistor works as a switch and driven with the RF input signal. The series resonant tank circuit is tuned approximately on but slightly lower than the carrier frequency depending on the resonance Q factor (Albulet, 2001). The shunt capacitance is composed of the external capacitor C_S' and the drain-source capacitance C_{DS}, which is nonlinear.

3 Circuit Simulation

3.1 Circuit Design and Simulation Model

The class-E amplifier is designed normally for continuous wave, for this study. The designed schematics are shown in Figs. 3 and 4. Each transistor is modeled with an ideal switch and an on-resistor where the drain-source capacitance C_{DS} is modeled as a linear one together with the shunt capacitor as $C_S =$
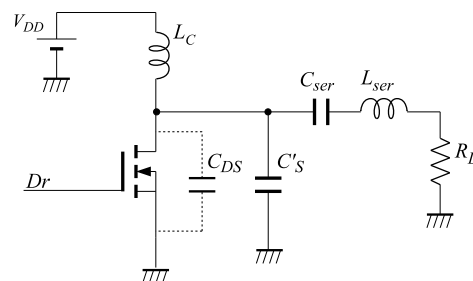
Figure 2: Class-E amplifier.
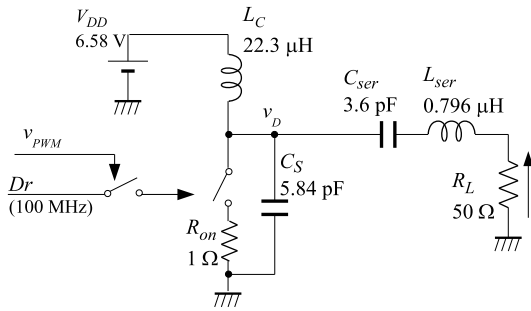
Figure 3: Simulation schematic of RF switching case. PWM pulse modulation is implemented at the RF inputs.

Figure 4: Simulation schematic of DC switching case. PWM pulse modulation is implemented at the drain DC bias circuits.

$C'_S + C_{DS}$. The Q factor of the series LC resonator is set to 10, and the carrier frequency is 100MHz. The load impedance $R = 50\,[\Omega]$, and the output power is 27 dBm for CW. All the inductance and capacitance values are designed in accordance with the way described in (Albulet, 2001). The on-resistance of the transistors are assumed $1\,\Omega$. In the case of Fig. 3, the envelope PWM modulation, making the burst switching of RF input, is implemented at the RF inputs as assumed or designed in (Wang, 2003; Dupuy and Wang, 2004), while it is done at the drain DC bias circuits in the case of Fig. 4 as described in (Choi et al., 2007). In this paper, the former and the latter configurations are hereafter called "RF switching" and "DC switching" respectively. Note that in the former case, the RF switching operation of both the transistors stops and they are kept open during each off duration of the PWM pulses, while they continue RF switching all the time. The diode in Fig. 4 at the right side of the PWM switch driven by the PWM pulse v_{PWM} work as a "free wheel diode" and they are turned-on by the current charged in the choke inductor L_C; the DC bias current of drain is somewhat filtered, and the pulsation due to PWM is smoothed.

3.2 Simulation Parameters and Condition

For PSPICE simulation, the input RF signal Dr is defined as rectangular pulses of 100 MHz without phase modulation (CW). The PWM pulse v_{pwm} is assumed to be a couple of the fixed period $T_{PWM} = 0.1, 1\,[\mu s]$, and the drain efficiency is evaluated varying the duty ratio of the PWM pulse. The drain efficiency is calculated from the averaged power consumption at the load R_L and the supplied DC power from the DC sources. It must be mentioned that the output power gradually rises where the time constant is determined by the choke inductance, the on-resistance and etc, so
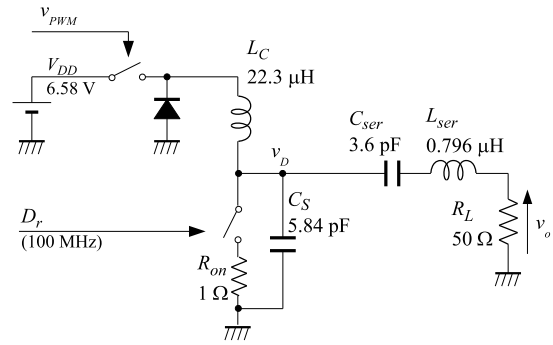
the power is averaged during the $5\,\mu s$ after elapsing $5\,\mu s$.

3.3 Simulation Results

Figure 5 shows the waveforms in the RF switching case, where the duty ratio of PWM is 50%. The upper waveform is the drain voltage of the main amplifier v_S, the lower ones are PWM pulse v_{PWM}, RF input Dr, which is rectangular waveform to drive the transistor modeled as a switch and a on-resistor, and the output signal v_o. Since the CW output is designed 0.5 W and the PWM duty is 0.5, the output power is expected $0.5 * 0.5^2 = 0.125$ W; however, It is seen that only 50 mW power is gained and not a few distortion is observed. Therefore, this configuration is unsuitable.

Figure 6 the wave forms in the DC switching case, where the duty ratio of PWM is 20%. The upper waveform is the drain voltage v_D, and the lower ones are PWM pulse v_{PWM}, RF input Dr defined as rectangular wave, and the output signal v_o. In this case, the output power is gained as expected since the root mean square of v_o is seen to be around 2.6 V. It can also be seen that there are little distortion and ripples of the envelope about v_o. The output spectrum is shown in Fig. 7. The spurious due to PWM switching, to apper 100 ± 10 MHz, is observed to be suppressed by 28 dB to the fundamental component of the carrier. Drain efficiency due to the duty ratio of the PWM pulse is shown in Fig. 8. The efficiency a little degrades in the lower duty region because of the switching loss.
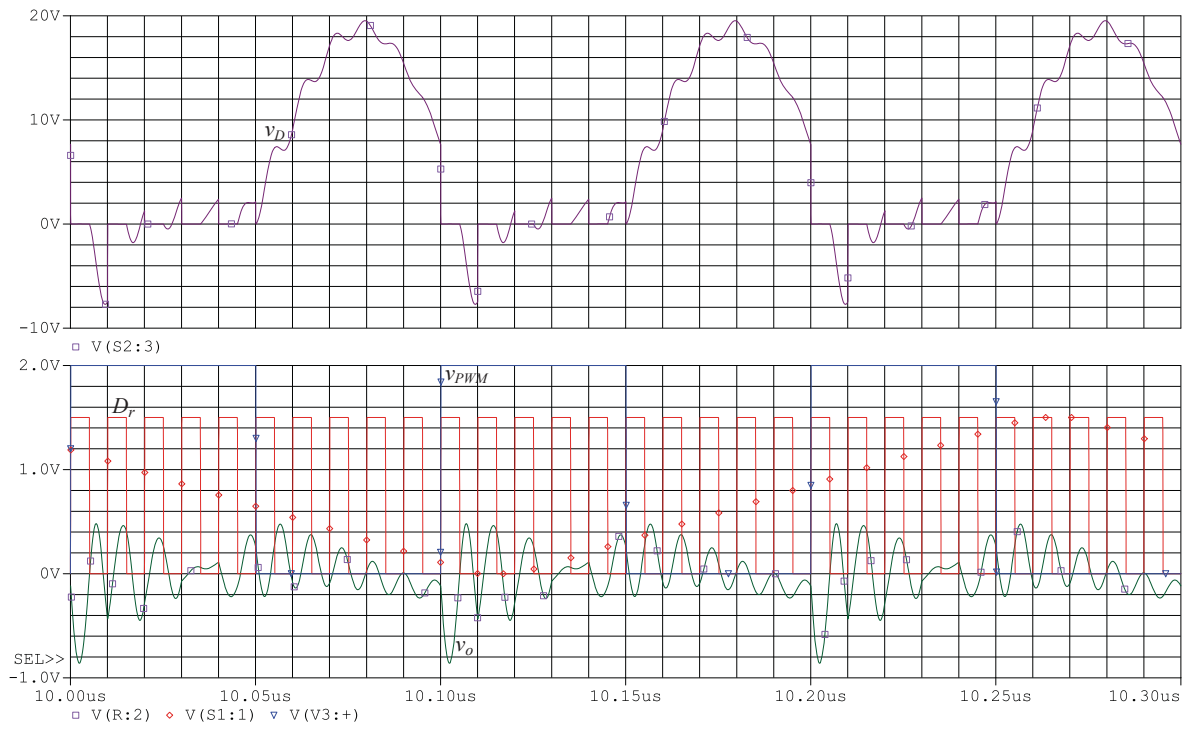
Figure 5: Simulated waveforms of RF switching case.
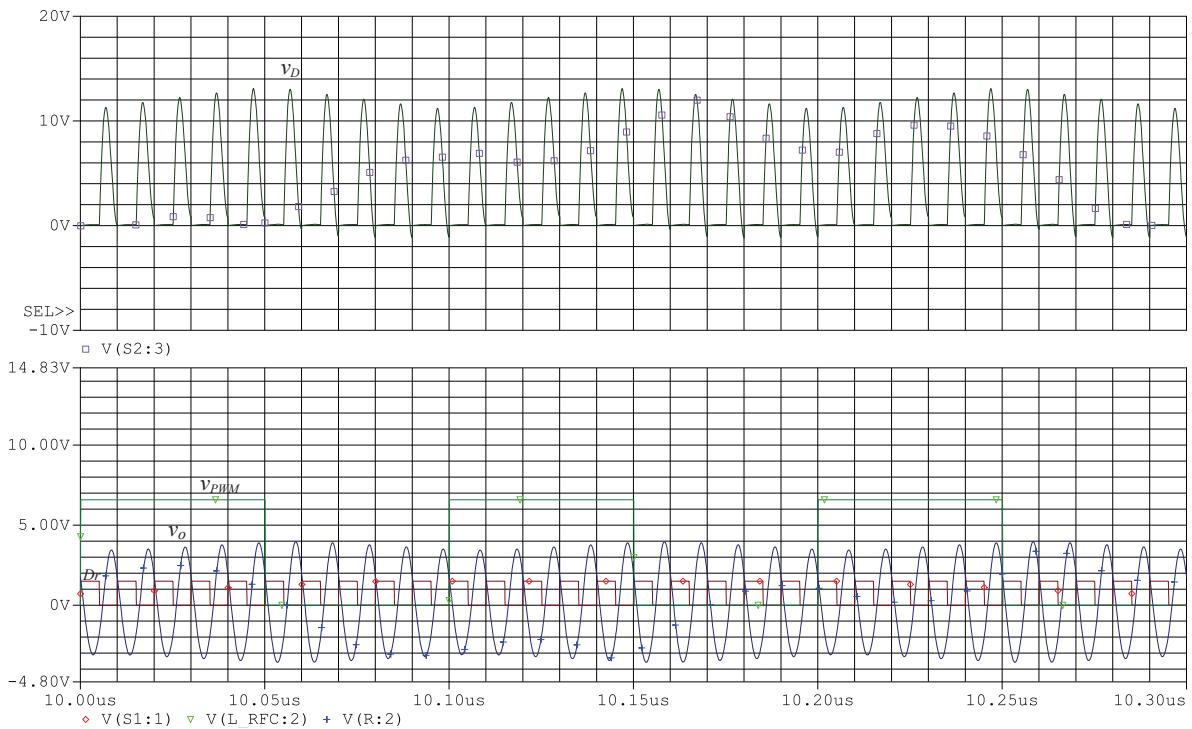
Figure 6: Simulated waveforms of DC switching case.
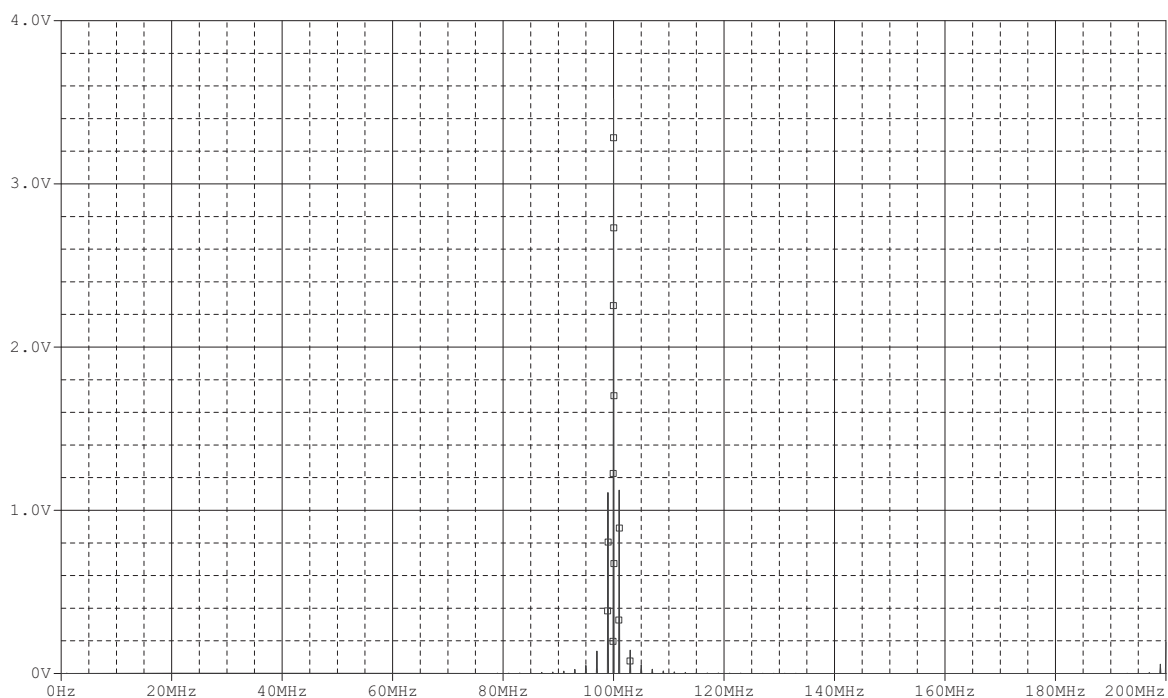
Figure 7: Output spectrum of DC switching case.

3.4 Discussions

Above-mentioned simulation results show that an EDSM/EPWM transmitter using a class-E amplifier should be configured as the DC switching for envelope pulse modulation. However, the PWM signal power to drive the switching device must be higher than the RF switching case and it might not be ignored. The degradation in the RF switching case is clearly caused by transient response after turn-off of every PWM pulse due to the charged current in the drain choke inductors. Note that the choke inductors operate as a low-pass filter to smooth the pulsation of PWM and reduce the PWM spurious or the quantization noise at the output more than the series resonator tank as the BPF where Q is only 10. Therefore, the undesired transient response and loss could be mitigated if the choke components are replaced by LC-resonators or quarter-wavelength stubs as the class-F amplifier case in (Takahashi and Yamao, 2010); however, the filtering effect of the choke inductor cannot be used any more, so the requirement of BPF characteristics becomes severe, sharper cutoff with low insertion loss. Combination of an inductor and a quarter-wavelength stub might be good.
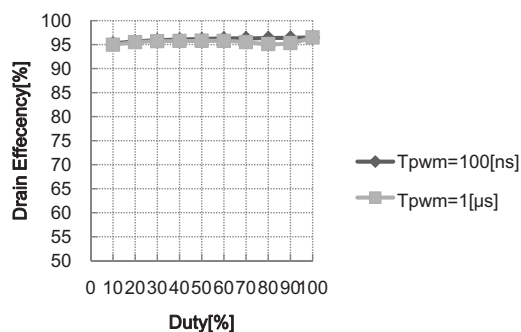
Figure 8: Drain efficiency due to PWM duty (DC switching case).

4 Conclusion

Drain efficiency of EDSM/EPWM transmitter composed of a class-E amplifier is evaluated by circuit simulation, especially on envelope pulse modulation method. Simulation results show that the RF switching method produces unnecessary transient responses and loss, and the output signal distorted, if the drain choke circuits are inductors. Another method that gates the drain DC bias by the PWM pulses works expectedly and the drain efficiency as high as expected; however, it must be noted that the DC switch-

ing is done by a transistor and the driving power may not be ignored. This transmitter architecture has to be carefully designed with above-mentioned trade-off.

REFERENCES

Adachi, T., Iida, M., and Asakura, H. (2002). Transmitting circuit apparatus and method. *United States Patent*, US 2002/0186440 A1.

Albulet, M. (2001). *RF power amplifiers*. Noble Publishing, Atlanta.

Choi, J., Yim, J., Yang, J., Kim, J., Cha, J., Kang, D., Kim, D., and Kim, B. (2007). A $\Delta\Sigma$-digitized polar rf transmitter. *IEEE Trans. Microwave Theory Tech.*, 55(12):2679–2689.

Diet, A., C. Berland, M. V., and Baudoin, G. (2004). EER architecture specifications for ofdm transmitter using a class E amplifier. *IEEE Microwave Wireless Compon. Lett.*, 14:389–391.

Doherty, W. H. (1936). A new high efficiency power amplifier for modulated waves. *Proc. IRE*, 24(9):1163–1182.

Dupuy, A. and Wang, Y. E. (2004). High efficiency power transmitter based on envelope delta-sigma modulation (edsm). In *Proc. 60th IEEE Vehicular Technology Conf. (VTC2004 Fall)*, pages 2092–2095.

Kahn, L. R. (1952). Single-sideband transmission by envelope elimination and restoration. *Proc. IRE*, 40(7):803–806.

Raab, F. H., P. Asbeck, S. C., Kenington, P. B., Popović, Z. B., Pothecary, N., Sevic, J. F., and Sokal, N. O. (2002). Power amplifier and transmitters for RF and microwave. *IEEE Trans. Microwave Theory Tech.*, 50(3):814–826.

Takahashi, S. and Yamao, Y. (2010). Burst RF signal amplification for EPWM transmitter. *IEICE Technical Report*, 110(307, MW2010-118):75–80.

Taromaru, M., Ando, N., Kodera, T., and Yano, K. (2007). An EER transmitter architecture with burst-width envelope modulation based on triangle-wave comparison PWM. In *Proc. 18th Int. Symp. Personal, Indoor and Mobile Radio Commun. (PIMRC 2007)*, page 819.

Wang, Y. (2003). An improved kahn transmitter architecture based on delta-sigma modulation. *IEEE MTT-S Microwave Symposium Digest 2003*, 2:1327–1330.

Yokozawa, S. and Yamao, Y. (2011). Suppression of quantization noise for EPWM transmitter with 2nd-order Δ-Σ modulator. In *Proc. 73rd IEEE Vehicular Technology Conf. (VTC2011 Spring)*.

A MINIMALLY INTRUSIVE WIRELESS SOLUTION FOR CONTEXT- AND SERVICE AWARENESS ENABLEMENT IN MOBILE COMMUNICATIONS

Máirtín O'Droma

Telecommunications Research Centre, University of Limerick, Limerick, Ireland
Mairtin.ODroma@ul.ie

Ivan Ganchev

Telecommunications Research Centre, University of Limerick, Limerick, Ireland;
Department of Computer Systems, Plovdiv University, Plovdiv, Bulgaria (on leave)
Ivan.Ganchev@ul.ie

Nikola.Nikolov

Department of Computer Sciense and Information Systems,University of Limerick, Limerick, Ireland;
Telecommunications Research Centre, University of Limerick, Limerick, Ireland
Nikola.Nikolov@ul.ie

Paul Flynn

Corvil, Dublin, Ireland;
Telecommunications Research Centre, University of Limerick, Limerick, Ireland
paulflynnpaul@gmail.com

Abstract: A wireless solution for context- and service-awareness in mobile communications is the theme of this paper. Respecting mobile users' desire for minimal intrusion of unsolicited advertisements, here we show how the novel push-advertisement technology and medium of 'wireless billboard channels' (WBCs) could be employed by service providers to broadcast advertisements of their wireless services to mobile terminals. While the word 'billboard' here seems to hint at in-your-face intrusiveness, in fact the service functions in the background in a near-transparent un-intrusive manner to the user. When combined with user-driven, dynamic, smart user-profile functionality, inclusive of smart optimisation of current user's 'always best connected and best served' (ABC&S) policies, the system has the potential to provide an effective, pro-active, wireless-based, context-aware and service-aware infrastructure.

The exposition here includes detailed descriptions of the WBC concept, its associated advertisement, discovery and association (ADA) functionality, full technical details of the WBC advertisement service description techniques, formats and attributes, and operational aspects, such as the WBC bit stream structure. It also includes discussion of algorithmic approaches towards optimising smart user profile functionality on mobile terminal which will drive the ABC&S decision-making in ways matched especially to the user needs, in particular those schemes utilising Personalised Information Retrieval (PIR) systems.

1 INTRODUCTION

Wireless billboard channels (WBCs) originated as a foundational infrastructural component in the recently proposed Ubiquitous Consumer Wireless World (UCWW), (O'Droma, 2007) & (O'Droma, 2010), with the main role of direct-to-user push-based advertisement, discovery and association (ADA) service for wireless access network providers (ANPs) and application service providers (ASPs) promoting use of their networks and services, (Flynn, 2007). Through the WBC-ADA service, mobile users, as consumers, may discover the 'best' services and associate with them following a user-driven 'always best connected and best served' (ABC&S) paradigm, (O'Droma, 2006). The physical radio characteristics of WBCs include them being narrowband, unidirectional, point-to-multipoint (P2MP) broadcast channels. They could be created in a number of different stand-alone infrastructures, but for various reasons, economic as well as technological, it would be better that they are integrated into existing wireless broadcast infrastructures, such as a digital television or digital radio broadcast platform.

The WBC service advertisement concept has the attractive advantage of being non-intrusive service advertisement vehicle and infrastructure. This contrasts with the current approach of cellular operators and service providers seeking to attract roaming travellers to use their networks and services by intrusive unsolicited SMS text message advertisements. It is a phenomenon, for example, experienced by many on turning on their mobile phone on arrival in the airport of a new country. While it is of the nature of being a consumer to want to get best value and thus to want to know about competing prices and services, and to have the freedom to choose among them, usually this SMS promotional bombardment does not serve this need in a reasonably informative way. Another growth area of these intrusive unsolicited SMS advertisements is location-based services and other such like services on offer in the area of the mobile user's present location.

The WBC-ADA service described in this paper is well fitted for this advertisement need and service, and to a much wider extent. Moreover, as it functions in the background in a near-transparent un-intrusive manner, it is a comprehensive solution to this growing consumer problem of 'spam' SMS.

Following an exposition of the WBC concept and underpinning technology, how these channels may be made to serve as a wireless solution for context- and service awareness in mobile communications is presented in this paper. The approach, which facilitates both the minimally-intrusiveness criterion and background near-transparent functionality, is presented as well.

2 WIRELESS BILLBOARD CHANNELS (WBC)

Taking into consideration the potentially huge range of wireless services already available to mobile users, the demand for an efficient and easy mechanism for services' ADA adapted to the terminal's capabilities, user preferences and user location, is clearly foreseen. The approach we are proposing to facilitate ADA is to use WBCs that will provide mobile terminals with information about the services available to them. Each terminal can compare this information with its capabilities, the current user profile's preferences, the user location, and other context information such as the time of day, to select the best services to use to achieve a particular goal. As well as advertising the service, the WBC will also provide information to help with the process of discovering and associating with that service.

The WBC should have the following characteristics (Flynn, 2007):

- *Simplex and broadcast:* Simplex here applies not just to the unidirectional physical nature of the channel but also to the unidirectional nature of the WBC service. This attribute has the additional benefit of easing the WBC physical deployment and operation. If the channel is duplex, then in a way it simply becomes another wireless access network infrastructure for two-way wireless communications, and thus in the end no different in its general attributes from any other wireless access network infrastructure. And if this, then bandwidth-spectrum allocation becomes a much more significant issue, as it has been for instance for existing cellular spectrum allocations.

- *Limited bandwidth:* Given the proposed usage – P2MP unidirectional service of advertisements – bandwidth requirements will be relatively narrow. This has the added advantage of enhancing the WBC likely success, e.g. of global agreements on spectrum allocations for them. With limited spectrum available, this would improve the

WBC's chances of becoming a worldwide standard.

- *Maximum coverage area:* These channels should ideally be available anywhere and at any time. No matter where it is (indoor or outdoor), a mobile terminal should have the ability to discover what services are available to it in the current location provided by local, regional, national or international service providers. Terminal mobility should not affect the ability to receive information on the channel.

- *Different versions for different areas:* The number and types of WBCs could correspond to the local/regional/national/international interests of advertisers and users. In practice there would be growth; perhaps a start-up situation would be one national WBC channel, advertising all the services that are relevant on a national level, which could include advertisements of local, regional or interregional significance. And then separate regional WBCs channels, advertising the services available in that region.

- *Operated by non-ANP service providers:* In consideration of the need for fair competition in the ANP marketplace and equity of access to WBC advertisement space, i.e. equally open to all ANPs, it is preferable for WBCs service providers (WBC-SPs) to be fully independent and physically separate from ANPs and their networks. This requirement may need the support of some regulation.

3 WBC-ADA MODEL

The main purpose of the WBC from the consumer's perspective is to allow wireless services to be discovered by mobile terminals. Service discovery is a networking concept whereby a client can automatically discover services that are available to it in a network. There are a number of protocols in existence that deal with service discovery. Three of the well-established protocols, namely Jini (Oaks, 2000), Service Location Protocol (SLP), (Guttman, 1999), and Salutation (Pascoe, 1999), were used as a basis for the development of the WBC-ADA model. Though very different, these protocols use the same basic model that relies on a central registry of service descriptions (SDs), which is accessible in a request-reply manner. A client makes a request for a service, based on the service type and attributes it would like, and receives a reply from the registry

containing information about services that match the request. A WBC, however, is a simplex broadcast channel, which does not allow for requests to be made. The solution then is to broadcast periodically all SDs over the WBC (making allowance for flexibility, e.g., that some SDs be broadcast more frequently than others).

The flow diagram for the WBC-ADA model is shown in Figure 1 and described below:

A. Service providers register their SDs with a WBC-SP's central registry using some external method, e.g. via a web portal.

B. WBC-SP broadcasts all registered SDs, repeatedly, on a WBC (*service advertisement*) in compliance with the specific agreements with each advertising service provider client (e.g., frequency of re-transmissions).

C. Mobile terminals tune to WBC and listen, selectively, to broadcast to receive desired SDs (*service discovery*).

D. Each terminal freely associates with the chosen service provider (server) to use its service (*association*).
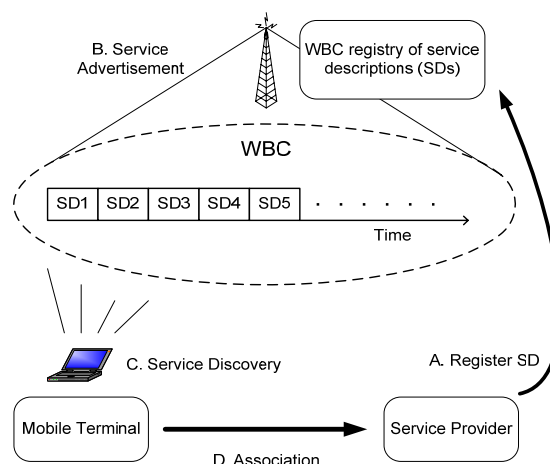
Figure 1: The WBC-ADA model.

3.1 WBC SD Format

The WBC SD format is based around some of the fields used in the well-established service discovery protocols mentioned above.

3.1.1 Service Type

Every wireless service is assigned a service type, which is a field that indicates the basic function performed by the service. The purpose of the *Service Type* field is to allow similar services to be grouped together in a WBC broadcast as this makes it possible to apply power saving techniques.

A hierarchical structure for the *Service Type* field is considered as this allows the order of SDs on a WBC broadcast to be more structured. It is a five-octet field, composed of four subfields.

```
Service-Type ::= SEQUENCE
{
   division  OCTET STRING(SIZE(1)),
   category  OCTET STRING(SIZE(1)),
   type      OCTET STRING(SIZE(2)),
   version   OCTET STRING(SIZE(1))
}
```

The *division* subfield specifies whether it is, for example, an access network's communication service or an application service. The *category* subfield describes what category of services within its division a service falls into. The *type* subfield specifies the actual type of service, within its category. The *version* subfield allows new versions of templates for service types to be published. This could be used to update service types or to create subtypes.

3.1.2 Scope List

The *Scope List* field identifies which scopes the service belongs to. Scopes are a way to administratively group services together. A service may have as many scopes as necessary. Mobile terminals are also configured with scopes. A terminal will only pay attention to SDs that belong to one of the same scopes as itself. Services may also belong to a *default* scope, meaning that all terminals will pay attention. If a terminal receives a SD that has neither one of the same scopes as itself nor the default scope, then it will ignore that SD.

An example of uses for scopes would be to advertise services that are only available to a certain group of people, e.g. government officials, emergency service employees, employees of large corporations, etc.

A scope list is a list of one or more scopes.

```
ScopeList ::= CHOICE
{
   defaultScope    SEQUENCE OF Scope
                   OPTIONAL,
   notDefaultScope SEQUENCE OF Scope
}
```

Any advertiser that wishes should be assigned a globally unique scope. For this reason, the *Scope List* field should be large enough so that scopes do not run out; or a variable length scheme is incorporated. For a fixed length, a 32-bit field seems more than sufficiently large to cater for future expansion.

```
Scope ::= OCTET STRING(SIZE(4))
```

3.1.3 Length

The *Length* field is an integer that specifies the length of the *Attributes* field in bytes. As 65,535 bytes is more than enough to accommodate any possible list of attributes, it could be defined as:

```
Length ::= INTEGER(0..65535)
```

This means that the *Length* field has a fixed size of two bytes.

3.1.4 Attributes

The *Attributes* field is the main one in a SD. It carries the information for advertisement, discovery and association of a service. Advertisement attributes are used by a terminal to decide if its user wants to use the service (based on information stored in the user profile). Discovery and association attributes are used to enable a user/terminal to use the service. The format of the *Attributes* field depends on the service type. The size of the field is not fixed, meaning that the total size of the SD is not fixed. Perhaps service providers would pay more for advertisement of a larger SD than for a smaller one.

3.2 WBC SD Encoding

One of the desired properties for the WBC is that it should use as little bandwidth as possible. In Jini, SDs are Java objects, and passing the descriptions involves serialising the objects. Serialised Java objects are a very inefficient way of encoding data. In SLP, the SDs are encoded as text which, while more efficient than Java objects, is still not efficient enough. The Salutation SD, which uses the Abstract Syntax Notation (ASN.1), (ITU-T, 2008a), is the most efficient approach in this case. ASN.1 data can be encoded in a number of different ways, depending on which encoding rules are followed. The Packed Encoding Rules (PER), (ITU-T, 2008b), give the most efficient encoding (close to optimal). For this reason we chose for the SDs to be ASN.1 structures and encode them using the PER.

The following is the SD format specified in ASN.1.

```
ServiceDescription ::= SEQUENCE
{
   service-Type    Service-Type,
   scopeList       ScopeList,
   length          SDLength,
   attributes      Attributes
}
```

The encoded SD ASN.1 structures are broadcast on a WBC. The *Service Type* and *Scope List* have

the same format in every SD so a terminal that receives a SD knows what is the type of service and to which scopes it belongs. For the *Attributes* field, however, the format depends on the service type. This field makes no sense unless the terminal knows what its format is. Therefore, for each service type an attribute template should exist, as there is in SLP, which lays out the format of the attributes for a particular service type. This way, advertisers, WBC-SPs and terminal manufacturers know what format to follow. Attribute templates would form additions to the basic WBC standard.

One of the benefits of using attribute templates is that terminal software only has to be programmed to understand the meaning of service types that are relevant to that terminal. For instance, a terminal with no video capabilities has no interest in SDs for video services. Another benefit is that as new service types come into existence, new templates can be published, without having to make changes to the main WBC standard. However, this could leave some terminals unable to understand the new formats, while other smarter terminals will be able to update their WBC software appropriately. It is necessary then, for a terminal to be able to ignore *Attributes* fields whose format it does not understand. This is why the *Length* field is needed, to tell terminals how many bytes they must ignore before the next SD begins.

4 SERVICE TYPES AND TEMPLATES

While WBCs would be used for ADA of access networks' communication services –for many its primary goal–, the focus of this paper is on the application services.

The vision for next generation networks (NGN) is for all-IP networks where terminals will receive application services from service providers over IP. There are many different service types currently available to terminals and in NGN that number will be greater. A service type should include all services that perform a similar function. For example, a voice-call service should be one service type rather than having many different service types depending on the Voice over IP (VoIP) protocol being used. These, instead, should be included as attributes of the voice-call service.

In addition service types can themselves be put into broader categories. For example, communication services, information services, location-based services, etc. This allows similar service types to be grouped together on the WBC broadcast. The ITU-T Focus Group on Next Generation Networks' (FGNGN), (ITU-T, 2004) Working Group 1 is concerned with NGN services. Drawing on its NGN Release 1 Service Classification (Carugi, 2005) as a guide to what services will be available in NGN, possible service categories and types advertised to users/terminals over the WBC would include, but by no means are limited to, the following:

- *Communication Services* – Voice call; Video call; Push-to-talk; Conference call; Multimedia interactive communication service; Incoming call; Voicemail; Call diversion.
- *Messaging Services* – SMS; MMS; Email; Fax; Instant messaging; Chat rooms; Bulletin boards.
- *Information Services* – News; Weather; Sport; Finance; Yellow pages directory.
- *Entertainment Services* – Games (download / play on-line / on-line multiplayer); Music (download / streaming); Video clips (download / streaming); Ringtones / Logos / Icons / Screensavers / etc (download); Television (streaming); Radio (streaming); Competitions; Gambling; Dating; Voting / Surveys (maybe related to TV programmes, e.g. reality TV).
- *Educational Services* – mLearning (lectures, tutorials, labs, tests, examinations).
- *mCommerce Services* – mPay facilities; mShopping portals; mBanking and share trading; Bookings and ticketing; M-market type services (eBay).
- *Location-Based Services* – Nearest restaurant, cinema etc; Local weather; City guide; Walking/driving directions; Car parking; Traffic information; Public transport services / timetables; Location-based advertising; Location-based dating.
- *Emergency Services* – Police, Fire brigade, First medical aid, Rescue service, Alerts for natural disasters (in the area), etc.
- *Terminal reconfiguration services* – upgrades of mobile software, operating systems and applications.
- *Other Services* – On-line data storage; Cloud computing; Organisational services – calendar / address book etc; Virtual Private Network (VPN); Social networking.

Some of these listed service types may not be suitable for advertising on the WBC, and other (suitable) service types may have been omitted. Also, some of the service types may belong to more than one service category.

Each service type needs a service template to specify the attributes that are included in a SD for advertisement, discovery, and association. Making decisions between different services is automatic, based on preferences specified by the user in his/her profile and by taking into account the cost, quality and supported features of the available services.

After selecting a service by the user, the terminal (operating in a background mode, i.e. without disturbing the user) will choose the 'best' available instance of the desired service and will associate with it by using information obtained from the WBC. The first thing needed is the client-side software to be installed on the terminal (if not already installed/pre-loaded). For this an attribute is needed, which tells the terminal how to download this software. There should then be an attribute specifying the software itself and its version so that the terminal can see if it needs to be updated. Rather than having an attribute that says where to get the software (or software update), it could be better to have one software-download service (which would also be advertised as any other service on the WBC), which allows for downloading of all additional software needed to use services advertised on the WBC. Having installed the software, there are some attributes specific to a particular service (e.g. IP address and port numbers) that also need to be known.

Each service type needs a service template, which is an ASN.1 specification of the attributes used to define a service of that type. Considering the voice-call service as an example, a list of attributes for its advertisement and association is presented in Table 1.

Table 1. Attributes for the voice-call service type.

Attribute		Meaning	Use
For advertisement	Cost	Contains information about the cost of using the voice-call service (e.g. cost per minute to various recipients in different regions, countries etc).	Used by a terminal to compare the cost of the service from one SP with the maximum cost for the call that the user wishes to pay, and with that for the same service offerings from other SPs.
	Quality of Service (QoS)	Contains third-party measurements of the quality of this service (e.g. calls dropping rate, sound quality, etc).	A terminal selects the service (provider) that is expected to perform 'best'.
	Protocols	Specifies which communication protocols are used by this service.	A terminal may not support the use of certain protocols. Reconfiguration requirements and decisions.
	Features	A list of features apart from the basic that might differentiate one voice-call service from another (e.g. ability to send text during a call, music playing in the background, etc).	Used by a terminal to compare additional features desired by the user in order to choose the 'best' service.
For association	Software	An identifier that tells a terminal what software is needed to access this service.	A terminal can see if this software is already installed. If not, it can be downloaded from a software-download service provider, etc.
	Supported versions	The version numbers of the software that are supported by this service.	A terminal can see if the version of the currently installed; software is suitable/up to date. If not, then if a new version may be downloaded, based on WBC advertisement information.
	Software parameters	Information about this particular service needed by the terminal software (e.g. IP address and port numbers). This may have different fields for each value of the software attribute.	A terminal software uses this information to associate with the service.

Specified in ASN.1, the coded voice-call service definition itself would have the following form:

```
VoiceCallService  ::= SEQUENCE
{
   cost       VoiceCallCost,
   performance
              VoiceCallPerformance,

protocols    VoiceCallProtocols,

features     VoiceCallFeatures,
   software  SoftwareIdentifier,
   versions  SoftwareVersion,
   softParams
        VoiceCallSoftwareParameters
}
```

It is worth noting that the ASN.1 service specifications are designed in such a way as to accommodate also future service types and updates.

5 WBC BIT-STREAM STRUCTURE

5.1 Data Scheduling

A SD contains the values of all the attributes that are specified in the service template. These are encoded into binary data using the PER of ASN.1. Depending on the service type and the values of certain attributes, SDs are not all going to be the same size. The WBC broadcasts SDs continuously so that terminals listening to the channel can receive the service descriptions they need. The simplest approach is to broadcast all the SDs, one after the other and when the end is reached, start at the beginning again (called a *flat broadcast*). This, however, might not be the most efficient way, or the way desired either by the advertisers or by the WBC-SP seeking ways to make their business more profitable. Also from the consumer's perspective 'flat broadcast' can result in inefficiencies and delays. If a certain SD is demanded by terminals more frequently than another, then it makes sense to broadcast it more frequently. The priority should be to minimise the average *access time* of the entire system. Access time is that time from the moment when a mobile terminal first starts accessing a data item (SD) on the WBC, until the moment it receives full data item (SD). Minimising that time, averaged across all required SDs by all terminals, is a common-sense goal.

There are quite a few data scheduling algorithms; however, most of these are pull-based, meaning that they rely on the clients making requests on a back channel for certain data items to be broadcast. These algorithms are not suitable for the WBCs, which are simplex broadcast channels. Hence only push-based algorithms, such as the Broadcast Disks and Priority Index Policies, were considered. A modified and improved version of the Broadcast Disks algorithm was elaborated and described in (Ji, 2008) for data scheduling on WBCs.

5.2 Data Indexing

Efficient use by mobile terminals of their limited battery energy is another factor. Any techniques to reduce power consumption thereby extending their battery charge-life are attractive especially if they are cost-neutral. Power is saved by minimising the time spent by terminals for listening to the WBC channel to receive the required SD (referred to as *tuning time*). Tuning time could be reduced by the use of indexing because without it, a terminal would have to tune into the WBC and listen to the broadcast continuously until the required SD is transmitted. By adding indexing data to the broadcast, terminals can tune in, find out when the required SD will be transmitted, then tune out and wait until that time to tune back in again. By adding redundant data to the broadcast, however, the average access time is going to be increased.

There are several indexing schemes that aim to provide a good trade-off between having a low tuning time and a low access time. All these schemes have several features in common: the attribute that the data items (records) are indexed by is called the *key* (in the case of the WBC, the key is the service type); the order of the records in the broadcast sequence is arranged by the value of their keys; the broadcast sequence is divided into fixed size parts called *buckets*; the indexing tells the client in which bucket to look to find the first record with the required key (as buckets are of a fixed size, the client will know the exact time that a particular bucket will be broadcast).

Short description and comparison of the main indexing schemes are provided in (Flynn, 2010). It may be that flat-broadcasting schemes could be adapted to accommodate non-flat broadcasting as well. Based on these, a new 'Simple Indexing Scheme' was elaborated for use in WBCs as described in (Flynn, 2010).

6 SMART USER-PROFILE FUNCTIONALITY

In future networks, the ultimate goal of service providers will be to provide services to mobile users in ABC&S mode, i.e. at the 'best' QoS and cost levels, and by applying personalisation and context awareness. As described in (Stavroulaki, 2009), personalisation supports different user types and roles, whereas context awareness considers the state of the user (user identity and roles), mobile terminal (capabilities) and environment (location and time zone). To achieve this, proper management of user preferences and terminal capabilities is required by means of accurate description and representation of information along with the configuration and update of user profiles.

The user profiles could be structured with two groups of parameters as proposed in (Stavroulaki, 2012):

- *Observable parameters* – these include the services that are currently running on the user terminal, corresponding QoS parameters, and context parameters such as user location, time zone, service rank, etc.
- *Output parameters* – the value of these is dynamically changed over time depending on the value of observable parameters. The main output parameter is the so called *utility volume*, which provides a ranking of service-QoS pairs by order of user preferences. The latter, of course, may change over time and may vary depending on the user context. An approach for dynamically learning of user preferences w.r.t. the perceived QoS level per service with the use of Bayesian statistics concept is presented in (Stavroulaki, 2009).

A generic intelligent iWBC client, which sits on the mobile terminal and operates in the background in support of the mobile user becoming fully aware of all relevant wireless services available (in the current location) and advertised according to the structured WBC format, has been designed and successfully implemented (Ji, 2011). Information about available services is proactively pushed to the terminal which, with the help of this application, can thus discover the services and all the necessary details about their offerings, sufficient to make informed ABC&S decisions about using them, including knowing how to associate with the access networks to obtain these services in the best possible way through the ADA procedure. Hence this novel iWBC application amounts to a significant advance in consumer-driven ABC&S capabilities and services.

Through the WBC system, including the iWBC client application, all wireless service advertisements, become a background activity. That is, the data is captured, analysed and filtered according to individual user's ABC&S policies and presented to the user as and when s/he likes. It is only when the user seeks to use a service that s/he might become aware of the service offerings garnered from the WBC advertisements by the iWBC application. The iWBC would then present these over a friendly user interface allowing the user to assess options and attributes in an information-structured and comparative manner, and make an ABC&S choice decision on which service to use.

In fact it can all be even more transparent and un-intrusive to the user, if the ABC&S decisions are also made in the background following default (e.g., lowest price) or preset ABC&S policies and profile settings. This 'full transparent ABC&S' mode will mean a minimum disruption to the user, and yet it will still be user-driven ABC&S.

(Ji, 2011) demonstrates a practical use case example when a new 'best' wireless service instance is becoming available in the current area of the mobile user. In this case, the iWBC client application automatically discovers this new service offering by a background extraction of this information from the WBC's service descriptions, logs this information in the terminal's database, examines it in accordance with the consumer-driven ABC&S policies and makes decisions on its usage, informing the user of the new service offerings, and so on.

7 PERSONALISED INFORMATION RETRIEVAL

The UCWW environment presents a shift from the currently dominating subscriber-based wireless access towards a consumer-centric one (O'Droma, 2007) & (O'Droma, 2010). Allowing the user to choose a provider for a particular service from a list of alternatives opens the opportunity for stronger competition between providers and a better service for the user as a result. However, giving the user the freedom to choose should not become an overwhelming burden when the number of options, as well as factors that choice depends on, is too large.

A possible solution is to introduce an extra feature to the WBC-ADA system that facilitates the

user's choice by suggesting a ranked list of providers for the desired service as per the past experience of other users in the same physical context. The retrieved list of service providers could then be adjusted and personalised for the user and their physical context by utilising the context parameters in the user profile.

Systems which retrieve information that is both relevant to the submitted queries and personalised for the user are known as *personalised information retrieval* (PIR) systems. They have been the subject of extensive research in the last couple of decades with a major application in Web search as well as in other areas such as eLearning and news dissemination (Ghorab, 2012). For example, a PIR framework for a wearable computer in ubiquitous computing environment was proposed by (Hong, 2005). This framework is particularly oriented towards retrieving personalised information from objects in physical proximity to the user in a typically cluttered with data environment. Although the iWBC client application would also work on wearable devices in a ubiquitous computing environment, it will need to retrieve information from a relatively less heterogeneous data source (the stream of SDs broadcast on WBC) than the complete variety of objects in physical proximity to the user. Thus, the design principles for a typical PIR system (for example, a PIR system for Web search) may be followed, taking into account also the physical context of the user.

In order to provide personalised results, an iWBC PIR client must gather and store data about the information needs of the user. There are two approaches to representing and storing the gathered information. It can be either stored in an individualised *user model* (Zhang, 2007) & (Speretta, 2005) or in an aggregated one (Agichtein, 2006) & (Smyth, 2006). A recent survey proposes a classification of PIR systems with respect to the scope of personalisation into three categories: *individualised personalisation*, *community-based personalisation*, and *aggregate-level personalisation* (Ghorab et al. 2012). The individualised personalisation is limited to the information gathered about the user who queries the system. Similar to it, the community-based personalisation also employs a user model for providing personalised information retrieval. However, it also allows sharing of information between users. The aggregate-level personalisation, on the other hand, makes no use of an explicit user model and decisions are based on aggregate usage data.

A community-based PIR (Teevan, 2009) & (Sugiyama, 2004) would seem to suit WBC needs best as it offers personalised results to the user based not only on their previous behaviour and experience

but also on the experience of other users who have used the service in a similar context. There are three aspects of a PIR system which need to be addressed in the design: information gathering, information representation, and implementation and execution of personalisation (Gauch, 2007). An immediate next step in the WBC research is to decide what information about users should be tracked, how this information will be gathered and stored in a user model and then how user models will be used for retrieving personalised results. The research literature offers a wide spectrum of solutions for each of the stages of PIR (Ghorab, 2012). The majority of them have been developed for the needs of Web information retrieval. However, they should be easily adaptable for the needs of selecting providers of services in NGN.

From another point of view, user modelling and PIR can be a feature that can make the concept of WBC-ADA attractive to the current wireless service providers. Instead of having third-party organisations providing the PIR service for all users, PIR can be distributed between SPs. That is, PIR can be a service that a user will request from a particular provider they are subscribed to or have used as a consumer. For example, consider the following scenario. User A is receives PIR services provided by SP X. User A needs to make an international phone call and tunes on WBC to receive information of a provider that can allow them make the call for a fixed price under 1€ The iWBC client finds a number of providers who satisfy this user request and returns a personalised ranked list. The top provider in the list is Y and the user selects it for the phone call. That is, the user has used the PIR provided by X to find out that Y is the provider that best suits their requirements for a phone call at their particular physical context. In this case, even though X will not provide the phone call, X can still be motivated in providing the best PIR for that user. Thus, the competition between providers can stay healthy and they can preserve their user base.

8 CONCLUSIONS

Advertisement and discovery are part of an important R&D challenge to find solutions for the automated enabling of the entire process of advertisement, discovery and association (ADA) of wireless services and for the evolution of wireless communications. It will contribute significantly to continuity of connection to wireless services provided to mobile terminals. To facilitate this, a wireless equivalent of the shop window and

billboard advertising, called a wireless billboard channel (WBC), was presented in this paper. This would provide access network providers (ANPs) and application service providers (ASPs), with a very active dynamic means to advertise (i.e. proactively 'push') their presence and services through WBCs operated by non-ANP service providers. The proactive push advertisement nature of the WBC would correspond well to ANP and ASP competitive desires to use all means to reach the mobile users from their existing 'loyal' subscribers through to the impulse buying consumers. Advertisement and discovery of wireless communication services and application services deployed and accessible in a particular area/location, and procedures for terminal association with these, are defining characteristics of contemporary networks.

WBCs would also benefit the users due to automated discovering functionality of terminals scanning the WBCs and updating service offerings and availability information, matching these against user profiles and proposing, and enabling casual or persistent consumer-type association links for different user-desired services. The result of this process will be more up-to-date information for user-driven always best connected and best served (ABC&S) decisions. Ideas on smart user profile functionality and user-driven ABC&S decision-making based on personalised information retrieval (PIR) systems adapted to this UCWW context have been set out and discussed.

Implicit in this vision is the global standardisation of these proposed WBCs as a vehicle and a wireless infrastructural support for ADA procedure. Practically it makes sense to have several WBCs directed at different geographic extensions.

The utilisation of the Digital Video Broadcast - Handheld (DVB-H) standard – a standard for broadcasting digital television to handheld devices (ETSI, 2004) – as a candidate carrier technology for WBC was extensively studied, e.g. in (Ji, 2010a). DVB-H extends the DVB-Terrestrial standard with time-slicing and other additions to greatly reduce receiver's power consumption. Designed for handheld devices, it allows for high terminal mobility and thus is ideal for WBC use. A 'WBC over DVB-H' prototype system was designed, implemented, evaluated and successfully tested, e.g. (Ji, 2010b) & (Ji, 2009).

REFERENCES

Agichtein, E., Brill, E., Dumais, S., Ragno, R., 2006. Learning user interaction models for predicting Web search result preferences. In *SIGIR 2006, 29th Annual International ACM SIGIR Conference on Research and Development in Information Retrieval*. ACM.

Carugi, M., Hirschman, B., Narita, A., 2005. Introduction to the ITU-T NGN Focus Group Release 1: Target Environment, Services, and Capabilities. In *IEEE Communications Magazine, 43(10)*.

ETSI, 2004. EN 302 304 V1.1.1. Digital Video Broadcasting (DVB); Transmission System for Handheld Terminals (DVB-H). http://www.etsi.org/deliver/etsi_en/302300_302399/302304/01.01.01_60/en_302304v010101p.pdf

Flynn, P., Ganchev, I., O'Droma, M., 2007. Wireless Billboard Channels: Vehicle and Infrastructural Support for Advertisement, Discovery, and Association of UCWW Services. In *Annual Review of Wireless Communications, vol. 2*. International Engineering Consortium, Chicago, Ill, USA.

Flynn, P., 2010. Wireless Billboard Channels for the Advertisement, Discovery and Association of Mobile Services in a Ubiquitous Consumer Wireless World. Master's Thesis. University of Limerick, Ireland.

Gauch, S., Speretta, M., Chandramouli, A., Micarelli, A., 2007. User profiles for personalized information access. In *The Adaptive Web*, Springer. Berlin, 1st ed.

Ghorab, M. R., Zhou, D., O'Connor, A. and Wade, V., 2012. Personalised Information Retrieval: survey and classification. In *User Modeling and User-Adapted Interaction*, Springer. Netherlands.

Guttman, E., Perkins, C., Veizades, J., Day, M., 1999. Service Location Protocol, version 2. IETF RFC 2608. http://www.ietf.org/rfc/rfc2608.txt

Hong, D., Park, Y.-K., Lee, J., Shin, V., Woo, W., 2005. Personalized Information Retrieval Framework. In *1st International Workshop on Personalized Context Modeling and Management for UbiComp Applications*.

ITU-T, 2004. Focus Group on Next Generation Networks (FGNGN). http://www.itu.int/ITU-T/ngn/fgngn/

ITU-T, 2008. Information technology - Abstract Syntax Notation One (ASN.1): Specification of basic notation (*Recommendation X.680*). http://www.itu.int/rec/T-REC-X.680-200811-I/en

ITU-T, 2008. Information technology – ASN.1 encoding rules: Specification of Packed Encoding Rules (*Recommendation X.691*). http://www.itu.int/rec/T-REC-X.691-200811-I/en

Ji, Zh., Ganchev, I., O'Droma, M., 2008. Efficient Collecting, Clustering, Scheduling, and Indexing Schemes for Advertisement of Services over Wireless Billboard Channels. In *ICT'2008, 15th International Conference on Telecommunications*.

Ji, Zh., Ganchev, I., O'Droma, M., 2009. Performance Evaluation of 'WBC over DVB-H' System. In *IEEE Transactions on Consumer Electronics, 55(2)*.

Ji, Zh., Ganchev, I., O'Droma, M., 2010. Performance Analysis of 'WBC over DVB-H' Link Layer. In *EURASIP Journal on Wireless Communications and Networking, vol. 2010*.

Ji, Zh., Ganchev, I., O'Droma, M., 2010. `WBC over DVB-H` Testbed Design, Development and Results. In *EURASIP Journal on Wireless Communications and Networking, vol. 2010*.

Ji, Zh., Ganchev, I., O'Droma, M., 2011. "An iWBC Consumer Application for 'Always Best Connected and Best Served': Design and Implementation". In *IEEE Transactions on Consumer Electronics, 57(2)*.

Oaks, S., Wong, H., 2000. *Jini in a Nutshell*. O'Reilly Media. 1st edition.

O'Droma, M., Ganchev, I., Chaouchi, H., Aghvami, H., Friderikos, V., 2006. `Always Best Connected and Served` Vision for a Future Wireless World. In *Journal of Information Technologies and Control, IV (3-4)*.

O'Droma, M., Ganchev, I., 2007. Toward a Ubiquitous Consumer Wireless World. In *IEEE Wireless Communications, 14(1)*.

O'Droma, M., Ganchev, I., 2010. The Creation of a Ubiquitous Consumer Wireless World through Strategic ITU-T Standardization. In *IEEE Communications Magazine, 48(10)*.

Pascoe, B., 1999. Salutation Architectures and the newly defined service discovery protocols from Microsoft and Sun *(white paper)*. Salutation Consortium. http://salutation.org/wp-content/uploads/2012/05/Jini-UPnP.pdf

Smyth, B., Balfe, E., 2006. Anonymous personalization in collaborative Web search. In *Inf. Retr. 9*.

Speretta, M., Gauch, S., 2005. Personalized search based on user search histories. In *WI 2005, International Conference on Web Intelligence*. IEEE/WIC/ACM.

Stavroulaki, V., Kritikou, Y., Darra, E., 2009. Acquiring and Learning User Information in the Context of Cognitive Device Management. In *IEEE ICC'2009, IEEE International Conference on Communications*.

Stavroulaki V. et al., 2012. Knowledge Management Toolbox: Machine Learning for Cognitive Radio Networks. In *IEEE Vehicular Technology, 7(2)*.

Sugiyama, K., Hatano, K., Yoshikawa, M., 2004. Adaptive Web search based on user profile constructed without any effort from users. In *WWW 2004, 13th International Conference on World Wide Web*. ACM.

Teevan, J., Morris, M.R., Bush, S., 2009. Discovering and using groups to improve personalized search. In *WSDM 2009, 2nd ACM International Conference on Web Search and Data Mining*. ACM.

Zhang, H., Song, Y., Song, H.-T., 2007. Construction of ontology-based user model for Web personalization. In *UM 2007, 11th International Conference on User Modeling*.

A NEW MODEL OF THE INTERNATIONAL REFERENCE IONOSPHERE IRI FOR TELECOMMUNICATION AND NAVIGATION SYSTEMS

Olga Maltseva, Natalia Mozhaeva, Gennadyi Zhbankov

Institute of Physics Southern Federal University, Stachki, 194, Rostov-on-Don, Russia
mal@ip.rsu.ru, mozh_75@mail.ru, zhbankov_ga@rambler.ru

Abstract: Telecommunication, navigation, positioning systems require knowledge of ionospheric Ne(h)-profiles up to high-altitude orbits of satellites. The only way to construct such profiles is associated with the use of the ionospheric total electron content TEC. New option IRI-Plas of the IRI2010 model allows us to construct Ne(h)-profiles by adjustment of the model to the current maximum values of the parameters of the ionospheric F2 layer (foF2, hmF2) and the TEC. This paper contains a comprehensive comparison of these profiles with the data of various experiments (ISR, CHAMP, DMSP). Results show the high efficiency of this adjustment. The proposed method of further adjustment of the IRI-Plas model to the plasma frequency at altitudes of CHAMP and DMSP satellites allows us to produce behaviors of Ne(h)-profiles during the disturbances, as well as to refine the values of TEC, which determine the accuracy of positioning.

1   INTRODUCTION

The operation of the various satellite communication, navigation, global positioning systems (GPS) depends on the state of the ionosphere and needs to know the electron distribution in height (Ne(h)-profiles) in near space. Methods for direct measurement of the Ne(h) at these altitudes are not exist, however, there are a number of theoretical and empirical models of Ne(h)-profiles. In many applications of radio and satellite communications, the empirical model of the ionosphere IRI (Bilitza, 2001; 2006) is most widely used, but it determines the Ne(h)-profile to a height of 2000 km. Ability to determine the profiles at high altitudes is associated with the total electron content (TEC) of the ionosphere. This parameter is defined as the number of electrons in the atmospheric column, measured by the navigation satellites (GPS, etc.) and directly related to the Ne(h)-profiles of the ionosphere. Despite the difficulties in determining the TEC (slips of signal phase, an idealization of the model of the ionosphere on the conversion of slant TEC into the vertical VTEC, the dependence on the type of receiver, etc.), it is widely used in various applications. However, the IRI model gives a large discrepancy when compared with the experimental TEC because of the profile shape of the topside ionosphere (e.g., Stankov et al., 2003; Uemoto et al. 2007; Bilitza, 2009; Maltseva et al., 2011), so that the model has been modified several times in this century (IRI2001 (Bilitza, 2001), IRI2007 (Bilitza and Reinish, 2006; 2008)) and modification continues. In 2010, a new version IRI2010 (Bilitza et al., 2010) of the IRI model was proposed, which included a model of T. Gulyaeva. Although this model has been developed for a long time, for example (Gulyaeva et al., 2002; Gulyaeva, 2003), it is formally incorporated as IRI-Plas just now. The main advantages of this model are accounting a plasmaspheric part of the magnetosphere, and the ability to be adapted to the experimental parameters of the ionosphere (the critical frequency foF2, the maximum height hmF2, TEC). This should allow us to determine the shape of Ne(h)-profiles. The purpose of this paper are: 1) validation of the IRI-Plas model according to various experiments (incoherent sounding radars ISR, satellite CHAMP (hsat~400 km) and DMSP measurements (hsat~800 km), 2) validation of the IRI-Plas model according to the particular ionospheric station of Sofia, 3) determination of the behavior of Ne(h) profiles during the disturbed conditions, 4) refinement of the values of TEC by means of further adaptation of the model to the plasma frequency at altitudes of satellites CHAMP and DMSP. These results may

have important implications for telecommunication, navigation, positioning systems.

2 ON THE IRI MODEL

As noted in (Bilitza, 2006), "The International Reference Ionosphere (IRI) project was initiated by the Committee on Space Research (COSPAR) and by the International Union of Radio Science (URSI) in the late sixties with the goal of establishing an international standard for the specification of ionospheric parameters based on all worldwide available data from ground-based as well as satellite observations. COSPAR and URSI specifically asked for an empirical data-based model to avoid the uncertainties of the evolving theoretical understanding of ionospheric processes. COSPAR's main interest is in a general description of the ionosphere as part of the terrestrial environment for the evaluation of environmental effects on spacecraft and experiments in space. URSI's prime interest is in the electron density part of IRI for defining the background ionosphere for radiowave propagation studies and applications. To accomplish these goals a joint COSPAR-URSI Working Group was established and tasked with the development of the model." IRI describes monthly averages of the electron density, electron temperature, ion composition ($O+$, $H+$, $N+$, $He+$, $O2 +$, $NO+$, Cluster+), ion temperature, and ion drift in the ionospheric altitude range (60 km to 1000 km). Some of the primary applications are listed in Table 1 in (Bilitza, 2006) together with typical usage examples. The model is recommended as the ionospheric standard. The model is located on the site: http:// modelweb.gsfc.nasa.gov/ionos/iri.html. The maximum parameters (foF2, hmF2) are provided by the ITU-R (former CCIR) or URSI maps. Drivers of the model are parameters characterizing solar and geomagnetic activity (RZ12, IG12, ap and others). Input parameters are day, month, year, coordinates of the point among others. TEC is calculated by the formula TEC=∫Nedh. The calculation ceiling of previous versions was 2000 km. The IRI-Plas model extended to the plasmasphere. Output parameters important for our purposes are the critical frequency foF2, the maximum height hmF2, TEC, Ne(h)-profiles. All versions provide adaptation of the model to current values of foF2, hmF2 and include the STORM-factor adapting the model to disturbed conditions (Araujo-Pradere et al. 2004).

3 VALIDATION OF THE IRI-PLAS MODEL ACCORDING TO DIFFERENT EXPERIMENTS

Experimental values of the parameters foF2 and hmF2 are taken from the SPIDR database. TEC values are computed from IONEX files of the global maps delivered online by four organizations: JPL (Mannucci et al., 1998), CODE (Schaer et al., 1995), UPC (Hernandez-Pajares et al., 1999), ESA (Sardon et al., 1994; Jakowski et al., 1996). Ne(h)-profiles of incoherent sounding radars for six stations are taken from (Zhang et al., 2007). These profiles show the Ne to a height of 500 km. In all cases, the coincidence of the model and experimental profiles was good. Quantitative results are presented in Table 1 in the form of the experimental and calculated values of the plasma frequency fne at an altitude of 500 km for the three European radars. These radars are Svaldbard (78.1°N, 16°E), StSantin (44.6°N, 2.2°E), Tromso (69.6°N, 19.2°E). The first column gives the shortening name of the station and the day of measurement (1 = 03/31/1999, 2 = 29/07/1999, 3 =11/26/2002). Data of (Zhang et al., 2007) refer to LT = 12, but calculations were done for UT corresponding to each radar. The following columns represent the results of different calculations, which should be compared with values in the last column (ISR) containing experimental ones. The results show that the model and experimental profiles match very well, but we can not specify a map, which would be consistent with all experiments, so it is advisable to choose a map that gives the closest value of fne.

Table 1: Comparison of the IRI-Plas model results with ISR data of three radars

	IRI	foF2	TEC	JPL	ESA	ISR
Sv(1)	3.57	2.37	3.37	3.35	3.33	3.19
Sv(2)	2.86	2.64	3.77	3.75	2.53	3.79
Sv(3)	2.84	1.57	1.62	2.22	2.15	2.01
St(1)	5.52	3.46	3.10	4.19	2.43	4.01
St(2)	3.57	2.70	3.09	3.85	3.42	4.01
St(3)	4.49	3.16	2.33	3.66	3.04	3.38
Tr(1)	4.00	2.37	2.24	2.74	0.71	3.66
Tr(2)	2.86	3.05	3.79	3.94	3.52	3.79
Tr(3)	3.50	2.47	1.59	2.41	2.37	3.38

4 VALIDATION OF THE IRI-PLAS MODEL ACCORDING TO DATA OF THE SOFIA STATION

Data of the Sofia station were selected to demonstrate results of validation of the IRI-Plas model and to show its new possibilities. Validation is carried out for four cases: (1) the original model IRI, (2) the IRI model, adapted to the experimental value of foF2, (3) the IRI model, adapted to the experimental value of the TEC, (4) the IRI model, adapted to the experimental values of foF2 and TEC, to show the difference between the results for these methods. Option 1 is used when there is no current information and determines the average ionospheric state. It is a standard for comparison with other options. Option 2 uses the current value of foF2 and completely defines the bottom part of the profile. Option 3 is widely used in connection with the TEC measurements with navigation satellites. The advantage of this option before the second one is in a continuous global monitoring. Adapting the model to the current values of the TEC allows us to obtain new (reconstructed) values of foF2. Option 4, as stated in the introduction, is one of the main differences between the new IRI model and previous versions. It allows to determine the Ne(h)-profile at the location of ionosondes. Validation of these options is to compare the plasma frequency at altitudes of satellites calculated for the model with the experimental values of fne. A comparison was carried out for two satellites CHAMP (hsat ~ 400 km) and DMSP (hsat ~ 840 km). Data of foF2 are taken from SPIDR, values of TEC – from global maps of JPL, CODE, UPC, ESA. Results are presented for April 2001 including two strong disturbances (1-2 April with minimum Dst=-228nT and 11-12 April with minimum Dst=-273 nT) and two weak disturbances (18 and 22-23 April) with minimum Dst~-100nT. Table 2 shows the results of comparisons of Ne(h)-profiles with satellite CHAMP data. Table includes day, time of observation, and the values of plasma frequencies for the respective versions and the CHAMP satellite. Figures in round brackets indicate numbers of options. The last column shows fne of the CHAMP satellite. Heights of the satellite were in range 410-460 km.

The best fit of model and the experimental values is provided by the fourth version. Examples of the profiles are shown in Fig. 1a, b. Fig. 1a presents night profiles (UT=1), Fig. 1b presents daytime profiles (UT=13). Examples for night

profiles are given for cases of foF2(obs)>foF2(IRI) (the left panel) and foF2(obs)<foF2(IRI) (the right panel).

Figures in round brackets after the name of the satellite indicate a time of observation if this time does not coincide with data of TEC. Values of the model and satellite plasma frequencies coincide for the forth version.

Table 2: Comparison of simulation results for different versions of the IRI model with the data of the CHAMP satellite

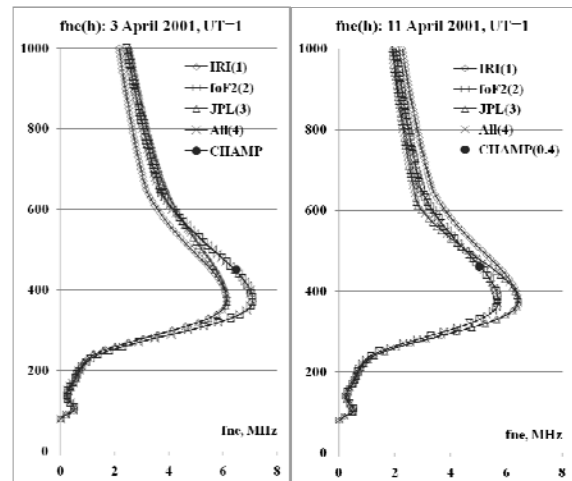| day	UT	IRI (1)	foF2 (2)	TEC (3)	All (4)	CH fne
3	1	5.57	6.45	5.75	6.44	6.50
3	13.1	9.27	10.70	10.14	10.94	11.14
6	12.6	9.33	9.97	9.84	10.15	10.01
11	0.4	5.72	5.07	5.41	5.06	5.04
13	12.6	9.16	11.09	9.96	10.87	11.16
19	23	6.51	5.02	5.07	4.92	4.37
21	23.2	6.52	6.53	6.45	6.46	6.21
23	23.4	6.52	5.80	5.91	5.67	5.35
24	22.7	6.53	6.15	6.30	6.11	6.00
26	22.9	6.53	6.53	6.55	6.55	6.92
29	11.2	8.14	8.88	8.60	8.65	8.74
29	22.5	6.54	5.85	6.04	5.78	5.74
30	10.5	8.10	8.05	8.21	8.20	7.76

Figure 1a: Comparison of model Ne(h)-profiles and the results for the CHAMP satellite (April 2001) for night time
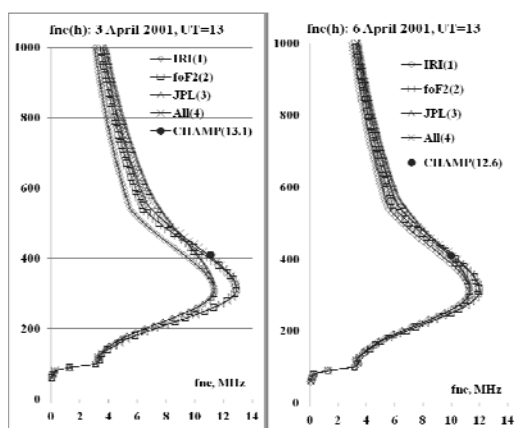
Figure 1b: Comparison of model Ne(h)-profiles and the results for the CHAMP satellite (April 2001) for day time

The same correspondence can be seen for the noon time profiles, although the time of the satellite flight is slightly different from the time of measurement of ionospheric parameters. Exact coincidence of these times is rare.

More often are the cases when the satellite passed over the station at even hours, whereas the values of TEC were only for the odd hours. Typical examples of calculations for these cases are shown in Fig. 2 for daytime and nighttime profiles for the forth option (full adjustment).
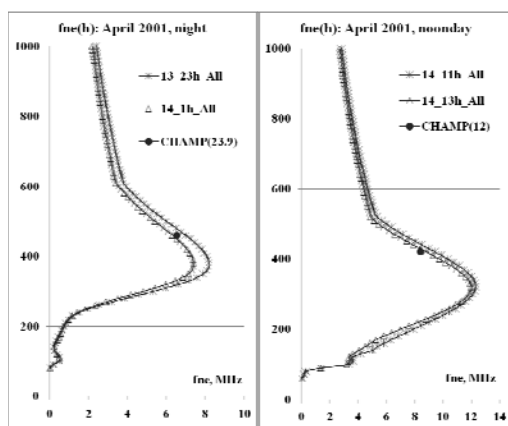

Figure 2: The cases of the satellite flight in the average hours between the measurements of the TEC

Orbit heights of DMSP satellites exceed 800 km. The results using data of DMSP were obtained under the same scenario. In this case data of three satellites were available (F12, F13, F15). Typical results are shown in the Table 3. They present plasma frequencies for four options and experimental values fne.

Table 3: Comparison of simulation results for different versions of the IRI model with data of DMSP satellites (hsat~840-860 km)

day	UT	IRI (1)	foF2 (2)	JPL (3)	All (4)	fne
1	5.5	2.10	1.22	1.71	2.07	2.15
1	8.7	3.46	2.73	2.88	3.40	2.71
1	15.3	3.32	3.17	3.67	3.76	3.36
1	17.4	3.10	2.95	3.61	3.67	3.02
2	5.3	2.13	2.13	2.77	2.77	2.38
2	7.5	2.76	3.00	3.74	3.62	2.94
2	17.2	3.11	3.41	3.77	3.61	2.75
3	7.3	2.77	3.28	4.06	3.79	2.89
3	8.2	3.47	4.03	4.68	4.35	3.41
3	16.5	3.15	3.69	4.20	3.92	3.33
4	4.9	2.15	2.73	3.44	3.22	2.76
4	7	2.77	3.17	3.97	3.77	3.04
4	19.4	2.96	3.38	3.89	3.70	3.44
5	19.2	2.97	2.87	3.31	3.35	2.81
11	19.4	3.04	3.60	3.60	3.27	3.52
12	4.8	2.23	1.39	1.38	1.95	1.73
12	7	2.82	1.69	1.93	2.64	2.19
12	19.2	3.05	2.75	2.45	2.68	1.60
13	4.6	2.24	2.08	2.19	2.29	1.80

The distinction of this case is the fact that the best agreement between the calculated and experimental values of fne is obtained for the original model or adaption of the model to current foF2. Using the experimental values of TEC leads to overvalued values of fne. A too high value for the map of JPL should be considered as a possible cause. This can be confirmed by the results for other maps presented in Fig. 3. Experimental plasma frequencies fne are shown by full points, the other values are corresponding to various maps.

It is seen that often experimental frequencies do not reach range of map values. Nevertheless, the agreement between the calculated and experimental values of fne exists. Typical examples of Ne(h)-profiles are shown in Fig. 4 as close to the moment of the flight time and for the middle of two hour period.
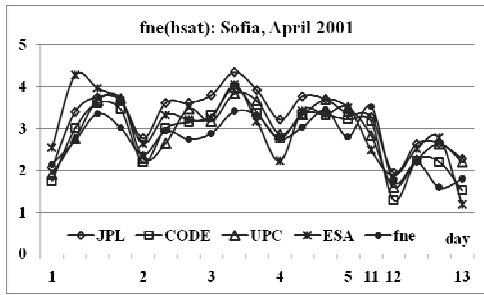
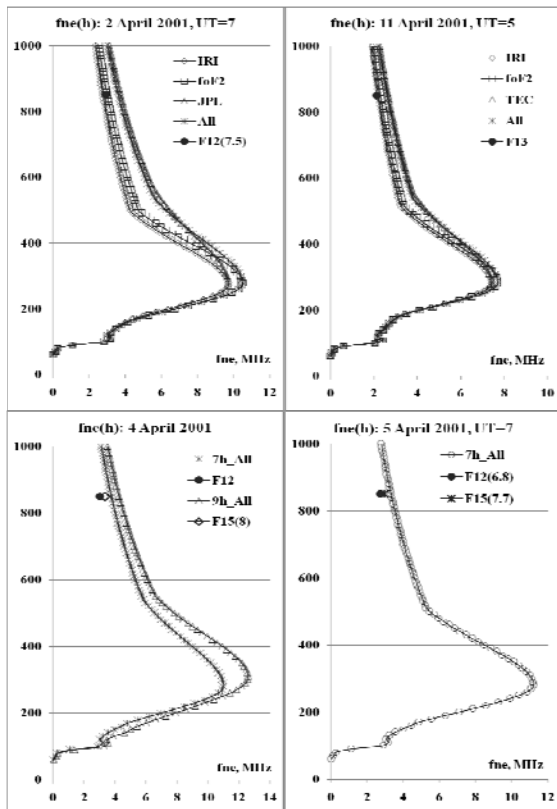Figure 3: Comparison of experimental plasma frequencies fne and frequencies provided by maps of JPL, CODE, UPC, ESA

Figure 4: Comparison of model Ne(h)-profiles and the results of the DMSP satellite (April 2001)

5 EXAMPLES OF THE BEHAVIOR OF Ne(h)-PROFILES AT THE SOFIA STATION DURING DISTURBANCES

The results of the previous section show that the profiles are rather well adapted to meet the satellite measurements. This allows us to study and simulate the height distribution of the ionospheric ionization. The choice of Ne(h)-profiles in the previous section was dictated by time of flight of the satellite. For a variety of tasks long periods of observation are important especially for disturbed conditions when the profiles can be strongly modified. Examples of the behavior of Ne(h)-profiles for the longitudinal (left panels) and latitudinal (right panels) chains connected with the Sofia station are shown in Fig. 5.The upper two sets of graphs display night profiles (UT = 1), the bottom two groups – daytime profiles (UT=11). The upper graphs of each group show the profiles during quiet conditions, the lower profiles - in the disturbed ones. In the night of 12 April, quiet conditions on the longitudinal chain (Sodankyla, Leningrad, Moscow, Sofia) are presented by Ne(h)-profiles of the IRI model. We can see the coincidence of the values of three northern stations and high values for Sofia because it is the most southerly. During the disturbance, which is negative, the profiles vary strongly, because all the ionospheric structures are shifted to the south. Thus, the Moscow station is in the area of the ionospheric trough, the Leningrad station falls from the plasmaspheric area into zone of subauroral amplification. The most strongly reduced is the concentration at the Sofia station reaching values less even than the values in the subauroral Sodankylä station. This leads to huge gradients of the electron concentration that must be considered in the propagation of radio waves. On the latitudinal chain (Sofia, Rome, Ebre), profiles of the Sofia station have the lowest ionization, indicating a positive gradient towards lower latitudes under quiet conditions. During the negative disturbance, a decrease in the concentration at all the stations can reduce gradients. During the day, the concentration distribution in the quiet time should be clearly decreased with increasing latitude. An example of the lower grafts shows that a positive (in this case) perturbation has the greatest effect on the concentration of the Sofia station. Example of daytime profiles for a quiet state and during the April 3 disturbance is shown in the lower right-hand chart. It is seen that if a negative disturbance during the night enveloped almost the entire European region, the daytime disturbance may influence by different manner at various stations.

Since the bottom and topside parts of the profile may respond differently to disturbance, such profiles can provide a quantitative assessment of effects of disturbances.
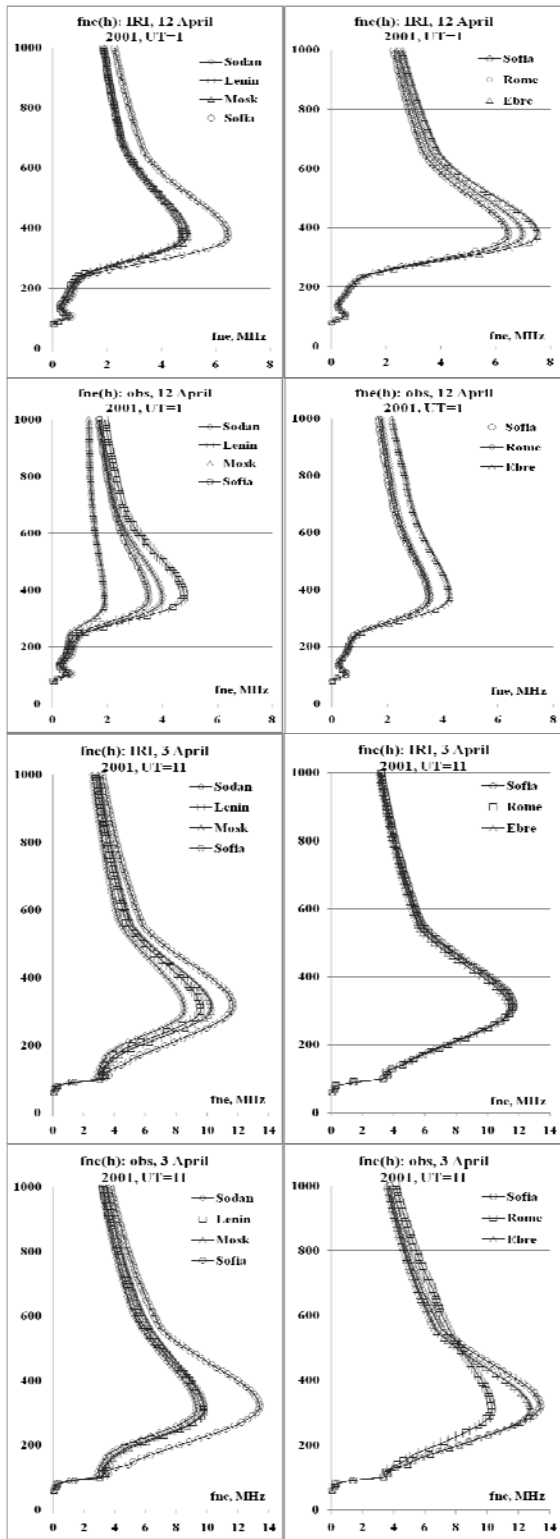
Figure 5: Sequence of Ne(h)-profiles showing their modification during the disturbances

6 CASES OF LACK OF MEASUREMENT OF IONOSPHERIC PARAMETERS AT THE STATION

In the absence of measurements of ionospheric parameters at the station there are at least two methods to obtain Ne(h)-profiles: (1) the use of the parameters of the original model, (2) the use of the median equivalent thickness of the ionosphere τ(med) in conjunction with the TEC. The first option coincides with the first option of the section 4 and provides good results for the conditions close to the quiet ones, but during the disturbances difference can be substantial, as illustrated in Fig. 6. Fig. 6 shows the results of calculations for all versions. It is evident that the difference is significant, not only near the peak of the layer F2, but at the top of the profile. The full points indicate the plasma frequency of DMSP satellites.
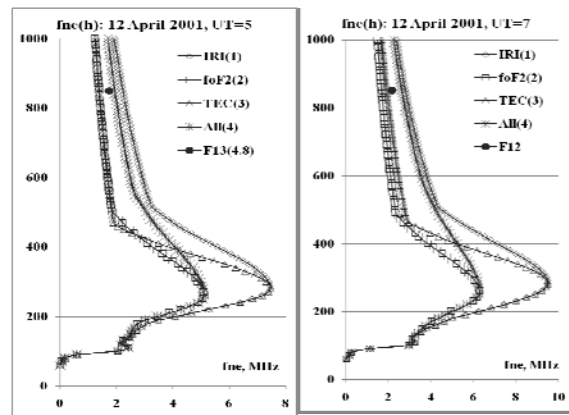

Figure 6: Comparison of Ne(h)-profiles in the case of strong differences in foF2 (IRI) and foF2 (obs), caused by a disturbance

These two successive profiles show an increase in the diurnal foF2, but the perturbation has a strong influence. Therefore, it is preferable to use the second method. In (Maltseva et al., 2012) is shown that the use of the median equivalent thickness of the ionosphere τ(med) in conjunction with the TEC allows us to fill in gaps in the data by means of using reconstructed values of foF2. The effectiveness of this approach is estimated using the deviations of the calculated and experimental values of foF2 for periods when there are complete data sets. For four disturbed periods in April 2001 for the Sofia station, these deviations are shown in Fig. 7.
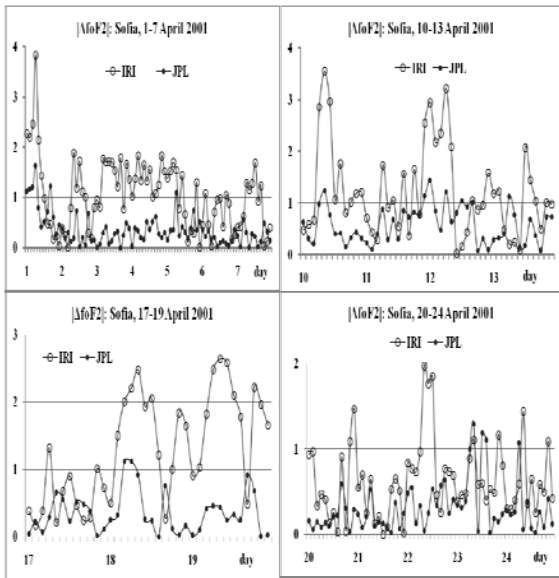
Figure 7: Deviations of the model and reconstructed values of foF2 from the experimental ones

It is seen that the greatest deviations of model foF2 values from the experimental ones account for the days of disturbances. Using τ(med) in conjunction with the TEC can increase compliance by many times. This section contains attempts to do the next step: to use τ(med) of one (reference) stations for the determination of foF2 of another station from its values of TEC. We validate this procedure with the help of satellite data. The results are shown in the example of May 2005, which was also marked by four disturbances with minimal index Dst:-127nT (8.05), -263nT (15.05), -103nT (20.5), -138nT (30.5). For the Sofia station, ionospheric observation data are absent in the SPIDR database since 2005. Rostov was chosen as the reference station to determine the values of foF2 for the Sofia station. Values of τ(med) of the Rostov station and TEC values of the Sofia station are used. To be sure in correctness of using τ(med) of the Rostov station we compared τ(med) of these stations for some previous years. Fig. 8 displays experimental and model values of median equivalent thickness τ of the ionosphere for stations of Sofia and Rostov in May of those years for which measurements were available simultaneously at both stations in the SPIDR. Model values (sign IRI) shown by the triangles and asterisks coincide. Namely these values are used in traditional methods of determining foF2 from TEC (McNamara, 1985; Houminer and Soicher, 1996, Gulyaeva, 2003). They ensure deviations between experimental and model values of foF2 shown in Fig. 7 by circles. The more important fact is the

closeness of the experimental values of τ(med) for both stations. Using these values ensures deviations shown in Fig. 7 by points.
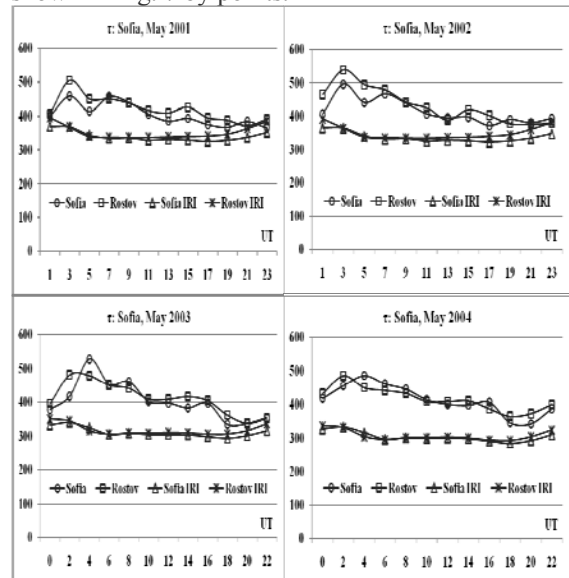

Figure 8: Comparison of equivalent thicknesses τ for Sofia station

Table 4: Comparison of simulation results for different versions of the IRI model with the data of CHAMP satellite in May 2005 (hsat~860 km)

day	UT	IRI	foF2	TEC	All	fne
1	9	5.73	5.69	5.95	5.93	5.41
2	21.3	4.82	3.67	4.76	3.70	3.91
3	8.4	4.99	5.33	5.48	5.65	5.45
4	20.7	5.69	5.31	5.66	5.34	3.99
6	8.3	4.97	5.33	5.47	5.65	4.59
12	8	4.91	5.34	5.44	5.66	4.55
12	19.9	5.87	5.97	5.99	6.07	6.02
18	19.6	5.96	5.08	5.77	5.15	4.87
21	19.5	5.97	5.38	5.93	5.48	5.27
23	7.1	4.88	4.97	5.26	5.30	3.81
24	19.3	5.99	5.83	6.09	5.95	5.78
28	6.3	4.65	5.59	5.34	5.93	5.46
28	18.5	6.07	6.45	6.41	6.72	6.55
29	18.6	6.06	6.38	6.39	6.65	7.05
30	5.7	4.65	4.48	4.89	4.81	4.07

The profiles obtained using the reconstructed values of foF2 are compared with data of CHAMP and

DMSP satellites. The results are shown in Tables 4-5 separately for each satellite. In this case, there were more flights with similar times for both satellites, so in the Table 5 we focus on the close passages.

Table 5: Comparison of simulation results for different versions of the IRI model with data of DMSP satellites in May 2005 (hsat~840 km).

day	UT	IRI	foF2	TEC	All	fne
1	7.2	1.89	1.99	2.33	2.29	1.81
3	8.4	1.88	1.99	2.33	2.28	1.61
4	19.6	1.91	1.79	1.81	1.90	1.12
6	6.2	1.85	1.97	2.30	2.26	1.48
18	19.4	1.93	1.66	1.61	1.84	1.18
23	5.3	1.77	1.82	2.14	2.12	1.46
29	18.2	1.92	2.02	2.52	2.46	1.58
30	5.3	1.77	1.71	1.96	1.99	1.48

The results are very similar to the results for April 2001, indicating the effectiveness of this approach. The proximity of the flight time allowed us to compare Ne(h)-profiles adapted to the values of

plasma frequencies for both satellites. Examples of such profiles are shown in Fig. 9.
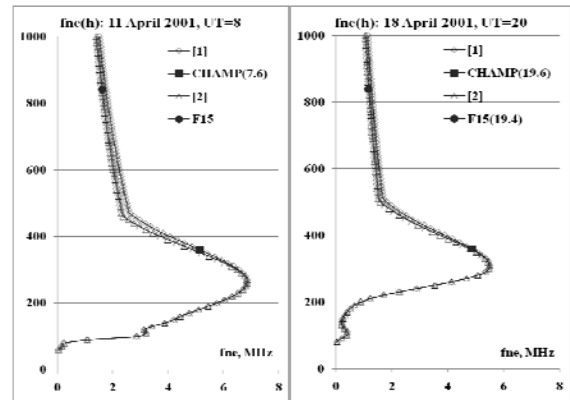

Figure 9: Examples of Ne(h)-profiles adapted to the data of both satellites

An important result is the fact that adaptation to data of various satellites leads to almost the same profile. This suggests that the behavior of the profiles will reflect the real situation. An example of the behavior of profiles during two disturbances in May 2005 is shown in Fig. 10.
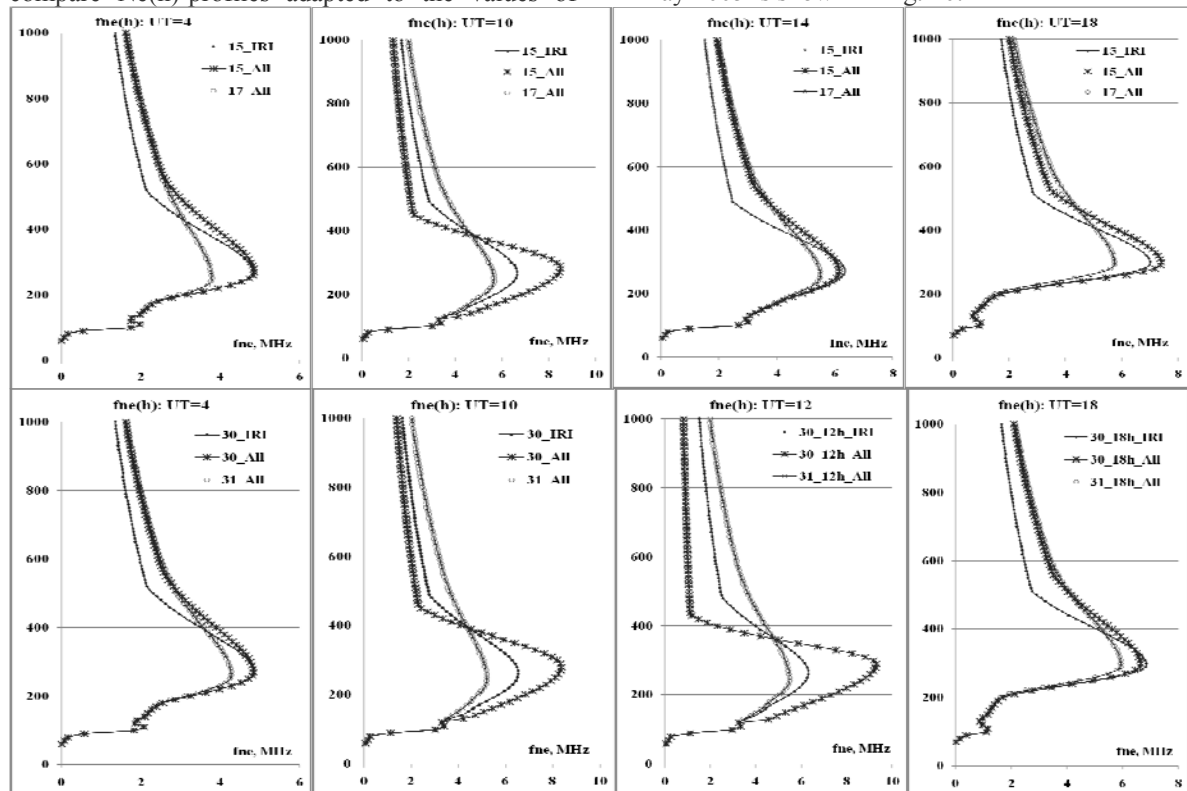

Figure 10: The behavior of the Ne(h)-profiles of the Sofia station during two disturbances in May 2005

Surprising is the identity of changes during these two disturbances, which may indicate some regularities. IRI profiles correspond to quiet conditions. Comparison with these profiles shows that in the early morning hours (UT = 4) on 15 and 30 May at the bottom, the ionosphere is close to the quiet state, and in the topside there is an increase of ionization. On 17 and 31 May, a decrease in the bottom part is observed along with an increase at the topside. This demonstrates the different responses of the upper and lower parts of the ionosphere on the disturbance. In moments of UT = 10 both disturbances are manifested in the form of large increases in the bottom part and the weakening of the ionization at the topside. On May 30 at UT = 12, this process is developing at the time, as on 15 May (chart is not shown), it decays. In UT = 18, both the profiles return back to its original state.

7 REFINEMENT OF THE TEC VALUES FROM SATELLITE EXPERIMENTS

Figure 3 shows that there is some variation in correspondence related to the difference in TEC. The difference of the TEC values related to one point and one moment of time is a known fact. The reasons for the differences may be very different. For global maps of JPL (Mannucci et al., 1998), CODE (Schaer et al., 1995), UPC (Hernandez-Pajares et al., 1999), ESA (Sardon et al., 1994; Jakowski et al., 1996), it is the difference in calculation methods. Various receivers may give difference of up to 10 TECU (e.g. Choi et al., 2010). A typical example is Figure 7 of the article (Arikan et al., 2003), which shows the values of TEC, obtained by different methods in the Kiruna station on 25 and 28 April 2001. The values of the global maps for the Sofia station for these two days are shown in Fig. 11.
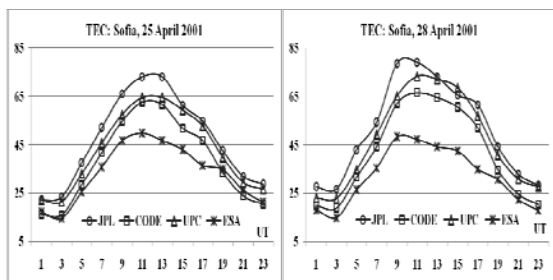

Figure 11: Differences of TEC for the Sofia station calculated from the various global maps

It is seen that the difference in the Sofia station for four maps may lie in the range of 10-30 TECU. In this paper is proposed to specify these values using the plasma frequency on satellites. Fig. 12 shows the values of TEC for four maps and the values obtained by adapting the model to fne on satellites. In the abscissa, day and hour of calculations are indicated.
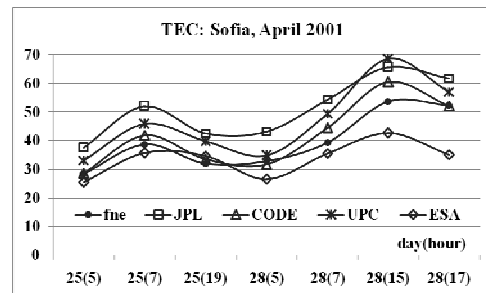

Figure 12: Comparison of TEC calculated from the various global maps with TEC obtained by adaptation to the satellite fne

It is seen that the values of the JPL map are overvalued. It is possible that such adaptation can be used to calibrate the TEC for a given station.

8 CONCLUSIONS

The ionosphere is the key factor for the operation of satellite systems. It is one of the largest sources of error in positioning and navigation. The associated error is proportional to the TEC. That is why a lot of attention paid to the development of the ionospheric model. Using the model of Klobuchar (e.g. 1987) allowed to increase the positioning accuracy in 2 times. The next step was done using the IRI model. However, the previous versions of this model also had limitations. This paper highlights the possibilities of a new model (Gulyaeva et al., 2002; Gulyaeva, 2003). They confine to the fact that adaptation of the IRI model to current ionospheric parameters foF2, hmF2 and TEC allows us to determine the state of the ionosphere up to altitudes of high-altitude satellites with greater accuracy than ever before. The use of plasma frequency fne, measured at altitudes of satellites, on the one hand, allows us to validate the model and determine the behavior of the Ne(h)-profiles, on the other hand, may provide refinement of TEC values which depend on the accuracy of satellite systems from. According to data of the Sofia station, effectiveness of the use of the median equivalent thickness of the

ionosphere τ (med) is confirmed not only to fill gaps of foF2 at one station, but also to determine the behavior of foF2 for the other stations in the absence of its experimental data.

ACKNOWLEDGEMENTS

REFERENCES

Araujo-Pradere, E.A., Fuller- Rowell, T.J., Bilitza, D., 2004. Time Empirical Ionospheric Correction Model (STORM) response in IRI2000 and challenges for empirical modeling in the future. *Radio Sci. 39, RS1S24, doi:10.1029/2002RS002805.*

Arikan, F., Erol, C. B., Arikan, O., 2003. Regularized estimation of vertical total electron content from Global Positioning System data. *J. Geophys. Res. 108 (A12), 1469, doi:10.1029/2002JA009605.*

Bilitza, D., 2001. International Reference Ionosphere. *Radio Sci. 36 (2), 261-275.*

Bilitza, D., 2006. The International Reference Ionosphere – Climatological Standard for the Ionosphere. In *Characterising the Ionosphere (pp. 32-1 – 32-12). Meeting Proceedings RTO-MP-IST-056, Paper 32. Neuilly-sur-Seine, France: RTO.* Available from: http://www.rto.nato.int/abstracts.asp.

Bilitza, D., 2009. Evaluation of the IRI-2007 Model Options for Topside Electron Density, *Adv. Space Res.*, 44(6), 701–706.

Bilitza, D., Reinisch, B.W., 2008. International Reference Ionosphere 2007: Improvements and New Parameters. *Adv. Space Res. 42. 599-609.*

Bilitza, D., Reinisch, B.W., Gulyaeva, T., 2010.ISO technical specification for the ionosphere – IRI recent activities. In *Report presented for COSPAR Scientific Assembly, Bremen, Germany, C01-0004-10.*

Choi, B.-K., Chung, J.-K., Cho, J.-H., 2010. Receiver DCB estimation and analysis by types of GPS receiver. *J. Astron. Space Sci., 27(2), 123-128.*

Gulyaeva, T.L., 2003. International standard model of the Earth's ionosphere and plasmasphere. *Astronomical and Astrophysical Transactions.* 22(4), 639-643.

Gulyaeva, T.L., Huang, X., Reinisch, B.W., 2002. Ionosphere-plasmasphere software for ISO. *Acta Geod. Geoph. Hung. 37, 143-152.*

Hernandez-Pajares, M., Juan, J.M., Sanz, J., 1999. New approaches in global ionospheric determination using ground GPS data. *J. Atmos. Sol. Terr. Phys.*, 61, 1237–1247.

Houminer, Z., Soicher, H., 1996. Improved short –term predictions of foF2 using GPS time delay measurements. *Radio Sci. 31 (5), 1099-1108.*

Jakowski, N., Sardon, E., Engler, E., Jungstand, A., Klahn, D., 1996. Relationships between GPS-signal propagation errors and EISCAT observations. *Ann. Geophys.*, 14, 1429-1436.

Klobuchar, J.A., 1987. Ionospheric time-delay algorithm for single-frequency GPS users. *IEEE Transactions on aerospace and electronic systems. AES-23(3), 325-331.*

Maltseva, O.A., Mozhaeva, N.S., Poltavsky, O.S., Zhbakov, G.A., 2012. Use of TEC global maps and the IRI model to study ionospheric response to geomagnetic disturbances. *Adv. Space Res. 49, 1076-1087.*

Maltseva, O.A., Zhbankov, G.A., Nikitenko, T.V., 2011. Effectiveness of Using Correcting Multipliers in Calculations of the Total Electron Content according to the IRI2007 Model. *Geomagnetism and Aeronomy, 51(4), 492–500.*

Mannucci, A. J., Wilson, B. D., Yuan, D. N., Ho, C. H., Lindqwister, U. J., Runge, T. F., 1998. A global mapping technique for GPS-derived ionospheric total electron content measurements. *Radio Science, 33(3), 565-582.*

McNamara, L.F., 1985. The use of total electron density measurements to validate empirical models of the ionosphere. *Adv. Space Res. 5(7), 81-90.*

Sardon, E., Rius, A., Zarraoa, N., 1994. Estimation of the receiver differential biases and the ionospheric total electron content from Global Positioning System observations. *Radio Sci., 29, 577-586.*

Schaer, S., Beutler, G., Mervart, L., Rothacher, M., Wild, U., 1995. Global and regional ionosphere models using the GPS double difference phase observable. In *IGS Workshop, Potsdam, Germany, May 15-17, 1-16.*

Stankov, S.M., Jakowski, N., Heise, S., Muhtarov, P.,Kutiev, I., Warnant, R., 2003. A New Method for Reconstruction of the Vertical Electron Density Distribution in the Upper Ionosphere and Plasmasphere. J. Geophys.Res., 108, 1164; doi:1029/2002JA009570.

Uemoto, J., Ono, T., Kumamoto, A., Iizima, M., 2007. Comparison of the IRI 2001 Model with Electron Density Profiles Observed from Topside Sounder On_Boardthe Ohzora (EXOS_C) and the Akebono (EXOS_D) Satellites, *Adv. Space Res.*, 39(5), 750–754.

Zhang, S.-R., Holt, J.M., Bilitza, D., van Eykan, T., McCready, M., Amazory-Mazaudier, C., Fukao, S., Sulzer, M. 2007. Multiple-site comparisons between models of incoherent scatter radar and IRI *Adv. Space Res. 39. 910-917.*

SOME EFFECTS OF THE ASSUMPTION OF ALL-POLE FILTER, USED TO DESCRIBE PROCESSES OF TYPE "PULSE SOURSE - FILTER", ON THE PROPERTIES OF THE GENERATD SIGNAL

Damyan Damyanov, Vassil Galabov

Technical University of Sofia, Faculty of Automation, Department for Industrial Automation,
Bulgaria, Sofia, Darvenitsa 1756,Bul. Kliment Ohridksi 8, block 9,rooms 9416 and 9420
damyan.damyanov@fdiba.tu-sofia.bg , vtg@tu-sofia.bg

Keywords: "pulse source – filter" model of speech production, speech communication in control systems.

Abstract: In practice, when analysing, processing and generating signals, it is often assumed, that the process is of type "pulse source - filter". Examples include the speech production process according to the theory of Fant, analysis of shockwaves, ECG, EEG, seismology. For determination of the parameters of the filter many methods exist, most of which require the assumption of linear, all-pole model of the filter. It dates from the time when the computational power of the processing systems was very low. From the 50-s on, many computational effective algorithms have been created. Their complexity is almost an order smaller compared to those, using other models of the filter. In frequency domain the all-pole filter describes very well the processes, for which it has been created. In most of the practical solutions it has became classics, and what follows is his application for other purposes, for which it may be inappropriate. In this paper, some general properties in the application of linear all-pole filter and pulse-source for generating of periodical signal are reviewed. These properties explain some phenomena of the modelled real process and give better interpretation for the constraints, which come out from the implementation of such model.

1 INTRODUCTION

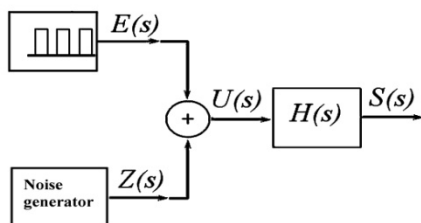A "pulse source – filter" model could be represented as shown on fig.1:

Figure 1: A "pulse source – filter" model.

The observed signal S(s) is defined by the parameters of the filter H(s), excitation pulses E(s) and by the noise Z(s) (Fant G., 1990. In practice statistical methods of autocorrelation and autocovariation are used (Epsy-Willson et.al, 2006, Prasana, S., et.al, 2006). If for sake of clarity we don't take into account the additive input noise, the generation of the signal in z-domain could be written as:

$$S(z) = E(z)H(z) \quad (1)$$

$$S(z) = Z\{s(nT)\}, \; s(nT) = s(t)\big|_{t=nT}$$

Without ignoring the importance of the derived conclusions, we can assume H(z) as a all-pole filter (Titze, 1984):

$$H(z) = \frac{1}{1 + \sum_{i=1}^{M} a_i z^{-i}} \quad (2)$$

The problem of finding the coefficients of the filter $a_i, i = \overline{1,M}$ can be defined as signal analysis. If the input of the filter with transfer function H(z) is a delta impulse, the output will be an envelope of a signal element, modelled with the current filter coefficients. The model of the signal analysis:

$$E(z) = S(z)A(z) \tag{3}$$

uses a filter, inverse with the exciting one, with transfer function:

$$A(z) = \frac{1}{H(z)} = 1 + \sum_{i=1}^{M} a_i z^{-i} \tag{4}$$

Two approaches for finding of the coefficients of the filter are possible – assuming asynchronous excitation, and assuming synchronous one. The first one assumes that the length of the analysed quasistationary intervals is set and known apriory, and the second assumes that the length of the analysed quasistationary intervals is multiple of the of the excitation period.

The method of linear prediction of M-th order (Wiener, 1966) approximates the current value of the signal $s(i)$ from a discrete time series $\{s(i)\}$ with a linear combination of M preceding values with the corresponding weighting coefficients a_i:

$$\hat{s}(n) = \sum_{i=1}^{M} a_i s(n-1) \tag{5}$$

The prediction error is:
$$e(n) = s(n) - \hat{s}(n) \tag{6}$$

For a signal segment, containing N samples, the weighting coefficients can be optimized in such way, that the sum of squares of the errors of prediction for all N samples is minimal. In this case the objective function for the optimization is:

$$\sum_{N} e^2(n) = \tag{7}$$

$$\sum_{N} \left[s(n) - \sum_{i=1}^{M} a_i s(n-i) \right]^2 \stackrel{!}{=} min$$

Setting the partial derivative of the sum of squares equal to zero we have the equation:

$$\sum_{i=1}^{M} a_i \sum_{N} s(n-i)s(n-k) = \tag{8}$$
$$\sum_{N} s(n)s(n-k), k = \overline{1,M}$$

Two common methods, differing in the limits of summation are known: autocorrelation and autocovariation.

The range of summation of the autocorrelation is $-\infty < n < \infty$:

$$\sum_{i=1}^{M} a_i \Phi(|i-k|) = \Phi(k), \qquad k = \overline{1,M} \tag{9}$$

with the coefficients of autocorrelation :

$$\Phi(|i-k|) = \sum_{n=-\infty}^{\infty} s(n-i)s(n-k) \tag{10}$$

The interval to be analysed is actually $0 < n < N$, the samples outside it could be eliminated with an appropriate window function $w(n)$, and the autocorrelation coefficients $R(i)$, can be evaluated as follows:

$$R(i) = \sum_{n=0}^{N-1-i} \zeta(n)\zeta(n+i), \tag{11}$$
$$\zeta(n) = w(n)s(n),$$
$$w(n) = \begin{cases} \neq 0, & 0 \le n < N \\ 0 \end{cases}$$
$$i = \overline{0.M}$$

The equality from the condition for unconditional optimization becomes:

$$\sum_{i=1}^{M} a_i R(|i-k|) = R(k), \qquad k = \overline{1,M} \tag{12}$$

and as a matrix notation:

$$\mathbf{R}(a_1, a_2, ..., a_M)^T = (R(1), R(2), ..., R(M))^T \tag{13}$$

The matrix **R** of the coefficients $R(|i-k|)$ is a *Toeplitz* matrix – it is symmetrical and the elements in the diagonals are identical (Grenader. U. et. al. , 1958) :

$$\mathbf{R} = \begin{pmatrix} R(0) & R(1) & \cdots & R(M-1) \\ R(1) & R(0) & \cdots & R(M-2) \\ R(2) & R(1) & \cdots & R(M-3) \\ \ldots & \ldots & \ldots & \ldots \\ R(M-1) & R(M-2) & \cdots & R(0) \end{pmatrix} \qquad (14)$$

There are a lot of methods for solving the system of equations. The most effective is the recursive method of *Durbin*, where the number of operations grows only with the square of the weighting coefficients (Makhoul, J., 1975).

Because their value is always less than one, the poles of the filter will always be within the unit circle on the z-plane, which guaranties its stability.

When using the covariation, the prediction error is minimized within the interval $0 < n < N$. The matrix of the coefficients in general isn't a *Toepliz* one and the methods for obtaining the filter coefficients aren't so effective (the Cholesky method for example (Werner, H, 1975)) and the stability of the filter isn't guaranteed.

Both the autocorrelation and covariation use the same two steps for evaluating the filter coefficients. – first they find the coefficients matrix, and then solve the system of linear equations (Madisetti V., Williams D, 1999). There are other possible methods, (for example using lattice structures), which combine the two steps. In can be proven (Makhoul, J., 1975) that the most effective method is the one of Durbin, which is the most preferred autocorrelation method.

2 IMPACT OF THE DURATION OF THE EXCITATION PHASE TO THE PERIOD OF THE SPECTRAL PEAK

We assume model of the filter is of order two:

$$H(s) = \frac{k_1 \omega_1^2}{s^2 + \omega_1^2} \qquad (15)$$

This means that the signal will contain only one spectral peak ω_1. If the filter is excited by a sequence of rectangular pulses, described by:

$$\begin{aligned} &e(t) \qquad (16) \\ &= \begin{cases} 1, (m-1)T_g \le t < t_{excitation\_phase} + (m-1)T_g \\ 0, t_{excitation\_phase} + (m-1)T_g \le t < mT_g \end{cases} \\ &\qquad m = \overline{1, N_{tmp} - 1} \end{aligned}$$

Where T_g is the excitation period, and $t_{excitation\_phase}$ is the duration of the excitation phase. The output signal for the first excitation period (m=1) is:

$$\begin{aligned} s_{excitation\_phase}^{1F}(t) &= AO_{excitation\_phase}^{1F} \qquad (17) \\ &- A_{excitation\_phase}^{1F} \sin(\omega_1 t \\ &\qquad + \varphi_{excitation\_phase}^{1F}) \end{aligned}$$

for $t < t_{excitation\_phase}$, i.e. in excitation phase, and:

$$\begin{aligned} s_{free\_vibration}^{1F}(t) &= \qquad (18) \\ A_{free\_vibration}^{1F} \sin(\omega_1 t + \varphi_{free\_vibration}^{1F}) \end{aligned}$$

for $t \ge t_{free\_vibration}$, i.e. in free vibration phase, where:

$AO_{excitation\_phase}^{1F} = k_1$ is the constant component of the signal in the excitation phase

$A_{excitation\_phase}^{1F} = k_1$ and

$A_{free\_vibration}^{1F} = 2k_1 \sin(\frac{\omega_1 t_{excitation\_phase}}{2})$ are the amplitudes of the signal in excitation phase and in the phase of free vibration

$\varphi_{excitation\_phase}^{1F} = \frac{\pi}{2}$ and

$\varphi_{free\_vibration}^{1F} = 2\pi - \frac{\omega_1 t_{excitation\_phase}}{2}$ are the angular phases of the signal in excitation phase and in the phase of free vibration

$\omega_1 = 2\pi f_1$ are the circular frequency, which corresponds to the spectral peak f_1.

We can observe the following:

- The amplitude of the signal in th excitation phase depends only on the gain constant of the filter
- The amplitude of the signal in the phase of free vibration depends again on the gain constant, but also in a complicated way on the ratio of duration of the preceding phase of excitation to the period of the spectral peak.
- The later holds true also for the angular phases.

This means that changes in the duration of the excitation phase can increase or decrease the amplitudes of the spectral peaks , without changing the parameters of the filter. To illustrate this impact, we define a dimensionless coefficient, proportional to the ratio of duration of the excitation phase to the period of the spectral peak :

$$r_{\omega_1 t_{excitation\_phase}} = \omega_1 t_{excitation\_phase} \qquad (19)$$

For the relation of the amplitudes of the signal in the excitation phase and in the phase of free vibration we define the coefficient:

$$r_{A^{1F}_{excitation\_phase} A^{1F}_{free\_vibration}} \tag{20}$$

$$= \frac{A^{1F}_{excitation\_phase}}{A^{1F}_{free\_vibration}}$$

Here $t_{free\_vibration} = T_g - t_{excitation\_phase}$ means the duration of the free vibration phase of one excitation period. The relation between these coefficients is:

$$r_{A^{1F}_{excitation\_phase} A^{1F}_{free\_vibration}} \tag{21}$$

$$= \left| 2\sin\left(\frac{\omega_1 t_{excitation\_phase}}{2}\right) \right|$$

Obviously this relation is periodical, and the first two periods are shown in fig.2
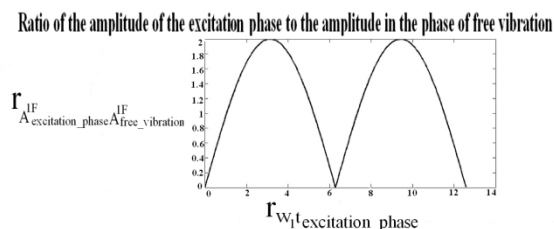
Figure 2: The relation of the amplitude of the generated signal in the excitation phase to the amplitude of the phase of free vibration as function of the coefficient

$$r_{\omega_1 t_{excitation\_phase}}.$$

As one can see, varying the duration of the excitation phase, without changing the filter coefficients, the amplitude of the spectral peak of the generated signal in the free vibration phase can take any value from zero (fig.3) to two times the amplitude in the excitation phase (fig.4).
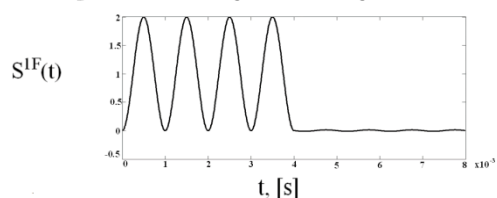
Figure 3: The generated signal in the excitation phase and in the phase of free vibration with

$$r_{\omega_1 t_{excitation\_phase}} = 2\pi n, n = 0, \pm1, \pm2 \dots \text{ and}$$

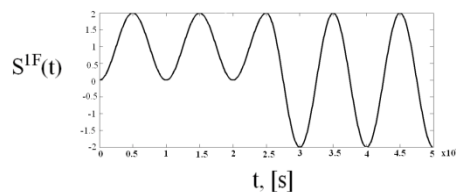$$r_{A^{1F}_{excitation\_phase} A^{1F}_{free\_vibration}} = 0$$

Figure 4: The generated signal in the excitation phase and in the phase of free vibration with

$$r_{\omega_1 t_{excitation\_phase}} = \pi n, n = \pm1, \pm3 \dots \text{ and}$$

$$r_{A^{1F}_{excitation\_phase} A^{1F}_{free\_vibration}} = 2$$

This effect becomes more apparent within a signal segment, containing more than one excitation period. In this case not only the coefficient $r_{\omega_1 t_{excitation\_phase}}$, but also the ratio of the duration of the excitation phase to the excitation period, which is actually the is mark-to-space ratio, will be of importance for the ratio of the amplitudes:

$$k_{full\_imp} = \frac{t_{excitation\_phase}}{T_g} \tag{22}$$

The derived analytical relations lead us to important conclusions. The ratio of the amplitudes of the signal in the excitation phase to the phase of free vibration for the second excitation period is given by the relation:

$$r_{A^{1F}_{excitation\_phase} A^{1F}_{free\_vibration}} \tag{23}$$

$$= \left[4k_1 \sin\left(\frac{r_{\omega_1 t_{excitation\_phase}}}{2}\right) \cos\left(\frac{r_{\omega_1 t_{excitation\_phase}}}{2k_{full_{imp}}}\right) \right]$$

$$\left[\left(k_1 \sin\left(r_{\omega_1 t_{excitation\_phase}} \right) \right. \right.$$

$$+ k_1 \sin\left(2\pi - \frac{r_{\omega_1 t_{excitation\_phase}}}{k_{full_{imp}}} \right) \right)^2$$

$$+ \left(-2k_1 \sin^2\left(\frac{r_{\omega_1 t_{excitation\_phase}}}{2} \right) \right.$$

$$\left. \left. + k_1 \sin\left(\frac{r_{\omega_1 t_{excitation\_phase}}}{k_{full_{imp}}} - \frac{\pi}{2} \right) \right)^2 \right]^{-\frac{1}{2}}$$

The graphical representation of this relation is shown in fig 5.
Obviously for the next periods the calculation of this ratio is getting more and more complicated and

some numerical methods are needed. Nevertheless, the following important observation can be made:
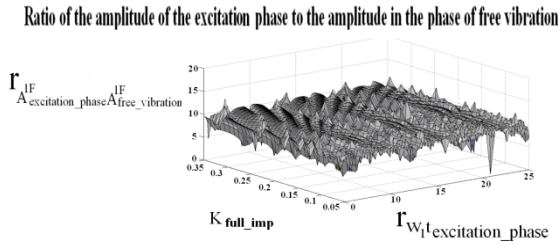

Figure 5: The relation of the amplitudes of the generated signal in the excitation phase to the phase of free vibration for the second excitation period.

Varying the ratio of the duration of the excitation phase to the duration of the period of excitation, and without changing the parameters of the filter, one can generate segments, in which the amplitude of the spectral peak for every following period of excitation increases, decreases, doesn't change considerably, or follows some analytical relation.

3 IMPACT OF THE DURATION OF THE EXCITATION PHASE WITH MORE THAN ONE SPECTRAL PEAK

The way, that the parameters of the excitation change the ratio between the amplitudes of the different spectral peaks in the generated signal, is similar to the one, presented in the previous chapter. We assume, that the we have all-pole filter of fourth order, and the poles all lie of the unit circle:

$$H(s) = \frac{1}{(s^2 + \omega_1^2)(s^2 + \omega_2^2)} \qquad (24)$$

If the excitation of the filter is one rectangular pulse, the output signal will contain two spectral peaks ω_1 and ω_2. If we assume, that $\omega_2 = k_2\omega_1$ and $k_2 > 1$, the components of the signal in the excitation phase are:

$$s^{1F}_{\text{excitation\_phase}}(t) = AO^{1F}_{\text{excitation\_phase}} \qquad (25)$$
$$- A^{1F}_{\text{excitation\_phase}}\sin(\omega_1 t + \varphi^{1F}_{\text{excitation\_phase}})$$

$$s^{2F}_{\text{excitation\_phase}}(t) = AO^{2F}_{\text{excitation\_phase}} \qquad (26)$$

$$- A^{2F}_{\text{excitation\_phase}}\sin(\omega_2 t + \varphi^{2F}_{\text{excitation\_phase}})$$

Where:
$AO^{1F}_{\text{excitation\_phase}} = \frac{1}{(k_2^2-1)\omega_1^4}$ and
$AO^{2F}_{\text{excitation\_phase}} = \frac{1}{-k_2^2(k_2^2-1)\omega_1^4}$ are the constant components of the first and second spectral peaks in the excitation phase
$A^{1F}_{\text{excitation\_phase}} = \frac{1}{(k_2^2-1)\omega_1^4}$ and $A^{2F}_{\text{excitation\_phase}} = \frac{1}{k_2^2(k_2^2-1)\omega_1^4}$ are the amplitudes of the first and second spectral peaks in the excitation phase
$\varphi^{1F}_{\text{excitation\_phase}} = \frac{\pi}{2}$ and $\varphi^{2F}_{\text{excitation\_phase}} = \frac{3\pi}{2}$ are the angular phases of the first and second spectral peaks in the excitation phase
$\omega_1 = 2\pi f_1$ and $\omega_2 = 2\pi f_2$ are the circular frequencies, which correspond to the spectral peaks f_1.and f_2
The signal components in the phase of free vibration are:

$$s^{1F}_{\text{free\_vibration}}(t) = A^{1F}_{\text{free\_vibration}} \qquad (27)$$
$$\sin(\omega_1 t + \varphi^{1F}_{\text{free\_vibration}})$$

$$s^{2F}_{\text{free\_vibration}}(t) = A^{2F}_{\text{free\_vibration}} \qquad (28)$$
$$\sin(\omega_2 t + \varphi^{2F}_{\text{free\_vibration}})$$

Where:
$A^{1F}_{\text{free\_vibration}} = \frac{1}{(k_2^2-1)\omega_1^4}\left|\sin\left(\frac{\omega_1 t_{\text{excitation\_phase}}}{2}\right)\right|$ and
$A^{2F}_{\text{free\_vibration}} = \frac{1}{k_2^2(k_2^2-1)\omega_1^4}\left|\sin\left(\frac{\omega_2 t_{\text{excitation\_phase}}}{2}\right)\right|$
are the amplitudes of the first and second spectral peaks in the free vibration phase
$\varphi^{1F}_{\text{free\_vibration}} = -\frac{\omega_1 t_{\text{excitation\_phase}}}{2}$ is the angular phase of the first spectral peak in the free vibration phase
if $4l\pi \le \omega_1 t_{\text{excitation\_phase}} < (4l+2)\pi$ and
$\varphi^{1F}_{\text{free\_vibration}} = \frac{\pi}{2} - \frac{\omega_1 t_{\text{excitation\_phase}}}{2}$
if $(4l+2)\pi \le \omega_1 t_{\text{excitation}_{\text{phase}}} < (4l+4)\pi$
$\varphi^{2F}_{\text{free\_vibration}} = -\frac{\omega_2 t_{\text{excitation\_phase}}}{2}$ is the angular phase of the second spectral peak in the free vibration phase
if $4l\pi \le \omega_2 t_{\text{excitation\_phase}} < (4l+2)\pi$ and
$\varphi^{2F}_{\text{free\_vibration}} = \frac{\pi}{2} - \frac{\omega_2 t_{\text{excitation\_phase}}}{2}$
if $(4l+4)\pi \le \omega_2 t_{\text{excitation}_{\text{phase}}} < (4l+4)\pi$
$$l = \pm1, \pm2 \dots$$
$\omega_1 = 2\pi f_1$ and $\omega_2 = 2\pi f_2$ are the circular frequencies, which correspond to the spectral peaks f_1.and f_2

As with the case with one spectral peak, we may expect that the dimensionless coefficients, proportional to the ratio of the duration of the excitation phase to the period of the spectral peak will have big influence on the parameters of the signal components in the phase of free vibration:

$$r_{\omega_1 t_{\text{excitation\_phase}}} = \omega_1 t_{\text{excitation\_phase}} \text{ and} \quad (29)$$
$$r_{\omega_2 t_{\text{excitation\_phase}}} = \omega_2 t_{\text{excitation\_phase}} = k_2 \omega_1 t_{\text{excitation\_phase}}$$

This can be represented with the dimensionless coefficient of the ratio of the amplitudes of the two spectral peaks in the signal

$$r_{A^{2F} A^{1F}} = \frac{A^{2F}}{A^{1F}} \quad (30)$$

In the excitation phase this coefficient will depend only on the filter parameters:

$$r_{A^{2F}_{\text{excitation\_phase}} A^{1F}_{\text{excitation\_phase}}} = \frac{1}{k_2^2} \quad (31)$$

In the free vibration phase, this ratio will depend of the filter parameters, but also in a complicated manner on the duration of the excitation phase:

$$r_{A^{2F}_{\text{free\_vibration}} A^{1F}_{\text{free\_vibration}}} \quad (32)$$
$$= \frac{1}{k_2^2} \left| \frac{\sin\left(\frac{k_2 r_{\omega_1 t_{\text{excitation\_phase}}}}{2}\right)}{\sin\left(\frac{r_{\omega_1 t_{\text{excitation\_phase}}}}{2}\right)} \right|$$

This means, that the change of the duration of the excitation phase can substantially change the predetermined from filter parameters constellation of spectral peaks in the signal. This influence can be easily seen from the next numerical example, with typical for a real speech signal values of the filter parameters (Damyanov D., Galabov V., 2012):

- First spectral peak $f_1 = 420\ Hz$;
- Second spectral peak $f_2 = 966\ Hz$; which means $k_2 = \frac{f_2}{f_1} = 2.3$;
- Nominal duration of the excitation phase $t_{\text{excitation\_phase}} = 2.8\ ms$;
- Fluctuation of the nominal duration of the excitation phase $\Delta t_{\text{exitation\_phase}} = \pm 0.4\ ms$;

In the excitation phase the ratio of the amplitudes depends only on the filter parameters:

$$r_{A^{2F}_{\text{excitation\_phase}} A^{1F}_{\text{excitation\_phase}}} \quad (33)$$
$$= \frac{A^{2F}_{\text{excitation\_phase}}}{A^{1F}_{\text{excitation\_phase}}} = k_2^{-2} \approx 0.189$$

In the phase of free vibration with nominal duration of the $t_{\text{excitation\_phase}} = 2.8\ ms$; this coefficient will be $r_{A^{2F}_{\text{excitation\_phase}} A^{1F}_{\text{excitation\_phase}}} \approx 0.288$. If the duration of the excitation phase is shortened with 4 ms, the coefficient will increase more than 20 times to $r_{A^{2F}_{\text{free\_vibration}} A^{1F}_{\text{free\_vibration}}} \approx 6.33$, and if the duration of the excitation phase is lengthened with 4ms, the coefficient will decrease more than 20 times to $r_{A^{2F}_{\text{free\_vibration}} A^{1F}_{\text{free\_vibration}}} \approx 0.061$. On fig.6 for the three cases the excitation rectangular pulse with duration, equal to the duration of the excitation phase, the generated signal and its spectra are shown.
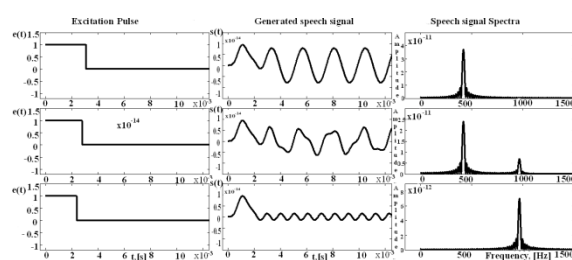

Figure 6: The three cases the excitation rectangular pulse with duration, equal to the duration of the excitation phase, the generated signal and its spectra.

4 CONCLUSIONS

When dealing with periodical and quasiperiodical processes, the "source-filter" model allows simplification of analysis and parameterization and makes the technical implementation easier. This facilitations can be achieved when filter and excitation source are treated independent. In this case for the parameterization of the filter very efficient techniques and methods can be used. This approach gives excellent results in most cases of use of the model – in systems for analysis, synthesis, coding and transmission of speech signals and others. In some cases this description is not relevant enough and additional complicated methods and information sources must be used. This paper shows that the model can be made more effective without further complications, using the cumulative effect of

simultaneous treatment of the processes, which happen on the source and the filter.

ACKNOWLEDGEMENTS

REFERENCES

Damyanov, D., Galabov, V., 2012, On the impact of duration of the phase of open glottis of the spectral characteristics if the phination process, *Proceedings of the Technical Universicty- Sofia Volume 62, Issue 2, 2012, pp. 173-180, ISSN 1311-0829*

Epsy-Willson, C., Manocha, S., Vishnubholta, S., 2006, A new set of features of text independent speaker identification. *In Proc Inter-speech 2006 (ICSLP), Pittsburgh, Pennsylvaniq, USA, September 2006 pp. 1475-1478*

Fant, G., 1990, *Acoustic Theory of Speech Production*, Mouton&Co, Hauge

Granader, U., G. Szego, 1958, *Toeplitz Form and Their Applications*, Berekeley CA, University of Californiq Press, 1958

Madisetti V, Williams D., 1999, *Digital Signal Processing Handbook*, New York, CRC Press, 1999

Makhoul, J, 1975, Linear Prediction: A tutorial Review, *Proceedings of the IEEE, vol. 63 1975, pp 561-580*

Prasana, S., Gupta, C., Yenganarayana, B., 2006, Extraction of speaker specific excitation information from linear prediction residual of speech. Speech Comm. 48, pp. 1243-1261

Titze, Ingo R., 1984, Parameterization of the glottal area, glottal flow and the vocal fold contract area, *JASA, 75(2), February, 1984, pp. 570-580*

Werner, H., 1975, *Praktische Mathematik, Bd. 1*, Berlin Spinger, 1975

Wiener, N., 1966, *Extrapolation Interpolation and Smoothing of Stationary Time Series*, M.I.T. Press. Cambridge, MA, 1966

DEVELOPMENT OF ORIGINAL OPTICAL AND QUANTUM ELECTRONICS DEVICES FOR APPLICATIONS IN COMMUNICATIONS, METROLOGY AND SCIENCES

Hristo Kisov, Margarita Deneva, Elena Stoykova, Marin Nenchev

Technical University of Sofia, Branch Plovdiv, Bulgaria
mdeneva@yahoo.com

Abstract: The goal of the report is to present the development – principles, theories and computer simulations, experiments and practical realizations, of original and competitive methods, elements and devices for quantum electronics, optical communications, metrology, remote sensing and sciences: multi-channel WDM system with independent tuning of each input/output, multi-wavelength laser with independent control of each wavelength, lasers with emission, spectrally fixed at reference atomic absorption line, injection-locking laser system for high ($\sim 10^6$-10^8) and linear amplification of low-power ($\sim \mu W$, nW) modulated laser light, optical analogue of the transistor action – optical transistor, system for remote (up to kilometres) measurement of small (mm) translational elongation – shrinking of objects, new solution of tunable sub-nanosecond lasers and lasers with rectangular nanosecond (~ 1 ns) pulse emission, including controlled duration and tunable wavelength. The basic element of the devices developed is stable and compact interference wedged structures in new composite solution with very narrow transmission (≤ 0.01 nm) in relatively large spectral range (≥ 1 nm). The laser active media used are solid-state, semiconductor and dye.

1 INTRODUCTION

The report is a review of our recent results, concerning the further development of original quantum electronics and optical devices with a potential for competitive applications in optical communications, metrology, scientific work, and atmospheric pollution monitoring. The aim of the report is to present as a whole complex our last achievements in the development – experiments, theories, and practical realizations of an original WDM system with independent tuning of each input and output, system for remote (to kilometres) measurement of small (mm) translational elongation - shrinking of objects, optical transistor, multi-wavelength lasers with independent control of each wavelength and with wavelength emission in single beam or in closely parallel or coaxial beams, the new solution of tunable sub-nanosecond lasers, the lasers with emission, spectrally fixed at reference atomic

absorption line. The basic elements, used and studied by us are a wedged interference structure (variation of the Fizeau Wedge), including some researched of found by us new properties. The essential part of the results is obtained in our group at the Technical University of Sofia, Branch Plovdiv and the University CNAM-Paris, the University of North Paris and the University "Sent Quentin" – Versailles, France. The principal authors' publications from the last years, where the discussed here results are given in details, are the firs 13 articles, given in the References at the end of the paper. The authors of the report, that are the main co-authors of the noted works, have selected and systematized the materials; also the essential part is based on their propositions – primarily given in their patents and previous articles followed the noted firs ones, except the last well known laser book [Svelto,1998]. The report includes also completely new, non-published results. The articles of the other authors, related with the subject of the presentation, are given as citation in the noted

authors' publications. Following the actual authors' professional activity, the report concerns mainly the technical aspects of the problems. Nevertheless, the necessary physical moments to clarify the principle of the developed methods and devices are also given shortly.

The general objective of the work is to establish these new and effective devices in science and practice as novel components of the main hardware basis in the indicated areas. In parallell, new knowledge in the field of quantum electronics and optical interferometry is obtained. The envisaged solutions have encountered their preliminary positive approbation firstly in the working laboratory models as well as in the cited below recent publications in the specialized journals.

2 NEW ELEMENTS AND DEVICES IN ACTUAL DEVELOPMENT

2.1 Original optical elements based on wedged interference structures and their applications

Furstly, we will present the further development and examine thoroughly the original optical elements and system for noted in the introduction applications. Proposed devices are based on the use of the wedged interference structure of Fizeau type Interferometer - Interference Wedge (IW). The development include ideas, experiments, theory and proposed applications developed by us. It is applicable in the case of limited diameter beam illumination [Nenchev, 1982; Stoykova, 2010; Nenchev, 1993; Stoykova, 1993; Deneva, 2007; Deneva, 1996]. The new proposition, except our previosly introduced new optical element based on a Reflecting Interference Wedge [Nenchev, 1982], includes a new WDM (wavelength division multiplexing) element with an important property allowing spectral tuning of inputs/outputs in the simplest manner. The importance of WDM structures for the optical communications is undisputable and is described in the most popular textbooks. Also, we describe the new system with IW for remote (meters, kilometers) measurement of the translational expansion and shrinking of objects.

The principle of our proposed WDM structure can be clarified with the Figures given below. The interference wedge (IW) of thickness of the order of micrometers plays the role of a spectrally selective

filter and a channel coupler, being a near totally reflecting mirror for the non-resonant wavelengths. The new, generalizing theoretical and experimental physical treatment of the IW is described in our cited papers [Stoykova 2010; Nenchev 1993; Stoykova 1996].

The Fizeau interferometer or interferential wedge (IW) consists of two reflecting plane surfaces separated by a gap with linearly increasing thickness. A low-reflectivity coated wedge has been used before us as un effective tool in surface topography, as a high-resolution broadband wave-meter. Multiple-beam interference in IW has been addressed for implementation of phase-shifting Fizeau interference microscopy. As a rule, theoretical and experimental analysis of the IW properties by the other authors were conducted mainly for the case of infinite plane-wave illumination assuming an extended wedged structure; different wedge applications have been also analyzed for this particular case. Inspired by IW incorporation in laser design, over the recent years we focused our efforts on the study of compact wedged interference structures under illumination with a narrow light beam of small diameter. We have succeeded to reveal unique properties of the IW when illuminated with laser light, and to propose various applications, thus insuring the IW as a competitive optical element in laser resonator design [Deneva, 2007; Louyer, 2003; Stoykova, 1996; Goris-Neveux, 1995]. A high-reflectivity coating IW with thickness of tens of millimetres has spectral resolution comparable to that of the Fabry-Perot interferometer, but at additional advantage of linear spectral tuning by means of translation in its plane. Such IW, with apex angle of 5–100 μrad and thickness of 5–500 μm has been used by us in laser resonators technique to create two-channel resonators with independently controlled characteristics of the produced two-wavelength emission, as a spectrally selective reflecting or transmitting optical element of resonant wavelength easily adjustable by translation of the interferometer. Selective wedge transmission and reflection has been used for continuous tuning of the selected mode in high-purity single mode lasers, unidirectional lasing in ring resonators, two-wavelength laser operation, narrow line selection and tuning of wide-gain lasers.

A simple and effective solution of a multi-wavelength spectrally selective resonant structure for two-wavelength lasers with independent tuning at each wavelength has been proposed by the authors [Nenchev, 1981; Deneva, 2007; Louyer, 2003,

Gorris-Neveux, 1995]. It makes the use of valuable optical features of the IWs. In particular, we advanced a reflecting IW as a completely new laser spectral selector. The proposed structure has been patented and successfully applied in multi-wavelength laser technology for dye, Ti:Sapphire Yb:YAG, and semiconductor lasers.
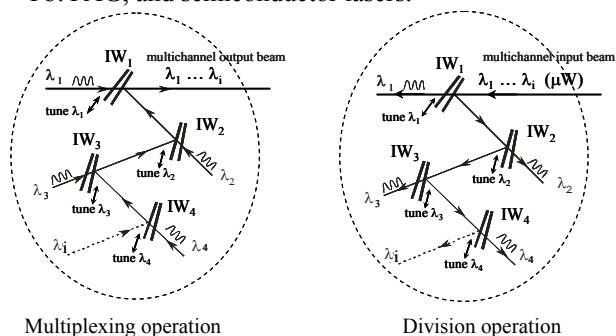

Figure 1. Schematic presentation of new WDM structure.

Generally speaking, it could be considered as a new and competitive solution of a WDM element for optical communications.

The high-reflectivity coatings IW of thickness of 5-300 μm acts simultaneously as a spectrally selective filter and a channel coupler, being a nearly totally reflecting mirror for the off-resonant wavelengths. In addition, tuning of the transmission maxima is provided by simple translation of the IW in its plane. Figure 1 represents schematically the operation of the proposed new WDM structure for the cases of multi-wavelength input or output beam. The tuning of each output by translation of the corresponding IW in its plane does not affect the geometry of the structure and the characteristics of the other outputs respectively. Also, as it is clear from the figure, the structure gives the possibility to obtain superposition of individual beams which have passed through each IW, thus serving as a multi-beam multiplexing element for the spectrally different beams (each of them being a resonant beam for the corresponding IW and off-resonant beam for the other IWs).

Analysis of the WDM element requires first to analyze the behaviour of a separate IW for laser (coherent) beam illumination.

We adopted the mathematical model for computer simulation and developed an adequate description of transmittance and reflection of the IW for a limited diameter laser (coherent) beam (~1-1.5 mm). [Nenchev, 1993; Stoykova, 2010] Thus, our treatment differs essentially from the plane-wave illumination approach.

The detailed calculations are given in our works [Stoikova, 2010; Nenchev, 1993; Stoykova, 2001].

The calculations were made for two types of interference wedges. The first one is a "sandwich type" IW, formed by sequential layer-by-layer deposition of a dielectric reflective coating of reflectivity 0.9 on both sides of the glass plate, which represents a wedged transparent layer with optical thickness of 5 μm. The other type of the IW is the silica wedge with optical thickness of 300 μm having dielectric layers on both surfaces of equal reflectivity of 0.9 in a spectral region of ~ 30 nm around the wavelength of 630 nm. The apex angle of both wedges is α = 0.05 mrad. The described IWs, which are of essential interest as high-resolution spectral selective elements, are simple for production and use. The "sandwich type" IW is very convenient for application in the new WDM structure due to its compactness.

A typical curve, calculated for illumination with a CW laser Gaussian beam in the region of its flat front (flat-concave resonator, near the flat output mirror), is shown in Figure 2. We see that the IW is a highly transmissive narrow-line filter for the resonant wavelength and approximately totally reflecting mirror for the off-resonant wavelength.
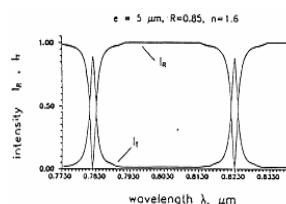

Figure 2. Calculated transmission and reflection curves as a function of the wavelength for a "sandwich"-type IW (CW laser beam illumination).

As a second step, we have studied wedge behavior for illumination with short laser pulses, including the sub-nanosecond light pulses. The calculations are made at different wavelengths near ~ 0.6 μm. The obtained results are similar to those in the case of CW beam illumination.
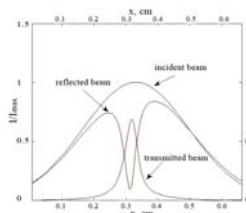

Figure 3. Transmission and reflection for pulse illumination (0.5 ns pulse duration); e=5 μm.

Figure 3 gives the typical computed curves for the "sandwich type" IW irradiated with pulses of duration of 0.5 ns (the axis x in Figure 3 gives the distance along the beam impact area from an arbitrary chosen zero-point) [Nenchev, 2011].

As it can be seen from the depicted curves, the transmission and reflection properties of the wedge do not change essentially. Transmission reaches about 60 % for the pulse duration of ~ 0.1 ns that may correspond to frequency repetition rate of ~ 10 GHz. Therefore, the presented calculation shows feasibility of the proposed WDM structure.

We realized experimentally our WDM structure for the case of CW beam illumination using a laboratory model of free-communication system. We formed a single laser beam by exact superposition of the emissions of three CW lasers – two He-Ne lasers emitting at 0.63 μm and at 0.59 μm respectively and the frequency doubled Nd:YAG laser (0.53 μm). The beam diameter was ~ 1 mm. Figure 4(a) presents the WDM structure, composed of 3 "sandwich type" wedges with thickness $e = 5$ μm, each of them tuned to one of the wavelengths in the green, yellow and red spectral regions, respectively.
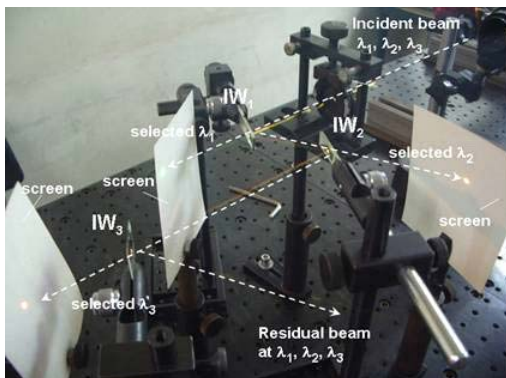

Figure 4(a). The experimental set-up presents the realized WDM device, composed of 3 wedges, each of them to a separate channel – green, yellow and red, respectively.
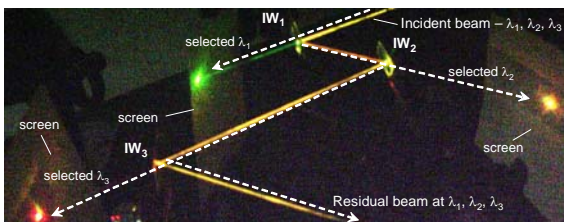

Figure 4(b). Visualization of the channel-separation (colors) by the new WDM-arrangement in the laboratory model

As it is shown in Figure 4(b) by using smoke visualization and screens, wavelengths separation has been achieved. By translation of the wedges, we can independently tune the resonance and the given output. The laboratory WDM is shown in Figure 5.
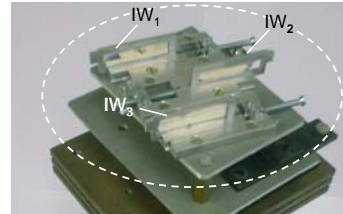

Figure 5. Realization of the compact working experimental model of the proposed WDM structure

The calculation shows the same type of dependences for the silica gap IW with optical thickness of 300 μm (Figure 6(a)) .

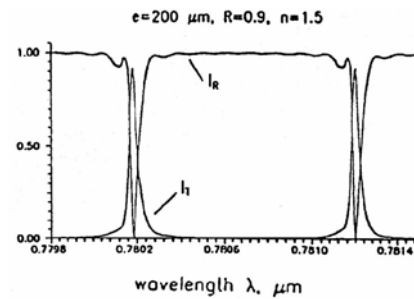
Figure 6(a). Calculated curves as in Figure 3, but for thick silica-gap 200 μm IW.

The essential advantage of this silica gap thick IW is the higher spectral resolution in comparison with the "sandwich type" structure whose thickness is technologically limited to few μm, and respectively does not permit to obtain a transmission line low than few part of nanometers. However, there is the problem related of obtaining a selection by the standard IW structure of a narrow line in combination with high separation between the resonant lines (Figure 6(a)). The calculations show that there are completely similar dependence between the width of the selected line $\delta\lambda$ and the spectral distance $\Delta\lambda$ between the lines as this one for FPI - e.g. $\delta\lambda = \Delta\lambda/F$, where F is the fines factor, depending on R. Thus the desired low value of $\delta\lambda$ leads to low value of $\Delta\lambda$. This limits the selectivity of the channels in optical communication system.

The principle of our solution of this problem is based on the use of composite wedged interference structure. It can be understood from Figure 6(b) where is given schematically one example of composed two-component structure.
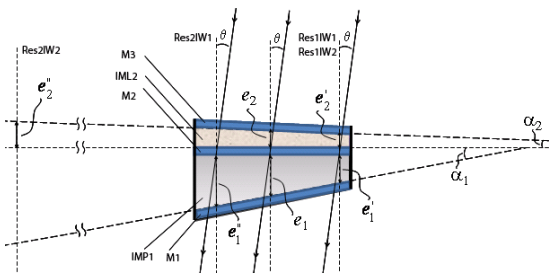
Figure 6(b). Schematic of the new composite wedged interference structure.

It consists of one thick wedge e.g. e_1=200 µm optical thickness silica glass wedge with two dielectric mirrors at each wedge plane with reflectivity of R=0.95%. The wedge angle α_1 of the plate in the example is α_1= 200 µrad. On the one of the mirrors is lay a transparent wedged layer with thickness e_2=10 µm and wedge angle α_2. The relatively simple calculations give that if the angle α_1 and thickness e_1, and the angle α_2 and the thickness e_2 are chosen to be in the relation

$$\alpha_2 = \alpha_1 . e_2 / e_1$$

the change of the resonant maximums of both connected wedges with the translation of the composite system in its plane is exactly equal. In this system the thick wedge gives a very low spectral width of the transmission of all system (~0.05 nm) and the thin wedge selects only single resonance of the thick wedge at high spectral range (~ 15 nm and higher). Typical example of computer calculated resonances at the described system is given in Figure 6(c).
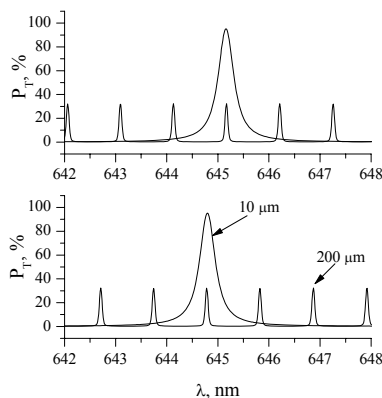

Figure 6(c). Computed transmission of the composite wedged structure, formed by two IW (10 µm and 200 µm) with convenient wedge angles and the tuning (see the text)

As a second task, we have proposed new and attractive utilization of the IW specific properties by designing devices, which allow distant (from few meters to millimeters) laser measurement of small (~mm) linear translation of a rigid object.

The principle of our device can be understood from Figure 7, which shows as an example - measurement of small linear stretching of a steel hammer-beam due to change of the IW transmission resonance in the beam incident point.

The set-up contains a comparative system of one beam-splitter and two photo-receivers. One of them records that part of the emitted beam, which forms reference intensity and the other one records the light transmitted by the IW. Due to translation of the IW, the transmitted light decreases. By tuning the laser, we can obtain new resonant wavelength, λ_2, corresponding to the new wedge thickness. Indication for this is the new peak in the transmitted light that is recorded by the corresponding receiver. From λ_1 and λ_2 it is easy to calculate the translation distance Δx, of the invar plate. Figure 8 proves the high sensitivity of the proposed method. For high precision measurements of translations in sub-millimeter region, a single-mode semiconductor, Titanium Sapphire or dye lasers can be used.
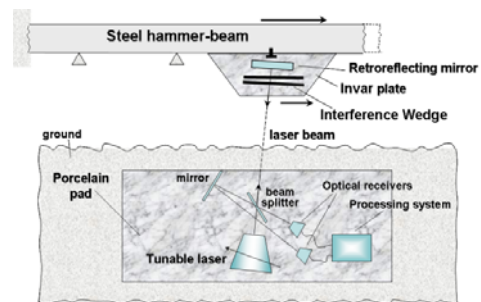

Figure 7. Device based on IW for distant measurement of small translation of a rigid object in its plane.
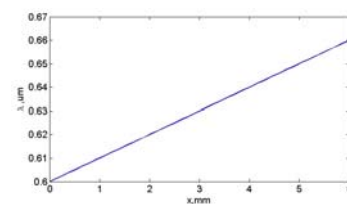

Figure 8. Calculated dependence of the resonance wavelength at different points along the IW.

For the case of remote (meters, kilometers) measurement of the translational stretching - contraction of objects the second type of system, which is other variant of the idea, discussed above, is developed. This system eliminates the increasing of the diameter of the laser beam due to the natural divergence, also the fluctuation of the illuminated intensity and the need of exact beam direction on

the Interference Wedge (which is a small dimension element). The action of the system is clarified from given Figure 9. Here, we introduce an Ulbricht sphere and lens, as it is shown in Figure 9, to eliminate the noted above problems for remote measurement at long distance. The radio-transmitter system or reflection of modulated by information about translation part of the incident light transmit the two signals in the processing system. Thus, we obtain the correct relative value of the transmitted signal, what eliminate the influences of the beam intensity fluctuations and the incident place of laser-beam cross-section, illuminating the lens.
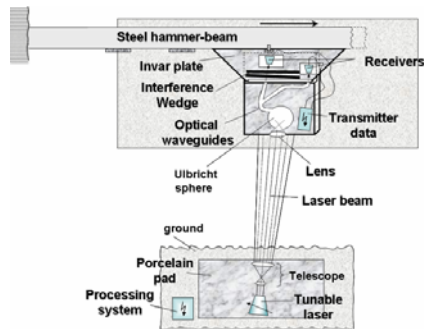

Figure 9. Device for remote (kilometers) measurement of small translations of a rigid object in its plane that uses IW and Ulbricht sphere.

The developed laser-Interference wedge devices can be of interest to control the metal or concrete hammer-beam length variation (with the temperature or earthquake) of bridges, of platforms for oil extraction in the sea, of walls of the buildings etc.

2.2. Original multi-wavelength lasers with independent control of each wavelength using the WDM structures developed in 2.1.

An important goal is the achievement of two- and multi-wavelength generation of nano- and sub-nanosecond pulses with implementation of our group's original methodology as well as development of multi wavelength generators of the same type based on semiconductor active media [Nenchev, 1995].

Our group has substantial expertise in the development of two-wavelength lasers [Deneva, 2010; Louyer, 2003; Slavov, 1998, Gorris-Neveux, 1995; Nenchev, 1981]. Using our original approach we were the first in the world to develop with the corresponding theoretical and experimental

background two-wavelength F-centers, Ti-Sapphire (in pulsed mode) and Yb:YAG lasers, (in a CW diode pumped mode) – [Loyer, 2003; Goris Neveux, 1995]). The laser solutions are based on our proposed effective multichannel resonator with a complex selector-coupler structure based of IWs [Nenchev, 1981]. Using the described above multi-channel WDM element new and simple solution of multi-wavelength lasers are proposed with independent tuning of each wavelength. Two types of solution are given in Figure 10(a) and 10(b). The scheme in Figure 10(a) is solution in which the emission of the two wavelengths is in single laser output beam. For many cases where single volume needs to be illuminated exactly (e.g. in remote atmosphere pollution control) and high speed processes (e.g. explosion) this solution is advantageous. The difficulty for multi-wavelength operation is related to strong wavelength competition effects in homogeneously broadened active medium – e.g. dye, semiconductors. It follows that it is necessary to make a very precise balance for net gain for all wavelengths at each tuning or strongly limit the tuning range around the gain maximum – in its flat part. The second scheme with closely spaced parallel beams at each wavelength – in Figure 10(b) - eliminates the problem of competition, however the laser light at the separated wavelengths acts upon different parts of the illuminated volume (superposition can be obtained after focusing in small length of ~ mm).
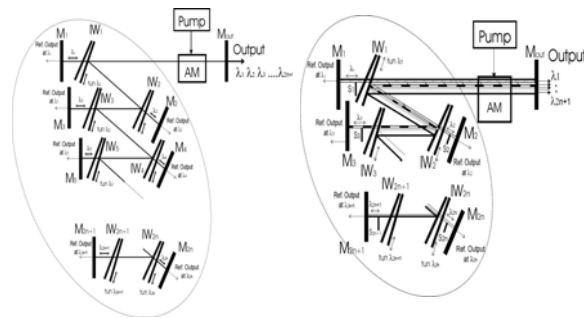

Figure10. WDM multi-wavelength laser resonator schemes with independent tuning at each wavelength; (a) –with output in single beam, (b) – with closely parallel outputs.

Except the previously realized, used and described in the specialized literature dye, Ti-Sapphire, F-colour centres and Yb:YAG lasers, in our recent works we have practically developed a two-wavelength semiconductor laser. The laser emits at two independently tunable wavelengths in a single beam. To obtain a small diameter of the

incident beam at the selected IWs, we modified the scheme in Figure 10(a) using the focussing and the flat end mirrors as it is shown in the Figure 11. We have realised (Figure 12) such two-wavelength semiconductor laser using a red laser diode with antireflection coated output surface. The laser
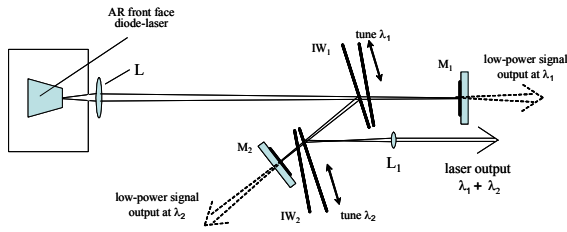

Figure 11. Schematic diagram of the modified resonator, given in Figure 10(a) and adapted for two-wavelength generation with independent tuning of each wavelength in large beam semiconductor active media.

operates successfully at two wavelengths. As a rule the lasing starts firstly in one of the channels. To obtain also lasing in the other channel we slowly increased the losses for the started generation, in practice by misalignment of the end mirror in its channel. This can be obtained if the wavelength is spectrally near the maximum of the gain. At each tuning of one wavelength it was necessary to arrange again the losses at the generated channel to obtain the lasing also at the second wavelength. In this manner tuning range of ~ 4 nm for each wavelength in two-wavelength operation can be achieved. By oscilloscope studies we found that both wavelengths are generated simultaneously. This laser can be useful in some experimental works needed in two-wavelength operation. Our next work is related to realization of the second, wavelength competition less, scheme given in Figure 10(b). The new solution is combined with passive self-injection [Keller, 2000] what abruptly increases the laser efficiency.
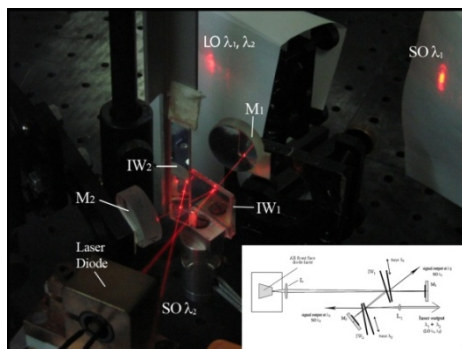

Figure 12. Photograph of the operating two-wavelength semiconductor red laser. The generation is at two wavelengths λ_1 and λ_2 in separated reference outputs and in main, common output.

2.3 Actual our development of a high-power two-wavelength wavelengths competition-less Nd:YAG laser

Earlier [Nenchev, 1978], we have patented a flashlamp pumped laser where single active element operates in two parts separately and at two different wavelength. Actually, we have developed this technique using single, flash-lamp pumped ($\sim$150 J pump) Nd:YAG crystal to obtain simultaneous or in controlled manner generation at two chosen lasing
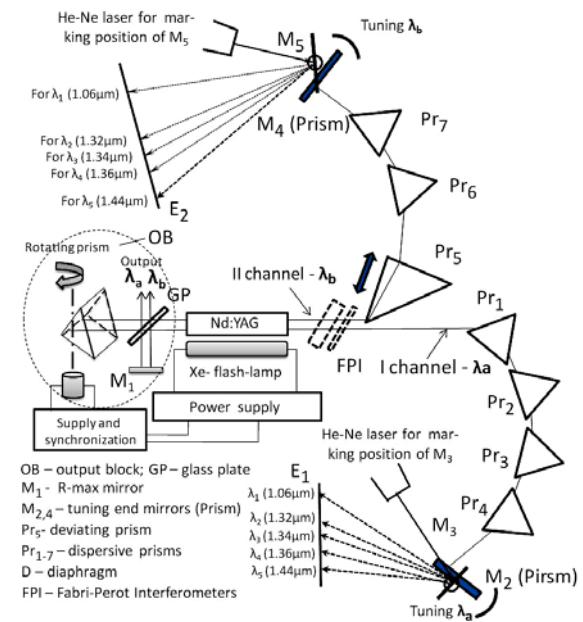

Figure 13(a). Schematic of the two-wavelength, flashlamp pumped, Q-switched, laser that uses two separate parts of a single Nd:YAG crystal and prisms selective structure.

lines - pair-combination from the possible generating lines: 1.06 μm (to 0.8 J), 1.32 μm, 1.34 μm, 1.36 μm (to $\sim$ 0.14 J) and 1.44 μm (to $\sim$0.03 mJ, none well reproducible) and avoiding the limiting wavelength-competition effect. The laser (Figure 13(a)) can also operate at two chosen modes at different frequency distance from the standard for single cavity lasers (c/2L). We use the generations in two separate parts of the single, flashlamp pumped Nd:YAG crystal in two manner: i) in coaxial separation and ii) in two closely spaced parts by prism selected-tuning resonators (for the single-mode case with introduced glass-plate Fabry-Perot interferometers).

The design of this laser was developed both theoretically and with practical realization, both for free lasing and Q-switched regime. To generate any

desired pair of the given lines we employ a rotated prism (axis in the plane or perpendicular) Q-switcher that is completely non-sensitive of the different wavelengths. The scheme of experimental realization of the described two-line and two-mode laser is shown in Figure 13. The typical oscilloscope traces of simultaneous generation at two markedly different lines – 1.06 μm and 1.36 μm, obtained for conveniently chosen parameters of both resonators and lasing volumes are shown in Figure 13(b).
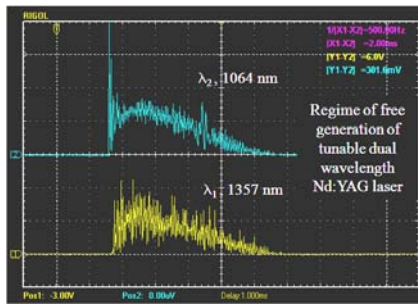

Figure 13(b). Simultaneous generation at 1.06 μm and 1.36 μm in free-running regime (for conveniently chosen parameters).

For the theoretical study we have adapted the rate differential equations system [Svelto, 1998] to obtain the optimal conditions for desired operation.

The theoretical considerations show the possibility to control the energy, time length of the pulses and delay between them, including also the possibility for simultaneous Q-switching operation - by conveniently chosen resonator parameters and parts of the lasing volumes. The experimental results are in agreement with the theory. As example in Figure 14 are presented the oscilloscope traces of Q-switched generation at the 1.06 μm and 1.36 μm (outputs ~1 MW).
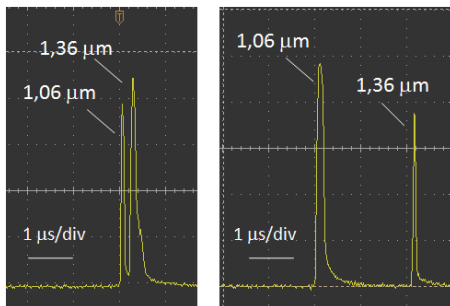

Figure 14. Experimental curves of temporal tuning of two wavelengths (the existence of a combination of parameters permitting simultaneous generation can be seen)

Note, that our rotating prism Q-switcher is very convenient for described operation due to its completely independence of the wavelength and its simplicity of operation.

The advantages of a developed laser in comparison with the system of two separated and coupled Nd:YAG lasers are: i) simple construction ii) essentially low cost and iii) increased efficiency due to the pumping of single active road

Such line-tunable and two-wavelength laser devices are of interest for applications in metrology, wavelength testing and study of non-linear effects in optical fibre, remote sensing and scientific works.

2.4 Generation of sub-nanosecond pulses implementing the original methodology with two-channel WDM-system based optical resonator

In detail, the original approach for realizing sub-nanosecond tunable laser is presented in our paper [Deneva, 2007]. The essence of the principle is to restrict the starting pulse-like generation with sub-nanosecond pulsations (~0.1 – 0.2 ns, "spikes") to single pulsation by using an active mirror, which forces damping the competitive generation in the second selective channel. Theoretical analysis and experimental test showed the improvement of the shape and shortening the duration of the sub-nanosecond pulse by using our technique in comparison with known methods. The principle is clarified by the scheme shown in Figure 15. The typical pulses obtained by known techniques for separation of a single spike (Figure 16, left) and by our proposed technique (Figure 16, right) demonstrate the advantage of our approach.
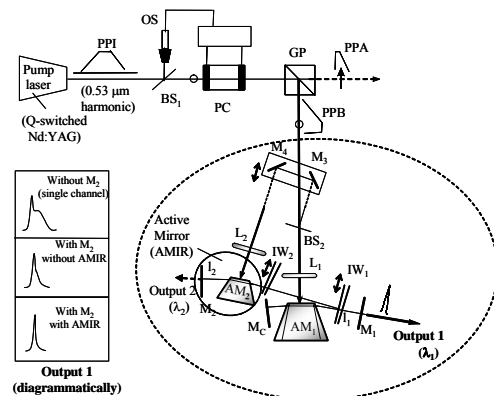

Figure 15. Set-up for selection of a single sub-nanosecond pulsation by active mirror in two-cannel cavity.
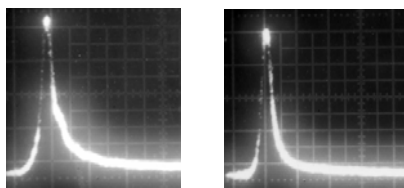
Figure 16. Typical oscilloscope traces (5 ns/div) of the optimized selected spike: left – for the known technique of competitive resonators and right- for our proposed AMIR- approach. Full confirmation of improvement of the selection by our predicted theoretical approach.

The generated sub-nanosecond pulses are of interest for testing system in optical communications, in systems for distance measurements, in scientific works and in remote sensing.

3 DEVELOPMENT OF LASERS WITH FIXED EMISSION FREQUENCY AT REFERENCE ATOMIC ABSORPTION LINE

A simple, all-optical technique for producing pulsed semiconductor laser light, spectrally narrowed and fixed at a chosen absorption atomic line, is realized and studied by us [Deneva, 2010]. The technique, which is not of laser locking type, is based on utilization of a conventional diode laser without any impact on its operation. For its implementation the diode laser output is fed to a modified Michelson interferometer, and controllable disturbing of phase and amplitude correlation between the interfering beams in the two arms of the interferometer is achieved by frequency scanning through a contour of reference absorption line of substance, introduced in one of the interferometer arms. Imbalance is produced by the absorption and the refractive index changes throughout the contour of the absorption line. The control of the imbalance is realized by variation of the optical path length of the other arm of the interferometer through an appropriate tilting of a glass plate introduced in this arm.

We have shown both by theory and experiment that under properly chosen conditions the spectrum of the obtained light partially overlaps the atomic line and has linewidth, comparable to the width of the absorption transition.

The set-up is given in Figure 16. A commercial single longitudinal mode pulsed diode laser (DBR type, model SDL-5702-H1) with emission line width of about 100 MHz was used as a light source. The wavelength of the selected mode of the diode laser

was repetitively scanned (forward -backward) within ± 10 GHz (~ 0.0210 nm) around the 852.1 nm Cs absorption line ($6S_{1/2}$-$6P_{3/2}$ transition - a single absorption line within the scanned frequency region. The scanning was accomplished by the pump current modulation within ± 5 mA around 44.3 mA. The line width of the chosen Cs-transition was $\approx$ 0.92 GHz (0.0019 nm, FWHM). The diode temperature was kept at 17.9^{o}C with accuracy of $\pm 0.1^{o}$C. The diode laser beam, after passing through an optical isolation system (Faraday Isolator or a combination of a polarizer and a quarter-wave plate, as shown in Figure 16), impinged the entrance beam-splitter of a modified Michelson interferometer composed of the beam-splitter and wedged full reflecting dielectric mirrors M_1 and M_2. The beams reflected from M_1 and M_2 interfered at the beam splitter and formed the useful interferometer output (Output 1 in Figure 17).

A cell with atomic Cs vapour at room temperature (22°C) was introduced to assure reference line in the first interferometer's arm between the beam-splitter and the mirror M_1 (at 852.1 nm Cs line).

If the wavelength of the selected mode remained outside the absorption line during the scanning of the diode driving current, the interference conditions did not change, and the Output 1 did not exist. Figure 18 shows the signals from the diodes PhD_1 and PhD_2; curve A corresponds to the Michelson interferometer Output 1 whereas the curve B depicts the signal from the diode PhD_2 (inverse polarity) that gives the absorption by the Cs line in the external reference Cs cell.
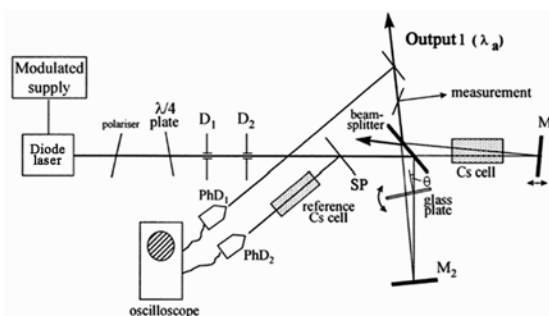

Figure 17. Experimental set-up for producing diode laser light spectrally fixed at the Cs absorption line.

When the laser diode wavelength fell into the contour of the chosen absorption line, the variation of the refractive index and the absorption changed the interference conditions. Thus the destructive interference was terminated and interferometer Output 1 appeared.

For the optimized conditions (Figure 18(c)), achieved by appropriate declination of the glass plate), the locked line is practically a single line with line width (~1.7 GHz, or 0.0035 nm) that is comparable to the absorption line width (0.9 GHz, 0.0019 nm) and overlaps the absorption by approximately 45%. The Output 1 is ~ 2 mW for ~10 mW laser diode emitted power. The performance is completely reproducible ($\sim$ hours).

The theory is in satisfactory agreement with the experiment and confirms the possibility of such kind of diode laser light generation.

The reported technique can be useful in a variety of spectroscopic applications when the target is a single transition which should be excited to monitor or separate a particular substance from a mixture of different substances.
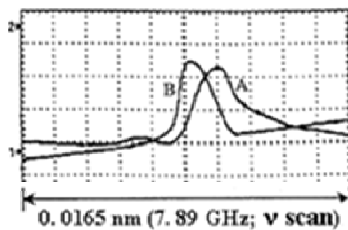

Figure 18. Spectrograms of the laser diode light emitted from Output 1 (curve A) and of the reference Cs cell (curve B; inverted signal). The exciting current is scanned.

Another simple system of spectral locking of the laser emission at the reference absorption line is also developed [Deneva, 2005; Gacheva, 2008]. Its principle is based on the disturbance of the competition between two injection-controlled generations in a two-channel resonator or two amplifications in single active medium. The injected light before the injection in one of the cannels or the amplifier input passes through a substance with the desired absorption line. This solution is clarified from the applied Figure 19.
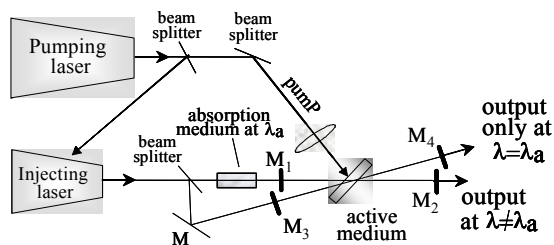

Figure 19. Frequency locking set-up.

The principle of our injection-locking technique is theoretically and experimentally demonstrated in our previous works [Keller, 2000; Slavov, 1998].

4 PRINCIPLE OF NEW INJECTION-LOCKING LINEAR AMPLIFIER OF AMPLITUDE MODULATED LASER LIGHT

At this point, we describe our principle of new injection-locking amplifier of amplitude modulated laser light using counter injection in a ring laser configuration. The last development includes the multichannel information laser light amplification (of the order of $\sim 10^6$ and more – from μW to W) with high linearity of the amplification. To amplify the injected in ring laser modulated laser light (simplest practical arrangement of the amplifier) we introduce counter-injection that compete with the modulated light and compel the amplification to follow exactly the modulation. The principle is clear from Figure 20 [Deneva, 1999].
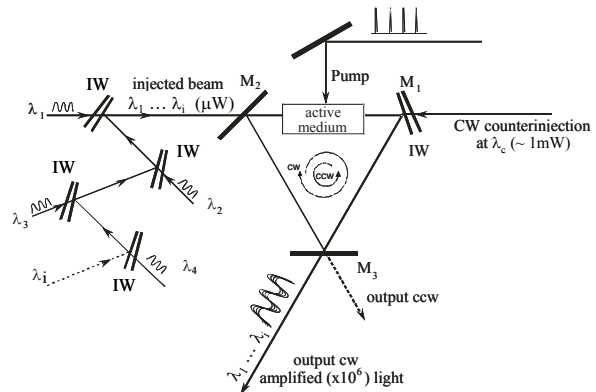

Figure 20. A new system for linear amplification based on injection–locking technique with counter- injection for linearization of the amplification (possibility – kW output power, $\sim 10^6$- 10^7 gain for injected modulated light of power $\sim$ mW and μW)

We describe the action of the new ring counter-injection amplifier for the case of multichannel (at 5 wavelength channels) modulated laser beam amplification by adapting the rate of differential equations, adding the members that describe modulated injection and counter-injection.

Figure 21 gives typical calculation for single sine modulated wave. We have shown the ability of our amplifier to amplify simultaneously and linearly a number of injected beams with different frequency in a large range of $\sim$ 800 GHz. The nonlinear distortions, defined by the harmonics relative power are less than 1 %. Such amplification is possible in very wide range of $\sim$ 2400 GHz. The calculated

curves of amplification for 4 wavelengths (communication channels) are shown in Figure 22.
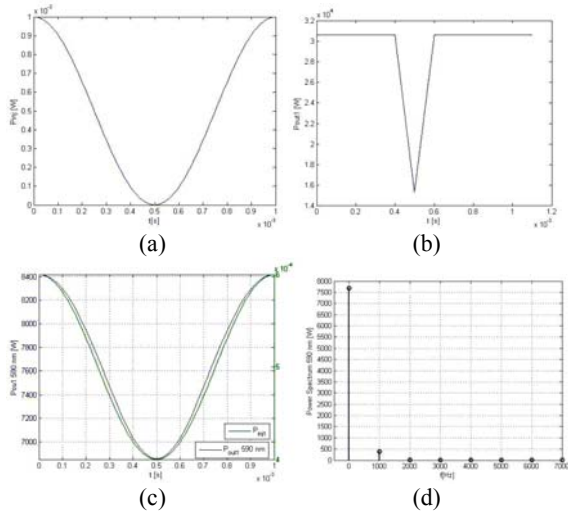

(a) (b)

(c) (d)

Figure 21. Example of operation of our ring-amplifier. (a) input signal, (b) and (c) – amplification without and with counter-injection, (d) Fourier spectrum of the (c).
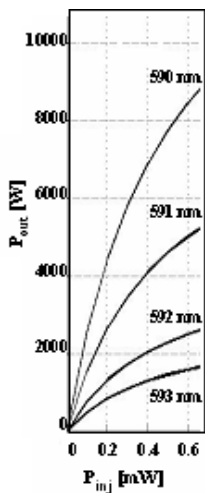

Figure. 22. The curves of simultaneous amplification of 4 injected lines in the presence of counter-injection (~1mW). It can be seen that the amplification is practically linear for injected power variation between 0.01mW and ~ 0.3mW. The amplification factor is ~ 10^5.

5 DEVELOPMENT OF OPTICAL TRANSISTOR

The new interferometer type device for light control by light (DLCL) uses on one hand the high sensitivity of the Fabry-Perot Interferometer (FPI) or IW to the losses in the interferometer's gap [Deneva, 2004]. Our original idea is to use the possibility to illuminate chosen volumes of the edge of interferometer's or wedge's gap in two quite different manners: i) through the interferometer mirrors (beam A- as shown in the figure); ii) directly into the gap (beam B). If the gap is full with saturable absorption medium and the mirrors are high reflective – e.g. 0.92–0.99, the beam A will affect the saturable absorber transmission only by transmitted small part through the mirror and respectively the FPI transmission will be drastically low for this beam. When the beam B illuminates directly the saturable absorber the effect of this illumination is very strong (no decreasing the illuminated light intensity by the mirror). Thus, with the low power beam B we can control in efficient manner (or to open and stop) the FPI or IW transmissivity for beam A. One first application of the new optical transistor will be to forms rectangular nano- and sub-nanosecond pulses as it can be understand from the Figure 23.
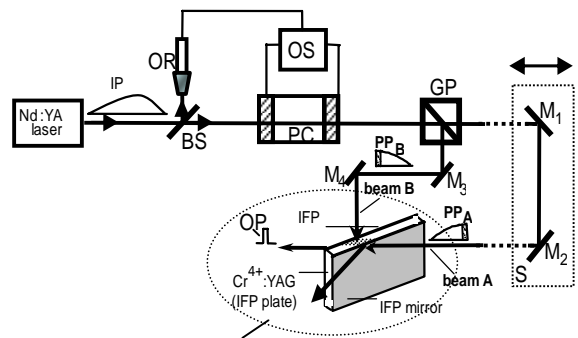

Figure 23. Schematic diagram of a Cr^{4+}:YAG- DCLC and of the experimental set-up for forming controlled duration rectangular laser light pulse. OR – optical receiver-synchronizer, PC-Pockel's cell, GP-Glan Prism, M_1,M_2-high reflectivity mirrors. The high speed switching PC (~ 1-2 ns), activated near the maximum of the input ~ 30 ns pulse, switches the polarization and the GP forms two spatially separated pulses that act in the described manner upon the Cr^{4+} gap FPI or IW.

Table 1: Example of transmissivity of new DLCL for Cr^{4+}:YAG as a saturable absorber [Nenchev, 2011]. The parameters of the DLCL are given in the table.

R of the mirrors	IFP or IW Thickness, mm	Illuminating beam energy density J/cm²	Controlling beam energy dens. J/cm²	T %
0.99	0.4	0.5 (0.5)	0 (0.1|)	3(8.6)
0.99	0.2	0.5 (0.5)	0 (0.1|	3(21)
0..99	0.1	0.5 (0.5)	0 (0.1)	9(40)
0.92	2.65	0.5 (0.5)	0 (0.1)	9(40)
0..52	20	0.5 (0.5)	0 (0.1)	1(10)

ACKNOWLEDGEMENTS

REFERENCES

(Principal authors' articles, used in the presentation; the used non-authors' articles are cited therein)

Stoykova E., Nenchev M., 2010. Gaussian Beam Interaction with Air-gap Fizeau. *Journal of the Optical Sociaty of America–JOSA A*, Vol.27, 58–68.

Deneva M., Stoykova E., Nenchev M., Barbe R., Keller J.C., 2010. Diode laser emission, spectrally fixed at atomic absorption line, *Optics&Laser Technology*, Vol.42, 301-307.

Deneva M., Uzunova P., Nenchev M., 2007. Tunable subnanosecond laser pulse operation using an active mirror concept, *Opt. Quant. Electron.,* Vol.39, 93-212.

Louyer Y., Wallerand J., Himbert M., Deneva M., Nenchev M., Two-wavelength passive self-injection controlled operation of diode-dumped cw Yb-doped crystal lasers, 2003, *Appl.Opt.*, Vol. 42, 4301-4315.

Slavov D., Nenchev M., 2001. A comparative study of approaches for spectral control of Ti:Sapphire lasers. *Optics Communications,* Vol.200/1-6, 283-301.

Delev A., Deneva M., Nenchev M., Stoykova E., Slavov D., 2001. Tunable subnanosecond pulse generation in a dye laser using overlapped pump pulses. *Rev. Sci. Instrum.*, Vol.72, N°3, 164- 168, USA

Keller J.C., Barbe R., Deneva M., Nenchev M., 2000. Unidirectional ring Ti³⁺:Sapphire laser generation at the wavelength of an atomic absorption line by bidirectional passive self-injection locking. *Applied Phys. Letters,* 76, 131-133.

Nenchev M., 1978. Multicolor laser, *Bul.pat. IIR,* No25954 (Bulgaria).

Slavov D., Deneva M., Stoykova E., Nenchev M., Barbe R., Keller J.C., 1998. Output control of a ring laser using bi-directional injection: a new approach for unidirectional generation at a reference atomic absorption line. *Optics Communications*.157,343 -351.

Stoykova E., Nenchev M., 2001. Strong optical asymmetry of an interference wedge with unequal reflectivity mirror and its use in unidirectional ring laser oscillator-amplifier system. *Applied Optics,* 40, 5402-5412.

Nenchev M., 1981. Tunable two-wavelength laser, *Bulg. Pat.* No 32703 (Bulgaria); Nenchev M., 1986. Two wavelength laser oscillator, *Bulg. Paent,.* No73793 (Bulgaria)

Stoykova E., Nenchev M., 1996. Reflection and transmission of unequal mirrors interference wedge, *Opt. Quantum. Electron.* 27, 155-167.

Deneva M., Stoykova E., Nenchev M., 1996. A novel technique for a narrow-line selection and wideband tuning of Ti³⁺:Sapphire and dye lasers, *Rev. Sci. Instrum.* 1705-1714.

Gorris-Neveux M., Nenchev M., Barbe R., Keller J.C., 1995. A two-wavelength, passively self-injection locked, cw Ti³⁺:Sapphire laser. *IEEE J. Quantum Electron.* 31, 1263-1260.

Nenchev M., Stoykova E., 1993. Interference wedge properties relevant to laser applications: transmission and reflection of the restricted light beams, *Opt. Quantum Electron.* 26, 789-799.

Stoykova E., Nenchev M., 1994. Strong optical asymmetry of an interference wedge with unequal mirrors and its use in unidirectional ring laser designs. *Opt Lett.* 19, 1925-1927.

Meyer Y., Nenchev M., 1984. Optical Selector Devices Using a Fizeu Wedge for Reflection. *US Patent* No4, 468, 775, USA

Deneva M., Nenchev M., 2004. Development and application of a new device for light control by light (optical transistor). *"Electronics-ET'04, International Conference,* book 1, 181-185, ISBN 954-438-445-6, Bulgaria.

Nenchev M., 1995. Device for forming of laser pulse, *Bul.pat. IIR,*No49797 (Bulgaria).

Nenchev M. N., Meyer Y.H., Continuous Scanning System for Single-Mode Wedge Dye Lasers, 1982. *Opt Lett. 7,* 199-200.

Gizrekht A., Kebedjiev A., Nenchev M., Peshev Z., Pestriakov E., 1989. Two wavelength emission from Ti³⁺:Sapphire crystal laser. *Sov. J. Quant. Electron.,*19, 1305-1306.

Deneva M., Nenchev M., 2005. Development of original simple quantum electronic devices with emission passively frequency locked at atomic absorption line. *"Electronics-ET'05", International Conference*, 186-193, Book 2, ISBN 954438185, Bulgaria; Method and device for laser pulse shortening, *Bulg. Patent* No 35164/1995, Bulgaria.

Gacheva L., Deneva M., Kalbanov M., Nenchev M., 2008. Development of original all-optical injection control competition and gain knock-down technique for laser line fixing at atomic absorption line. *Inern. Confer. "Electronics ET'2008".* 135-142, Bulgaria.

Deneva M., Nenchev M., 1999. Injection-locked linear amplifiers of a periodically modulated linear radiation using competitive second injection. *LTL Plovdiv'99, International Symposium*, 87-94, Bulgaria.

Nenchev M., Deneva M., Recent results in the development of original quantum electronics and optical devices for applictions in communictions and metrology, *J. Technical University of Plovdiv*, 2011. Vol.16, book 1, 27-42, Bulgaria.

Svelto O., *Principle of lasers*, 1998. Plenum, New York, 4-th edn.

GENERALIZED NET MODEL FOR TELECOMMUNICATION PROCESSES IN TELECARE SERVICES

Velin Andonov, Todor Stojanov, Krassimir Atanassov

Dept. of Bioinformatics and Mathematical Modelling Inst. of Biophysics and Biomedical Engineering,
Bulgarian Academy of Sciences Acad. G. Bonchev Str., Block 105, Sofia-1113, Bulgaria
velin_andonov@yahoo.com, todor@clbme.bas.bg, krat@bas.bg

Peter Kovachev

National Institute of Geophysics, Geodesy and Geography,
Bulgarian Academy of Sciences, Acad. G. Bonchev Str., Block 3, Sofia-1113, Bulgaria
pkov@abv.bg

words: telecare services, generalized nets.

Abstract: In (Andonov et al., 2012) a Generalized Net (see (Atanassov, 2003, 2007)) model of processes, related to tracking the changes in health status of adult patients has been presented. The contemporary state-of-the-art of the telecommunications and navigation technologies allow this model to be extended to the case of active and mobile patient. This enforces the inclusion of patient's current location as a new and significant variable of the model. Various opportunities are considered for the retrieval of this information, with a focus on the optimal ones, and a refined Generalized Net model is proposedt.

.

1   INTRODUCTION

Let us take a look into life sensors attached to a person's body and one other type of sensors.The sensors can be divided into two main groups. The first group is the group of the stationary sensors. They   are placed in the rooms to monitor for CO, CO_2 concentration, temperature and other parameters which can endanger one's life. These types of sensors are patient independent and can work autonomously. They are connected to the server with internet connection (WiFi or LAN).Their alarm events in most of the cases are True positive, can be recognized and a decision can be easily taken.

The second type of sensors are looking for biomedical parameters e.g. ECG signal, SPO2. They collect the biomedical signals, analyze them and consequently   take the most expected decision. Alarm message is sent sent to the server and, if necessary,   part of untypical biomedical signal or parameter value. The server can send requests to the sensor to confirm the alarm event or resend biomedical signal or parameter. In these sensors we can have the False positive event. For this reason the server has to have very smart filter for False positive removing or translate the alarm event to human operator if the case is complicated.

The second type of sensors can work with a cheap smart module for connecting to the GSM network.   Because this network allows more flexibility and the patient is free to go wherever he wants. These sensors can make communication to smart   phone   by   Bluetooth   or   direct   cable communication. Nowadays, the existing GSM network has enough speed and possibility for data translation via e.g. network type 3G and 4G too. Also these GSM modules can have the GPS module.

This GPS module is necessary in case that the medical center has to localize the person in urgent cases such as earthquake, fires, etc. The smart module can send the GPS coordinates to the rescue center for easy localization of the person or persons.

In order to carry out the connection between GSM networks, the sensor should have a GSM module or a smart module. Another requirement to prevent connection break is that the GSM module

has to be connected to at least two networks available or a WiFi network connection should be accessible.

2   LOCATION TECHNOLOGIES

There are three most commonly used location technologies: stand-alone (typical stand-alone technology is dead reckoning), satellite-based and terrestrial radio-based.

2.1 Satellite-based Systems

Global Navigation Satellite System (GNSS) are systems of satellites that provide autonomous geo-spatial positioning with global coverage. Only the United States NAVSTAR Global Positioning System (GPS) (Hofmann-Wellenhof) and the Russian GLONASS are fully globally operational GNSSs.

Satellite navigation systems that provide enhanced accuracy and integrity monitoring usable for civil navigation are classified as follows: the combination of existing satellite navigation systems (GPS and GLONASS), with Satellite Based Augmentation Systems (SBAS) or Ground Based Augmentation Systems (GBAS) (2010 FEDERAL RADIONAVIGATION PLAN). In the United States, the satellite based component is the Wide Area Augmentation System (WAAS), in Europe it is the European Geostationary Navigation Overlay Service (EGNOS) (Gauthier,2001; Filip, 2001), and in Japan it is the Multi-Functional Satellite Augmentation System (MSAS). Ground based augmentation is provided by systems like the Local Area Augmentation System (LAAS).

2.2 GPS Receivers

There are three types of GPS receivers which are available in today's marketplace. Each of the three types offers different levels of accuracy. To this point, the discussion in this paper has focused on Coarse Acquisition (C/A code) GPS receivers. The two remaining types of GPS receiver are Carrier Phase receivers and Dual Frequency receivers. C/A Code receivers typically provide 1-5 meter GPS position accuracy with differential corrections (Filip, №5/2001). C/A Code GPS receivers provide a sufficient degree of accuracy to make them useful in most GIS and emergency applications. A *GPS tracking unit* is a device that uses the Global Positioning System to determine the precise location of a vehicle, person, to which it is attached and to record the position of the asset at regular intervals. The recorded location data can be stored within the tracking unit, or it may be transmitted to a central location data base, or internet-connected computer, using a cellular, radio, or satellite modem embedded in the unit. This allows the asset's location to be displayed against a map backdrop either in real time or when analyzing the track later, using GPS tracking software http://www.liveviewgps.com/. GPS personal tracking devices assist in the care of the elderly and vulnerable. Devices allow users to call for assistance and optionally allow designated carers to locate the user's position, typically within 5 to 10 meters. Their use helps promote independent living and social inclusion for the elderly. Devices often incorporate either 1-way or 2-way voice communication which is activated by pressing a button. Some devices also allow the user to call several phone numbers using pre-programmed speed dial buttons. GPS personal tracking devices are used in several countries to help in monitoring people with early stage of dementia and Alzheimer http://www.eurogps.eu/bg/world-news/tracking/99-gps-tracking-alzheimer.

2.3 Positioning in 3G Networks

- Mobile-based technologies: Cell-ID, time advance;
- Network-based technologies: TDOA (time difference of arrival), AOA (angle of arrival);
- Mobile-assisted technologies: A-GPS (assisted GPS), AFLT (advanced forward link trilateration), E-OTD (enhanced observed time difference), U-TDOA;

These technologies typically use base stations, satellites or devices emitting radio signals to the mobile receiver to determine the position of its user. Signals can also be emitted from the mobile device to the base. Commonly studied techniques are angle of arrival (AOA) positioning, time of arrival (TOA) positioning, and time difference of arrival (TDOA) positioning. All these methods require radio transmitters, receivers, or transceivers. To determine the location, these methods generally have the assumption that one end of the positioning system is fixed and the other end is moveable such as a mobile phone. However, the location determination capability can be either at the fixed end or at the mobile end. For performance improvement, hybridmethods (various combinations of the techniques) are possible (Overview of 2G LCS

Technnologies and Standards, London, UK, January 2001).

Other methods based based on measuring the signal strength or measuring the signal characteristic patterns and multipath characteristics of radio signals arriving at a cell site from a caller. For measuring the signal strength, it employs multiple cell sites to find the location. For measuring the signal characteristic patterns, it identifies the unique radio frequency pattern or "signature" of the call and matches it to a similar pattern stored in its central database (Shu Wang, Jungwon Min, Byung K. Yi, 2008; Y. Zhao, 2000).

TOA and TDOA are time-based measurement technologies. They can be implemented either based on the forward (down) link signal or reserved (up) link signal. In addition, the location determination capability can reside either at the network side or at the mobile phone. In order to locate several base stations or cell sites, the sensitivity of the mobile phone may need to be increased. These methods also require software modification on the mobile phone and additional location determination units and related software in the network. As discussed above, the mobile phone needs to listen to the signals of at least three base stations or cell sites. The visibility and geographical locations of these base stations will affect the availability and the accuracy of the location determination (Overview of 2G LCS Technnologies and Standards, London, UK, January 2001).

The performance of the satellite-based GPS receiver is getting better and better while the receiver size and price keep going down. To develop an assisted GPS (A-GPS) solution for the mobile phone requires software and hardware modifications of both the mobile phone and its communications network.

The A-GPS use a GPS reference network (or a wide-area DGPS network) whose receivers have clear views of the sky and can operate continuously. This reference network is also connected with the cellular infrastructure, and continuously monitors the real-time constellation status and provides precise data such as satellite visibility, ephemeris and clock correction, Doppler, and even the pseudorandom noise code phase for each satellite at a particular epoch time. At the request of the mobile phone or location-based application, the assist data derived from the GPS reference network are transmitted to the mobile phone GPS receiver (or sensor) to aid fast start-up and to increase the sensor sensitivity. Acquisition time is reduced because the Doppler versus code phase uncertainty space is much smaller than in conventional GPS due to the fact that the search space has been predicted by the reference receiver and network. This allows for

rapid search speed and for a much narrower signal search bandwidth which enhances sensitivity. Once the embedded GPS receiver acquires the available satellite signals, the pseudorange measurements can be delivered to network-based position determination entity (PDE) for position calculation or used internally to compute position in the handset.

Additional assisted data, such as DGPS corrections, approximate handset location or cell base station (BS) location, and other information such as the satellite almanac, ionospheric delay, universal time coordinated (UTC) offset can be transmitted to improve the location accuracy, decrease acquisition time, and allow for handset-based position computation. Several schemes have been proposed in the standards which reduce the number of bits necessary to be exchanged between the handset and the network by using compression techniques such as transmitting only the non-redundant or the changes to parameters instead of the raw parameters themselves. Other satellite systems could be used, such as the Russian GLONASS system, but none of the standards have made provision for anything except GPS and the GPS Wide Area Augmentation System (WAAS) signals. Besides adding a GPS reference network and additional location determination units in the network, the mobile phone must embed, at a minimum, a GPS antenna and RF down converter circuits, as well as make provision for some form of digital signal processing software or dedicated hardware (Overview of 2G LCS Technnologies and Standards, London, UK, January 2001). All the radio-based technologies discussed can be affected by interference, blockage, and multipath.

3. GENERALIZED NET MODEL

In our model, we consider n patients. The i-th patient has i_k different sensors. The sensors for the i-th patient are represented by the tokens $\delta_{i,1}$, $\delta_{i,2}$, ... ,$\delta_{i,ik}$. The tokens $\delta_{i,1}$, $\delta_{i,2}$, ... ,$\delta_{i,ik}$ enter the net in place l_2 with initial characteristics:

"name of the patient; sensor's parameters"

The criterion for the correctness of the signal detected by the sensors is represented by the token α which stays permanently in place l_7 with initial characteristic:

"criterion for the corectness of the signal"

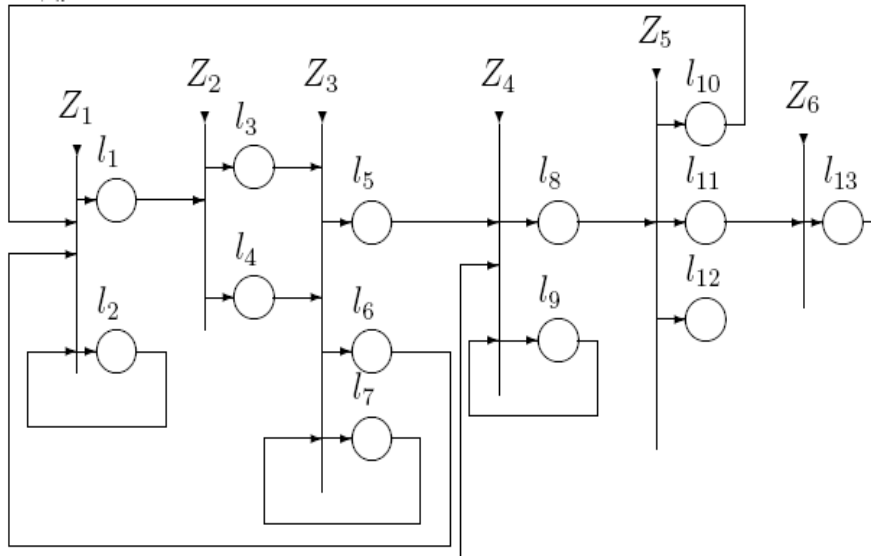The tokens $d_{i,1}$, $d_{i,2}$, ... ,$d_{i,ik}$ stay permanently in

Figure 1: Generalized Net

place l_9 with initial characteristic:

"name of the patient; previously recorded sensor
data and respective action taken"

We use the tokens $d_{i,j}$ to keep record of the sensor's data which can be used in future to decide whether the patient should be sent to a medical doctor.

Below is a formal description of the transitions of the net.

$$Z_1 = <\{l_1, l_6, l_{10}\}, \{l_1, l_2\}, \quad \begin{array}{c|cc} & l_1 & l_2 \\ \hline l_2 & W_{2,1} & W_{2,2} \\ l_6 & \text{false} & \text{true} \\ l_{10} & \text{false} & \text{true} \end{array} >,$$

where
$W_{2,1} = $ "the sensor detected the patient's body signals",
$W_{2,2} = \neg W_{2,1}$,
where $\neg P$ is the negation of the predicate P.

When the truth-value of the predicate $W_{2,1} =$true the token $\delta_{i,j}$ enters place l_1 with characteristic:

"signal of the sensor about the current patient"

When the truth-value of the predicate $W_{2,2} =$true the token $\delta_{i,j}$ enters place l_2 without a new characteristic.

$$Z_2 = <\{l_1\}, \{l_3, l_4\}, \quad \begin{array}{c|cc} & l_3 & l_4 \\ \hline l_1 & W_{1,3} & W_{1,4} \end{array} >,$$

where
$W_{1,3} = $ "the signal comes from a stationary sensor",
$W_{1,4} = \neg W_{1,3}$.

When the truth-value of the predicate $W_{1,3} =$true the token $\delta_{i,j}$ enters place l_3 and does not obtain any new characteristic. When the truth-value of the predicate $W_{1,4} =$true the token $\delta_{i,j}$ enters place l_4.

$$Z_3 = <\{l_3, l_4, l_7\}, \{l_5, l_6, l_7\}, \quad \begin{array}{c|ccc} & l_5 & l_6 & l_7 \\ \hline l_3 & \text{true} & \text{false} & \text{false} \\ l_4 & W_{4,5} & W_{4,6} & \text{false} \\ l_7 & \text{false} & \text{false} & \text{true} \end{array} >,$$

where
$W_{4,5} = $ "the criterion shows that the signal of the sensor is correct and it must be further evaluated whether a medical doctor's reaction is necessary",
$W_{4,6} = $ "the criterion shows that the current signal must be confirmed".

When the current $\delta_{i,j}$ token enters places l_5 or l_6 it does not obtain any new characteristics.

$$Z_4 = <\{l_5, l_9, l_{13}\}, \{l_8, l_9\}, \quad \begin{array}{c|cc} & l_8 & l_9 \\ \hline l_5 & \text{true} & \text{false} \\ l_9 & \text{false} & \text{true} \\ l_{13} & \text{false} & \text{true} \end{array} \quad >,$$

When the current $\delta_{i,j}$ token enters place l_8 it obtains the characteristics of the respective $d_{i,j}$ token. In place l_9 the token $d_{i,j}$ obtains as characteristic the signal parameters of the respective $\delta_{i,j}$ token and the decision that has been made. In place l_{13} the current $\delta_{i,j}$ token splits into two tokens, the original $\delta_{i,j}$ token which continues to stay in place l_{13} and a new token $d'_{i,j}$ with the same characteristics which enters place l_9. and it unites there with the respective $d_{i,j}$ token.

$$Z_5 = <\{l_8\}, \{l_{10}, l_{11,} l_{12}\}, \quad \begin{array}{c|ccc} & l_{10} & l_{11} & l_{12} \\ \hline l_3 & W_{8,10} & W_{8,11} & W_{8,12} \end{array} \quad >,$$

where

$W_{8,10}$="the history shows that the signal should be confirmed",

$W_{8,11}$= "there is no similar sensor data in the history or the history suggests that the patient should be sent to a medical doctor"

$W_{8,12}$= "the history suggests that no action should be taken",

$$Z_6 = <\{l_{11}\}, \{l_{13}\}, \quad \begin{array}{c|c} & l_{13} \\ \hline l_{11} & \text{true} \end{array} \quad >,$$

When the current $\delta_{i,j}$ token enters place l_{13} it obtains the characteristic:

"send the patient to a medical doctor"

REFERENCES

Andonov, V., et al. Generalized Net Model for Telecare Services, IEEE Conf. "Intelligent Systems"< Sofia, 6-8 Sept. 2012 (in press).

Atanassov, K. Generalized nets, World Scientific, Singapore, 1991.

Atanassov, K., On Generalized Nets Theory, "Prof. Marin Drinov" Publishing House of the Bulgarian Academy of Sciences, 2007.

Hofmann-Wellenhof, B., Lichtenegger, H., GPS Theory and Practice, ISBN 3-211-82839-7 4th d. Springer-Verlag Wien New York

2010 Federal Radionavigation Plan, Published by Department of Defense, Department of Homeland Security, and Department of Transportation, This document is available to the public through the National Technical Information Service, Springfield, Virginia 22161DOT-VNTSC-RITA-08-02/DoD 4650.05

Gauthier, L., P. Michel, J. Ventura-Traveset, J. Benedicto. EGNOS: The First Step in Europe's Contribution to the Global Navigation Satellite System. *ESA bulletin* 105 February 2001, p. 35-42

Filip, A., H. Mocek, L. Bazant. GPS/GNSS Based Train Positioning for Safety Critical Application. *Signal+Draht*, (93) №5/2001, p. 51-55

Filip, A., H. Mocek, L. Bazant. GPS/GNSS Based Train Positioning for Safety Critical Application. *Signal+Draht*, (93) №5/2001, p. 51-55

3GPP TSG SA2 LCS Workshop LCS-010019, Overview of 2G LCS Technnologies and Standards, London, UK, January 2001, 11 – 12, Source: Motorola, Inc.

Location Based Services (LBS) for mobiles: Technologies and Standards – WCNC/ICC 2008, Shu Wang, Jungwon Min, Byung K. Yi, LG Electronics Mobile Research, USA

Zhao, Y., "Mobile Phone Location Determination and Its Impact on Intelligent Transportation Systems", IEEE Transactions on Intelligent Transportation Systems, vol. 1, no. 1, pp. 55-64, Mar. 2000.

CONSISTENT DATA AND DECISION FUSION OF HETEROGENEOUS INFORMATION DENOISING IN COMPLEX SYSTEMS DIAGNOSIS

Mincho Hadjiski

Institute of Information and Communication Technologies – BAS;
University of Chemical Technology and Metallurgy,
hadjiski@uctm.edu

Lyubka Doukovska

Institute of Information and Communication Technologies – BAS
l.doukovska@mail.bg

Abstract: In the diagnosis of complex industrial systems arise a lot of sever problems to solve due to the heterogeneous information sources, a large number of directly unmeasurable variables, which should be replaced by softsensing, big uncertainty of current information, temporal uncoherency of some measurements because of the very different requirements for the spectral window of corresponding signals in the different stages of the FDD (Fault Detection and Diagnosis) procedure. In the paper a hybrid approach of multistep procedure is considered for denoising of diagnostic information in order to achieve more realistic and more effective decision in a comparison with the conventional statistical approaches using some techniques from the Computational Intelligence like Neural Networks and Case- Based Reasoning. The main statements accepted in this investigation are: the different stages of complex diagnosis could require different information, different methods of partial diagnosis and different methods of decision making; the main method of hybridization is accepted to be consistent data and decision fusion; signal processing in particular diagnosis stages should be relevant to the main diagnostic goals in the stage. In the paper the proposed method for consistent fusion of data and decisions is implemented for on-line vibrodiagnosis of mechanical condition of the industrial mill fan of steam boiler in Power plant.

1   INTRODUCTION

Modern diagnosis significantly extends the scope of measurements, information and methods used, as traditional techniques themselves turns out unable to work in the case of complex problems [10, 16]. Along with approved approaches based on models, intelligent methods using various techniques of computational intelligence increasingly enter: Neural Networks [16], Case Based Reasoning (CBR) [3,13,15,16], data and decision fusion [3,5,6]. A combination of different intelligent methods is increasingly observed [5,16,8] for using the advantages of each component in the hybrid scheme. Diagnosis of complex technological plants is a key element in the rapidly evolving field of Condition Based Monitoring and Maintenance (CBM) [1,9,10,12,14,16]. The complexity of CBM requires

a new approach in decision making, given the great variety of possible solutions and the significant uncertainty [1,9,12]. The intelligent methods for decision making are an area of intense research in recent years [1.12].

The present work presents a method for intelligent decision making, based on consistent fusion of data and knowledge in conditions of heterogeneous information, large uncertainty and nonlinearity, using some ideas of last achievements in the area of signal denoising some new structures are proposed in order to overcome the drawbacks in complex systems diagnosis.

It is recognized that the methods of hybridization in the field of intelligent decision making are promising approach, but require specific research to expand all its features for at least sufficiently wide class of problems.

2 PROBLEM STATEMENT

In the diagnosis tasks of complex technological and mechanical plants emerge a set of difficulties. This paper tries to handle with them using intelligent techniques to obtain more realistic and more effective solutions than the existing conventional technologies.

Some assumptions are stated below:

- The problem of deep diagnosis is decided as multistage procedure.
- The different steps may require a different amount of information, different methods for diagnosis and different methods for decision making.
- As a basic method for hybridization scheme with weighted linear combination of solutions is preferred.
- The weights in fusion are determined by various metrics of closeness.
- The quality of decision-making procedure of diagnostic solution is improved by:
  - Training to optimize the weights;
  - Inclusion of variable number of components in the procedure for decision making;
  - Using different number of information resources.

The task becomes the combining of three different approaches – intelligent filtration with analytical models, logical analysis based on Case Based Reasoning and conventional statistical analysis to achieve better diagnosis decision making quality.

3 DATA AND DECISION FUSION

3.1 Data fusion

In the case of data alternatives solutions for intelligent data processing include:

- Rejection of corrupted sections of data (non-stationary, with gaps);
- Replacement of data and/or sections of data (strings) to preserve the integrity of the processing sample (training of neural networks, statistical analysis);
- Selection of parameters of the chosen filters with predefined structure (moving average, exponential smoothing);
- Correction of available data sets of synchronized data, incompatible (data

reconciliation) in respect of the fundamental requirements (material balance, heat balance). Decisions DM_{1i} are made for particular action in the signals processing process, and in combining several actions A_{1i} .

3.2 Decision fusion at higher diagnosis level

Figure 1 shows a generalized scheme for the proposed multi-stage intelligent decision-making for diagnosis tasks of complex plants and systems. A three-stage procedure for Intelligent Decision Making (IDM) is adopted:

- IDM1: solutions to the basic level, mainly related to faults detection;
- IDM2: solutions to average depth of diagnosis, most often - without specific measurements;
- IDM3: solutions for identification of complex faults or multiple faults.

Generalized scheme for intelligent decision making diagnosis tasks for complex plants is shown in Figure 2. In addition to her local feedback, the main feedback from the plant itself is shown (Figure 1) to improve the quality of decisions making. Thus, assessing both the procedure of decision making and the actions realizing it(A_{1i}).
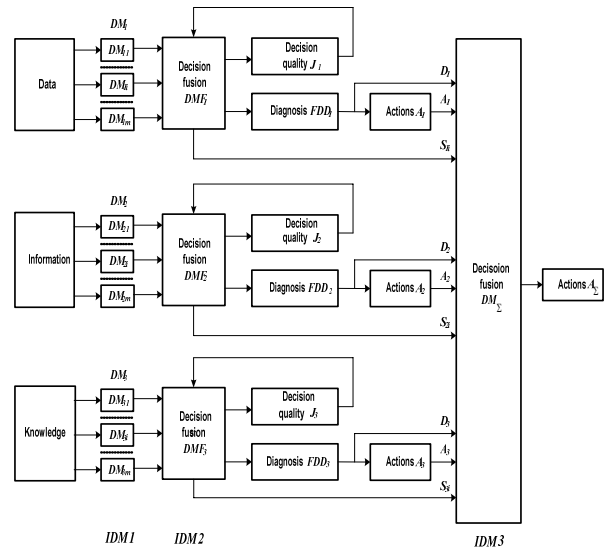

Figure 1: Intelligent Decision Making

Combining the solutions multi alternative for each level of IDM. The quality of decisions is measured by assessing the effectiveness of diagnosis and is improved by training based on modifying the

methods of decision making at the basic level IDM_{ij}, their number, as well as the fusion weights.
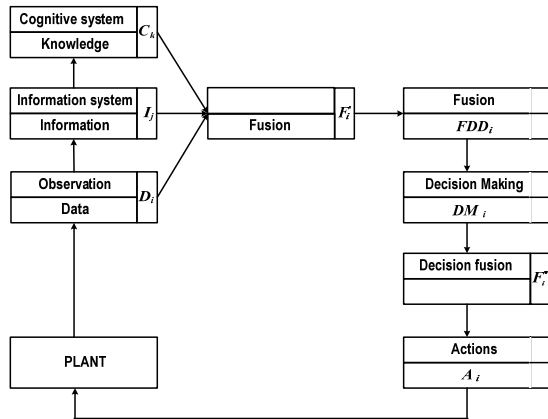

Figure 2: Generalized scheme of IDM

3.3 Intelligent diagnosis decision making by fusion of data, information and knowledge.

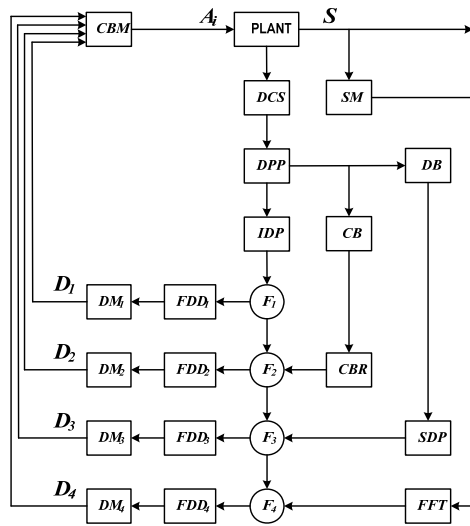A scheme for consecutive diagnosis through fusion is shown in Figure 3.

Figure 3: Consistent data and decision fusion

With minor modifications, this scheme retains its validity in diagnosis of a broad class of complex plants from similar class.

4 APPLICATION OF THE PROPOSED METHOD FOR DIAGNOSIS OF MILL FAN

4.1 Characteristics of mill fans as objects of diagnosis

Mill fans (MF) are key element in ensuring the reliable functioning of energy boilers burning low-grade lignite. The structural scheme of MF with the necessary signage is shown in Figure 4, but details are given in [7, 8, 9].
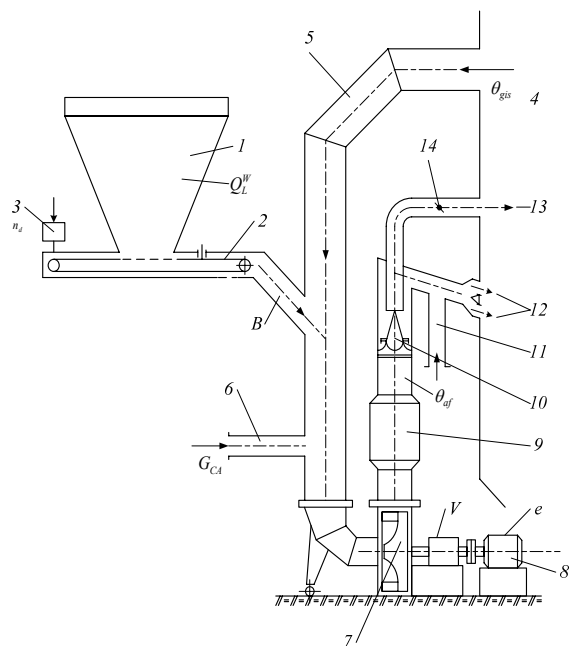
Figure 4: Structure scheme,

where 1 - Row fuel bunker, 2 - Row fuel feeder, 3 - Controller of row fuel feeder, 4 – Upper side of the furnace chamber, 5 - Gas intake shaft, 6 - Added cold air, 7 - Mill fan, 8 – Electric motor, 9 - Separator, 10 - Dust concentrator, 11 - Hot secondary air, 12 - Main burners, 13 - Discharge burner, 14 - Synchronized valves of discharge burners, $_{af}$ – temperature of air-fuel mixture, $_{gis}$ – temperature of intake drying gases, V – vibration, e – relative electric energy consumption, B – Throughput capacity of fuel, G_{CA} – Flow rate of added cold air, n_d – Position of discharge duct valve, Q_L^W – Low fuel caloricity of working mass.

The MF diagnosis is embarrassed due to certain circumstances:

- A lot of diagnostic parameters are hardly or are impossible to be measured fuel consummation, granulometric composition, coefficient of grindability, coal quality.
- Real operation shows asymmetric wear of operative wheel blades, variable fan and grinding capacity between two successive repairs.
- The measurements of abig number mill fan variables in the DCS or SCADA system are rather inaccurate due to the significant changeability of the conditions for measurements (wear, slagging, sensor pollution) and the great amount of external disturbances (dust and humidity of fuel, imprecise of coal, stohasticity of temperature of the intake oven gases due to non-stationarity of the flame position)
- The mill fan state is multidimensional. The basic components are grinding productiveness B [t/h], fan productiveness W [m³/h] and vibration state.

Because of listed circumstances the vibrations of MF could be considered as nonlinear and extremely noised with very low relation vibrosignal/noise under certain assumptions. The MF nonlinear vibration could be represented with the next equation [9]:

$$\frac{d^2y}{dt^2} + 2\xi\frac{dy}{dt} + F(y,t) = f_1(q_M(t)) + f_2(q_P(t)) \quad (1)$$

where y is amplitude of vibration, the disturbances in the right side of the equation may be presented as a function of exciting mechanical disturbances (damaged bearings, unbalanceness due to wear, etc.) q_M and due to operational disturbances (loading, hydrodynamic instability) q_P.

The exciting effect of the mode disturbances $q_P(t)$ must be eliminated or to be reduced substantially at the stage of analysis. The exciting disturbance $f_1(.)$ is of a deterministic nature and it is possible to be nonstationary if the fault evolves (e.g. most often progressive wear leading to debalance). The operational disturbance $f_2(.)$ is of a cumulative nature (due to the co-effect of a variable loading, change in the coal composition, hydrodynamic instability) and stochastic. This may be used for processing of measured vibration signal to separate the effect from the mechanical excitement $f_1(.)$ of the observed vibrations.

4.2 Experimental investigations

To verify the effectiveness of the proposed above method of cascade data and decision fusion historical data for 8 months work of MF are used.

The Fig.5 presents raw measurement data from the Experion DCS system for vibrations amplitude of the mill fan motor bearing block. The data are collected with 1 minute interval.
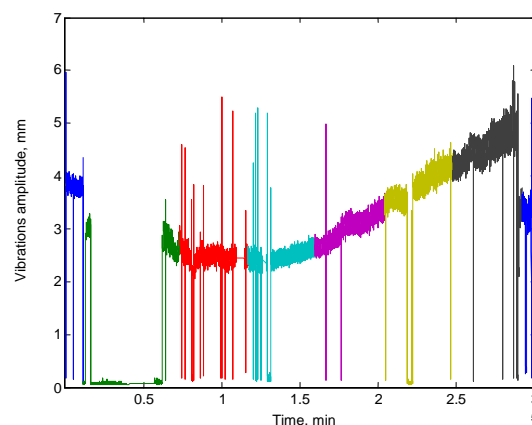

Figure 5: Vibrations amplitude for entire period of observations

The following conclusions may be drawn from these data:

- Because of the large discretization time $T_0 = 1$ min these data belong to uncorrelated (due to the big values of T_0) random processes. Therefore these temporal series may be used to isolate events in the MF vibration state but not for the detailed MF bearings' diagnostics because it is impossible to determine spectra of MF vibrations in successive time intervals due to the general non-stationarity of the process as a result of the wearing-out of the working wheel.
- Vibrosignals demonstrate significant unstability of the MF oscillations due to series of random exciting powers q_p (equation (1)) – a change in the fuel composition, non-homogeneous filling of sectors in the working wheel, hydrodynamic instability due to a change in the flow for the input and output cross sections of the MF. This instability is also due to often interrupts and load changes.
- There is observed non-monotonous rise of vibrations due to the joint action of leading factors – erosive wearing-out of the blades leading to a debalance of the working wheel and a random combined influence of the enumerated above exciting the oscillations mode factors (B_{MF}

– Throughput capacity of fuel, Q_L^W – Low fuel caloricity of working mass, θ_{af} – Temperature of air-fuel mixture, θ_{gis} – Temperature of intake drying gases, n_d – Position of discharge duct valve).

▪ The root mean square deviation of the vibration amplitude σ_V is changed during the cycle of the working wheel from one repair to another. This could be used an additional symptom for an isolation of an abnormity and also for a forecast.

▪ Vibrosignals must be analyzed synchronously together with the extracts for the operational

parameters (θ_{af} , θ_{gis} , n_d) due to the high level of the noise in the causal-effective relations.

4.3 Implementation of the proposed method

In order to make denoising of heterogeneous information from vibrosensors and a various regime parameters a consistent data and decision fusion is accomplished according the Fig. 6.
fusion in Mill Fan state estimation
As a main approach for data fusion Neural Networks (NN) are accepted. The intermediate result of the proposed intelligent filtration is illustrated in the Fig.7.
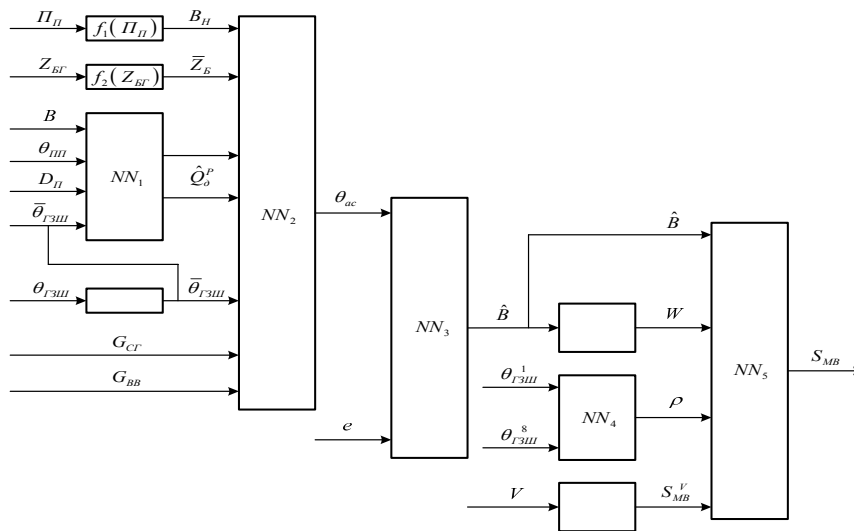
Figure 6: Scheme of sequential data and decision
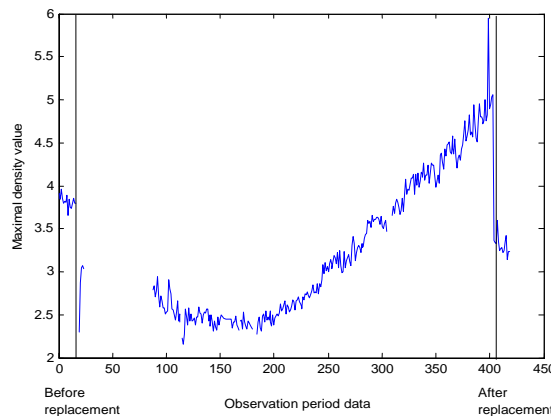
Figure 7: Maximal density values of vibrations amplitude

4.4. Application for Condition Based Maintenance of MF

The MF vibration state may become a rather useful component of their diagnostics to determine their affiliation to some zone of efficiency - S_1 – the normal one; S_2 – partial damages; still possible exploitation with lowered mode parameters (e.g. loading) and measures for current maintenance (lubrication, jamming bolt joints of MF to the bearers, technological adjustments (angles of rotation of valves, jalousie); S_3 – zone of serious damages, requiring immediate stopping at the first opportunity (stop the unit).

Each of the diagnostic states S_j is related to a given discrete moment of time k and it also possesses a structure of the "attribute-value" type.

$$S_j(k) = (G, H(k)) \quad (i = 1, 2, 3) \qquad (2)$$

The current state $S_{MB}(k)$ of a mill fan is related to some diagnostic state $S_j(k)$ using a classifier of the "comparison-with defined-thresholds" type based on the values $h_i(k)$ using a system of N rules R_i, for ($i=1,N$).

According the proposed above method (Fig.3) a multistage procedure is accepted to estimate the mill fan vibrational state – S_{MB}^V, where the defined limits h_i^t are changed adaptively depending on the estimate of the root-mean-square value for the reduced noise in the registered vibrations.

The actions for technical support M are represented as a multiset:

$$M = (M_1, M_2, M_3, M_4) \qquad (3)$$

The components $M_i(i = 1, 4)$ are subsets with the following components:

M_1 – change in the mode parameters in cases of conditionally allowed diagnostic state, e.g. with 3 elements.

M_2 – current repair, e.g. with 5 elements.

M_3 – replacing elements without big breaks of the mill fan operation, e.g. with 4 elements.

M_4 – stopping for repair, e.g. with 7 elements.

It is accepted in the present paper that the basic part of the attributes in the problem section P and the solution S are presented by the simplest type of data: "number" and "symbol". Still for some attributes such representation by pairs "attribute-value" is incomplete and they (especially in the portion for the supporting activities M (13)) may include free text or they may contain links to other related external information. Part of this information may not be directly used in the CBR algorithm but it gives the operators an additional knowledge for secondary using of archived results from the mill fan exploitation.

Independently on the presented significant difficulties during the determination of the vibration state of MF - S_{MB}^V, it is advisable to include it as an important component in the assessment of the overall technical state of mill fan. The assessment of the mill fan vibration state is a complex problem due to the exceptionally big uncertainty in the measurements which follows from the temporally re-covered changes of multimode factors. The mill fan vibration state (S_{MB}^V) is a valuable integral indicator for its working capacity. The determination and the usage of mill fan vibration state indicators are realistic and profitable for the operative staff because vibrosensors are obligatory for contemporary decentralized control DCS systems.

5 CONCLUSIONS

1. The proposed method allows resolving complex diagnostic tasks in multistage hierarchical sequence, which cannot be done in single stage procedure.

2. Heterogeneous data from different resources could be used – direct and indirect measurements, data bases, case bases and knowledge bases.

3. At each stage of decision making process the most appropriate method for fusion, FFD and decision making could be used. This allows improvement of decision making quality, based on the specific characteristics of the considered diagnostic problem.

4. The method allows the fusion of particular procedures of decision making, which have different time evaluation scope, because of the different time characteristics.

5. This method allows estimation of the decision quality at each hierarchical level, and based on this to improve the particular and the common procedure of decision making.

ACKNOWLEDGEMENTS

REFERENCES

1. Advances in Intelligent Decision Tehnologies, (G.Phillips-Wren, Ed.), Springer, 2010.

2. Belsak, A., and J. Prezelj, Analysis of Vibrations and Noise to Determine the Condition of Gear Unit, Advances in Vibration Analysis Research, No. 2, 2007.

3. Das,S., High Level Data Fusion, Artech House, 2008.

4. Donoho,D., Denoising by Soft-Thresholding, IEEE Trans. On Information Theory, V.41, 1995.

5. Dong,J., D.Zhang, Y.Huang, and J.Fu, Advances in Multi-Sensor Data Fusion: Algorithms and Applications, Sensors, 9, 2009.

6. Elmenreich,W., A Review on System Architectures for Sensor Fusion Application, LNCS 476, Springer, 2007.

7. Hadjiski M., L. Doukovska, CBR approach for Technical Diagnostic on Mill Fan System, Comptes rendus de l'Academie bulgare des Sciences, ISSN 0861-1459, 2012 (to be published). IF – 0.219.

8. Hadjiski M., L. Doukovska, St. Kojnov, Nonlinear Trend Analysis of Mill Fan System Vibrations for Diagnostics and Predictive Maintenance, International Journal of Electronics and Telecommunications (JET), Versita, Warsaw, Poland, ISSN 0867-6747, 2012, (to be published).

9. Hadjiski M., L. Doukovska, P. Koprinkova-Hristova, Intelligent Diagnostic on Mill Fan System, Proc. of the 6th IEEE International Conference on Intelligent Systems IS'12, 6-8 September 2012, Sofia, Bulgaria (to be published).

10. Iserman,R., Fault Diagnosis Systems, Springer, 2006.

11. Krishnan,S. and R.Rangayyan, Denoising Knee Joint Vibration Signals Using Adaptive Time-Frequency representation, Canadian Conf. on Electrical and Computer Engineering, V.3, 1999.

12. Li Hai Cheng, Qi Zhi, Application of Evidence Fusion Theory in Water Turbine Model, In: Intelligent Decision Technologies (J.Vatada, G.Phillips-Wren, C.Lakhimi, R.Howlett, Eds.), Springer, 2011.

13. Rasovska,I., B.Chebel-Mollero and N.Zerhouni, A Case Elaboration Methodology for a Diagnostic and Repair Help System Based on Case-Based Reasoning, Proc. of AAAI, 2007 (www.aaai.org).

14. Rafiee, J., F. Arvani, A. Narifi and M. H. Saheghi, Intelligent Condition Monitoring of a Gearbox Using Artificial Neural Networks, Mechanical Systems and Signal Processing, No. 21, 2007.

15. Recèo-Garcia, J.A., B.Diaz-Agudo, A.A.Sanches-Ruiz, and P.A.Gonzales-Calero, Lessons Learned in the Development of a CBR Framework, Expert Update, Vol.10, №1, 2010.

16. Vachtsevanos,G., F.Lewis, M.Roemer, A.Hess and B.Wu, Intelligent Fault Diagnosis and Prognosis for Engineering Systems, John Wiley, 2006.

A NOVEL PTS SCHEME FOR PAPR REDUCTION IN OFDM SYSTEMS

Mihail P. Iliev, Viktor V. Hadzhivasilev

University of Ruse "Angel Kanchev", Ruse, Bulgaria
miliev@uni-ruse.bg, vhadzhivasilev@uni-ruse.bg

Abstract: One of the main drawbacks of orthogonal frequency division multiplexing /OFDM/ is the high peak-to-average power ratio /PAPR/ of the transmitted OFDM signal. Partial transmit sequence /PTS/ technique can improve the PAPR statistics of an OFDM signal. As ordinary PTS technique requires an exhaustive search over all combinations of allowed phase factors, the search complexity increases exponentially with the number of sub-blocks. This paper proposed a novel scheme which has an adjustable parameter enables us to be able to obtain the best performance. Simulation results show that this scheme can significantly improve the ordinal PTS scheme and greatly reduce the computation complexity.

1 INTRODUCTION

Orthogonal frequency division multiplexing /OFDM/ is an attractive technique for wide-band radio communication because of OFDM's capability to convert a frequency selective fading channel to multiple flat fading channels. Thus, there is no need to implement any equalizers in the receiver. However, multi-carrier signals such as OFDM inherently have a high peak-to-average power ratio /PAPR/ problem. Transmitting the OFDM signals without any distortion requires a sufficient back-off of power amplifiers. This property is not acceptable for handsets with limited resources. Many proposals to reduce the PAPR of OFDM signals have been presented. Amplitude clipping and filtering /ACF/ is a simple and effective method. However, clipping causes signal distortion and degrades detection performance in specific to QAM. Selective mapping /SLM/ (Ib. Abdullah, 2011) and partial transmit sequence /PTS/ are based on the same idea that the PAPR of an OFDM symbol can be reduced by applying a certain phase rotation to a part of the transmit data or sequence. In general, SLM needs more IFFT operations but provides better PAPR reduction. Both SLM and PTS are distortionless unlike ACF. However, side information on the phase rotation pattern must be transmitted besides the main data. The side information requirement slightly decreases the transmission efficiency and impacts on the standardization defining the transmitted signal design.

In the paper, we propose a novel scheme for partial transmit sequence, which is based on finding the lowest PAPR from all binary weighting factors combinations.

The paper is organized as follows: In Section 2, the principle of PTS is described. In Section 3 ordinal PTS and a novel PTS technique is presented. In Section 4, the simulation results are given. Finally, we conclude the paper in Section 5.

2 PRINCIPLE OF PTS /PARTIAL TRANSMIT SEQUENCE/

Partial Transmit Sequence /PTS/ algorithm was first proposed by Müller S. H., Huber J. B., (S. H. Muller, 1997) which is a technique for improving the statistics of a multi-carrier signal. The basic idea of partial transmit sequences algorithm is to divide the original OFDM sequence into several sub-sequences, and for each sub-sequence, multiplied by different weights until an optimum value is chosen.

Fig. 1 is the block diagram of PTS algorithm. We have added Hadamard transform to reduce the occurrence of the high peaks comparing the original OFDM system. The idea to use the hadamard
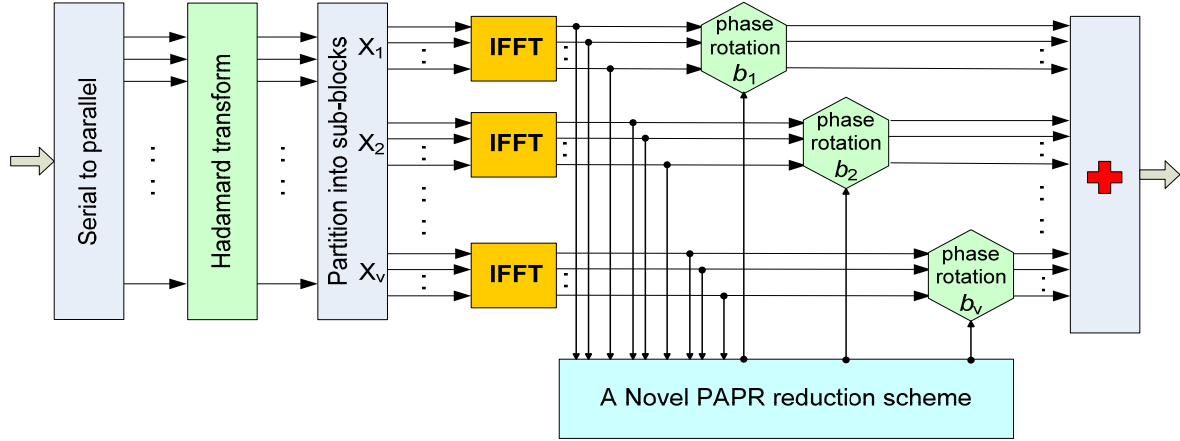
Figure 1: Block diagram of PTS algorithm.

transform is to reduce the autocorrelation of the input sequence to reduce the peak to average power problem and it requires no side information to be transmitted to the receiver.

From the left side of diagram, we see that the data information in frequency domain X is separated into V non-overlapping sub-blocks and each sub-block vectors has the same size N. Hence, we know that for every sub-block, it contains N/V nonzero elements and set the rest part to zero. Assume that these sub-blocks have the same size and no gap between each other, the sub-block vector is given by

$$\hat{X} = \sum_{v=1}^{V} b_v X_v \qquad (1)$$

where $b_v = e^{j\varphi_v} (\varphi_v \in [0, 2\pi])\{v = 1, 2, ..., V\}$ is a weighting factor been used for phase rotation.

The signal in time domain is obtained by applying IFFT operation on X_v, that is

$$\hat{x} = IFFT(\hat{X}) = \sum_{v=1}^{V} b_v IFFT(X_v) = \sum_{v=1}^{V} b_v x_v \qquad (2)$$

Select one suitable factor combination $b = [b_1, b_2, ..., b_v]$ which makes the result achieve optimum. The combination can be given by

$$b = [b_1, b_2, ..., b_v] = \arg\min_{(b_1, b_2, ..., b_v)} (\max_{1 \le v \le N} \left| \sum_{v=1}^{V} b_v x_v \right|^2) \qquad (3)$$

where argmin $(\cdot)$ is the judgment condition tat output the minimum value of function. In this way we can find the best b so as to optimize the PAPR performance. The additional cost we have to pay is the extra V-1 times IFFTs operation.

In conventional PTS approach, it requires the PAPR value to be calculated at each step of the optimization algorithm, which will introduce tremendous trials to achieve the optimum value. Furthermore, in order to enable the receiver to identify different phases, phase factor b is required to send to the receiver as sideband information (usually the first sub-block $b1$, is set to 1). So the redundancy bits account for $(V-1)\log_2 W$, in which V represents the number of sub-block, W indicates possible variations of the phase. This causes a huge burden for OFDM system, so studying on how to reduce the computational complexity of PTS has drawn more attentions, nowadays.

The optimization is achieved by searching thoroughly for the best phase factor. Theoretically, $b = [b_1, b_2, ..., b_v]$ is a set of discrete values, and numerous computation will be required for the system when this phase collection is very large. For example, if φ_v contains W possible values, theoretically, b will have W^v different combinations, therefore, a total of $V * W^v$ IFFTs will be introduced.

By increasing the V, W, the computational cost of PTS algorithm will increase exponentially. For instance, define phase factor b_v contains only four possible values, that means $b_v \in [\pm 1, \pm j]$, then for each OFDM symbol, $2*(V-1)$ bits are transmitted as side information. Therefore, in practical applications, computation burden can be reduced by limiting the value range of phase factor $b = [b_1, b_2, ..., b_v]$ to a proper level. At the same time, it can also be changed by different sub-block partition schemes.

3 ORDINAL PTS TECHNIQUE

Cimini and Sollenberger's (L. J. Cimini, 2000) ordinal technique is developed as a sub-optimal technique for the PTS algorithm. In their original

paper, they only use binary weighting factors. That is $b_v = 1$ or $b_v = -1$. These can be expanded to more phase factors. The algorithm is as follows. After dividing the data block into V disjoint sub-blocks, one assumes that $b_v = 1$, ($v = 1, 2, \ldots ,V$) for all of sub-blocks and calculates PAPR of the OFDM signal. Then one changes the sign of the first sub-block phase factor from 1 to -1 ($b_1 = -1$), and calculates the PAPR of the signal again. If the PAPR of the previously calculated signal is larger than that of the current signal, keep $b_1 = -1$. Otherwise, revert to the previous phase factor, $b_1 = 1$. Suppose one chooses $b_1 = -1$. Then the first phase factor is decided, and thus kept fixed for the remaining part of the algorithm. Next, we follow the same procedure for the second sub-block. Since one assumed all of the phase factors were 1, in the second sub-block, one also changes $b_2 = 1$ to $b_2 = -1$, and calculates the PAPR of the OFDM signal. If the PAPR of the previously calculated signal is larger than that of the current signal, keep $b_2 = -1$. Otherwise, revert to the previous phase factor, $b_2 = 1$. This means the procedure with the second sub-block is the same as that with the first sub-block. One continues performing this procedure iteratively until one reaches the end of sub-blocks (Vth sub-block and phase factor b_v).

4   MODIFIED PTS TECHNIQUE

In this section, we present a modified PTS technique which is similar to Cimini and Sollenberger's technique. We made simulation with 4 and 8 phase factors to reduce the PAPR of the OFDM signal:

$$W=4 \quad b_v=[1 \quad j \quad -1 \quad -j]$$

And

$$W=8 \quad b_v=\left[1 \quad 1/\sqrt{2}+j/\sqrt{2} \quad j \quad -1/\sqrt{2}+j/\sqrt{2} \quad -1 \quad -1/\sqrt{2}-j/\sqrt{2} \quad -j \quad 1/\sqrt{2}-j/\sqrt{2}\right]$$

The basic idea of the proposed algorithm is first to find and use this combination of binary weighting factors, which gives the lowest PAPR. Secondly we can repeat the process using changed matrix in first step. The result phase factor $b = [b_1, b_2, \ldots, b_v]$ will be multiplication from all found binary weighting factors. We can reduce all possible combinations, using only this binary weighting factors which begun with 1. The process is repeated P times, where P is an adjustable parameter.
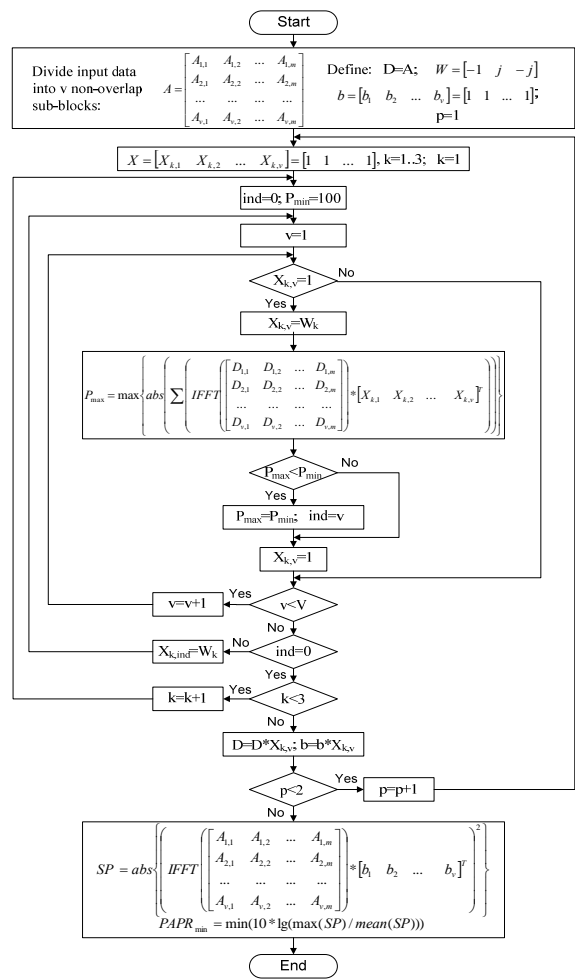

Figure 2: Block scheme of proposed PTS algorithm.

There is and another feature – when finding the lowest PAPR, we first chose this sub-block which gives minimum PAPR and then we try to find next sub-block, which will reduces mostly PAPR. If there is no one /no further improvement is possible/, we may try next binary combinations. Finally we choose this combination of binary weighting factors, which gives lowest PAPR.

The basic structure of the modified PTS technique is illustrated in Fig 2. For the clarity we choose $P=2$ and $W=4$. In this case we will have only three /k=3/ binary combinations: (1, -1), (1, j), (1,-j) we are interested in.

After dividing the data block into V disjoint sub-blocks, let one choose first combination $k=1$ and $X_{k,v} =1$, ($v=1, 2, \ldots ,V$) for all sub-blocks and calculates PAPR of the OFDM signal. Then one changes the first sub-block /$v=1$/ phase factor from 1 to $W_k= -1$ /$X_{k,v} = -1$/, and calculates the PAPR of

the signal again. If PAPR of the current signal is lower than previously calculated signal, remember index /$ind=v$/ and PAPR minimum. Restore current phase factor to 1 /$X_{k,v} = 1$/. Repeat this procedure until the end of the sub-blocks. Then if there is a PAPR improvement, change sub-block with the remembered index to W_k /$X_{k,ind} = -1$/. One continues performing this algorithm iteratively until there is a PAPR improvement for those sub-blocks, which has phase factor set to 1.

If there is no further improvement, we can try next binary combination $k=2$ /W_k=j/ and so on, until the end of all possible combinations.

Finally, we choose these binary weighting factors $X_{k,v}$, (v=1, 2, … ,V) which gives the lowest PAPR.

At last, if we multiply the input matrix with the chosen weighting factors, we can repeat the entire process /$P=2$/. The result phase factor $b = [b_1, b_2, ..., b_v]$ will be multiplication from all found binary weighting factors $X_{k,v}$, (v=1, 2, … ,V).

5 SIMULATION RESULTS
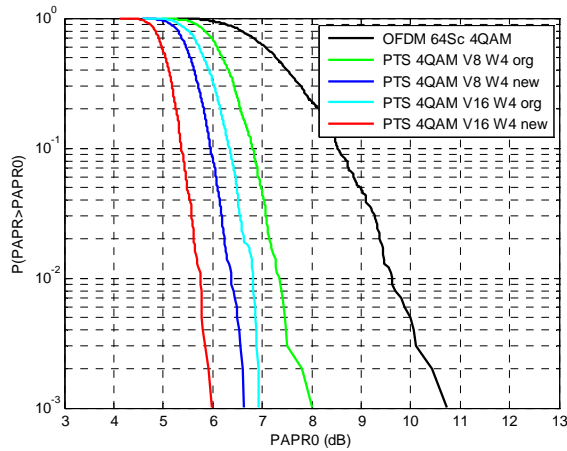
Figure 3: Comparison between ordinal and a novel PTS technique of PAPR reduction performances with different values of V.

From Fig. 3, it can be seen that a novel PTS algorithm undeniably improve the performance of OFDM system, moreover, with the increasing of V, the improvement of PAPR reduction performance becomes better and better. Assume that we fix the probability of PAPR at 0.1% and compare the CCDF curve with different values of V. Form the figure, we

notice that the CCDF curve has nearly 1.5dB improvement when V=8, compared to the ordinal PTS algorithm. When V=16, the 0.1% PAPR is about 6dB, so an optimization of 1dB is achieved. If we compare PAPR reduction to the conventional OFDM system, we can observe that an improvement of nearly 5dB is reached.

However, the downward trend of CCDF curve is tended to be slow when we keep on increasing V, which means too large sub-block numbers V will result in small improvement of PAPR reduction performance, but anyway we have to increase sub-block numbers V, if we have a many of sub-curriers.

Therefore, practically, we prefer to choose a suitable value of V.

The simulation result in Fig. 4 shows the varying PAPR reduction performance with different W, when using ordinal and modified PTS reduction scheme. Simulation specific parameters are: the number of sub-carriers N=64, 4-QAM constellation modulation, the number of sub-blocks V=8. From the figure we notice that the CCDF curve has al least 1/3dB improvement when W=8, compared to W=4. We can conclude that the larger W value takes, the better PAPR performance will be obtained when the number of sub-block V is fixed, but pay for the enormous computation time. Therefore, practically, we prefer to fix W=4.
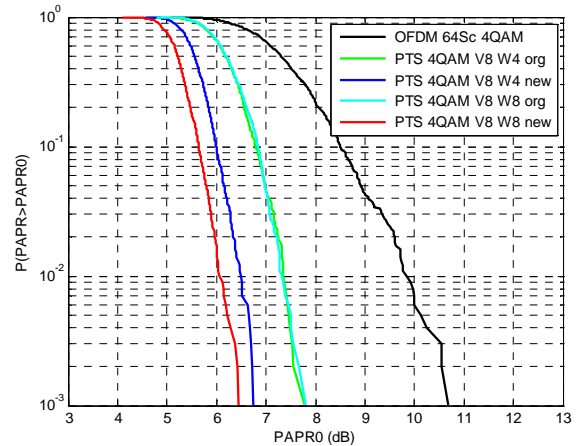

Figure 4: Comparison between ordinal and modified PTS technique of PAPR reduction performances with different values of W.

On the next scheme, shown on Fig. 5, we compare PAPR reduction performances with different number of sub-carriers, when W is fixed /four phase rotations/ and modulation is 4-QAM. We observe that if the number of sub-curries is increased

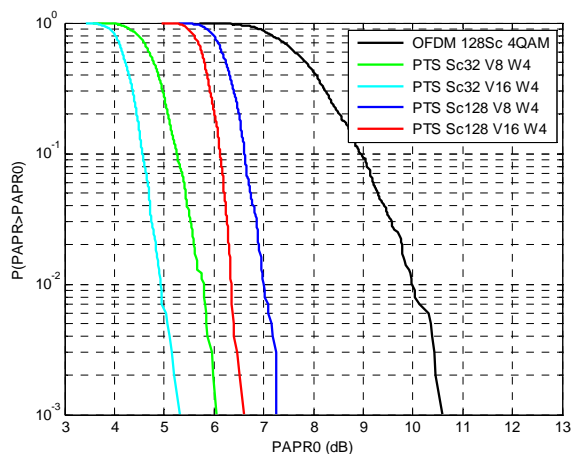the PAPR reduction performance has been slowed down.

Figure 5: Comparison of PAPR reduction performances with different values of *V* and number of sub-curriers.

The simulation results in Fig. 6 compares PAPR reduction performances with different modulation schemes /4-QAM and 16-QAM/ and fixed values of *V*, *W* and number of sub-curriers. We may notice that the number of constellation points almost has no effect of PAPR characteristics.
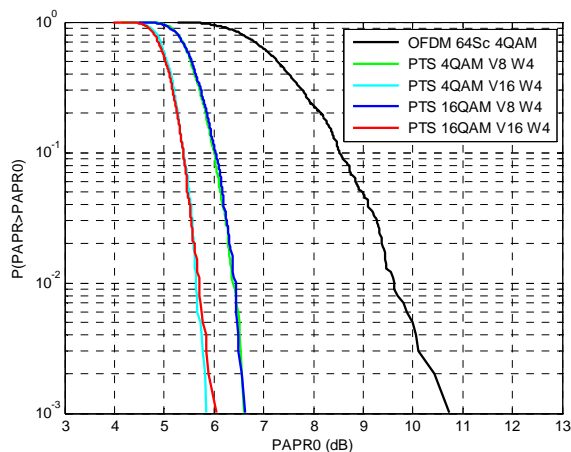

Figure 6: Comparison of PAPR reduction performances with different values of V and variable QAM size.

Finally, on the Fig. 7 we made comparison between different number of sub-blocks and an adjustable parameter - *P*. We can see that the trend of CCDF curve is tended quickly to be slow-down when we keep on increasing *P*. Therefore,

practically it is suitable to choose *P*=2 and to determinate the number of sub-blocks on dependency of sub-curriers, as we discuss above - see Fig. 3.
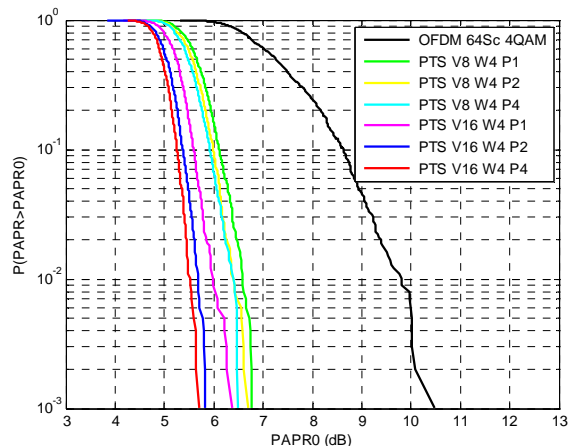
Figure 7: Comparison of PAPR reduction performances with different values of *P* and number of sub-blocks.

6 CONCLUSION

One of the major problems associated with OFDM is its high PAPR. In this chapter, we proposed a novel PTS algorithm to reduce efficiently the PAPR of OFDM signal. There is an adjustable parameter, which enables us to be able to obtain the best performance.

Simulation results show that the proposed novel algorithm can yield good PAPR reduction with low computational complexity.

REFERENCES

Ib. Abdullah, Z. Mahamud, Sh. Hossain, "Reduction of PAPR in OFDM using SLM for different route number", IJRRCS, June 2011

S. H. Muller, J. B. Huber, "OFDM with reduced peak-to-average power ratio by optimum combination of partial transmit sequence," *IEEE Electronic Letters*, Vol. 33, No. 5, Feb. 1997

L. J. Cimini, Jr. and N.R. Sollenberger, "Peak-to-average power ratio reduction of an OFDM signal using partial transmit sequences," *IEEE Communication Letters*, vol. 4, Mart 2000

Y. Cho, J. Kim, W. Yang, Ch. Kang, "MIMO-OFDM Wireless Communications With MATLAB", John Wiley & Sons, Singapore, 2010

WEB ASSISTED DESIGN OF COMMUNICATION CIRCUITS AND SYSTEMS

Galia Marinova

Telecommunications Faculty, Technical University – Sofia-1000,
8, bul. Kliment Ohridski, Sofia, Bulgaria,
gim@tu-sofia.bg

Abstract: Online calculators, generators, wizards and free design tools increased considerably the accessibility of communication circuits and systems design. The paper presents a study on the online design tools and defines design tasks that can be solved with their assistance. The concept of Local resources, assisted by Web assistants in a Web portal, is considered. The Web assistants in the portal integrate Sets of connexions and e-Content. The paper gives examples combining online tools with locally installed Computer-aided design (CAD) tools for more effective communication circuits and systems design.

1 INTRODUCTION

Nowadays we are witnessing a boom of specialized web resources, online platforms, portals, programs, calculators. Smaller or bigger centers make research, characterization, categorization and development of sets of connections to these web resources. One of the biggest centers for connections with specialized online resources is the MARTINDALE'S Calculators Online Center (MARTINDALES) where connections are built forward 24385 online calculators, 4145 e-learning materials and lecture courses and 1000 films, video and animation products and simulations, created by more than 8620 authors from all over the world. The web connections in the Center are categorized by areas, covering a very wide specter, from agriculture and archeology passing through mathematics and engineering and ending by physics and chemistry.

Smaller specialized portals in the area of communications exist, as for example, the portals of the SPICE community (YOUSPICE, e-CircuitCenter, etc.), the portals for audio design, which have built sets of tens to hundreds of connections to useful resources in the Web. Besides the disconnected online resources, online platforms for solving complex research and design tasks in communications became accessible during the last years. The Free online platform for switch-mode power supply (SMPS) design, on web address www.PowerEsim.com   and the SCA-Based Open

Source Software Defined Radio on web address http://ossie.wireless.vt.edu/ are such examples. Both are developed as result of serious scientific projects. PowerEsim is the result of a research project in Hong Kong, and SCA-Based Open Source Software Defined Radio is the result from a project of the National Research Foundation in USA. All specialized online platforms and portals can be used in education, but this is neither their main application, nor the unique one. They make accessible an environment for solving real tasks from system design in communications with elements of business analysis and decisions. Some of these platforms integrate local resources with online resources for solving design and test tasks. The platforms as WeBench Designer of Texas Instruments: for designing SMPS, LED, FPGA, Sensors, which make available considerable free resources, are between the most popular in this category. We have experienced applying online resources mainly in e-education and most universities have e-Learning Centers or Distance Learning Centers. In the present work the accent is on the Useful resource on the web and the development of Sets of connections in order to solve Computer-aided design (CAD) tasks in the area as communications. Thus acceleration of scientific research can be achieved.

2 CONCEPT OF PORTAL WITH WEB ASSISTANTS TO LOCAL RESOURCES FOR CAD OF COMMUNICATION CIRCUITS AND SYSTEMS

A Multitool environment for Computer-Aided Design in Communications was described in (Marinova, 2010). The goal was to combine multiple tools in order to design a communication system. The set, of locally installed CAD tools in the environment, is composed from the following programs:

- MATLAB,
- ORCAD/Capture, ORCAD/Layout,
- PSpice A/D and Advanced analysis,
- WARP 6.2,
- ISE WEBPACK,
- QUARTUS II,
- MMICAD,
- FilterCAD,
- PAC Designer,
- MICROWIND.

The integration of these tools for solving different tasks is described in details in (Marinova, 2010). At a next step it becomes interesting to assist these Local resources by a Set of Useful online resources. This is realised through definition of a Set of CAD tasks suitable for the Local resources. Then a Portal is developed with Web assistants in order to provide knowledge from the web helping the task solution. The Web assistants are composed by a Set of connections to the Useful web resources and e-Content. The Useful net resources are determined after a serious research in the web and selection of online tools suitable for the Set of CAD task. Additional tests and verifications of the online tools are performed before admitting them as a Useful resource. A characterization is made for their application area. The Concept of the Web assistants combined to Local resources, for CAD of communication circuits and systems is presented on Figure 1. The Portal with Web assistants for CAD of communication circuits and systems is presented on Figure 2.

A set of CAD tasks is defined:

- Antenna design;
- LED array, controller and driver design;
- Switch-mode power supplies (SMPS) design;
- Design with PSpice;
- PCB trace estimation;
- PCB design price estimation.
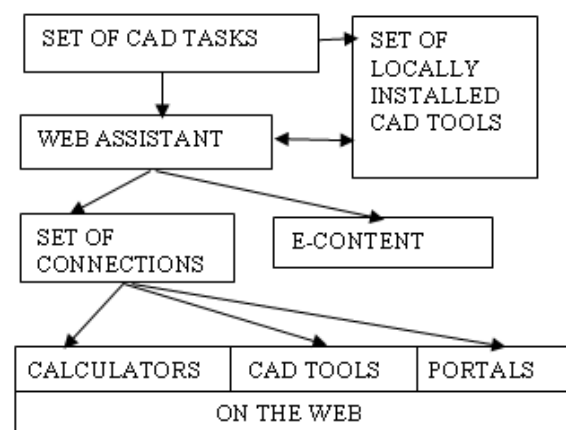
Figure 1.

Figure 2.

3 SETS OF CONNECTIONS IN THE WEB ASSISTANTS

The Set of connections for each Web assistant is built after a serious research in the web for online calculators, tools and materials, related to the corresponding Set of CAD tasks. Each online tool is tested and if the test result is satisfactory the web address is added to the Set of connections. Each online tool is accompanied by short characteristics, describing its specific functions. Six Sets of

connections are built in order to assist solving the Set of CAD tasks described above:

Set of connections for Antenna design: 10 online calculators are considered for the design of 7 of the most popular types of antennas: LPDA, Yagi, Moxon, Helix, Microstrip Patch, Delta loop and Magnetic loop. The Set is presented in Table 1.

Set of connections for LED array, driver and controller design: 5 online calculators and one free downloadable program for LED array design, Current limiting resistor calculation, LED driver design and LED controller programming are selected and presented in Table 2.

Set of connections for SMPS design: The free online platform for SMPS design PowerEsim, as well as WEBENCH POWER DESIGNER (TI) and a portal for SMPS projects simulated with PSpice are selected and presented in Table 3. The PowerEsim platform was tested. Verification with PSpice was performed for the design of a Full bridge DC-DC converter and the results from the verification are presented in (Marinova, July 2012). The content of the portal SMPS was studied in details and an application limitation coming from the paid PSpice projects of SMPS was observed.

Set of connections for Design with Spice – Three portals – eCircuitCenter, YOUSPICE and SMPS are selected and considered and the set of connections is presented in Table 4. The free Circuits collections were tested with a local PSpice A/D tool and several remarks and corrections were reported for some of the projects in these portals. The specific advantage of the portal YOUSPICE is the mechanism for SPICE project exchange. New point in the portal eCircuitCenter is the online EXCEL based design calculations for the design of certain circuits – audio amplifiers for example. The PSpice projects of the portal SMPS are entirely paid and even the electrical circuit of the SMPS is not fully visible without registration.

Set of connections for PCB trace estimation – 6 online calculators are selected and a free downloadable tool Saturn and their main characteristics are presented in Table 5.

Set of connections for PCB design price estimation – an online calculator and 2 tabular online tools are selected and presented in Table 6.

The research covers until now 32 resources from the Web which are selected, studied and added to the Sets of connections to the Web assistants in the Portal for computer-aided design of communication circuits and systems. The research continues by adding new Sets of connections with:

- Online calculators for resistors and capacitors;
- Online matching network tools – Smith Chart diagram tools;
- Online analogue/digital/crystal filters design tools;
- Online 555 timer calculators;
- Online design tools for loudspeakers and microphones (mono and stereo);
- Online SCA based open source software defined radio - OSSIE.

4 ILLUSTRATIVE EXAMPLES OF WEB ASSISTED COMPUTER-AIDED DESIGN

In (Marinova, June 2012) there are some examples given for web assisted computer aided design. Two additional examples, design with WENENCH LED DESIGNER and design with WARP 6.2. and LED current limiting resistor calculator, are given further.

4.1 Design of LED array with 5x7 orange LEDs and a driver in WEBENCH LED DESIGNER

Orange LEDs 35 (5x7), with forward voltage 2.9 V and forward current of 0.35 mA, are chosen. The power supply is 12 V. The LEDs chosen for the design are Philips LXML Ph01.

WEBENCH LED DESIGNER proposes a list of drivers suitable for such LEDs. Besides the driver IC and the datasheet, an electrical circuit is proposed for each driver. The drivers with the highest efficiency are selected. Then they are compared for their dimensions and price. The driver chosen for the design is LM3424MH and the electrical circuit of the design is presented on Figure 3.

4.2 Design of LED array 16x4 controlled by shift registers and pseudo-random vector generator

The electrical circuit in ORCAD/Capture of the LED array 16x4 controlled by shift registers and pseudo-random vector generator (PRVG) is presented on Figure 4. The 4 shift registers and the PRVG are described in VHDL and simulated on CYPRESS CPLD in WARP 6.2 (www.cypress.com). The limiting current resistors R1-R64 from Fig. 3 are calculated in the online calculator Ledz. From Table 2.

Table 1: Set of connections for Antenna design
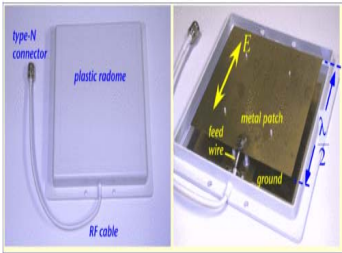
Antenna	Picture	Calculator	Web address in the Set of connections
Log Periodic antenna LPDA		Changpuak	http://www.changpuak.ch/electronics/lpda.php
Yagi antenna		Radiohobby	http://radiohobby.hit.bg/antcalc.htm
		Va3css	http://www.va3css.ca/calculators.html
Moxon antenna		Vp9kf	http://w4.vp9kf.com/moxon_design.htm
Helix antenna		Jcoppens	http://jcoppens.com/ant/helix/calc.en.php
		Daycounter	http://www.daycounter.com/Calculators/Helical-Antenna-Design-Calculator.phtml
Microstrip patch antenna		Emtalk	http://www.emtalk.com/mpacalc.php
Delta loop antenna		DxZone	http://www.dxzone.com/catalog/Antennas/Antenna_Calculators/
Magnetic loop antenna		66pacific	http://www.66pacific.com/calculators/small_tx_loop_calc.aspx
		Am-dx	http://www.am-dx.com/loop_calc.htm

Table 2: Set of connections for LED array, controller and driver design
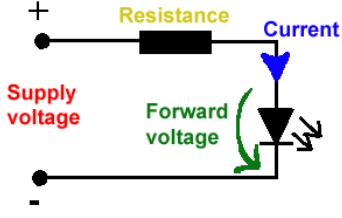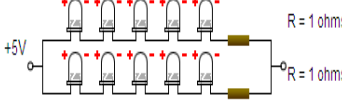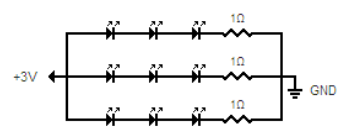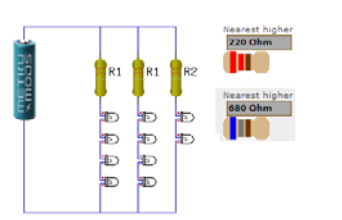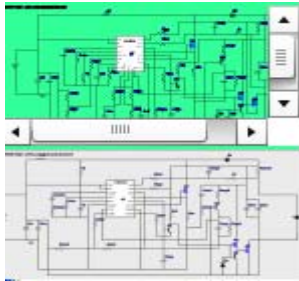
LED calculator	Illustration	Functions	Web address in the Set of connections
Ledz		Current limiting resistor calculation for one or several LEDs connected serially or in parallel	http://ledz.com/?p=zz.led.resistor.calculator
Ledlinear		LED serial/parallel array design	http://led.linear1.org/
LedCalculator		LED serial/parallel array design	http://ledcalculator.net/
LedCalc		LED serial/parallel array design	http://ledcalc.com/
WEBENCH LED Designer		LED driver circuit design and efficiency calculation	http://www.ti.com/ww/en/analog/webench/led.shtml
MAX6952		Programming LED controllers	http://www.scienceprog.com/drive-dot-led-matrix-display-using-lpt-port-and-driver-ic/

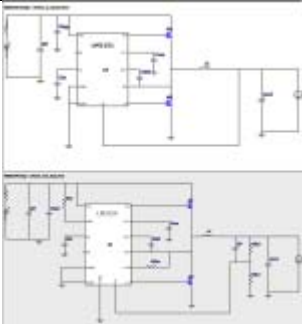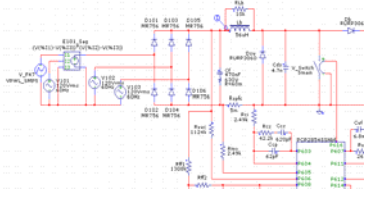Table 3: Set of connections for SMPS design

CAD tool or Portal	Illustration	Characteristics	Web address in the Set of connections
PowerEsim		Online platform for SMPS design – free Transformer calculator Simulation tool	www.poweresim.com
WEBENCH POWER DESIGNER		Multiple circuit synthesis and optimization	http://webench.ti.com/webench5/power
SMPS		PSpice projects for SMPS – all paid	www.smps.com

Table 4: Set of connections for Design with PSpice

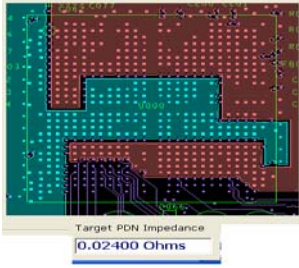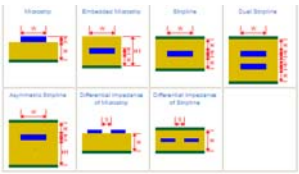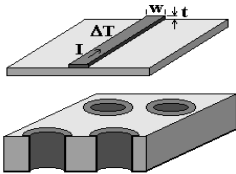| Portal	Characteristics	CAD tools	Circuit collection	Free or paid	Web address in the Set of connections
eCircuitCenter	Project design with EXCEL and simulation with PSpice	PSpice EXCEL	115 projects in 16 categories	Free	www.ecircuitcenter.com
YOUSPICE	Project exchange	ORCAD PSpice; Micro-Cap; LTspice; TINA; EDWinXP; Proteus; NI Multisim; Altium Designer; SPICE OPUS.	392 projects in 14 categories	Free and Paid 72 free projects	www.youspice.com
SMPS	SMPS projects	PSpice	SMPS projects	Paid	www.smps.com

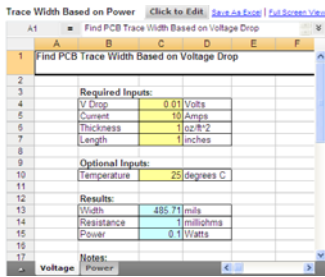Table 5: Set of connections for PCB trace estimation
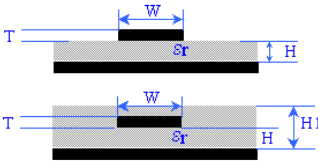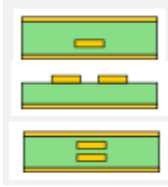
Calculator	Characteristic	Illustration	Web address in the Set of connections
Saturn PCB Design toolkit v.5.6.	Free downloadable software for Via, Conductor, Signal properties calculation, PDN impedance, Thermal, Fusing current etc.		http://www.saturnpcb.com/pcb_toolkit.htm
TECHNIK	Impedance, Inductance, capacity calculation for 7 different geometries		http://www.technick.net/public/code/cp_dpage.php?aiocp_dp=util_pcb_imp_calculator
Selektronik	Impedance, crosstalk, current carrying capacity, thermo-via calculation		http://www.skottanselektronik.com/
Wordpress	Trace Width calculation based on power, using EXCEL		http://circuitcalculator.com/wordpress/2006/04/20/find-pcb-trace-width-based-on-power/
EMCLAB	Trace impedance calculation for 4 different geometries		http://emclab.mst.edu/pcbtlc2/
EEWEB	Trace impedance calculation for 9 different geometries of microstrip, striplines and coupled and/or embedded striplines		http://www.eeweb.com/toolbox/microstrip-impedance/

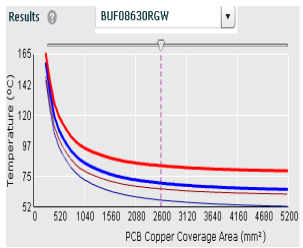Table 5: Set of connections for PCB trace estimation (continue)

TI PCB THERMAL CALCULATOR	Device junction temperature estimation More than 200 TI ICs supported		http://www.ti.com/adc/docs/midlevel.tsp ?contentId=76735

Table 6: Set of connections for PCB design price estimation

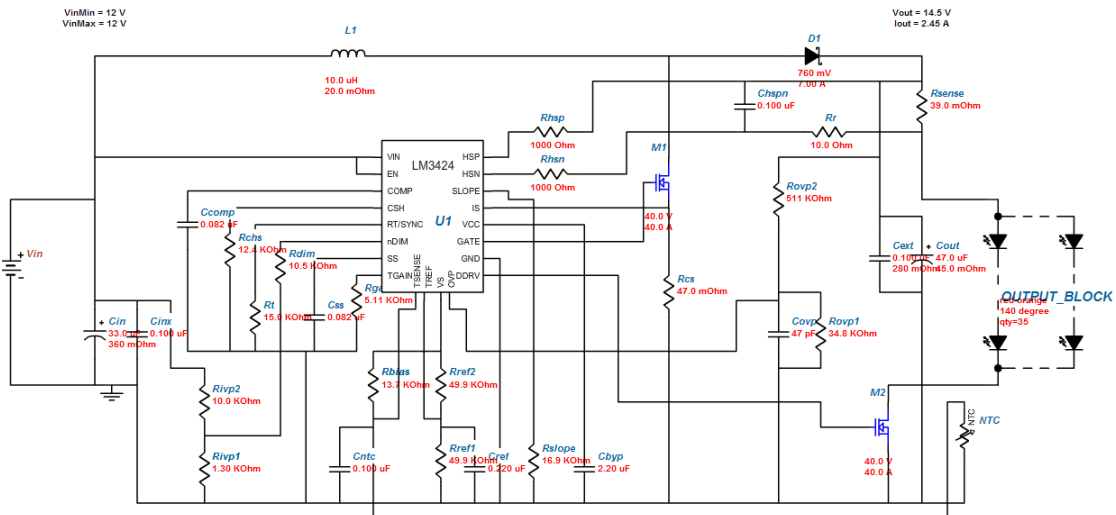| PCB design price calculator	Characteristics	Web address in the Set of connections
MIKRON 20	Calculates the price of PCB production and assembly	http://www.micron20.com/bg/orders/calculator-production/ http://www.micron20.com/bg/orders/calculator-assembly/
SKA	Prices for PCB production are presented in tables as well as percentage for additional services	http://www.cka-bg.com/index.php?page=tseni-pechatni-platki&hl=bg_BG
MLAD KONSTRUKTOR	Prices for PCB production are presented in tables	http://constructor.bg/shop/pcb_order_2.php

Figure 3.

Figure 4.

The VHDL description of the 4 bit pseudo random vector generator is:

```
library IEEE;
use IEEE.STD_LOGIC_1164.ALL;
entity rng is
     generic ( wd : integer := 32 );
     port (clk : in std_logic;
             random_num : out std_logic;
             random_4bit: out
std_logic_vector (3 downto 0));
end rng;

architecture Behavioral of rng is
signal rand_temp : std_logic_vector(wd-1
downto 0);
signal temp : std_logic;
  begin
      process(clk)
          begin
        if(clk'event and clk='1') then
        temp <= not(rand_temp(wd-1) xor
        rand_temp(wd-2));
        rand_temp(wd-1 downto 1) <=
        rand_temp(wd-2 downto 0);
        rand_temp(0) <= temp;
        end if;
      end process;
random_num <= rand_temp(wd-1);
random_4bit(3)<= rand_temp(wd-1);
random_4bit(2)<= rand_temp(wd-2);
random_4bit(1)<= rand_temp(wd-3);
random_4bit(0)<= rand_temp(wd-4);
end Behavioral;
```

The PRVG described in VHDL is simulated in WARP 6.2 and the waveforms obtained are presented on Figure 5. The input is the clock signal and the 4-bit vectors generated are obtained at random_4bit. The random numbers are presented in decimal form.

Figure 5.

The functionality of the circuit from Figure 4 is presented on Figure 6, where red circles indicate lighting LEDs.

11	1011				
7	0111	○	●	●	●
15	1111	●	●	●	●
14	1110	●	●	●	○
12	1100	●	●	○	○
8	1000	●	○	○	○
0	0000	○	○	○	○
1	0001	○	○	○	●
3	0011	○	○	●	●
7	0111	○	●	●	●
15	1111	●	●	●	●
14	1110	●	●	●	○
12	1100	●	●	○	○
8	1000	●	○	○	○
0	0000	○	○	○	○
1	0001	○	○	○	●
3	0011	○	○	●	●

Figure 6.

This design is a good illustration of the advantages of combined utilization of Local resources as WARP 6.2 and online calculator as Ledz.

5 CONCLUSIONS

The paper illustrates the concept of a Portal with Web assistants, developed to help the solutions of Tasks for computer aided design in communications.

The Web assistants are composed by Sets of connections with Useful web resources and e-Content. The research work concerning 6 tasks for CAD is presented in the paper and the Sets of connections with online calculators and other web resources of the Web assistant in the Portal are considered in details. Two examples of LED design are described in order to illustrate the approach. Further work is planned in order to enlarge the Portal with new Web assistants and new Sets of connections for solving new Tasks for CAD in communications.

REFERENCES

Marinova, G., June 2012, Multitool online assisted design of communication circuits and systems, *ICEST'2012*, Veliko Tarnovo

Marinova, G., 2010, Multidisciplinary approach for teaching Computer-Aided Design in communications using multiple software tools, *Advanced Aspects of Theoretical Electrical Engineering Sozopol '2010,* Sozopol, Bulgaria, Plenary lectures, pp. 34 -42

Marinova, G., July 2012, PSpice as a Verification Tool for Switch Mode Power Supply Design with PowerEsim, *NDES'2012*, Wofenbuttel, Germany, pp.140-143, ISBN:978-3-8007-3444-3

MARTINDALE'S Calculators Online Center http://www.martindalecenter.com/Calculators.html

ABSTRACTS

WHISTLER-MODE CHORUS WAVE-NORMAL DISTRIBUTION EFFECTS FOR AND ELECTRON SCATTERING IN THE RADIATION BELTS

Oleksiy Agapitov

LPC2E/CNRS University of Orleans, Orleans, France;
National Taras Shevchenko University of Kiev, Kiev, Ukraine
.oleksiy.agapitov@gmail.com

A. Artemyev

LPC2E/CNRS University of Orleans, Orleans, France;
Space Research Institute,RAS, Moscow, Russia

H. Breuillard, V. Krasnoselskikh

LPC2E/CNRS University of Orleans, Orleans, France;

G. Rolland

CNES, Toulouse, France

Abstract: VLF waves play a crucial role in the dynamics of radiation belts, and are responsible for the loss and the acceleration of energetic electrons. Modeling wave-particle interactions requires the best possible knowledge of wave energy and wave-normal directions in L-shells for different magnetic latitudes and magnetic activity conditions. In this work, we performed a statistical study for VLF emissions using a whistler frequency range for ten years (2001-2010) of Cluster measurements. We performed a statistical study for VLF emissions using a whistler frequency range for ten years (2001-2010) of Cluster measurements. We utilized data from the STAFF-SA experiment, which spans the frequency range from 8.8 Hz to 3.56 kHz and present distributions of wave magnetic and electric field amplitude and wave-normals in dependence on MLat, MLT, L-shell and geomagnetic activity in a form of probability levels, which were directly applied for electrons diffusion coefficients estimation in the outer radiation belt. The propagation direction of chorus waves rapidly deflects from the magnetic field with the increase of latitude. The width of the distribution increases also. Results were proved by use of numerical ray tracing simulation. Distributions for the diffusion coefficients for day and night sectors and for different geomagnetic activity regimes are obtained. The diffusion coefficients from these distributions are compared with coefficients calculated under assumption of whistler parallel propagation with constant value of variance and wave amplitude along magnetic field line. The increase of the mean value and the variance of the wave vector.

AUTHOR INDEX